Characterization of planetary subsurfaces with permittivity probes : analysis of the SESAME-PP/Philae and PWA-MIP/HASI/Huygens data

Anthony Lethuillier

NNT : 2016SACLV071

THESE DE DOCTORAT
DE
L'UNIVERSITE PARIS-SACLAY
PREPAREE A
L'UNIVERSITE DE VERSAILLES ST-QUENTIN-EN-YVELINES

ECOLE DOCTORALE N° (127)
Astronomie et astrophysique d'Ile-de-France

Sciences de l'Univers

Par

Mr Lethuillier Anthony

Characterization of planetary subsurfaces with permittivity probes: analysis of the SESAME-PP/Philae and PWA-MIP/HASI/Huygens data.

Thèse présentée et soutenue à Guyancourt, le 21 septembre 2016 :

Composition du Jury :

Mme, Carrasco Nathalie	Professeure / UVSQ	Présidente du Jury
Mme, Pettinelli Elena	Professeure / Université de Rome 3	Rapporteur
M, Quirico Eric	Professeur / Université Joseph Fourier Grenoble	Rapporteur
M, Lasue Jérémie	Astronome-Adjoint / Université de Toulouse	Examinateur
M, Lebreton Jean-Pierre	Chargée de Recherche / LPC2E	Examinateur
Mme, Ciarletti Valérie	Professeure / UVSQ	Directeur de thèse
Mme, Le Gall Alice	Maître de Conférences / UVSQ	Co-directeur de thèse
M, Grard Réjean	Chercheur ESA/ESTEC	Invité

université PARIS-SACLAY | ÉCOLE DOCTORALE Astronomie et Astrophysique d'île-de-France

Titre : Caractérisation des subsurfaces planétaires à l'aide de sondes de permittivité : analyse des données SESAME-PP/Philae/Rosetta et PWA-MIP/HASI/Huygens/Cassini-Huygens.

Mots clés : Rosetta/Philae, Cassini/Huygens, comètes, Titan, sous-surface, permittivité

Résumé : Les sondes de permittivité sont des instruments de prospection géophysique non destructifs qui donnent accès aux propriétés électriques, aux basses fréquences (10 Hz-10 kHz), de la proche subsurface. Ce faisant, elles renseignent sur la composition, porosité, température et éventuelle hétérogénéité des premiers mètres sous la surface.

Utilisant généralement 4 électrodes, le principe des sondes de permittivité est simple : il consiste à injecter un courant sinusoïdal de phase et d'amplitude connues entre deux électrodes (dipôle émetteur) et à mesurer l'impédance mutuelle (le rapport complexe entre la tension et le courant injecté) entre ce dipôle émetteur et un dipôle récepteur. La permittivité complexe du matériau de surface, à savoir sa constante diélectrique et sa conductivité électrique, sont alors déduites de la mesure de l'amplitude et de la phase de cette impédance mutuelle. Les fréquences d'opération des sondes de permittivités sont basses là où l'approximation quasi-statique s'applique. A ce jour, les propriétés électriques de seulement deux surfaces planétaires extraterrestres ont été étudiées par des sondes de permittivité : celle de Titan par l'instrument PWA-MIP/HASI/Huygens/Cassini-Huygens et celle du noyau de la comète 67P/Churyumov–Gerasimenko par SESAME-PP/Philae/Rosetta.

Nous présentons la première analyse des données obtenues par SESAME-PP à la surface de la comète 67P/Churyumov–Gerasimenko. Grâce à un travail précis (1) de modélisation numérique de l'instrument et de son fonctionnement, (2) de campagne de mesures (en laboratoire et dans des grottes de glace) afin de valider la méthode d'analyse et (3) d'hypothèses réalistes sur l'environnement proche de la sonde, nous avons pu contraindre la composition et surtout la porosité des premiers mètres du noyau cométaire montrant qu'ils étaient plus compacts que son intérieur. Nous avons également travaillé à une nouvelle analyse des données obtenues en 2005 par PWA-MIP proposant notamment de nouveaux scénarios pour le changement brutal de propriétés électriques observé 11 min après l'atterrissage de Huygens. Ces nouveaux scénarios s'appuient, entre autres, sur les mesures de caractérisation électrique menées au LATMOS sur des échantillons de composés organiques (tholins), analogues possibles des matériaux recouvrant la surface de Titan.

Title: Characterization of planetary subsurfaces with permittivity probes: analysis of the SESAME-PP/Philae and PWA-MIP/HASI/Huygens data.

Keywords: Rosetta/Philae, Cassini/Huygens, Comets, Titan, subsurface, permittivity

Abstract: Permittivity probes are non-destructive geophysical prospecting instruments that give access to the low frequency (10 Hz – 10 kHz) electrical properties of the close subsurface. This provides us with information on the composition, porosity, temperature, and heterogeneity of the first meters of the subsurface.

Using 4 electrodes, the technique consists in injecting a sinusoidal current of known phase and amplitude between two electrodes (transmitting dipole) and measuring the mutual impedance (complex ratio of measured potential over injected current) between this dipole and a receiving dipole. The complex permittivity (i.e. dielectric constant and conductivity) of the subsurface material is derived from the measured phase and amplitude of the mutual impedance. The frequency range of operation of permittivity probes is low, therefore the quasi static approximation applies. To this day the electrical properties of only two extra-terrestrial surfaces have been studied by permittivity probes, the surface of Titan by the instrument PWA-MIP/HASI/Huygens/Cassini-Huygens and the surface of the nucleus of comet 67P/Churyumov–Gerasimenko by SESAME-PP/Philae/Rosetta.

We present a first analysis of the data collected by SESAME-PP at the surface of the comet 67P/Churyumov–Gerasimenko. With the help of (1) precise numerical models of the instrument, (2) field measurements (in a controlled and natural environment) in order to validate the analysis method, and (3) realistic hypothesis on the close environment we were able to constrain the composition and porosity of the first meters of the comet's nucleus, showing that the subsurface is more compact than its interior. We also reanalysed of the data collected in 2005 by PWA-MIP, offering new explanations for the abrupt change in the electrical properties observed 11 minutes after the landing of Huygens. These new scenarios were built in the light of lab measurements performed at LATMOS on samples of organic matter (tholins), possible analogue of Titan's surface material.

"In the beginning the Universe was created. This has made a lot of people very angry and been widely regarded as a bad move."

Douglas Adams

"You need to read more science fiction. Nobody who reads science fiction comes out with this crap about the end of history"

Iain M Banks

To my Grandad,

Acknowledgments

During my three years at LATMOS I have had the opportunity to work, interact, and exchange with many people all around the world, without their help and support this work would not be what it is today.

First and foremost, I would like to thank my two advisors, Alice Le Gall and Valerie Ciarletti who gave me the opportunity to pursue this work and helped me (with a lot of patience) to get through it. It was an honor and a pleasure working under their supervision and they taught me many invaluable lessons which will serve me greatly in the future.

I would like to also thank the people who reviewed my manuscript, Elena Pettinelli and Eric Quirico and those that examined it, Nathalie Carrasco, Jean-Pierre Lebreton and Jérémie Lasue. They helped make this work shine to the fullest.

At LATMOS I was helped immensely by Michel Hamelin and Sylvain Caujolle-Bert who assisted me in many parts of my research. They also had the ungrateful job of explaining electronics to a geologist.

I am grateful to all the members of the SESAME-PP team, Rejean Grard, Walter Schmidt, Klaus J. Seidensticker, Hans-Herbert Fischer and Roland Trautner, and to the Rosetta team in general without whom the SESAME-PP/Philae/Rosetta instrument would not have been possible.

Thanks also to everybody at LATMOS (IT, administration staff, service personnel, engineers and scientists) for making the lab a great work environment, I want to thank the IMPEC team in particular, with whom it was always a pleasure to exchange ideas about our research and who provided many pertinent criticisms that helped me improve as a scientist (especially through the young scientist meetings).

The measurement on tholins would not have been possible without the help of Williams Brett, Francis Schreiber and the ATMOSIM team who provided us with the samples studied.

Finally, but by no means least, a big thanks to all my friends who were always there for me, thank you to my family who always pushed me and helped me get through my studies and gave me the freedom of studying what I loved. A most loving thanks to my wife Alexia for her unbelievable support, proofreading, and cooking; I am infinitely grateful to her for having the patience of dealing with a perpetually distracted husband.

“My gratitude extends beyond the limits of my capacity to express it”

Acronyms

67/C-G	67P/Churyumov–Gerasimenko
ADC	Analog-to-Digital-Converter
APXS	Alpha-P-X-ray Spectrometer
CASSE	Comet Acoustic Surface Sounding Experiment
CIMM	Capacitance-Influence Matrix Method
CIVA	Comet Infrared and Visible Analyzer
CONSERT	Comet Nucleus Sounding Experiment by Radio wave Transmission
COSAC	COmetary SAmpling and Composition
COSIMA	Cometary Secondary Ion Mass Analyzer
DAC	Digital-to-Analog-Converter
DIM	Dust Impact Monitor
EGSE	Electrical Ground Support Equipment
ELF	Extremely Low Frequency
ESA	European Space Agency
FMI	Finnish Meteorological Institute
FPGA	Field-Programmable Gate Array
FSS	First Science Sequence
GIADA	Grain Impact Analyser and Dust Accumulator
HASI	Huygens Atmospheric Structure Instrument
HF	High Frequency
LATMOS	Laboratoire Atmosphères, Milieux, Observations Spatiales
LTS	Long Term Science
MARSIS	Mars Advanced Radar for Subsurface and Ionosphere Sounding
MIDAS	Micro-Imaging Dust Analysis System
MIP	Mutual Impedance Probe
MUPUS	MUlti PUrpose Sensor for Surface and Subsurface Science
MIRO	Microwave Instrument for the Rosetta Orbiter
NASA	National Aeronautics and Space Administration
OSIRIS	Optical, Spectroscopic and Infrared Remote Imaging System
PP	Permittivity Probe

PWA-MIP	Permittivity, Waves and Altimetry-MIP
Radars	RAdio Detection And Ranging
ROLIS	ROsetta Lander Imaging System
ROMAP	ROsetta lander Magnetometer And Plasma monitor
ROSINA	Rosetta Orbiter Spectrometer for Ion and Neutral Analysis
RPC	Rosetta Plasma Consortium
RSI	Radio Science Investigation
RSSD	Research and Scientific Support Department
SD2	Sample Drilling and Distribution
SDL	Separation Descent and Landing
SESAME	Surface Electrical, Seismic and Acoustic Monitoring Experiments
SHARAD	SHAllow RADar
TDEM	Time Domain Electromagnetic Method
UHF	Ultra High Frequency
VES	Vertical Electrical Sounding
VIRTIS	Visible and Infrared Mapping Spectrometer
VLF	Very Low Frequency

Notations

$\vec{E}$	electric field
$\vec{B}$	magnetic field
t	time
$\vec{D}$	electric displacement field
$\vec{H}$	magnetizing field
$\vec{J}_T$	total current density
$\vec{J}_c$	current density
$\vec{J}_D$	displacement current
$\bar{\rho}$	the charge density
$\vec{P}$	polarization field
ε_0	permittivity of free space
μ_0	vacuum magnetic permeability

$\vec{M}$	the magnetization field
χ	electrical susceptibility
ϵ	permittivity
σ	conductivity
ρ	resistivity
ϵ_{eff}	effective permittivity
σ_{eff}	effective electric conductivity
ϵ_r	complex relative permittivity
ϵ_r'	dielectric constant
ϵ_r''	imaginary part of the complex relative permittivity
ω	rotational frequency
$\tan\delta$	loss tangent
ϵ_{rs}	static permittivity
$\epsilon_{r\infty}$	relative high-frequency limit permittivity
τ	relaxation time
T	temperature
k_B	Boltzmann constant
E	activation energy
V	electric potential
ΔV	potential difference
A	period of atomic vibrations
R, r	distances
I	current
Q, q	electric charge
δ_s, δ	geometrical factor of an array
Z_m	mutual impedance
Z_0	mutual impedance in vacuum
Re	real part
Im	imaginary part
δ_{sd}	electrical skin depth
λ	wavelength
v	velocity of the electromagnetic wave

c	velocity of light in vacuum
K_{kn}^{m}	coefficients of the medium capacitance-influence matrix
$[\boldsymbol{K}]$	capacitance-influence matrix of the multi-conductor system
$[\boldsymbol{K^e}]$	electronic matrix
$[\boldsymbol{K^m}]$	environnement capacitance-influence matrix
C	capacitance
P_{surf}	the power of the echoes reflected by the first interface

Index

Introduction

The subsurfaces of planetary objects, i.e. the interface between their deep interior and an atmosphere or a vacuum, are the hosts of exogenic (weathering, thermal stress, impacts, radiations…) and/or endogenic (volcanism, tectonism, …) processes whose signatures may still be measurable. The exploration of planetary subsurfaces has the potential of unveiling these processes and thus the story of the formation and evolution of celestial objects.

Among the techniques developed to study planetary subsurfaces, electromagnetic sounding methods have the advantage of being non-destructive. The first recorded use of such a method dates back to the beginning of the 20th century when Wenner published an article entitled "A method for measuring earth resistivity" in the Bulletin of the Bureau of Standards. Since then, other techniques have been proposed, RADAR being one of the most used, and rapidly found applications in research as well as in industry. However, in space and planetary exploration, the use of electromagnetic method is relatively recent. Earth-based radars were used in the fifties for the observation of the Moon and meteors but the first sounding experiments (Surface Electrical Properties experiment & ASLE) to fly on board a spacecraft was conducted in the frame of the Apollo 17 lunar mission (1967) and the first planetary radar sounder (MARSIS/Mars Express) was sent to Mars in 2004.

Mutual Impedance Probes (MIP), also called Permittivity Probes (PP), are one of these electromagnetic sounding methods. They are commonly used on Earth, in agronomical and archaeological surveys, to map the electrical properties of soils. MIP measure the complex permittivity, i.e. the dielectric polarizability (or dielectric constant) and electrical conductivity, within the first meters below the surface. These parameters depend on composition and physical state (porosity, heterogeneity…) of the subsurface. Monitoring the variation of the permittivity as a function of space (geological structure), time (day, season) and other environmental properties (temperature) thus provides key insights on the subsurface that can be correlated with the data collected by other means.

Mutual Impedance Probes are based on the quadrupole array technique. The principle of the measurement is as follows. The instrument uses 4 electrodes, generally (but not necessarily) in contact with the ground. In the active mode, a sinusoidal current of frequency generally between 10 Hz and 10 kHz, and known phase and amplitude is injected between two electrodes (transmitting monopole), and the voltage induced between two other electrodes (receiving dipole) is measured. The inferred transfer, or Mutual Impedance (MI) of the array in the quasi-static approximation, i.e. the complex ratio of measured voltage upon injected current, gives access to the complex permittivity of the

subsurface at a given frequency that can be varied in the ELF-VLF (Extremely Low Frequency-Very Low Frequency) range. Of importance, at frequencies below 10 kHz, the electrical signature of a material is especially sensitive to the presence of water ice and to its temperature; MIP are thus well suited to the soundings of icy objects such as comets.

To date, two MIPs have flown on space missions. The complex permittivity at low frequency of an extraterrestrial surface was investigated *in situ* for the first time by PWA-MIP/HASI (Permittivity, Waves and Altimetry-MIP/Huygens Atmospheric Structure Instrument) carried by the ESA Huygens Probe that landed on the surface of Titan, the largest moon of Saturn, on 14 January 2005 in the frame of the Cassini-Huygens mission (NASA/ESA/ASI). Almost ten years later, on November 13, 2014, the SESAME-PP/Philae (Surface Electrical, Seismic and Acoustic Monitoring Experiments - Permittivity Probe) performed measurements on the surface of the nucleus of comet 67P/Churyumov-Gerasimenko in the frame of the Rosetta mission (ESA). The present work is dedicated to the analysis of the data collected by SESAME-PP at the final landing site (called Abydos) of the Philae module as well as to the re-assement of the derivation of the complex permittivity of Titan's surface with PWA-MIP/HASI. Titan and comets being of great interest for the understanding of the origin of the Solar System and of life on Earth as well as for the search of potential extraterrestrial life, this work is a contribution to key scientific questions.

The present manuscript is composed of five chapters. The first chapter presents the theoretical background of electromagnetic wave interaction with matter as well as a non-exhaustive review of electrical properties of materials relevant to planetary subsurfaces and of the main electromagnetic sounding methods. The second chapter is dedicated to the description of MIP and the approach that we have developed to analyze their data. If the principle of a MIP is simple in theory, in practice, the conductive environment of the instrument (e.g., due to the vicinity of a lander body), the configuration of operation and the electronic circuit have a strong influence on the measurements and thus on the retrieval of the subsurface electrical properties. To address this issue, a numerical approach, based on the Capacitance-Influence Matrix Method (CIMM), has been proposed. In Chapter 2, we present and validate this approach in order to assess the general performances of MIP (sounding depth, heterogeneous subsurface characterization). In Chapter 3, we present the numerical models especially developed for the analysis of SESAME-PP data and validated them by comparison with measurements performed with a laboratory replica of the SESAME-PP instrument, both in a controlled environment (over a perfect electrical reflector) and over a natural icy surface (in the Austrian caves of Dachstein). Chapter 4 describes the data collected by SESAME-PP at Philae final landing site and their analysis. We emphasize that the analysis approach that we have developed takes into account the attitude of the instrument in its environment, which, in the case of Philae at Abydos, was far from

nominal. We reconstituted the attitude and environment of Philae using all available constraints from other Rosetta instruments. The results of SESAME-PP data analysis and their implications are discussed in the light of other (Rosetta and non-Rosetta) instrument findings. Lastly, we present in Chapter 5 the re-assement of the data collected at the surface of Titan by PWA-MIP/HASI, accounting for new insights on the final resting position of the Huygens capsule. We also propose scenarios to explain the sudden change of the subsurface electrical properties detected about 11 min after Huygens landing. In support of this analysis, laboratory measurements were performed at LATMOS to characterize the electrical properties of tholins, potential analogs of the complex organic molecules formed by photolysis in the atmosphere of Titan. These measurements are presented and used to constrain the composition of the first meters of Titan using PWA-MIP/HASI result.

This work was performed at the LATMOS (Laboratoire Atmosphères, Milieux, Observations Spatiales, UMR 8190) laboratory as part of the IMPEC (Instrumentation, Modélisation en Planétologie, Exobiologie et Comètes) team. It was financed by the Ile-De-France region through a DIM-ACAV (Domaine d'Intêret Majeur – Astrophysique et Conditions d'Apparition de la Vie) grant. The CNES (Centre National d'Etude Spatial) provided financial help for human and material resources. Logistical help was also received from ESA (European Space Agency), RSSD (Research and Scientific Support Department), DLR (Deutsches Zentrum für Luft- und Raumfahrt) and FMI (Finnish Meteorological Institute).

Chapter 1: Characterizing subsurface electric properties

The geophysical sounding of planetary subsurfaces provides clues on their current state and history. Several electromagnetic methods have been developed and used on Earth since the beginning on the 20th century with multiple applications: hydrology (detection of ground water), geology (mapping of stratigraphic layers, detection of fossil hydrocarbons), glaciology (detection of isochronic layers) or even archaeology (detection of buried construction sites and archaeology digs). These methods generally aim at determining, in a non-destructive way, the subsurface electromagnetic properties, namely the dielectric constant ϵ, the electrical conductivity σ (or its inverse, the resistivity ρ), and the magnetic permeability μ. These parameters provide information on the composition, the porosity, the temperature, and the structure of the subsurface.

In Section 1 of this chapter I present the Maxwell laws that control the interaction of electromagnetic fields with matter. Section 2 is dedicated to the state of art on electromagnetic properties of materials relevant to planetary subsurfaces. We then present some of the most used electromagnetic methods, namely, radars, microwave radiometers, vertical electrical sounding, time domain electromagnetic method, self-impedance probes and mutual impedance probes. Finally, we compare these different techniques and show how they are complementary in various ways.

1. Interaction of electromagnetic fields with matter

The electromagnetic investigation methods that will be presented in this manuscript, including the theory behind the two permittivity probes on-board the Rosetta and Cassini missions (SESAME-PP/Philae and PWA-MIP/HASI/Huygens), rely on the interaction of electromagnetic fields with matter as described by Maxwell's equations.

1.1. Maxwell's equations

In the second half of the 19th century, James Clerk Maxwell published a set of differential equations that link the electrical parameters $\vec{E}$ and $\vec{D}$ and the magnetic parameters $\vec{B}$ and $\vec{H}$:

$$\vec{\nabla}\times\vec{E}(\vec{r},t) = -\frac{\partial\vec{B}(\vec{r},t)}{\partial t} \qquad \text{(Faraday's law)} \qquad (1)$$

$$\vec{\nabla}.\vec{D}(\vec{r},t) = \bar{\rho}(\vec{r},t) \quad \text{(Gauss' law)} \quad (2)$$

$$\vec{\nabla}\times\vec{H}(\vec{r},t) = \vec{J}_T(\vec{r},t) = -\frac{\partial\vec{D}(\vec{r},t)}{\partial t} + \vec{J}_C(\vec{r},t) \quad \text{(Ampère's law extension)} \quad (3)$$

$$\vec{\nabla}.\vec{B}(\vec{r},t) = 0 \quad \text{(Gauss law for magnetism)} \quad (4)$$

with $\vec{E}$ [V/m] the electric field, $\bar{\rho}$ [C/m^3] the charge density, $\vec{B}$ [T] the magnetic field, $\vec{D}$[C/m^2] the electric displacement field, $\vec{H}$ [A/m] the magnetizing field, $\vec{J}_c$ [A/m^2] the current density. All the vectors are dependent on space $\vec{r}$ and time t.

Maxwell's equations describe how fields are related, but in order to describe the interaction of these fields with matter, they have to be combined with the constitutive relations which relate the dielectric displacement to the electric field and the magnetic field to the magnetic magnetizing field. The constitutive relations are generally presented in the following form:

$$\vec{D}(\vec{r},t) = \epsilon_0\,\vec{E}(\vec{r},t) + \vec{P}(\vec{r},t) \quad (5)$$

where $\varepsilon_0 = 8.85418782 \cdot 10^{-12}$ m^{-3} kg^{-1} s^4 A^2 is the permittivity of free space and $\vec{P}$ [C/m^2] represents the polarization field.

$$\vec{H}(\vec{r},t) = \frac{\vec{B}(\vec{r},t)}{\mu_0} - \vec{M}(\vec{r},t) \quad (6)$$

with $\mu_0 = 4\pi \cdot 10^{-7}\ \mathrm{H}\cdot\mathrm{m}^{-1}$ being the vacuum magnetic permeability and $\vec{M}$ the magnetization field.

We assume in the rest of the manuscript that the mediums studied are:

I. Linear, i.e. the polarization and magnetization fields evolve linearly with the amplitude of the electromagnetic fields. This can be considered accurate if the amplitudes of the fields are weak.
II. Isotropic, the properties of the material are independent of the orientation of the fields (magnetic or electric).
III. Stationary in time

For such mediums, the polarization field can be written as:

$$\vec{P}(\vec{r},t) = \int_0^{\infty} \epsilon_0 \chi(\tau) \vec{E}(\vec{r}, t-\tau)\, d\tau \tag{7}$$

Considering a harmonic regime, we introduce complex notations for the fields with a time dependence in $\exp(j\omega t)$ and equation (7) becomes in frequency domain (we use the same notation for the functions in time domain or in frequency domain):

$$\vec{P}(\vec{r},\omega) = \epsilon_0\, \chi(\vec{r},\omega) \vec{E}(\vec{r},\omega) \tag{8}$$

with χ the electrical susceptibility defined in the time domain as:

$$\chi(t) = \frac{\epsilon}{\epsilon_0} - 1 \tag{9}$$

and $\chi(\vec{r},\omega)$ the Fourier transform of $\chi(t)$.

$$\chi(\vec{r},\omega) = \frac{\epsilon(\vec{r},\omega)}{\epsilon_0} - 1 \tag{10}$$

In the harmonic regime, the constitutive equation for the electric field is:

$$\vec{D}(\vec{r},\omega) = \epsilon(\vec{r},\omega)\, \vec{E}(\vec{r},\omega) \tag{11}$$

The permittivity ϵ represents the polarization, i.e. the change of position of charged particles to compensate for the applied electric field. Polarization occurs when charged particles move very short distances and/or reorient themselves. The real part of the permittivity represents how easily these charged particles reorient themselves. When charged particles move or reorient themselves they cause a dissipation of energy in the form of heat which is represented by the imaginary part of the permittivity. The complex notation of permittivity is:

$$\epsilon = \epsilon' - i\epsilon'' \tag{12}$$

The total current density flowing through a medium $\vec{J}_T$ [A/m^2], that appears in the Ampère's law extension, can be seen as the sum of the displacement current $\vec{J}_D$ [A/m^2] (that describes the movement of bound charges) and of the conduction current $\vec{J}_C$ [A/m^2] (that describes the movement of free charges). They have the following expression in the time domain:

$$\overrightarrow{J_D}(\vec{r},t) = \frac{\partial \vec{D}(\vec{r},t)}{\partial t} \tag{13}$$

$$\overrightarrow{J_C}(\vec{r},t) = \sigma\vec{E}(\vec{r},t) \tag{14}$$

And in the harmonic regime:

$$\overrightarrow{J_D}(\vec{r},\omega) = i\omega\vec{D}(\vec{r},\omega) \tag{15}$$

$$\overrightarrow{J_C}(\vec{r},\omega) = \sigma(\vec{r},\omega)\,\vec{E}(\vec{r},\omega) \tag{16}$$

Equations (14) and (16) are known as Ohm's law. The electric conductivity σ [S/m] of the matter represents the capacity of motion of free charges in the matter. These free charges can either be electrons or ions. The movement of free charges leads to an accumulation of energy which is represented by the real part of the complex conductivity and also leads to a polarization of the material which contributes to the imaginary part of the conductivity. Its complex mathematical representation is:

$$\sigma = \sigma' + i\sigma'' \tag{17}$$

We often refer to its inverse, called the resistivity ρ $[\Omega \cdot \mathrm{m}]$:

$$\rho = \frac{1}{\sigma} \tag{18}$$

Using equations (11), (15) and (16), we derive the following equation in the harmonic regime (we omitted the frequency and spatial dependence for sake of simplicity):

$$\overrightarrow{J_t} = \overrightarrow{J_C} + \overrightarrow{J_D} = \sigma\vec{E} + i\omega\vec{D} = \sigma\vec{E} + i\omega\left(\epsilon_0\vec{E} + (\epsilon - \epsilon_0)\vec{E}\right) = (\sigma + i\omega\epsilon)\vec{E} \tag{19}$$

From which, we introduce the effective permittivity:

$$\epsilon_{eff} = (\sigma + i\omega\epsilon) \tag{20}$$

Hence:

$$\epsilon_{eff} = \left(\epsilon' + \frac{\sigma''}{\omega}\right) - i\left(\epsilon'' + \frac{\sigma'}{\omega}\right) \tag{21}$$

According to Equation (21) even in a pure dielectric (i.e. $\sigma' = 0$ and $\sigma'' = 0$) the effective permittivity remains complex. The effective permittivity is generally normalized by its vacuum value ϵ_0, and we refer to a relative complex permittivity:

$$\epsilon_r = \frac{\epsilon_{eff}}{\epsilon_0} = \left(\frac{\epsilon'\omega + \sigma''}{\epsilon_0\omega}\right) - i\left(\frac{\epsilon''\omega + \sigma'}{\epsilon_0\omega}\right) = \epsilon_r' - i\frac{\sigma_{eff}}{\epsilon_0\omega} \quad (22)$$

In practice, we only have access to the real and imaginary parts of the relative permittivity. The respective contributions of the conductivity and permittivity to the real and imaginary parts are indistinguishable and only the relative values can be measured. For the remainder of the paper, we will refer to the dielectric constant as ϵ_r', the imaginary part of the relative permittivity as ϵ_r'' and the effective conductivity as σ_{eff} with:

$$\epsilon_r'' = \frac{\sigma_{eff}}{\epsilon_0\omega} \quad (23)$$

To estimate electrical loss, we commonly define the loss tangent $\tan\delta$ that characterizes the dissipation of heat of an electromagnetic wave in matter:

$$\tan\delta = \frac{\epsilon_r''}{\epsilon_r'} \quad (24)$$

Lastly, most non-metallic geologic materials have a magnetic permeability close to that of vacuum, therefore we assume for the rest of the manuscript that μ is that of vacuum. Equation (6) becomes in the harmonic regime:

$$\vec{H}(\vec{r},\omega) = \frac{\vec{B}(\vec{r},\omega)}{\mu_0} \quad (25)$$

1.2. Frequency dependence of the relative permittivity

The electrical properties of a dispersive material are frequency dependent (most materials are dispersive and can only be considered non-dispersive in a defined frequency range). This is related to the different polarization mechanisms at play. There are four different polarization mechanisms that contribute to the total polarization of the matter and therefore to the relative permittivity (Kingery 1976). Each of them is characterized by a specific relaxation time, τ, which characterizes the delay of establishment of the polarization mechanisms in response to the applied electrical field. When the frequency of the applied field is small, all the polarization mechanisms are able to follow the field oscillations. When the frequency is large, some mechanisms are not able to follow the rapidly changing electric field and therefore do not contribute to the total polarization.

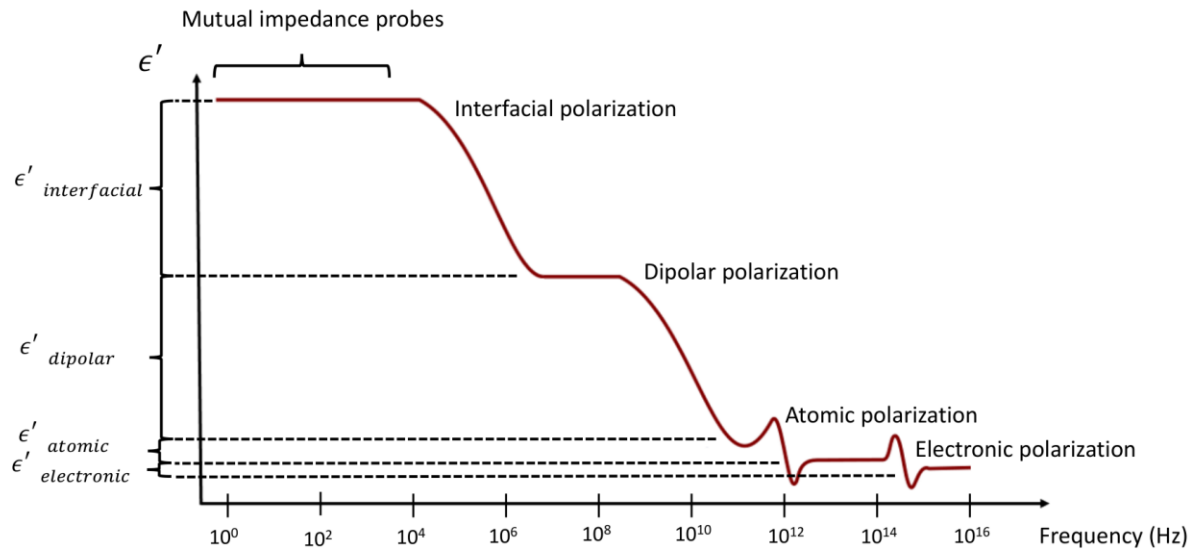

Figure 1: Real part of the permittivity as a function of the frequency of the applied field. The different polarization mechanisms are indicated (adapted from Guéguen & Palciauskas 1994)

Figure 1 represents the contribution of the different polarization mechanisms to the total ϵ' (dielectric constant) as a function of the frequency of the applied field. The mechanisms are:

I. Electronic polarization

Electronic polarization represents the displacement of the electronic cloud around the atoms in response to the applied field.

II. Ionic or atomic polarization

Ionic polarization represents the motion of ions inside a molecule in response to the applied field.

III. Dipolar polarization

Dipolar polarization occurs in polar molecules: permanent or temporary molecular dipoles align themselves opposite to the electric field. Water is particularly affected by this polarization due to the permanent electric moment of the H_2O molecule.

IV. Interfacial or space charge polarization

Interfacial polarization occurs when bound or free charges accumulate at the interfaces between different materials. This mechanism is especially present in heterogeneous mediums. The very long relaxation time associated with space charge polarization makes this mechanism only effective at low frequencies.

The respective contribution to the dielectric constant of these polarization mechanisms depends on the frequency of the applied electric field. Electronic and atomic polarization contribute at all frequencies whereas dipolar and space charge polarizations only contribute at low frequencies. The dielectric constant of a material also depends on its temperature because molecular vibrations and polarization are related to temperature. When the temperature decreases, the orientation and space charge polarization mechanisms become less efficient because the dipoles and charge carriers react more slowly to the changes in the electrical field orientation, resulting in smaller dielectric constants.

1.3. Propagation and diffusion domains

At high frequencies ($\omega \gg \epsilon'/\sigma'$, neglecting σ'' the conductive polarization mechanisms) the conduction currents can be considered negligible when compared to the displacement currents. This is the propagation domain. At low frequencies ($\omega \ll \epsilon'/\sigma'$) the displacement currents can be considered negligible when compared to the conduction currents. This is the diffusion domain. Mutual impedance probes operate at low frequencies (smaller than 10 kHz) and therefore operate in the diffusion domain (for most materials).

It is now pertinent to consider the characteristic values of the electromagnetic properties of materials that could be found on the surface or in the subsurface of planetary objects.

2. Electrical properties of natural matter

The electrical properties of matter vary as a function of composition, porosity, temperature and frequency. The dielectric constant varies from 1 in vacuum to roughly 100 for both water ice at -20°C at ELF (Extremely Low Frequency, 3 Hz to 30 Hz) and liquid water at 20°C in HF (High Frequency, 3 MHz to 30 MHz). The effective conductivity presents much larger variations ranging from 0 in vacuum to 10^{12} S.m^{-1} in superconductive metals. We will present typical values for natural materials found in literature. The frequency domain of validity of some of the measurements and models are restrained because they were performed for the application of a given instrument.

2.1. Water ice

The case of water ice is of great interest for the study of the cold bodies of the Solar System (comets, asteroids, satellites and Kuiper objects). In its pure form, this compound has well known electrical properties that have been investigated by many authors (see Petrenko & Whitworth (2002) for a comprehensive review and, more recently, Mattei et al. (2014)). In the frequency range of the mutual impedances probes ($10 - 10^4$ Hz), the relative complex permittivity of water ice is well described by the Debye model (Debye 1929):

$$\epsilon_r = \epsilon_{r\infty} + \frac{\epsilon_{rs} - \epsilon_{r\infty}}{1 - i\omega\tau} \tag{26}$$

where $\epsilon_{r\infty}$ is the relative high-frequency limit permittivity, ϵ_{rs} the static (low-frequency limit) relative permittivity and τ the relaxation time of water ice in seconds. The relative high-frequency limit of the dielectric constant has a slight temperature dependence that can be approximated by a linear function (Gough 1972):

$$\epsilon_{r\infty}(T) = 3.02 + 6.41 \cdot 10^{-4}\,\mathrm{T} \tag{27}$$

In contrast, the static permittivity, ϵ_{rs} is highly dependent on the temperature; it follows an empirical law established by Cole in 1969 (Touloukian 1981):

$$\epsilon_{rs}(T) = \epsilon_{r\infty} + \frac{A_c}{T - T_c} \tag{28}$$

where T is the temperature in Kelvin; $T_c = 15\ \mathrm{K}$ and $A_c = 2.34 \cdot 10^4\ \mathrm{K}$ were determined by fitting equation (28) to experimental data for temperatures in the range 200 – 270 K (Johari & Jones 1978).

The relaxation time of water ice τ is also temperature dependent; it increases when temperature decreases following the empirical Arrhenius' law, as determined experimentally over the range of temperature from 200 K to 278 K by Auty & Cole (1952) and Kawada (1978) as follows:

$$\tau(T) = A \exp\left(\frac{E}{k_B T}\right) \tag{29}$$

where $k_B\ [\mathrm{eV \cdot K^{-1}}]$ is the Boltzmann constant ($k_B = 8.6173324 \cdot 10^{-5}\ \mathrm{eV \cdot K^{-1}}$), $E = 0.571\ \mathrm{eV}$ is the activation energy of water ice, and $A = 5.30 \cdot 10^{-16}\ \mathrm{s}$ is the period of atomic vibrations (Kovach & Chyba 2001). Separating the real and imaginary parts in equation (26) yields:

$$\epsilon'_r(\omega, T) = \epsilon_{r\infty} + \frac{\epsilon_{rs}(T) - \epsilon_{r\infty}(T)}{1 + \omega^2\tau(T)^2} \tag{30}$$

and,

$$\sigma_{eff}(\omega, T) = \omega^2 \tau \epsilon_0 \frac{\epsilon_{rs}(T) - \epsilon_{r\infty}(T)}{1 + \omega^2\tau(T)^2} \tag{31}$$

The variations with temperature and frequency of the electrical properties of pure water ice as described by equation (30) and (31) are shown in Figure 2 (after extrapolation at low temperatures). These equations provide a fair estimate of the dielectric constant and losses of pure water ice. However, we note that the presence of impurities may significantly affect their validity and increase the conductivity.

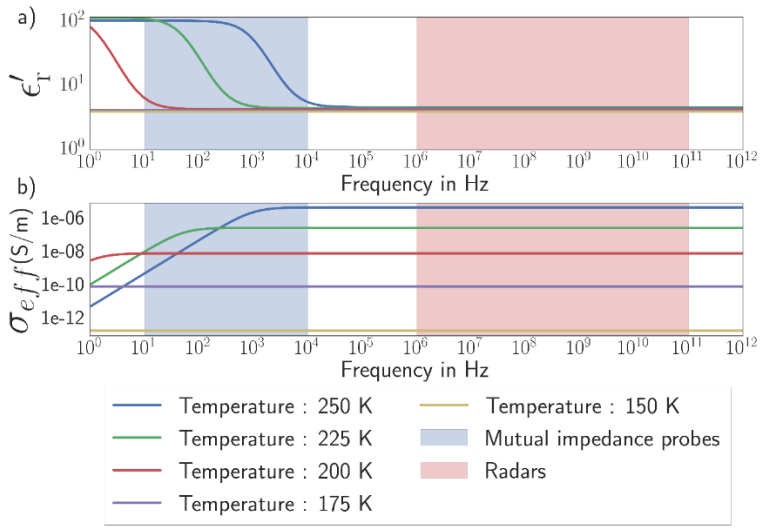

Figure 2: Dielectric constant (a) and electrical conductivity (b) of pure water ice as a function of frequency and temperature. The respective operating frequencies of mutual impedance probes and radars are indicated.

At frequencies below 10^4 Hz, the dielectric constant rapidly decreases with temperature, ranging from ~ 100 at 250 K to ~ 3.1 below 175 K. This is not the case at higher frequencies for which the relative dielectric constant of water ice can be regarded as constant, equal to about 3.1, for all temperatures. Of importance for the analysis of the data collected over a cold objects, such as comets, we highlight that below ~ 175 K, or 150 K according to the laboratory measurements conducted by Mattei et al. (2014), the temperature does not affect the relative dielectric constant of water ice anymore, which remains equal to the high-frequency limit value, i.e. ~ 3.1. This is due to a very long relaxation time at cryogenic temperatures.

The value of the water ice dielectric constant at low frequencies (10 Hz to 10 kHz) and for a moderately low temperature (200 K to 250 K) is especially high (between 10 and 100, as shown in Figure 2) compared to typical planetary surface materials (most of these have a relative dielectric constant lower than 10). Water ice also displays rapid increases in a relatively narrow frequency range (which depends on the temperature at ELF and VLF). This is the reason why surface mutual impedance (see section 4.4) probes are well suited to its detection.

The conductivity of water ice strongly varies with temperature at all frequencies. It decreases when the temperature decreases and progressively loses its frequency dependence. The conductivity increases with the degree of impurity of the ice.

2.2. Liquid water

The complex permittivity of liquid water can also be described by a Debye model. The static permittivity of water has a temperature dependence that has been measured experimentally and is

well modeled in the least square sense by Liebe et al. (1991) in the range of temperatures (-20 °C - 60 °C):

$$\epsilon_{rs}(T) = 77.66 - 103.3\times\left(1 - \frac{300}{T(K)}\right) \tag{32}$$

The high frequency limit permittivity verifies:

$$\epsilon_{\infty} = 0.066\,\epsilon_{rs} \tag{33}$$

and the relaxation time is dependent on temperature as described in Table 1.

Table 1: Relaxation time of liquid water as a function of temperature (from Kumbharkhane et al. 1996)

Temperature (°C)	τ **(ps)**
0	14.8
10	10.3
25	8.7
40	6.9

The variations with temperature and frequency of the electrical properties of pure liquid water as described by equation (32) and (33) are shown in Figure 3. These equations provide a fair estimate of the dielectric constant and losses of pure liquid water. However, pure water is rarely found in natural environments and the presence of impurities may significantly affect their validity and, in particular, increase the conductivity and lower the dielectric constant. Liquid water has a very high dielectric constant (80) in the microwave domain, this is the reason why radars are well suited for its detection.

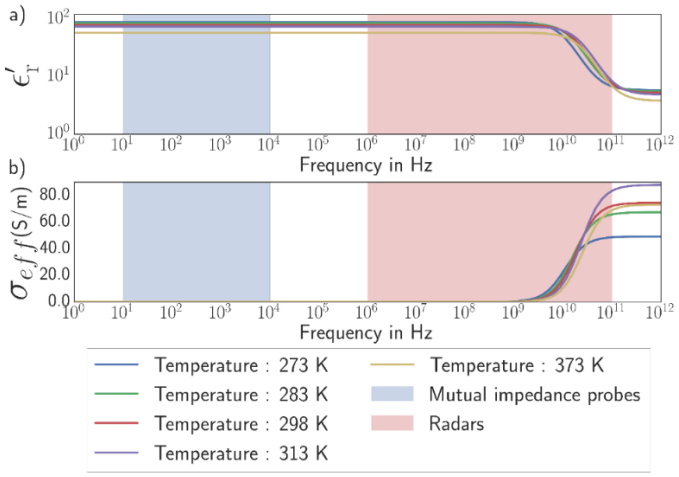

Figure 3: Dielectric constant (a) and electrical conductivity (b) of pure liquid water as a function of frequency and temperature. The respective operating frequencies of mutual impedance probes and radars are indicated.

2.3. Rocks

The term "Rocks" covers a variety of compositions, porosity, density, water content and complex permittivity values. However tendencies can be derived: for example, porosity will systematically diminish the dielectric constant and the conductivity (simply because $\epsilon_{r_{vacuum}} = 1$ and $\sigma_{vacuum} = 0$) while the presence of water (liquid at HF and ice at ELF) will increase the dielectric constant. Further relationships between dielectric constant and water content have been determined empirically but for a limited domain of validity. For example, Topp et al. established in 1980 the following equation:

$$\theta = -5.3 \cdot 10^{-2} + 2.92 \cdot 10^{-2}\epsilon_r - 5.5 \cdot 10^{-4}{\epsilon_r}^2 + 4.3 \cdot 10^{-6}\,{\epsilon_r}^3 \qquad (34)$$

with θ the volumetric liquid water content $[\mathrm{m}^3 \cdot \mathrm{m}^{-3}]$ and ϵ_r the dielectric constant of the subsurface. This equation can only be used in the frequency domain 500 MHz – 1 GHz.

Table 2: Dielectric constant and conductivity of common rocks and materials at two different frequencies in the ELF and HF ranges

Material	$f = 100$ **Hz**		$f = 100$ **MHz**	
	ϵ_r'	σ_{eff} **(S/m)**	ϵ_r'	σ_{eff} **(S/m)**
Sandy soil (dry)	3.41 [a]	N/A	2.56 [a]	10^{-5} [c]
Sandstone	13.0 [a]	10^{-4} [b]	5.20 [a]	1-10^{-3} [b]
Quartz	4.60 [a]	10^{-6}-10^{-5} [b]	4.60 [a]	10^{-5}-10^{-3} [c]
Limestone (dry)	10.4 [a]	10^{-5}-10^{-3} [b]	8.56 [a]	10^{-4}-10^{-3} [b]
Diorite	17 [a]	10^{-5}-10^{-4} [b]	8.57 [a]	N/A
Granite (dry)	8.47 [a]	10^{-5} [b]	6.68 [a]	10^{-8}-10^{-6} [c]

[a](Clark 1966), [b](Lowrie 2007), [c](Davis & Annan 1989)

Table 2 shows values of dielectric constant and conductivity of typical rocky materials. As expected, the dielectric constant is higher at low frequencies due to the additive effect of polarization mechanisms. The conductivity also tends to have lower values at lower frequencies (except for dry granite). Table 2 illustrate the wide range of electrical properties of "rocks"; on Earth this is mainly due to different water content and porosity and one must be cautious when trying to infer composition from the electrical properties. We will later discuss the mixing laws (see Section 3) that can be used to determine the complex permittivity of mixtures of rocks, water, and vacuum.

One must be cautious in using values measured for rocks to infer the composition of a subsurface as these are extremely dependent on the many parameters described above. Whenever possible a sample of material should be characterized by lab measurements.

2.4. Chondrites

The study of chondrites is of particular interest for the exploration of primitive objects such as asteroids and comets and for the origin of organic material on Earth. Chondritic material is indeed the most common material found in non-differentiated, non-metallic asteroids. Chondritic samples are generally found in meteorites (they represent 80% of the meteorites found). They are characterized by the presence of chondrules, round inclusions embedded in a matrix of different composition (see Figure 4).

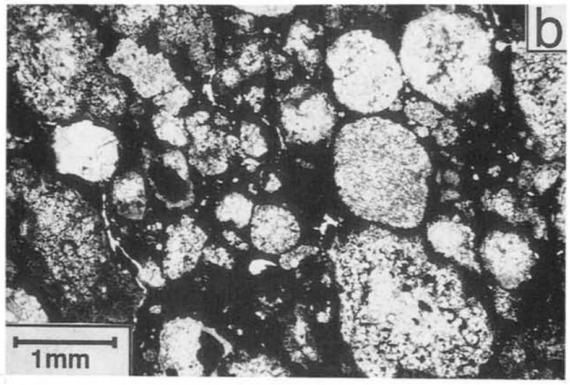

Figure 4: Plane-polarized light photomicrographs of the Renazzo meteorite, the spherical inclusions are the chondrules (Weisberg et al. 1993)

We typically distinguish 15 different types of chondrites based on the composition of the matrix and chondrules (Van Schmus & Wood 1967).The two most common groups are:

- carbonaceous chondrites whose main characteristics are the presence of water, organic compounds, silicates, oxides and sulfides (Mcsween 1977)
- ordinary chondrites which contain mainly silicates but also have a non-negligible amount of iron and iron oxide (Nakamura 1974; Kallemeyn et al. 1989)

Few studies have investigated the electrical properties of chondrites. In particular Fensler et al. (1962) measured the DC conductivity and UHF (Ultra High Frequency, 300 MHz to 3000 MHz) dielectric constant and loss tangent of these two types of chondrites.

Table 3: Dielectric constant, conductivity and loss tangent of chondrites (Fensler et al. 1962)

	ϵ_r'	σ_{eff}	$tan\ \delta$

DC	N/A	$0.08 \cdot 10^{-3}$ - $0.20 \cdot 10^{-3}$	N/A
UHF	11.9 to 45.9	N/A	0.193 to 0.0261

Lab measurements were also performed in preparation for the CONSERT (Comet Nucleus Sounding Experiment by Radio wave Transmission) bistatic radar experiment on board the Rosetta spacecraft. Heggy et al. (2012) studied the electromagnetic properties of ordinary chondrites (LEW 85320, MET 01260 and MAC 88122 are different samples of ordinary chondrites, additional details can be found in Heggy et al. 2012) over a large range of porosities and temperatures. The results are summarized in Figure 5. We note that there seems to be no variation as a function of frequency of either the loss tangent or the dielectric constant in the frequency range from 0.5 to 90 MHz (CONSERT operates at 90 MHz). The values for the dielectric constant are in the range 4.8-6.0 for ordinary chondrites (RKP A79015 is not an ordinary chondrite).

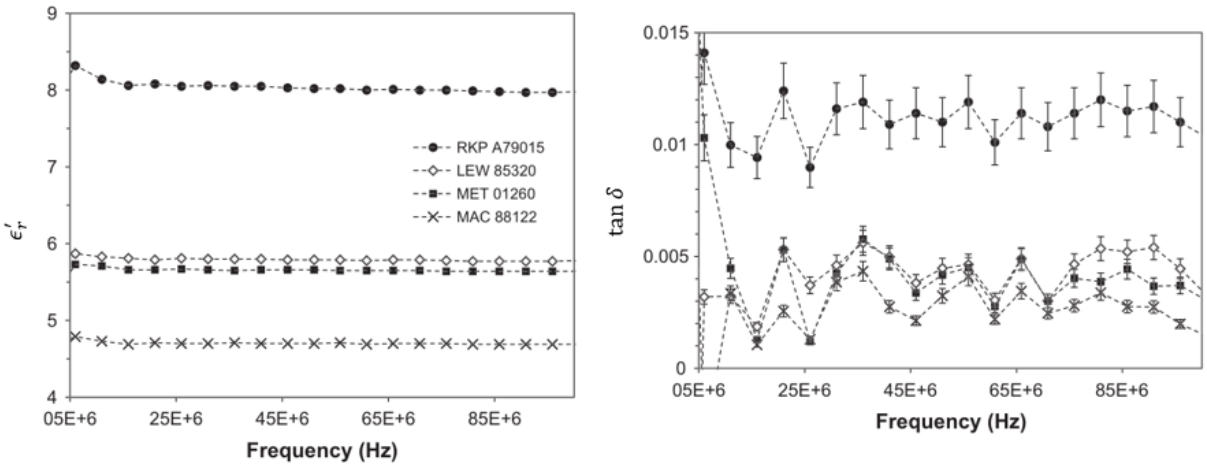

Figure 5: Real part of the complex permittivity and loss tangent of ordinary chondrites as a function of frequency (Heggy et al. 2012)

Additional measurements of the dielectric constant of carbonaceous chondrites are reported in Kofman et al. (2015, see Figure 6). The values for the dielectric constant are in the range 2.9-3.2 (between 20 and 110 MHz) and do not show great variations with frequency.

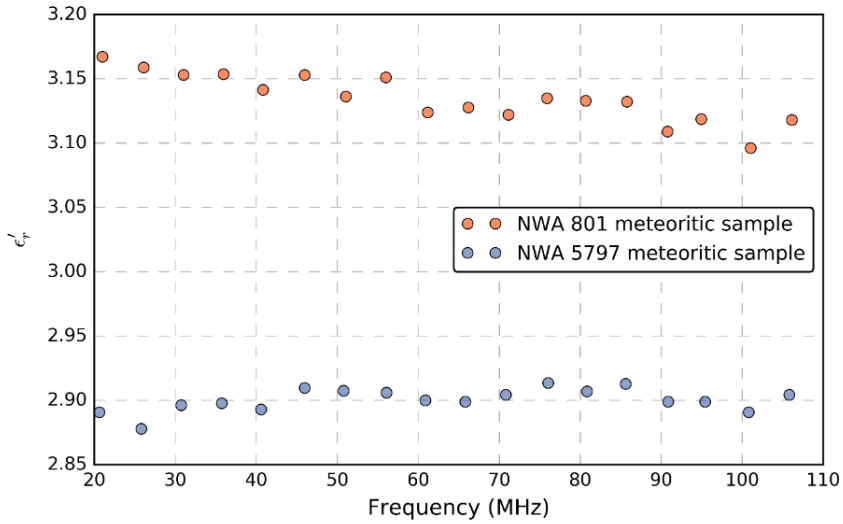

Figure 6: Real part of the complex permittivity of carbonaceous chondrites as a function of frequency. These measurements were made on two meteoritic samples in the CONSERT frequency range (Kofman et al. 2015)

Even if their study did not extend to lower frequencies, they can be extrapolated under certain hypotheses (see Chapter 4, Section Chapter 4:5).

2.5. Lunar regolith

The complex permittivity at HF of lunar regolith sample brought to Earth by the Apollo missions was investigated by Bassett & Shackelford (1972) and Bussey (1978). The values found are reported in Table 4 showing an increasing dielectric constant with frequency (except for the last value) which is unexpected (see section 2.2). This could be explained by the small number of measurements or by the fact that they were performed in the frame of two different studies.

Table 4: Dielectric constants of lunar soil from Bassett & Shackelford (1972) and Bussey (1978).

Frequency (GHz)	ϵ_r'
2.0	2.04
9.375	2.10
18.0	3.71
24.0	3.18

We note that the values are higher than that of carbonaceous chondrites but lower than that of ordinary chondrites.

2.6. Martian analogs

The electromagnetic properties of Martian analogs have been extensively studied in support of two radar sounding experiments: SHARAD/Mars (SHAllow RADar) Reconnaissance Orbiter and

MARSIS/Mars (Mars Advanced Radar for Subsurface and Ionosphere Sounding) Express experiments (Paillou et al. 2001; Heggy et al. 2001; Williams & Greeley 2004; Stillman & Olhoeft 2008; Stillman et al. 2010; Elshafie & Heggy 2013). Figure 7 shows the dielectric constant and loss tangent of the mars simulant JSC-Mars-1 (Allen et al. 1979) analog as function of temperature and frequency (Simões et al. 2004; Simões et al. 2007). We note an increase of the dielectric constant as the frequency decreases and a decrease in the dielectric constant and loss tangent as the temperature decreases.

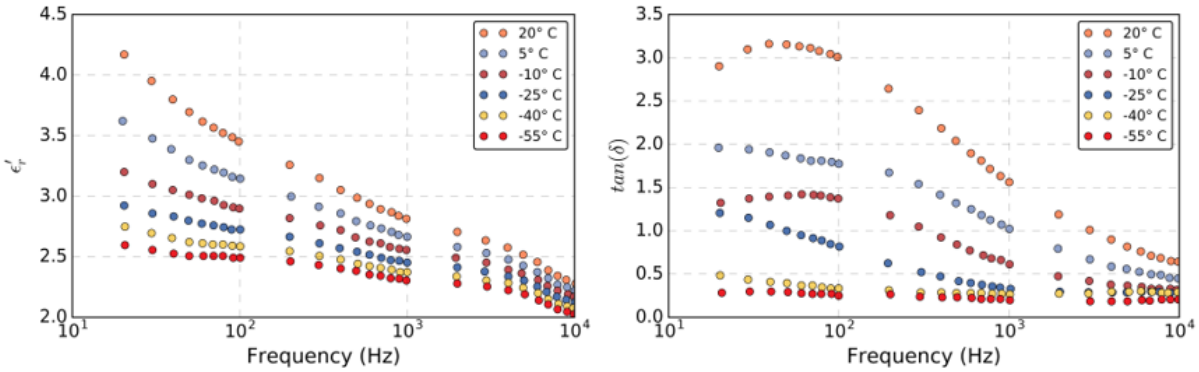

Figure 7: Dielectric constant and loss tangent for the JSC-Mars-1 analog with 1% volumetric water and 54% porosity for 6 different temperatures in the 20 Hz – 10 kHz frequency range (Simões et al. 2004)

2.7. Europa crust analog

Europa, one of Jupiter's moons, is of great interest for the search of life, or at least habitable environment in the Solar System. The surface of Europa is one of the youngest of the solar system. Its crust is composed of silicates-water ice mixture probably overlying a liquid water ocean and the potential presence of thermal vents suggests that conditions similar to those in which life emerged on Earth could exist in this ocean (Chyba et al. 2000). Future missions to Europa and, in particular, the JUICE (JUpiter ICy moons Explorer, ESA) and Europa Clipper (NASA), include ground penetrating radars designed to probe Europa's crust (thought the chances of detection of the underground ocean are very small). the reasons for which the electromagnetic properties of Europa's icy crust were investigated was to estimate the attenuation of the electromagnetic signal and the ability of the instrument to probe depths of the order of several kilometers or a few tens of kilometers. Pettinelli et al. (2016) performed dielectric measurements on ice/$MgSO_4 \cdot 11H_2O$ mixtures, a possible composition for Europa's crust.

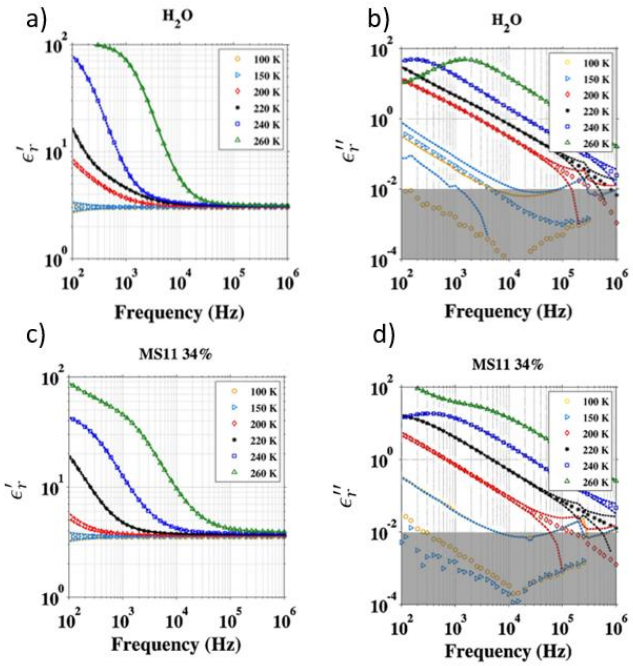

Figure 8: Dielectric constant (a and c) and imaginary part of the relative permittivity (c and d) of Europa's ice crust analog for different $MgSO_4.11H_2O/H_2O$ ratios, a) & b): pure water ice c) & d): 32 % of $MgSO_4.11H_2O$. (from Pettinelli et al. 2016). The grey areas represent the limit of detection of the instrument.

The results, presented in Figure 8 show the real and imaginary parts of the complex permittivity of mixtures as a function of ratio of $MgSO_4/H_2O$, temperature and frequency. As expected both the real and imaginary parts increase with lower frequencies and higher temperatures. The presence of $MgSO_4.11H_2O$ affects mainly, though moderately (compare Figure 8a to Figure 8c), the real part by changing its frequency dependence. The presence of $MgSO_4.11H_2O$ introduces moderate additional losses (compare Figure 8b to Figure 8d). In order to retrieve the permittivity of pure $MgSO_4.11H_2O$, Pettinelli et al. (2016) used a mixing law relating the permittivity of the mixture to the permittivity of the 2 phases and the fraction of $MgSO_4.11H_2O$. In the next section, we will present the most commonly used mixing laws and the hypotheses behind them.

3. Mixing laws

Mixing laws can be used to estimate the electrical properties of planetary surfaces when they consist of a heterogeneous mixture of different compounds and/or phases. They generally apply when the heterogeneities are sufficiently small (a conservative rule of thumb is that the size of the heterogeneities has to be smaller than a tenth of the wavelength, which implies that mixing laws are more accurate at lower frequencies). Numerous mixing laws have been proposed (see Sihvola (1999) for a complete review), We will present here the most common formulas found in literature.

The effective relative permittivity of a homogeneous matrix with small spherical inclusions (Figure 9) can be estimated using the Maxwell-Garnett mixing rule of Effective Medium Theory (Bohren & Huffman 1998):

$$\epsilon_{r_{mixture}} = \epsilon_{r_m} + 3f\epsilon_{r_m} \frac{\epsilon_{r_i} - \epsilon_{r_m}}{\epsilon_{r_i} + 2\epsilon_{r_m} - f\left(\epsilon_{r_i} - \epsilon_{r_m}\right)} \tag{35}$$

where ϵ_{r_m} and ϵ_{r_i} are the complex relative permittivities of the inclusions and the matrix respectively, and f the volume fraction of the inclusions. This law satisfies well the two limits:

$$f \to 0, \qquad \epsilon_{r_{mixture}} \to \epsilon_{r_m}$$

$$f \to 1, \qquad \epsilon_{r_{mixture}} \to \epsilon_{r_i}$$

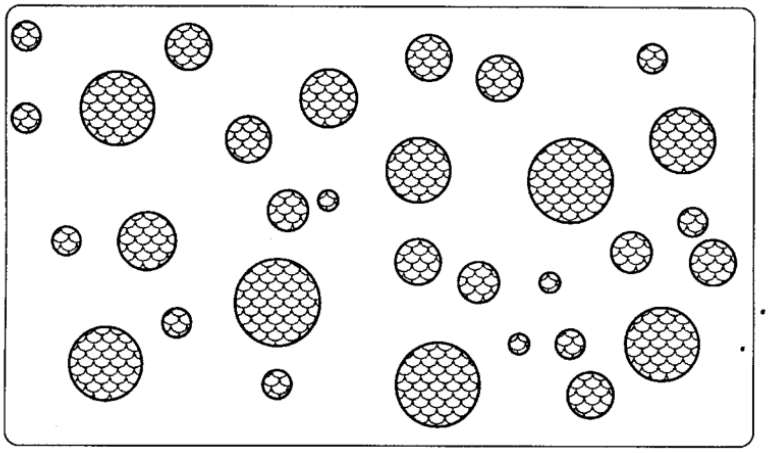

Figure 9: Spherical inclusions in a homogeneous matrix, the size of the spherical inclusions has to be smaller than a tenth of the wavelength of the electromagnetic wave (Sihvola 2000).

The Maxwell-Garnett mixing rule treats one material as the matrix (host material) in which other materials (the guest material) are embedded in the form of small inclusions. However, this model is not symmetric as the host and guest materials do not contribute on an equal basis to the effective permittivity. This is the main shortcoming of this law: it relies on a good assumption of which material is the host and which is the guest. In some cases, this assumption is straightforward but in other, and in particular when the volume fraction of inclusions is close to 0.5, the choice of the host and guest material can have significant impact on the estimate of the mixture permittivity as illustrated by Figure 10.

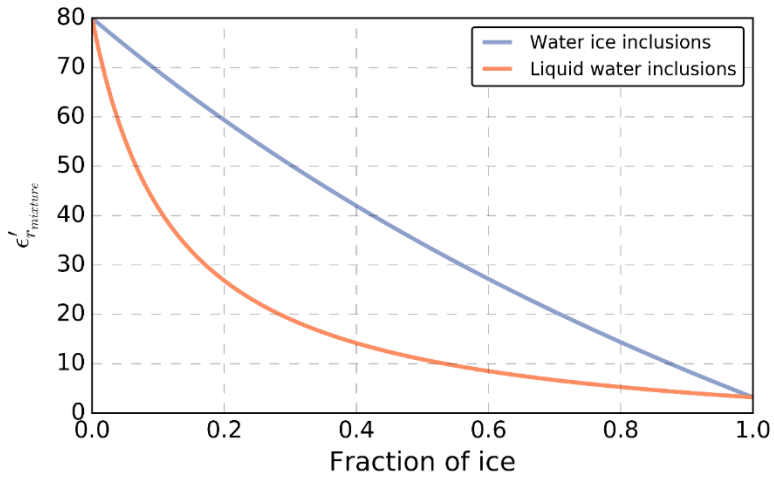

Figure 10: Dielectric constant of a liquid water/water ice mixture at HF ($\epsilon'_{r_{liquid}} = 80$ & $\epsilon'_{r_{solid}} = 3.2$) as inferred with equation (35). The orange curve represents the case of liquid water inclusions in water ice and the blue curve represents the case of water ice inclusions in liquid water. The mixing law is verified in the extreme cases $f_{ice} = 0$ and $f_{ice} = 1$ but between 0 & 1 the dielectric constant is dependant on the choice of matrix/inclusions. It is especially inefficient when the volumetric fraction of inclusions is close to 50%.

Equation (35) can be generalized for a medium with multiple spherical inclusions embedded in the host matrix as follows:

$$\epsilon_{r_{mixture}} = \epsilon_{r_m} + 3\epsilon_{r_m} \frac{\sum_{n=1}^{N} f_n \frac{\epsilon_{r_{i,n}} - \epsilon_{r_m}}{\epsilon_{r_{i,n}} + 2\epsilon_{r_m}}}{1 - \sum_{n=1}^{N} f_n \frac{\epsilon_{r_{i,n}} - \epsilon_{r_m}}{\epsilon_{r_{i,n}} + 2\epsilon_{r_m}}} \tag{36}$$

where $\epsilon_{r_{i,n}}$ is the complex permittivity and f_n the fraction of the n^{th} inclusion type. Equation (36) satisfies well the limit:

$$\sum_{n=1}^{N} f_n \to 0, \qquad \epsilon_{r_{mixture}} \to \epsilon_{r_m}$$

However, when $\sum_{n=1}^{N} f_n = 1$, i.e. when there is no matrix the mixture relative permittivity still depends on ϵ_{r_m}.

The Bruggeman mixing formula is a corrected version of the Maxwell-Garnett formula that does not have the same shortcoming when considering multiphase mixtures (Sihvola 2000):

$$\sum_{n=1}^{N} f_n \left(\frac{\epsilon_{r_{i,n}} - \epsilon_{r_m}}{\epsilon_{r_{i,n}} + 2\epsilon_{r_m}} \right) = 0 \tag{37}$$

We further emphasized that the use of the mixing laws in medium of non-null imaginary part of the relative permittivity is valid only under the condition that the loss mechanisms are the same in the inclusions and in the matrix. In the special case where the matrix has a dielectric constant of ϵ_{r_m}

and the inclusions are purely conductive (with a conductivity σ_{eff_i}) then the global conductivity of the medium can be written (Sihvola 2000):

$$\sigma_{mixture} = \frac{9\epsilon_{r_m}^2 f \sigma_{eff_i}}{2\epsilon_{r_m}^2 + \frac{\sigma_{eff_i}^2}{\omega^2}} \tag{38}$$

The Maxwell-Garnett and Bruggeman formulas are not suitable for dense materials (Sihvola 2000). In these cases, it has been shown that is it more reliable to use the following power law approximation (Sihvola 2000; Zhou et al. 2008):

$$\epsilon_{r_{mixture}}^{\alpha} = \sum_{n=1}^{N} f_n \epsilon_r^{\alpha}{}_n \tag{39}$$

with α the mean depolarization factor and ϵ_{r_n} the relative permittivity of the nth phase type. The depolarization factor typically takes two values: ⅓ in the Birchak formula (Birchak et al. 1974) or 1/3 in the Landau-Lifshitz-Looyenga's formula (Landau et al. 1984).

Rather than taking a fixed value for the relative permittivity of the mixture, it is more conservative to determine a range of values that encompasses all estimates from previously presented formulas. In 1962, Hashin & Shtrikman (1962) defined an upper and lower bound to the range by reworking the Maxwell-Garnett formula (for a 2 phase material):

$$\epsilon_{r_{mixture}}^{min} = \epsilon_m + \frac{f}{\frac{1}{\epsilon_{r_i} - \epsilon_{r_m}} + (1-f)(2\epsilon_{r_m})} \tag{40}$$

$$\epsilon_{r_{mixture}}^{max} = \epsilon_i + \frac{1-f}{\frac{1}{\epsilon_{r_m} - \epsilon_{r_i}} + \frac{f}{2\epsilon_{r_i}}} \tag{41}$$

These bounds correspond to the two cases presented in Figure 10 where we at turn take one of the phases as the matrix and the other as the inclusion. In the case of a three-phase mixture the same formulas can be used by taking alternatively each phase as the matrix and the other two as inclusions. The effective permittivity of the mixture can safely be assumed to lie between the maximum and minimum values. For illustration Figure 11 presents the effective permittivity of the mixture as calculated by the laws mentioned above. We observe that all estimates are included between the Hashin and Shtrikman bounds. These bounds, though probably over conservative, are good tools to avoid the mis-estimation of the effective permittivity of heterogeneous subsurfaces

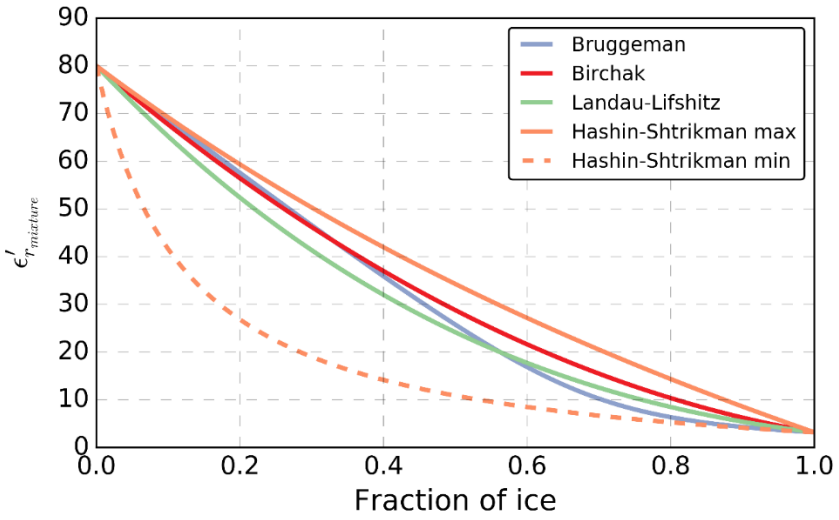

Figure 11: Estimate of the dielectric constant of a liquid water mixture with water ice spherical inclusions using different mixing laws. To be noted is that the Hashin-Shtrikman estimates bound all the others.

As a conclusion, the available mixing laws have their limits and only apply well in specific conditions. A safe assumption is to consider that the relative permittivity of the mixture can be found between the Hashin-Shtrikman bounds. It is recommended, when possible, to directly measure in laboratory the complex relative permittivity of mixtures rather than trying to apply a mixing law. The frequency range reliability of these formulas is dependent on the size of the inclusions: as mentioned previously a conservative rule of thumb is that the size of the inclusions must remain smaller than a tenth of the wavelength (Sihvola 2000). In the case of Mutual Impedance Probes (MIP) the wavelength is very high, making the use of mixing laws justified for this type of instrument.

4. Methods for the characterization of subsurface electric properties

The relative permittivity of the subsurface of planetary objects can be measured with a variety of methods *in situ* or by remote sensing. We will first present methods that can only be used on or close to the surface, i.e. *in situ*. Then, we will describe the radar technique, a technique suitable for many different configurations of operation. Lastly, we will present the passive microwave radiometry which has only been used on orbiters. Other methods exist and this list is not exhaustive.

4.1. Vertical Electrical Sounding (VES)

Historically the first electromagnetic sounding method, the resistivity method patented by Wenner (1916) consists in using a DC generated current to measure the effective apparent resistivity (inverse of the effective apparent conductivity) of the subsurface. The general configuration of operation is presented in Figure 12 where two transmitting electrodes (A and B) deliver a DC current

into the ground and the induced voltage between two receiving electrodes (C and D) is measured. The apparent resistivity is then derived from (Kearey et al. 2013):

$$\rho = \frac{2\pi\Delta V}{I\left\{\left(\frac{1}{r_B} - \frac{1}{r_B}\right) - \left(\frac{1}{R_A} - \frac{1}{R_B}\right)\right\}} \tag{42}$$

with ΔV the potential difference between the two receiving electrodes, I is the injected current and r_A, r_B, R_A and R_B are the distances between the pin point electrodes as indicated in Figure 12.

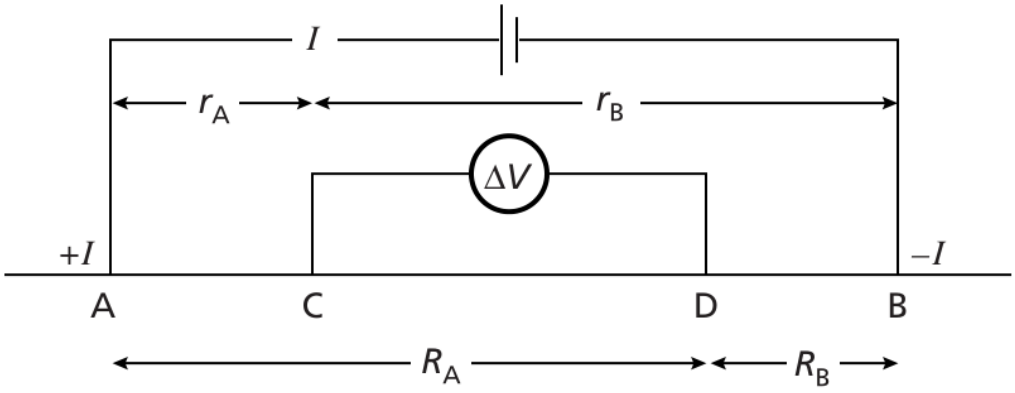

Figure 12: General setup of a resistivity measurement (Kearey et al. 2013).

By setting different distances between the electrodes, it is possible to sound multiple depths and thus map the vertical variations of the resistivity. By moving the system, it is also possible to map the horizontal variations of apparent effective conductivity. The true conductivity of the subsurface can be retrieved by inversions based on models. This method is used mainly on Earth for hydrogeological investigations (due to the high conductivity of ground water), the detection of groundwater pollution (Merkel 1972) and to investigate future construction sites (Barker 1997). The typical output of this method is a horizontal and vertical resistivity map of the subsurface as shown in Figure 13.

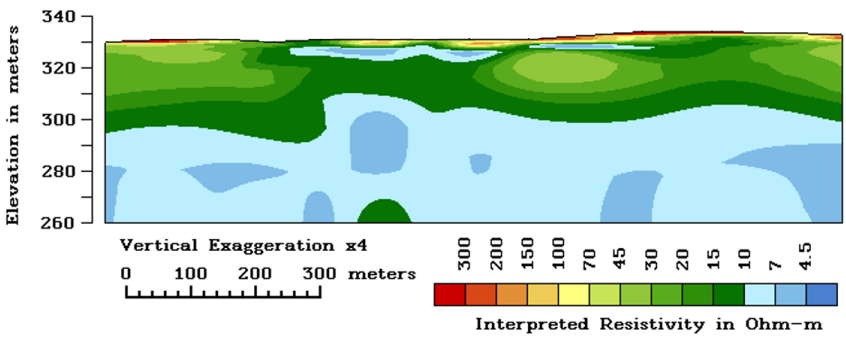

Figure 13: Typical output of a resistivity sounding. The resistivity of the subsurface is mapped horizontally and vertically (Geological Survey, USGS.gov).

4.2. Time Domain Electromagnetic Method (TDEM)

Time Domain Electromagnetic Methods were developed in Russia in the eighties. It involves in a transmitter loop (generally square shaped) in which we inject a periodic square wave current (see Figure 14).

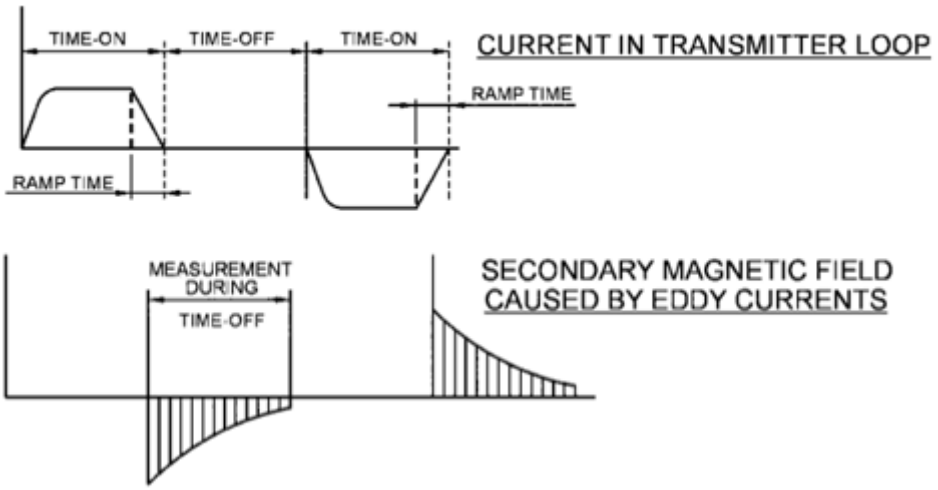

Figure 14: Shape of the current pulse in the transmitting coil and of the measured secondary magnetic field (Adams & Hinze 1990).

The current pulse generates a magnetic field (called primary magnetic field) when it falls to 0 (i.e. at the beginning of the time-off (see Figure 14), then, according to Faraday's law, this primary magnetic field induces horizontal current loops (called Eddy currents) in the subsurface that progressively extend vertically and horizontally (see Figure 15). Each Eddy current loop decreases in amplitude with depth following a law that depends on the conductivity of the subsurface. In turn, these current loops generate a secondary magnetic field that can be measured with a receiving coil on the surface with a separate receiver or with the same loop as in transmission.

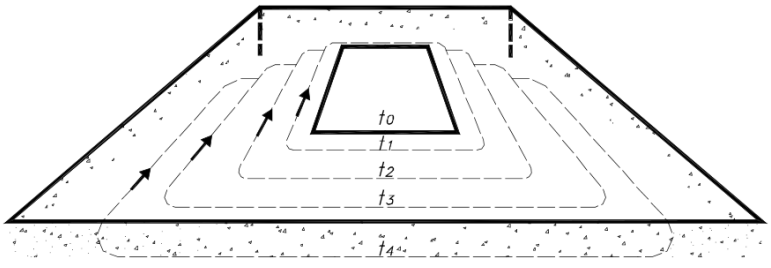

Figure 15 Transmitting coil (t0) and induced Eddy current (t1 to t4) in the subsurface (Barrocu & Ranieri 2000).

The effective conductivity is derived from (Adams & Hinze 1990):

$$\frac{1}{\sigma_{eff}(t)} = \frac{\mu_0}{4\pi}\left[\frac{2I_0\mu_0 k}{5t^{\frac{5}{2}}V(t)}\right]^{2/3} \quad (43)$$

with I_0, the current injected into the transmitting loop, k a constant that takes in account the size of the receiving and transmitting loops, t the time elapsedsince the beginning of the time-off (see Figure 14) and $V(t)$ the potential measured with the receiving coil. The longer the time t, the deeper the sounding.

The TDEM sounding does not require long electrode arrays and can therefore be deployed in areas with space constraints. It also has the advantage of having a higher depth resolution than VES and is also less affected by the presence of a resistive layer on the surface. A typical output of the technique is shown in Figure 16.

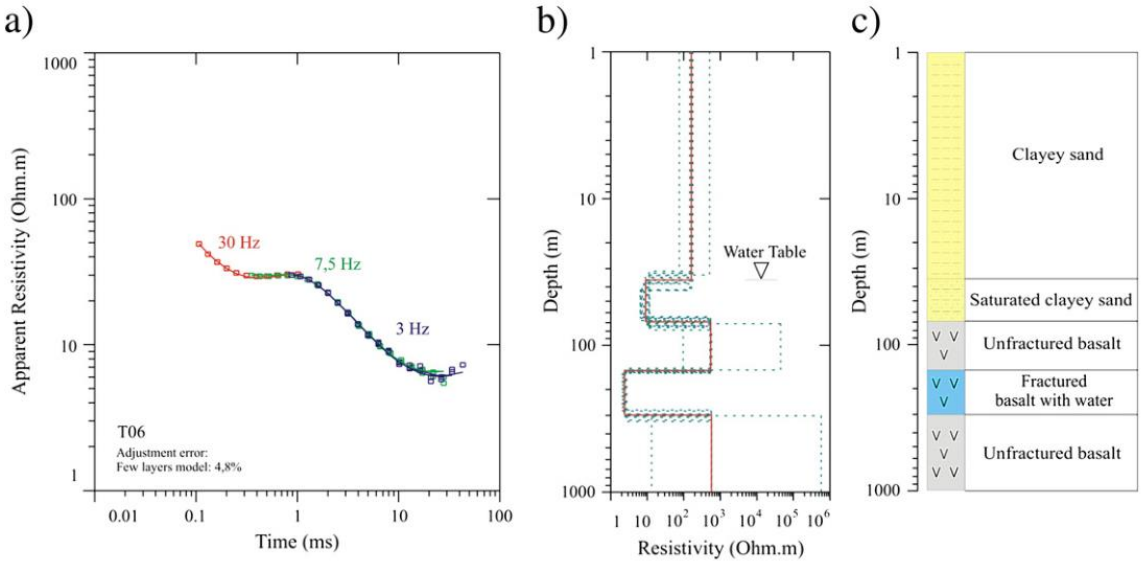

Figure 16: a) Apparent resistivity as a function of time since time-off for three different frequencies. b) Derived resistivity as a function of depth. c) Geological interpretation of the detected layers. The area studied was Northern São Paulo State, Brazil (Porsani et al. 2012).

TDEM based instruments have been envisioned for the subsurface sounding of Mars as they are very sensitive to saline groundwater that could be present in the subsurface (Grimm 2003; Vannaroni et al. 2004). This technique is well suited to space missions because the electrodes can be relatively small and can still perform efficiently without a good surface contact (Filippini et al. 2003).

4.3. Self-impedance probes

Self-impedance probes use the coupling of an electric dipole (Figure 17) with a surface to derive the complex permittivity of the subsurface. A sinusoidal low-frequency (diffusive regime)

current I is injected by two transmitting electrodes and we measure the induced potential difference between them. The charge on the electrodes is:

$$q = \frac{Ie^{-\frac{i\pi}{2}}}{2\pi f} \tag{44}$$

The potential created by a point charge q in an infinite medium of relative permittivity ϵ_r is:

$$V(r) = \frac{q}{4\pi\epsilon_0\epsilon_r r} \tag{45}$$

with r the distance to the charge. In the case of a dipole made of two spherical electrodes of radius a and separated by a distance l, the potential on the surface of each electrode is (see Chapter 2 Section 3.1 for details):

$$\mathrm{V}_1 = \frac{q}{4\pi\epsilon_0\epsilon_r}\left[\frac{1}{a} - \frac{1}{l-a}\right] \tag{46}$$

$$\mathrm{V}_2 = \frac{q}{4\pi\epsilon_0\epsilon_r}\left[\frac{1}{l-a} - \frac{1}{a}\right] \tag{47}$$

And the potential difference can be written as:

$$\Delta V = V_1 - V_2 = \frac{q}{2\pi\epsilon_0\epsilon_r}\left[\frac{1}{a} - \frac{1}{l-a}\right] \tag{48}$$

The measured self-impedance for electrodes located at an interface (Figure 17) is thus:

$$Z_s = \frac{\Delta V}{I} = \frac{\mathrm{e}^{-\frac{i\pi}{2}}}{\omega 2\pi\epsilon_0(\epsilon_r + 1)}\delta_s \tag{49}$$

with ω the angular frequency, ϵ_0 the vacuum permittivity, δ_s [m^{-1}] the dipoles geometrical factor defined as:

$$\delta_s = \left[\frac{1}{a} - \frac{1}{l-a}\right] \tag{50}$$

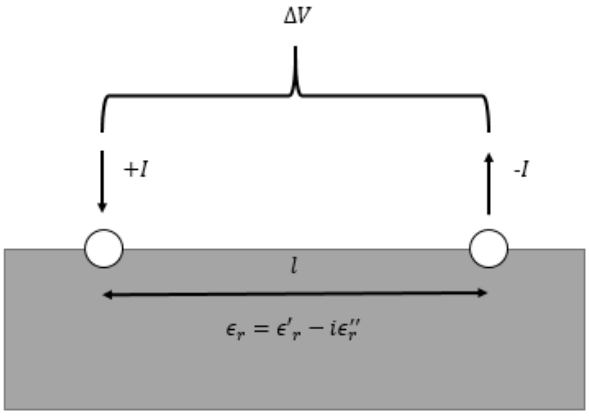

Figure 17: Schematic representation of the self-impedance dipole with two spherical electrodes with a radius $\boldsymbol{a}$ over a subsurface with a relative permittivity $\boldsymbol{\epsilon_r}$.

The complex permittivity of the subsurface on which the probe is lying can be derived from Equation (49).

One can measure the current I injected into the dipole and the potential difference ΔV induced between them and then derive the relative permittivity from their ratio.

The main shortcomings of the self-impedance probe method are its shallow sounding depth (see Chapter 2, Section 4.2) and its sensitivity to the presence of heterogeneities close to the electrodes. The use of a quadrupole allows to overcome these two shortcomings.

4.4. Mutual impedance probes (MIP)

The two permittivity probes that are the focus of this manuscript, namely the SESAME-PP/Philae instrument operated on the nucleus of comet 67P/Churyumov–Gerasimenko (67/C-G) and the PWA-MIP/HASI/Huygens instrument used on Titan, are based on the MIP investigation method. Before going into the detail of the theory behind this method (see Chapter 2), and in the interest of comparing it to the methods previously described, we will briefly summarize the main features of the MIP technique.

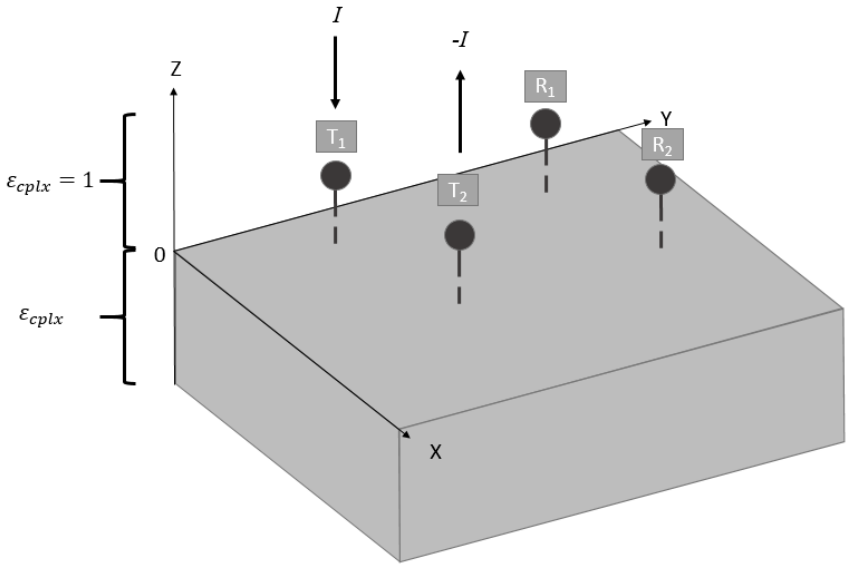

Figure 18: Schematic representation of the mutual-impedance quadrupole with a transmitting dipole (T1 and T2) and a receiving dipole (R1 and R2) over a subsurface with a relative permittivity ϵ_r

The MIP technique consists in injecting an alternating low frequency current into the subsurface with two transmitting electrodes capacitively coupled with the surface and measuring the induced potential on two receiving electrodes located at a certain distance (Figure 18). The amplitude and phase variation between the injected current and the received potential difference is related to the electric properties of the subsurface which can be retrieved by the following equation (the mathematical development of this equation will be presented in Chapter 2, Section Chapter 2:1.2 and can be found in Grard et al. 1990):

$$\varepsilon_r' = Re\left(\frac{Z_0(\delta+1) - Z_m}{Z_0(\delta-1) + Z_m}\right) \tag{51}$$

$$\sigma_{eff} = \omega\epsilon_0 Im\left(\frac{Z_0(\delta+1) - Z_m}{Z_0(\delta-1) + Z_m}\right) \tag{52}$$

with Z_0 [Ω] the mutual impedance of the quadrupole in vacuum, Z_m [Ω] the mutual impedance of the quadrupole on a surface assumed to be horizontal and δ the geometrical factor of the quadrupole (defined in Chapter 2, Equation (71)). The MIP technique has a theoretical sounding depth close to the distance separating the electrodes (see Chapter 2, Section 4.2). In order to ensure the simultaneous determination of the dielectric constant and conductivity with similar accuracy MIP are generally operated at a frequency in the order of (Grard et al. 1990):

$$\omega_0 = \frac{\sigma_{eff}}{\epsilon_0 \epsilon_r'} \tag{53}$$

for which the real and imaginary parts of the relative permittivity are equal. On Earth, the electrical properties of the ground are dependent on temperature and very dependent on moisture content; they are typically $\epsilon'_r = 20$ and $\sigma_{eff} = 10^{-2}$ S/m for rocks and sediments (see Section 2.3), which implies an optimal working frequency of ~10 MHz. On an icy body at cryogenic temperatures and, in particular, on the surface of a comet, the expected conductivity is much lower ($10^{-8} - 10^{-5}$ S/m, see Section 2.1), which leads to a much lower optimal working frequency range of $10 - 10^4$Hz.

4.5. Radars

Radars (Davis & Annan 1989) characterize the subsurface of planetary bodies by studying the propagation of electromagnetic waves through them. Depending on their design, radars can be used from the surface or in remote-sensing and operate in reflection or transmission (though more rarely). High frequency (MHz to GHz) electromagnetic waves are transmitted between two antennas or emitted and received by the same antenna.

4.5.1. Radars in reflection

When an electromagnetic wave encounters a change in electromagnetic properties, part of the energy is reflected and the rest is transmitted or absorbed. GPR measure the delay and amplitude of each received echoes. In case of a reflection upon an interface between a medium and vacuum P_{surf} (the power of the echoes reflected by the first interface) is given by:

$$P_{surf} = \frac{P_T(GR)\lambda^2}{4\pi^2 d} \tag{54}$$

with d the distance between the target and the antenna. G the antenna gain, λ the wavelength of the transmitted signal and R the Fresnel coefficient between the vacuum and the top layer of the subsurface defined as (for vertical incidence):

$$R = \frac{\left(\sqrt{\epsilon'_{r_{top}}} - \sqrt{\epsilon'_{r_{bot}}}\right)^2}{\left(\sqrt{\epsilon'_{r_{top}}} + \sqrt{\epsilon'_{r_{bot}}}\right)^2} \tag{55}$$

with $\epsilon'_{r_{top}}$ the dielectric constant of the top layer (vacuum in the case of the surface echo, i.e. $\epsilon'_{r_{top}} = 1$) and $\epsilon'_{r_{bot}}$ the dielectric constant of the bottom layer.

If secondary echoes are received it is possible to derive the dielectric constant of this deeper layer and the conductivity of the top layer using:

$$\frac{P_{subsurf}}{P_{surf}} = A_{Att}\left(\frac{R'}{R}\right) \quad (56)$$

with P_{surf} the power of the echoes reflected by the first interface (the one separating vacuum and the surface), $P_{subsurf}$ the power of the echoes reflected by the second interface (the one separating the surface layer and the second layer), R the Fresnel coefficient of the first interface, R' the Fresnel coefficient of the second interface and A_{Att} the attenuation in the medium due to electrical loss (from both polarization and conduction) and in the case of low loss medium with negligible scattering (i.e. with heterogeneities smaller than the wavelength λ) :

$$A_{Att} = e^{-\frac{2\pi\epsilon_r''}{\lambda\sqrt{\epsilon_r'}}2d} \quad (57)$$

with ϵ_r' the dielectric constant and $\epsilon_r''$the imaginary part of the surface layer. The amplitude of the echoes received from the subsurface can be used to constrain the loss and dielectric constant of the upper layer.

Radars in reflection are widely used in geophysics and archeology (Dabas et al. 2000). They are also very suited for hydrogeological exploration due to the high dielectric constant of liquid water in the HF range (see Section 2.2). The sounding depth, also called “penetration depth” of a radar, depends on the operating frequency (the lower the frequency of operation the larger the sounding depth) and on the absorption and scattering properties of the material. More specifically, it can be approximated by the electrical skin depth defined as the distance at which the amplitude of the electromagnetic wave is dampened by a factor $\frac{1}{e} = 37\%$:

$$\delta_{sd} = \frac{\lambda}{4\pi}\left(\frac{\epsilon'}{2}\left(\sqrt{1+tan\delta^2}-1\right)\right)^{-1/2} \quad (58)$$

Radars have also been used for extra-terrestrial subsurface soundings, for example the SEP (Surface Electrical Properties experiment) and ASLE (Apollo 17 Lunar and Sounder Experiment) experiments allowed the characterization of the first kilometer of the lunar regolith (Simmons et al. 1972; Olhoeft & Strangway 1975), the SHARAD (Seu et al. 2007) and MARSIS experiments (Mouginot et al. 2012, see Figure 19) are currently studying the subsurface of Mars. The radar of Cassini (Elachi et al. 2005) revealed the surface of Titan through the opaque veil of its atmosphere and, using the Cassini radar (in altimetry mode), data Mastrogiuseppe et al. (2014) were able to determine the loss tangent of the Ligeai Mare lake on Titan ($\tan\delta = 4.4^{+0.9}_{-0.9}\times10^{-5}$) consistent with liquid hydrocarbons (71% CH_4, 12% C_2H_6, 17% N_2). Additionally, a maximum depth of 160 m was also inferred.

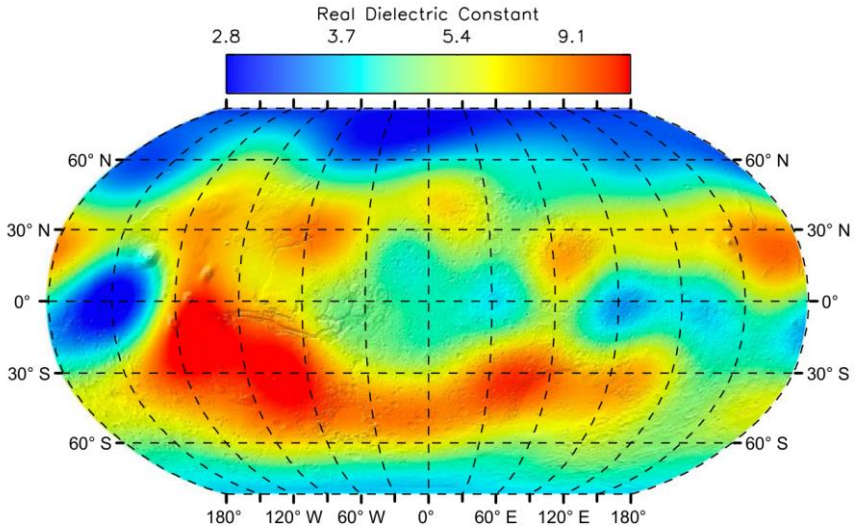

Figure 19: Dielectric constant on the surface of Mars derived from MARSIS radar measurements at 4 MHz (Mouginot et al. 2012).

4.5.2. Radars in transmission

The transmission method involves a separate emitter and receiver located around the object to be studied (see Figure 20 for an example). The electromagnetic waves travel through the object and the measured propagation delay gives access to the dielectric constant (its value drives the waves velocity for low loss materials):

$$v = \frac{c}{\sqrt{\mu_r \epsilon_r'}} \tag{59}$$

with c the velocity of light in vacuum. The attenuation of the received signal is indicative of the loses in the materials and can be related to the conductivity.

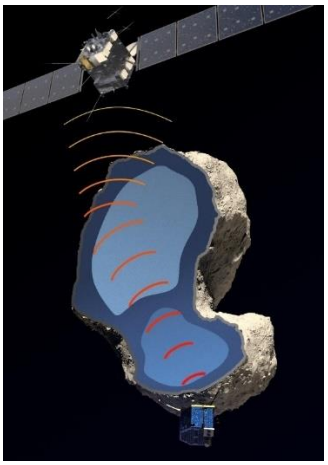

Figure 20: Schematic representation of the radar in transmission where the lander transmits the signals that travels thought the comet and is received by the lander. Credits: ESA/ATG medialab

The most recent example of such a radar is the bistatic radar CONSERT onboard Rosetta. From the time of arrival of the signal Kofman et al. (2015) estimate the dielectric constant of a part of the 67P/C-G nucleus to be ~1.3, consistent with a very porous and carbonaceous chondritic comet.

4.6. Microwave radiometers

Microwave radiometers are instruments designed to measure the thermal emission from a surface at sub-millimeter to centimeter wavelengths. Radiometers give access to the surface brightness temperature which, in the Rayleigh-Jeans domain, is proportional to the surface emissivity. In the case of a smooth surface the emissivity is:

$$e_p(\theta, \phi) = 1 - R_p(\theta) \tag{60}$$

with θ the angle of observation and R_p the Fresnel reflection which, depending on the polarization p (perpendicular or parallel), is defined as:

$$R_\perp(\theta) = \left(\frac{cos\theta - \sqrt{\epsilon'_r - \sin^2\theta}}{cos\theta + \sqrt{\epsilon'_r - \sin^2\theta}} \right)^2 \tag{61}$$

$$R_\parallel(\theta) = \left(\frac{\epsilon cos\theta - \sqrt{\epsilon'_r - \sin^2\theta}}{\epsilon cos\theta + \sqrt{\epsilon'_r - \sin^2\theta}} \right)^2 \tag{62}$$

The sounding depth is estimated in the same way as radars with Equation (58). The degree of polarization (i.e. $\frac{e_p - e_p}{e_p + e_p}$) of the measured thermal emission is thus related to the effective dielectric constant of the surface and can be used for its estimation. The map of ϵ'_r of Titan (Figure 21) was obtained in this way from polarized observations of the Cassini radiometer (Janssen et al. 2009; Janssen et al. 2016).

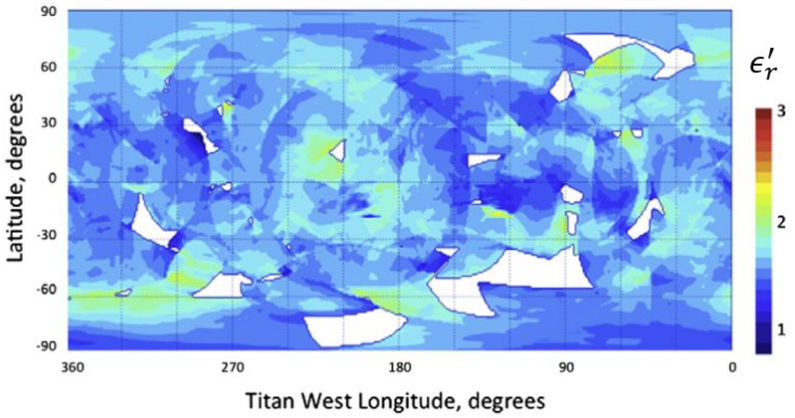

Figure 21: Dielectric constant derived from the Cassini radiometer measurements at 2cm wavelength (Janssen et al. 2016).

The dielectric constant of the Moon's surface was mapped by the Chang'E-1 (CE-1) probe in 2007 (Figure 22) in the frequency range 3.0-37.0 GHz, using the brightness temperatures mapped by the CELMS instrument (CE-2 Lunar Microwave Sounder). The Moon's dielectric constant is higher on the far side and patches of brighter ϵ'_r can be seen on the South Pole whereas it appears more uniform for the North pole. The values are in the range of those presented in section 3.1.5 and the differences are probably due to porosity variations on the surface (Wang et al. 2010).

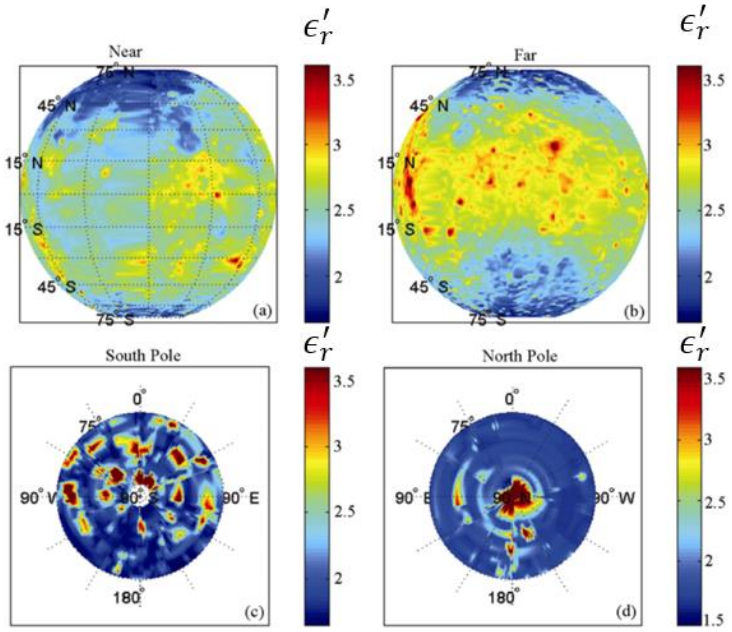

Figure 22: Dielectric constant of the Moon's subsurface as measured by the CELMS passive microwave radiometer 3.0, 7.8, 19.35, and 37.0 GHz (Wang et al. 2010).

4.7. Comparing techniques

The techniques described above represent multiple ways of measuring the complex permittivity of the subsurface of planetary objects. These methods are complementary in two ways. First, since these techniques are not operated in the same frequency domain, they provide complementary information on the investigated subsurface (Figure 23). For example, mutual impedance probes operating at very low frequencies are efficiently used for the detection and estimation of the shallow subsurface water ice content, while high-frequency measurement instruments such as radars are better suited for the detection of liquid water, which has a high dielectric constant (80) in the HF domain. The operating frequencies of the instrument determine the electromagnetic laws that describe the interaction of the electromagnetic waves with matter: high frequencies in the propagation domain and at low frequencies in the diffusion domain.

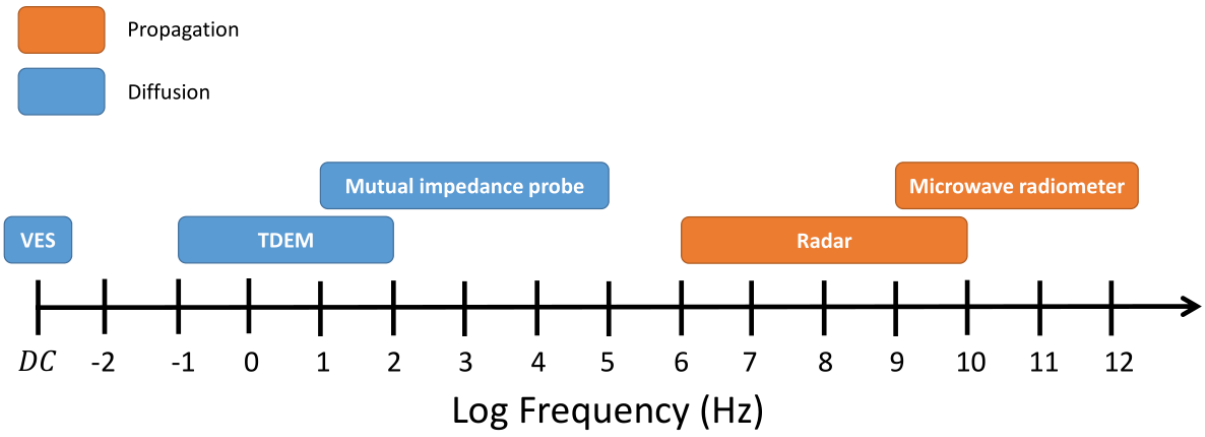

Figure 23: Frequency ranges of different electromagnetic subsurface exploration methods

Second, the techniques have different sounding capabilities. Figure 24 represents the theoretical sounding depths of the different electromagnetic methods. The sounding depth in the propagation domain is dependent on the loss tangent of the sounded material and on the frequency range of the instrument. In the diffusion domain, the sounding depth is dependent of the distance between the electrodes.

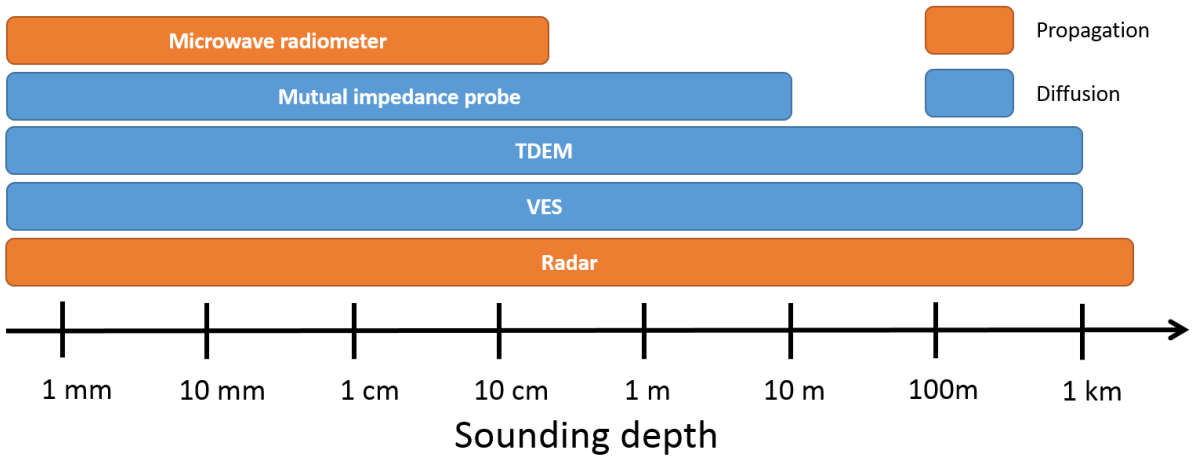

Figure 24: Sounding depth of different electromagnetic subsurface exploration methods

5. Concluding remarks

In this chapter, we first presented the theoretical background required for understanding the electromagnetic investigation of planetary subsurfaces. We described how these parameters are linked and presented the microscopic mechanisms at play. We also showed that the parameters measured encompass multiple phenomena that cannot be separate. Only an integrated complex quantity called the relative permittivity can be measured:

$$\epsilon_r = \epsilon_r' - i\epsilon_r''$$

We then presented the complex permittivity of water in its solid and liquid form and that of rocks and minerals found on Earth, as well as results derived from extraterrestrial rocks or analogs.

Lastly, we briefly described the methods and instruments that give access to the relative permittivity of subsurfaces. We showed how they are complementary in frequencies and sounding depths.

As mentioned previously, the two instruments that we will study in the rest of the manuscript are based on the mutual impedance probe technique. This method, albeit simple in theory, requires the development of a sophisticated analysis method. In the next chapter, we present a more detailed description of MIP and explain how their shortcomings can be overcome.

Chapter 2: Mutual Impedance Probes, numerical modelling and performances

The SESAME-PP/Philae and PWA-HASI/Huygens instruments are both mutual impedance probes designed to operate on or near the surface of planetary objects. They are based on the quadrupole array technique; an electric investigation method that allows a non-destructive sounding of the subsurface of planetary objects. They are cost, energy and space efficient instruments that can easily be added on landers (Grard et al. 1995; Seidensticker et al. 2007) or rovers (Hamelin et al. 2003; Vannaroni et al. 2004; Del Vento & Vannaroni 2005) to explore the low frequency electrical properties of the first meters of the subsurface of planetary objects.

We will first present the history and theoretical background of mutual impedance probes in planetary exploration. Although their principle applies well to isolated idealized pinpoint electrodes, it must be adapted in the case of more complex and realistic configurations of operation. We will illustrate these shortcomings by comparing simple examples to more realistic cases. To overcome these shortcomings a new method was developed. This method, baptized the Capacitance-Influence Matrix Method (CIMM), relies on numerical simulations performed with the help a finite element analysis software (COMSOL Multiphysics©). We will present its theoretical background, capabilities and limitations as well as its validation by comparison to results obtained in cases that can be solved analytically. Lastly, we will use the CIMM and analytical calculations to estimate the performances (sounding depth, heterogeneous subsurface characterization) of mutual impedance probes.

1. History and theory of surface Mutual Impedance Probes (MIP)

1.1. History of MIP

Mutual impedance probes have been used on Earth for many decades to measure the subsurface resistivity in a non-destructive way. They were first introduced by Wenner (1916) and consist of four electrodes. In their early version, a DC current was injected between two transmitting electrodes and the potential difference induced by this current was measured between two receiving electrodes in contact with the ground. The ratio of the received voltage potential over the injected current i.e., the mutual impedance of the quadrupole, yields the conductivity of the subjacent ground down to a depth comparable to the separation between the electrodes (see section 4.2). Compared to the self-impedance technique (presented in Chapter 1, section 4.3), the MIP technique is much less sensitive to the presence of heterogeneities in the vicinity of the electrodes and to the quality of the

contact between the electrodes and the medium. Alternatively, the electrodes can be buried at various depths below the surface.

Later, Grard (1990) proposed to use the same technique with AC instead of DC signals in order to measure not only the conductivity, but also the dielectric constant i.e., the complex permittivity of the ground. This technique, which had been successfully applied in space plasmas (Storey et al. 1969) in the frame of many ionospheric and magnetospheric experiments around the Earth (Chasseriaux et al. 1972; Décréau et al. 1982; Décréau et al. 1987); it was subsequently validated on Earth (Tabbagh et al. 1993) and used on the surface of a planetary body. The PWA analyzer (Grard et al. 1995) a unit of the HASI package (Fulchignoni et al. 2002) onboard the ESA Huygens probe that landed on the surface of Titan on January 14, 2005 (Fulchignoni et al. 2005; Grard et al. 2006). The Titan surface data was recently revisited with more accurate numerical models (see Hamelin et al. 2016 & Chapter 5). A laboratory MIP called HP3-PP (Stiegler & Kargl 2004) had been designed to be part of the ExoMars Humboldt surface station, which was ultimately cancelled. Lastly, the SESAME-PP/Philae MIP (Seidensticker et al. 2007) acquired a set of measurement on the surface of the nucleus of comet 67P/C-G (Lethuillier et al. 2016 & Chapter 4).

1.2. Mutual impedance for a quadrupole above a surface: derivation of the surface complex permittivity

Herein we summarize the theory of the quadrupolar array and show how to derive the relative permittivity ϵ_r of a planetary surface. This approach was first proposed by Grard (1990) and Grard & Tabbagh (1991). It assumes quasi-static approximation, as the wavelength of operation is much larger than the distance between the electrodes, and neglects magnetic induction.

In vacuum, the potential V at a distance r from a point charge Q is

$$V = \frac{Q}{4\pi\varepsilon_0 r} \tag{63}$$

When this charge is at a height h above an interface separating vacuum from a half-space of relative complex permittivity ϵ_r, the potential distribution can be determined with the image charge theory (see Section 3.1) in which we evaluate the effect of the interface by an image charge located at a distance h under the interface. The charge of the image is equal to (Griffiths 1999):

$$Q' = -\frac{\epsilon_r - 1}{\epsilon_r + 1} Q = -\alpha_m Q \tag{64}$$

The potential of a point located above the interface is then:

$$V = \frac{Q}{4\pi\varepsilon_0}\left(\frac{1}{r} - \frac{\alpha_m}{r'}\right) \tag{65}$$

where r' is the distance between the point and image of the charge.

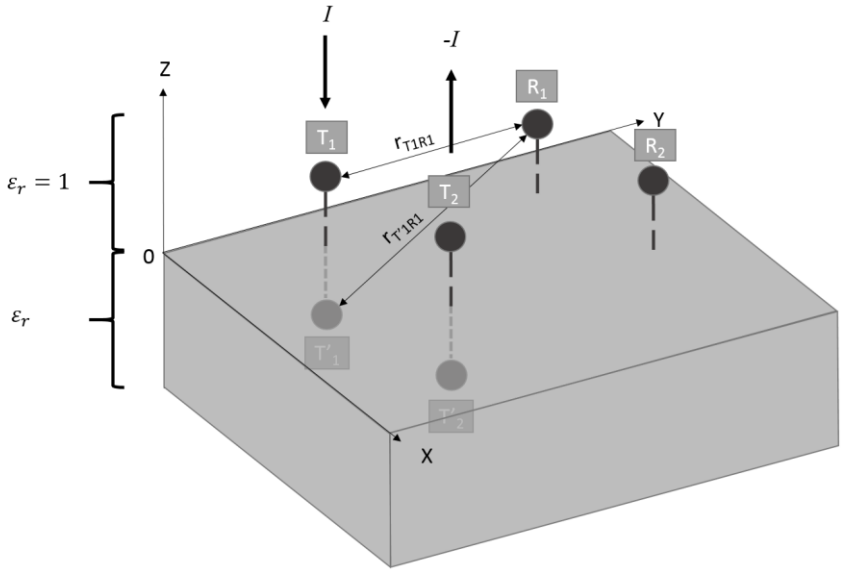

Figure 25: Quadrupolar array above an interface separating a half-space with a relative permittivity ϵ_r and vacuum. T_1 and T_2 are the transmitting electrodes, while R_1 and R_2 are the receiving electrodes. T'_1 and T'_2 are the images of the transmitting electrodes by the interface. The parameter $r_{T_nR_m}$ is the distance between the Tn and Rm electrodes. The parameter I is the current flowing through the transmitting electrodes.

We now consider a system of four pin point electrodes located above an interface separating a half-space with a uniform relative complex permittivity ϵ_r and vacuum as illustrated by Figure 25. A sinusoidal current I of angular frequency ω is fed into the two transmitting electrodes (T_1 and T_2). In the harmonic regime, $I = I_0 e^{j\omega t}$ and the charge $Q = \int I dt$ applied on a transmitting electrode is then:

$$Q = \frac{I}{j\omega} = \frac{I e^{-j\pi/2}}{\omega} \tag{66}$$

Using equation (65) and the theorem of superposition, the potentials induced on the receiving electrodes (R_1 and R_2) can be written:

$$V_{R_1} = \frac{Q}{4\,\pi\,\varepsilon_0}\left[\left(\frac{1}{r_{T_2R_1}} - \frac{1}{r_{T_1R_1}}\right) - \alpha_m\left(\frac{1}{r_{T'_2R_1}} - \frac{1}{r_{T'_1R_1}}\right)\right] \tag{67}$$

$$V_{R_2} = \frac{Q}{4\,\pi\,\varepsilon_0}\left[\left(\frac{1}{r_{T_2R_2}} - \frac{1}{r_{T_1R_2}}\right) - \alpha_m\left(\frac{1}{r_{T'_2R_2}} - \frac{1}{r_{T'_1R_2}}\right)\right] \tag{68}$$

where $r_{T_nR_m}$ is the distance between the transmitting T_n and the receiving R_m electrodes and $r_{T'_mR_n}$ is the distance between the image T'_m (image of the transmitting electrode T_m) and the receiving electrode R_n.

The mutual impedance of the quadrupole can therefore be written as:

$$Z_m = \frac{\Delta V}{I} = \frac{V_{R_2} - V_{R_1}}{I} = \frac{1}{4\pi j \varepsilon_0 \omega}\left[\left(\frac{1}{r_{T_1R_1}} + \frac{1}{r_{T_2R_2}} - \frac{1}{r_{T_1R_2}} - \frac{1}{r_{T_2R_1}}\right) - \alpha_m\left(\frac{1}{r_{T'_1R_1}} + \frac{1}{r_{T'_2R_2}} - \frac{1}{r_{T'_1R_2}} - \frac{1}{r_{T'_2R_1}}\right)\right] \quad (69)$$

where ΔV is the potential difference between the two receiving electrodes. Normalizing Z_m by Z_0, the mutual impedance in vacuum (corresponding to $\alpha_m = 0$), we further obtain:

$$\frac{Z_m}{Z_0} = 1 - \delta\alpha_m \quad (70)$$

with δ, the quadrupole geometrical factor, defined as

$$\delta = \left(\frac{1}{r_{T'_1R_1}} + \frac{1}{r_{T'_2R_2}} - \frac{1}{r_{T'_1R_2}} - \frac{1}{r_{T'_2R_1}}\right) \Bigg/ \left(\frac{1}{r_{T_1R_1}} + \frac{1}{r_{T_2R_2}} - \frac{1}{r_{T_1R_2}} - \frac{1}{r_{T_2R_1}}\right) \quad (71)$$

The complex permittivity of the lower half-space can then be derived from measurements of both the mutual impedance in vacuum and above the half-space using the following equation:

$$\varepsilon_r = \frac{Z_0(\delta + 1) - Z_m}{Z_0(\delta - 1) + Z_m} \quad (72)$$

However, equation (72) has limitations: it applies well to isolated idealized pinpoint electrodes, but does not account for the effect of the close environment of the MIP (for instance, in the case of a MIP mounted on lander), the presence of the lander's body nor for the electronic circuit that links the electrodes and the shape of the electrodes. For a more realistic approach, we used a method called the Capacitance-Influence Matrix Method, which was successfully applied to the analysis of the data collected by both PWA-HASI/Huygens on the surface of Titan (Hamelin et al. 2016, Chapter 5) and SESAME-PP on the surface of the nucleus of comet 67P/C-G (Lethuillier et al. 2016, Chapter 4).

2. Numerical modelling and Capacity-Influence Matrix method

2.1. Application to realistic problems

Even if, in theory, equation (72) allows one to derive the complex permittivity of the subsurface from the measured mutual impedance in vacuum and on the surface, certain conditions must be met:

I. The electrodes are small enough to be considered as punctual.
II. There are no conducting elements close to the electrodes (at distances smaller than the dimension and sounding depth of the quadrupole, see section 4.2).
III. The surface studied is planar and the subsurface properties are homogeneous.
IV. The electronic circuit has no significant influence on the measurements (i.e. that the current generator and voltmeter are perfect)

In realistic cases, for example with the SESAME-PP or PWA-HASI instruments, these conditions do not apply. And therefore, equation (72) will give an approximate estimate of the subsurface permittivity. We will present in the rest of the chapter the approach adopted to overcome these problems

Problem I. can be solved with an analytical calculation, for example by using the image charge method.

Problems II. and III. can be solved with a numerical code that solves the Laplace equations for complex configurations of operation (e.g., non-planar surface, complete instrumental set up), see Cadène (1995) for a numerical code built for the PWA-HASI/Huygens instrument and a homogeneous subsurface.

Lastly, problem IV. requires a new approach to account for the non-negligible influence of the electronic circuitry that we named the Capacitance-Influence Matrix Method (a similar method was applied in Hamelin et al. 2007). The latter offers the advantage of also addressing the other problems at the expense of calculation time.

2.2. Derived complex permittivity

The information derived from MIP measurements is an averaged value of the permittivity of the subsurface in the vicinity of the instrument. The measurement is also affected by the MIP carrier (lander or rover) and the electronic circuit.

2.3. Comparing simple examples to more realistic cases

2.3.1. Finite size electrodes

In order to illustrate problems I. and thus the need for the Capacitance-Influence Matrix Method (presented in section 2.4), we build a numerical model of a MIP consisting of 4 cylindrical electrodes with a radius $r = 0.05$ m (a size comparable to the SESAME-PP/Philae electrodes), forming a square of side $d = 0.5\ m$ and located on the interface (height = 0) between a vacuum and a pure dielectric subsurface (i.e., $\epsilon_r = \epsilon_r'$ & $\sigma_{eff} = 0$, Figure 26).

We then run numerical simulations with the COMSOL Multiphysics© software which is a finite element analysis software that solves the Laplace equation in 3D. The model is meshed and boundary conditions are set (see www.comsol.com for more information) to estimate the mutual impedance measured by the MIP. Equation (72) is used to derive the dielectric constant that is plotted in Figure 27 against the nominal dielectric constant of the subsurface. We note a small difference (maximum 1.8 % for a dielectric constant of 5), between the pin point electrodes model and the cylindrical electrodes model. This demonstrates that representing the electrodes by pin point electrodes yields a good approximation of the dielectric constant of the subsurface, for more accurate results, numerical simulations are necessary.

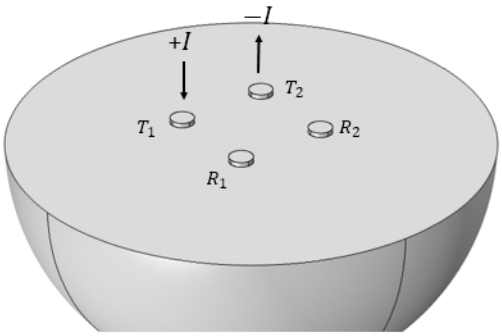

Figure 26: Cylindrical electrodes with a radius $r = 0.05$ m similar to those of the SESAME-PP/Philae electrodes lying on a dielectric subsurface (height = 0).

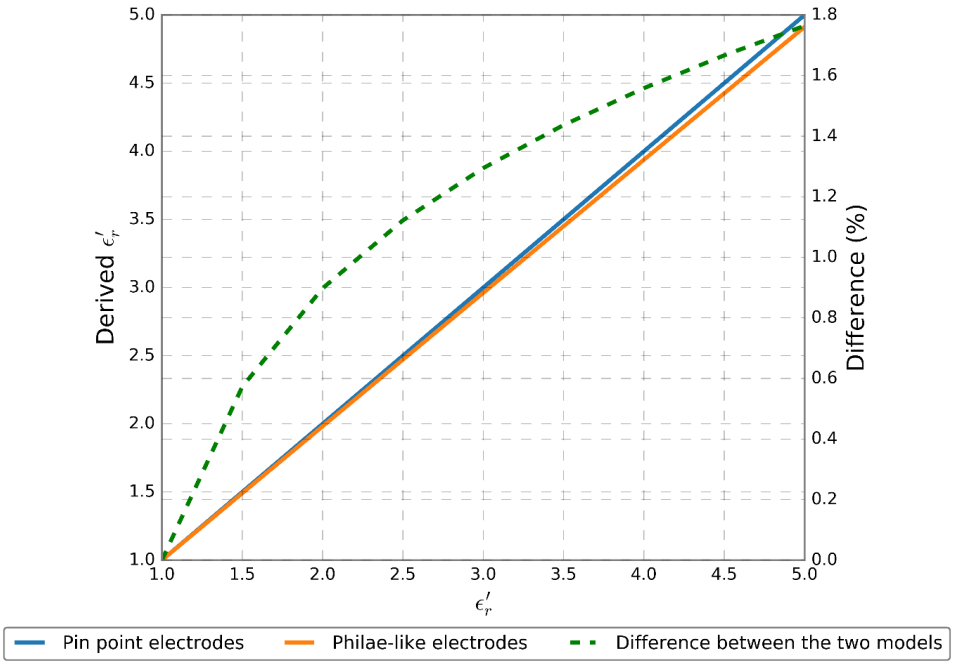

Figure 27: Derived dielectric constant as a function of the nominal true dielectric constant for pin point and cylindrical electrodes.

2.3.2. Presence of conducting elements close to the electrodes

To illustrate problem II. we build a numerical model of MIP consisting in 4 spherical electrodes with a radius of 5 cm (close to that of SESAME-PP electrodes) located at 3 cm over the surface as shown in Figure 28a. We add to this model a 5th conductive sphere with a radius of 50 cm. This element is similar in size to the Philae-body and is located at a height of 75 cm above the surface (Figure 28b). The permittivity derived from Equation (72) with the numerically computed mutual impedance for the model described above is shown in Figure 29 (orange curve). The presence of a large conductive element close to the MIP electrodes has an obvious and significant influence on the derived permittivity (dotted orange curve, ~70 % relative error for a subsurface dielectric constant of 5). It leads to the underestimation of the subsurface dielectric constant. Furthermore, this influence varies with the shape of the conductive element as illustrated by the green curve in Figure 29 which is obtained after replacing the spherical conductor by the actual shape model of the body of Philae (see Figure 28c, the model is described in more detail in Chapter 3, Section 2.1).

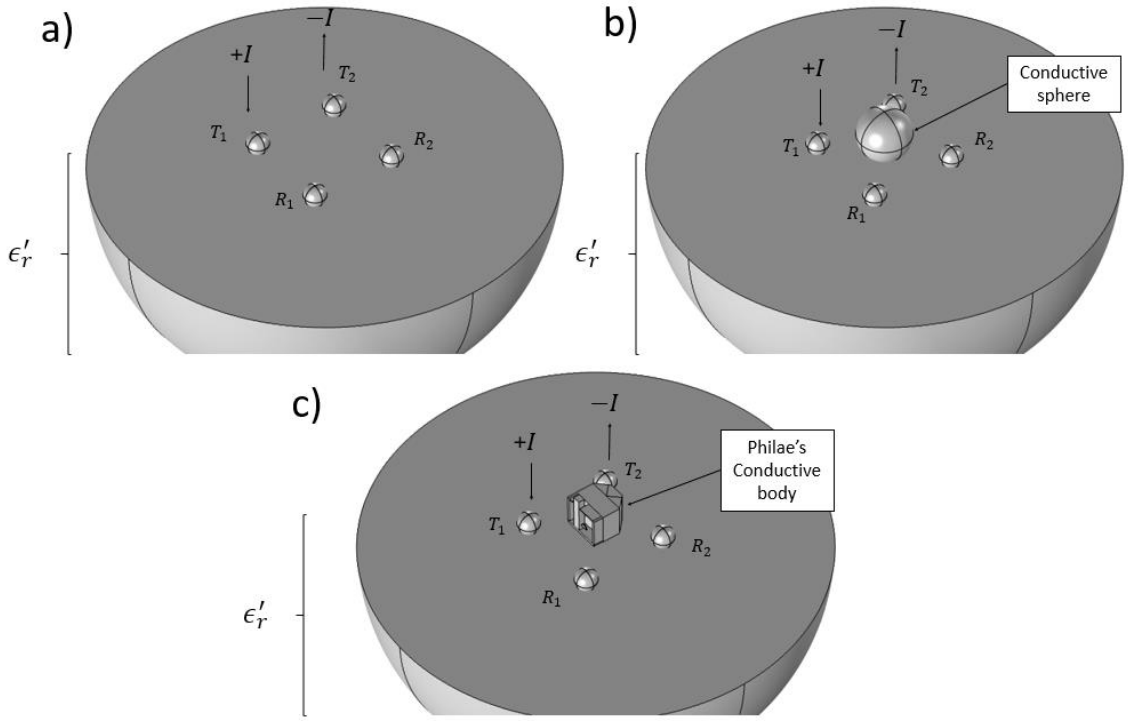

Figure 28: a) MIP composed of 5 cm-radius spherical electrodes lying 3 cm above the dielectric surface. b) Addition of a conductive spherical element (of radius 50 cm) at the center of the MIP array. The sphere is 75 cm above the surface. c) The actual shape of the Philae body is substituted to the spherical element.

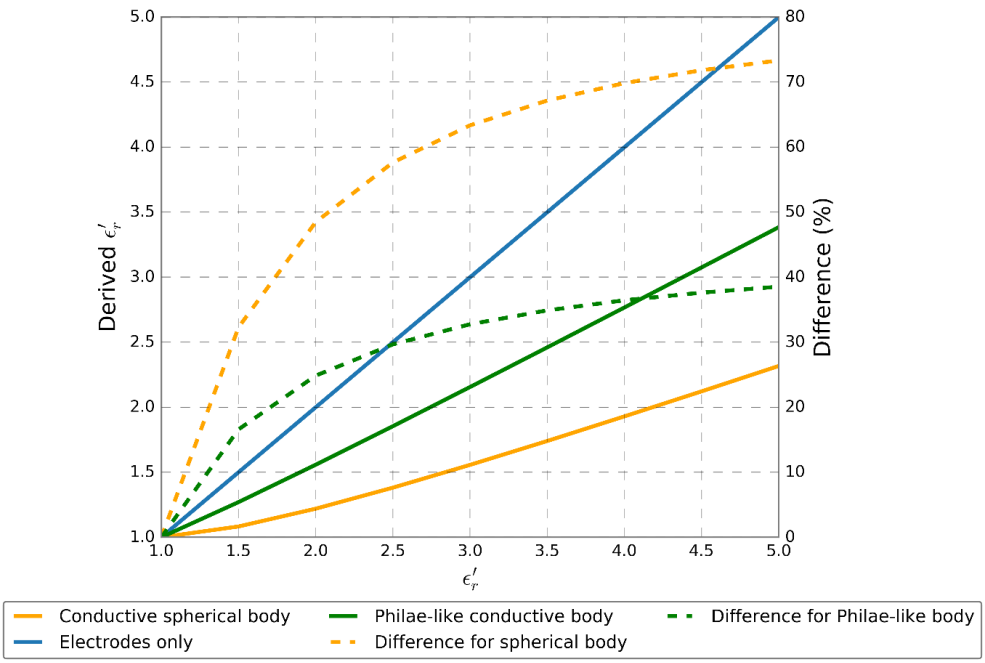

Figure 29: Derived measured dielectric constant as a function of the subsurface true dielectric constant for the three configurations of operation illustrated by Figure 28. Ignoring The presence of a conducting element close to the MIP leads to an underestimation of the dielectric constant.

2.3.3. Influence of the electronics circuit

Lastly, we use the CIMM described in Section 2.4 in order to illustrate the influence of the electronic circuit. Numerical simulations are run for the complete model of SESAME-PP in the Philae environment (see Chapter 3, Section 2.1 for a more detailed description) in a three-foot configuration where a current is injected in one foot and the potential difference between the two other feet is measured. The simulations and estimate of the dielectric constant are performed with and without accounting for the effects of the electronic circuit (see Section 3.2 for the general approach and Chapter 3, Section 2.1 for a realistic example). Figure 30 clearly shows that the effect of electronic circuit cannot be neglected.

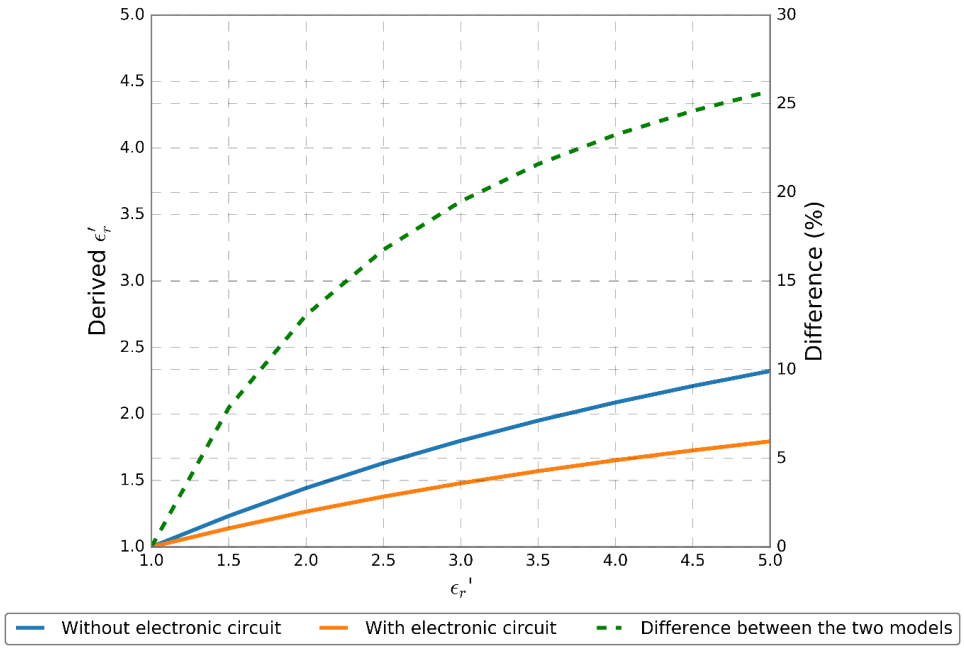

Figure 30: Derived dielectric constant as a function of the nominal subsurface dielectric constant with and without the influence of the electronic circuit, the full geometry of SESAME-PP and its environment (described in Chapter 3, Section Chapter 3:2.1) is taken into account.

We have shown that the presence of conducting elements close to the electrodes, the electronic circuit and, to a lesser extent, the shape of the electrodes, prohibit the use of Equation (72) for the derivation of the permittivity from MIP measurements, and requires the use of the Capacitance-Influence Matrix Method described below.

2.4. The Capacitance-Influence Matrix Method (CIMM)

The Capacitance-Influence Matrix Method is based on the lumped element model, which consists in representing the electrical characteristics of the MIP and its environment as a network of fictive lumped elements. These conducting elements can, additionally, be linked together by an

electronic circuit. This approach enables us to establish and use for prediction a set of linear equations that describes the whole system.

We consider the case of N disconnected conductors in a dielectric medium. By superposition, the charge Q_k on the k^{th} conductor due to the $N-1$ charged conductors of the system is given by:

$$Q_k = \sum_{n=1}^{N} K_{kn}^{m} V_n, \tag{73}$$

where K_{kn}^{m} with $n = 0, 1, 2, \dots, N$ are the coefficients of the medium capacitance-influence matrix $[\boldsymbol{K^m}]$ and V_n is the potential on the n^{th} conductor. This results in the matricial equation:

$$\boldsymbol{Q} = [\boldsymbol{K^m}]\boldsymbol{V} \tag{74}$$

and using equation (66):

$$\boldsymbol{I} = j\omega[\boldsymbol{K^m}]\boldsymbol{V} \tag{75}$$

where $\boldsymbol{Q} = [Q_1, Q_2, \dots, Q_N]$ is the vector of the charges on the discrete conductors, $\boldsymbol{V} = [V_1, V_2, \dots, V_N]$ the vector of the potentials of the discrete conductors, and $\boldsymbol{I} = [I_1, I_2, \dots, I_N]$ the vector of currents injected into the medium by the electronic circuit that is represented by its electronic admittance matrix $j\omega[\boldsymbol{K^e}]$. The system, composed of the electronic circuit and the medium, is described by the equations (Hamelin et al. 2007):

$$\boldsymbol{I} = j\omega[\boldsymbol{K}]\boldsymbol{V} \tag{76}$$

Or:

$$\boldsymbol{V} = \frac{[\boldsymbol{K}]^{-1}\boldsymbol{I}}{j\omega} \tag{77}$$

With:

$$[\boldsymbol{K}] = [\boldsymbol{K^e}] + [\boldsymbol{K^m}] \tag{78}$$

The matrix $[\boldsymbol{K}]$ is the capacitance-influence matrix of the multi-conductor system. The matrix $[\boldsymbol{K^e}]$ is obtained from the electronic circuit analytical model. $[\boldsymbol{K^m}]$ can be obtained by modeling: in practice, we build a numerical geometry model of the instrument and of its conductive environment (including the planetary dielectric surface) and we use the software COMSOL Multiphysics©. The matrix $[\boldsymbol{K^m}]$ varies with the configuration (location/attitude of the electrodes with respect to the surface) and with the complex permittivity of the near-surface material.

The CIMM consists in using equation (78), a set of N equations, with some additional constraints on the vectors $\boldsymbol{I}$ and $\boldsymbol{V}$ (see Section 3.2 or for a more realistic case Chapter 3, Section 2.1.4) to predict the potentials on the receiving electrodes and the current injected into the surface by the transmitting electrodes, which yields the mutual impedance for a given planetary surface electrical properties ($Z_m = \Delta V / I$, with ΔV the predicted potential difference between the two receiving electrodes and I the predicted current injected into the surface). These predictions can then be compared to the MIP data to find the complex permittivity that fits best the observations, namely, the measured received potentials and/or their difference and the injected current, or directly the mutual impedance.

For a MIP used on Earth, the electronic matrix is often known. In contrast, in space missions, the determination of $[\boldsymbol{K^e}]$ can be a significant source of uncertainty because the electronic circuit, which is generally well characterized before launch, is subject to changes during the journey of the spacecraft to its destination. These changes are all the more likely as the journey is long and as the constraints, in terms of temperature, pressure and radiation, imposed on the electronics are important. Frequent tests on a spare model or, whenever possible, tests performed with the flight model in vacuum (for example during the descent of a probe to a planetary surface) can reduce the uncertainty associated with the determination of $[\boldsymbol{K^e}]$. On the other hand, the estimation of the matrix $[\boldsymbol{K^m}]$ requires good knowledge of the configuration of operation of the MIP.

2.5. Derivation of $\boldsymbol{\epsilon_r}$

Provided that the MIP operation configuration and the electronic circuit are known, the Capacitance-Influence Matrix Method can be used to predict the measured mutual impedance measured by a quadrupole lying on a surface of a given permittivity.

From these predictions, we build charts in the complex plane showing the expected normalized complex impedance as a function of the real and imaginary parts of the relative permittivity of the subsurface. Figure 31 shows an example for the case of a simple quadrupole array composed of small ($r = 0.01$ m) spherical electrodes lying on a horizontal surface. The blue lines represent expected normalized mutual impedance for a constant real part of the relative permittivity and the red lines for a constant imaginary part of the relative permittivity. It therefore stands that the intersection of the blue and red lines provides the expected normalized mutual impedance for a given relative complex permittivity of the subsurface. The normalized (with regard to vacuum) mutual impedance measured by the MIP can be plotted on the chart and the complex permittivity of the near-surface is deduced by reading the associated values of ε_r' and ε_r''.

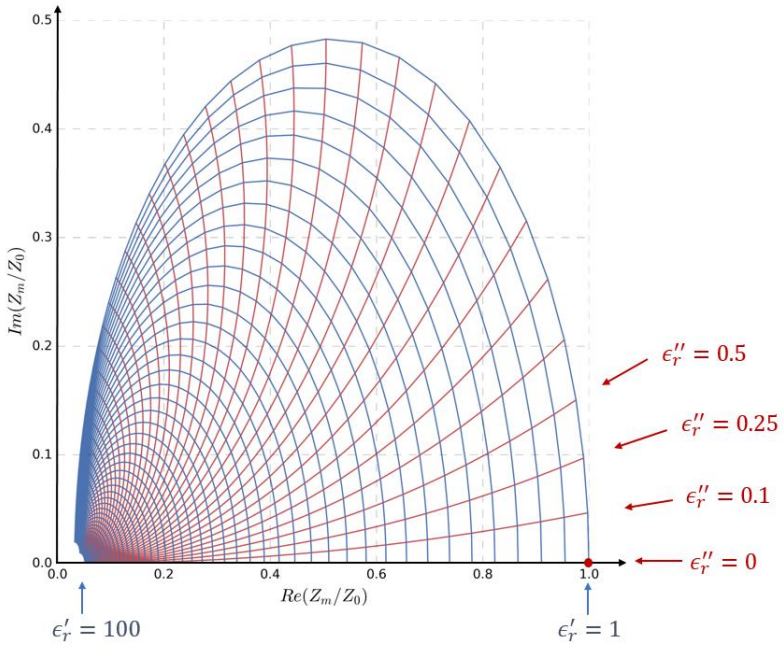

Figure 31: Predicted normalized mutual impedance of a simple MIP lying over a horizontal surface. The expected mutual impedance is shown in the complex plane as a function of the real and imaginary parts of the relative permittivity of the near-surface (for a frequency of operation of 758 Hz). The dielectric constant of the subsurface ranges from 1 to 100 and the imaginary part from 0 to 100 on logarithmic scales. The red dot indicates the vacuum relative permittivity.

These charts are geometry specific, which means that for any change in the attitude of the MIP with respect to the surface and/or a change in the surface topography, new simulations have to be performed. The building of these charts being CPU time-consuming, it is important to gather all available information on the attitude and geometry of the MIP before running numerical simulations.

It can also be noted that the effects of the real and imaginary parts of the relative permittivity of the subsurface on the mutual impedance decrease when their values increase. Therefore, it is important to envision the accuracy of the measurements according to the expected subsurface complex permittivity. For a subsurface with high dielectric constant and conductivity, a very accurate instrument is required. For a subsurface with low dielectric constant and conductivity a less accurate instrument can still yield precious information.

3. Validation of the use of numerical models

The Capacitance-Influence Matrix Method requires the derivation of the medium capacitance-influence matrix $[\boldsymbol{K^m}]$**.** For simple cases an analytical calculation can be used (for example in the cases of spheres) but for more complex and realistic cases $[\boldsymbol{K^m}]$ must be derived with numerical models. In the present work, we use the COMSOL Multiphysics© software. We compare the results of a model that can be solved analytically to validate the numerical models. To derive $[\boldsymbol{K^m}]$ analytically we use the method of image charges described below.

3.1. Method of image charges

The method of the image charges (or mirror charges) is an analytical problem-solving tool in electrostatics. The method consists in replacing perfect electrical reflectors or interfaces separating 2 layers of different permittivity by a set of imaginary charges that satisfies the boundary conditions of the problem (Dirichlet or Neumann boundary conditions). The method relies on the uniqueness theorem which states that the electric potential in a volume is uniquely determined if both the charge density throughout the region and the value of V on all boundaries are specified (Griffiths 1999).

A basic problem to solve is that of a charge q (i.e., a pin point electrode) above an interface (Figure 32). The boundary condition is $V = 0$ at infinity (and $V = 0$ on the interface for a grounded plane). In order to calculate the potential at all points we use the image method and replace the interface by an image charge q' symmetrically opposite with respect to the plane ($q' = \left(\frac{\epsilon_{r0}-\epsilon_{r1}}{\epsilon_{r0}+\epsilon_{r1}}\right) q$, in the case of a plane separating two mediums of respective relative permittivity $\epsilon_{r_0}$and ϵ_{r_1} and $q' = -q$, in the case of a grounded plane). By taking into account these two charges the boundary conditions are still respected and the potential can be analytically expressed in all space (Griffiths et al 2004):

$$V(M) = \frac{q}{4\pi\epsilon_0}\left[\frac{1}{d(M,q)} - \frac{1}{d(M,-q)}\right] \tag{79}$$

for a grounded plane and:

$$V(M) = \frac{q}{4\pi\epsilon_0}\left[\frac{1}{d(M,q)} - \frac{\left(\frac{\epsilon_{r0}-\epsilon_{r1}}{\epsilon_{r0}+\epsilon_{r1}}\right)}{d(M,-q)}\right] \tag{80}$$

for an interface separating two mediums of permittivity $\epsilon_{r_0}$and ϵ_{r_1}

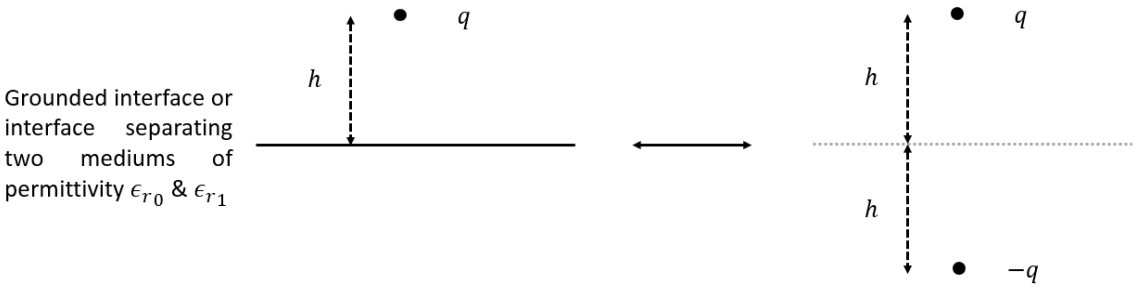

Figure 32: Example of the application of the method of image charges for a charge $\boldsymbol{q}$ located a distance $\boldsymbol{h}$ above an interface. The method of image charges consists in replacing the grounded surface by a charge $-\boldsymbol{q}$ located symmetrically opposite of charge $\boldsymbol{q}$ with respect to the grounded surface and in replacing the interface between two mediums of permittivity $\boldsymbol{\epsilon_{r_1}}$ & $\boldsymbol{\epsilon_{r_2}}$ by a charge $\boldsymbol{q'} = \left(\frac{\epsilon_{r0}-\epsilon_{r1}}{\epsilon_{r0}+\epsilon_{r1}}\right)\boldsymbol{q}$ located symmetrically opposite of charge $\boldsymbol{q}$ with respect to the interface.

The method of the image charges can also be applied to perfectly electrically conductive spheres. In Figure 33, two spheres of radius R_x (x being the sphere index), are separated by a distance $D > (R_1 + R_2)$ and carry a charge Q_x.

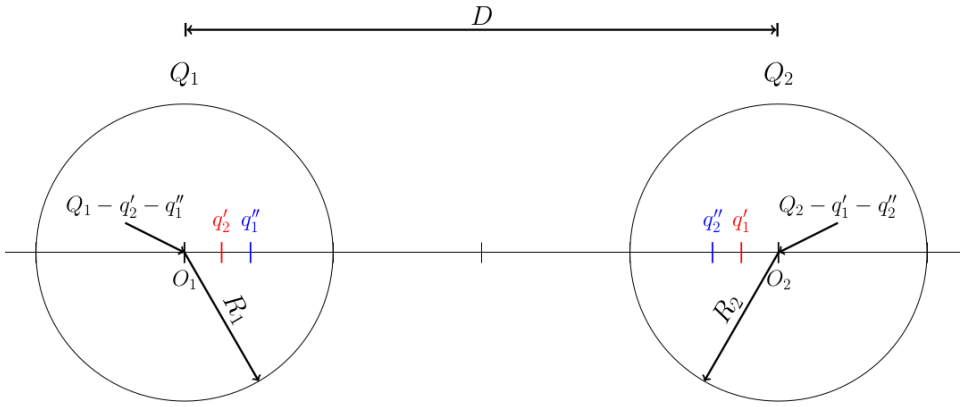

Figure 33: Schematic representation of two spherical conductors and of the induced charge images.

According to the method of image charges, it is possible to take in account the conducting surfaces of the spheres by replacing them by sets of image charges (Durand 1953):

- Q_1 produces an image $q_1' = Q_1 \frac{-R_2}{D}$ located at an algebraic distance $\left(\frac{R_2^2}{D}\right)$ from O_2
- Q_2 produces an image $q_2' = Q_2 \frac{-R_1}{D}$ located at an algebraic distance $\left(\frac{R_1^2}{D}\right)$ from O_1

These images induce themselves image charges in the other sphere:

- q_1' produces an image $q_1'' = q_1' \frac{-R_1}{d(q_1', O_1)}$ located at an algebraic distance $\left(\frac{R_1^2}{d(q_1', O_1)}\right)$ from O_1
- q_2' produces an image $q_2'' = q_2' \frac{-R_2}{d(q_1', O_1)}$ located at an algebraic distance $\left(\frac{R_2^2}{d(q_2', O_2)}\right)$ from O_2

where $d(x, y)$ is the distance between the charge x and the point y.

The charge image distribution is obtained with an accuracy of 1% obtained after 10 iterations. In addition, in order to keep the charges carried by the spheres equal to Q_1 and Q_2 , we must place a charge equal to:

- $Q_1 - q_2' - q_1'' - \ldots - q_2'^n - q_1'^{n+1}$ at the centre O_1

and:

- $Q_2 - q_1' - q_2'' - \ldots - q_1'^n - q_2'^{n+1}$ at the centre O_2

The potential at a point *M* can then be written:

$$V(M) = \frac{1}{4\pi\epsilon_0}\left(\frac{Q1 + \sum_{n=1}^{\infty} -q_2'^n - q_1'^{n+1}}{d(M,O_1)} + \frac{Q2 + \sum_{n=1}^{\infty} -q_1'^n - q_2'^{n+1}}{d(M,O_2)}\right) + \sum_{n=1}^{\infty} \frac{q_1'^n}{d(M,q_1'^n)} + \frac{q_2'^n}{d(M,q_2'^n)} \quad (81)$$

Using this approach, we can predict the potential of four spherical electrodes (i.e., a simplified MIP) lying over a surface separating two medias of different permittivity. The potential and charge are related by:

$$\boldsymbol{Q} = [\boldsymbol{K^m}]\boldsymbol{V} \quad (82)$$

The elements of the capacitance influence matrix $[\boldsymbol{K^m}]$ of the system are derived by setting the charge carried by one electrode to 1Cand the charges carried by the other electrodes to 0. The potential induced by each electrode can be derived by repeating this operation.

3.1. Simplified model of a MIP

The MIP model is shown in Figure 34 and its characteristics are given in Table 5.

Table 5: Characteristics of the model used for the numeric/analytic comparison

	Radius (m)	**X (m)**	**Y (m)**	**Z (m)**
Body (T_2)	0.8	0.2	0.0	1.0
T_1	0.05	0.0	1.5	0.05
R_1	0.05	1.0	-1.5	0.05
R_2	0.05	-1.0	-1.5	0.05

In this simplified representation of the SESAME-PP MIP, 3 electrodes are represented by spheres of radius = 5 cm and the Philae lander by a large conductive sphere of radius = 0.8 m. The electrodes are located 5 cm above a dielectric surface with a relative permittivity ϵ_r.

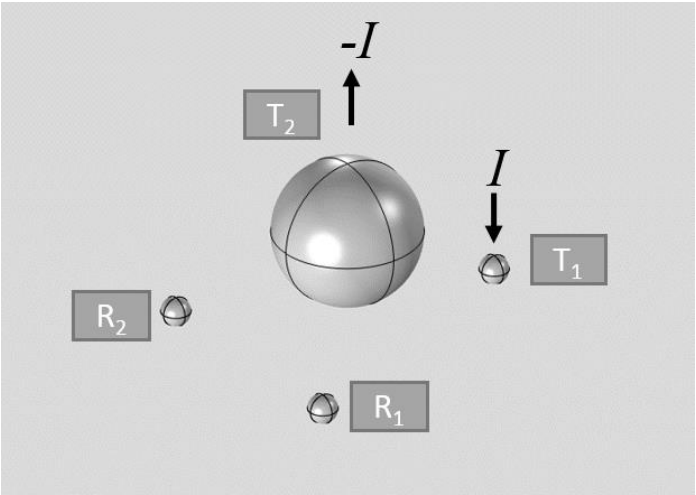

Figure 34: Schematic representation of the 3 electrodes SESAME-PP and the Philae lander

3.2. Comparison

Using the CIMM with the analytically derived $[\boldsymbol{K^m}]$ (with the method of image charges) and the additional constraints listed in Table 6 we simulate the injection of a current between one of the electrodes and the Philae body (then acting as second transmitting electrode) and calculate the induced potentials on the two receiving electrodes (see Chapter 3 for more details on SESAME-PP), in order to build the charts relating normalized mutual impedance to ϵ_r as described in Section 2.5.

Table 6: Constraints applied to the potentials and currents to solve Equation (82)

Variable	Constraint	Comments
$\boldsymbol{I_{R_1}, I_{R_2}}$	0 A	Current injected in a passive conductor is null.
$\boldsymbol{I_{R_1} + I_{R_2} + I_{T_1} + I_{T_2} = 0}$	0 A	Kirchhoff's law.
$\boldsymbol{V_{T_1} - V_{T_2} = 10\ \mathrm{V}}$	10 V	Potential difference between the two transmitting electrodes is set.

We then used the CIMM with the numerically derived $[\boldsymbol{K^m}]$ (with the COMSOL software) over subsurfaces of relative permittivity ϵ_r and the charts to retrieve ϵ_r. If the numerical results were perfect we would retrieve exactly the permittivity of the subsurface. In fact due to the use of the finite element method, the numerical results are an approximation leading to a derived value of ϵ_r different to the real one.

The numerical and analytical approaches are compared in Figure 35 for a pure dielectric surface (ϵ'_r ranging from 1 to 10 and $\epsilon''_r = 0$) and for a lossy medium ($\epsilon'_r = 5$ and ϵ''_r ranging from 0.1 to 1). In both cases the electrodes are in vacuum ($\epsilon_r = 1$).

The analytical model yields the correct ϵ_r and was used to build the charts relating normalized mutual impedance to ϵ_r. The numerical model yields similar results both for the derivations of ϵ'_r and ϵ''_r. The difference in the derived permittivity remains <1% (<1.2% for the imaginary part), which validates the use of numerical models, for this configuration.

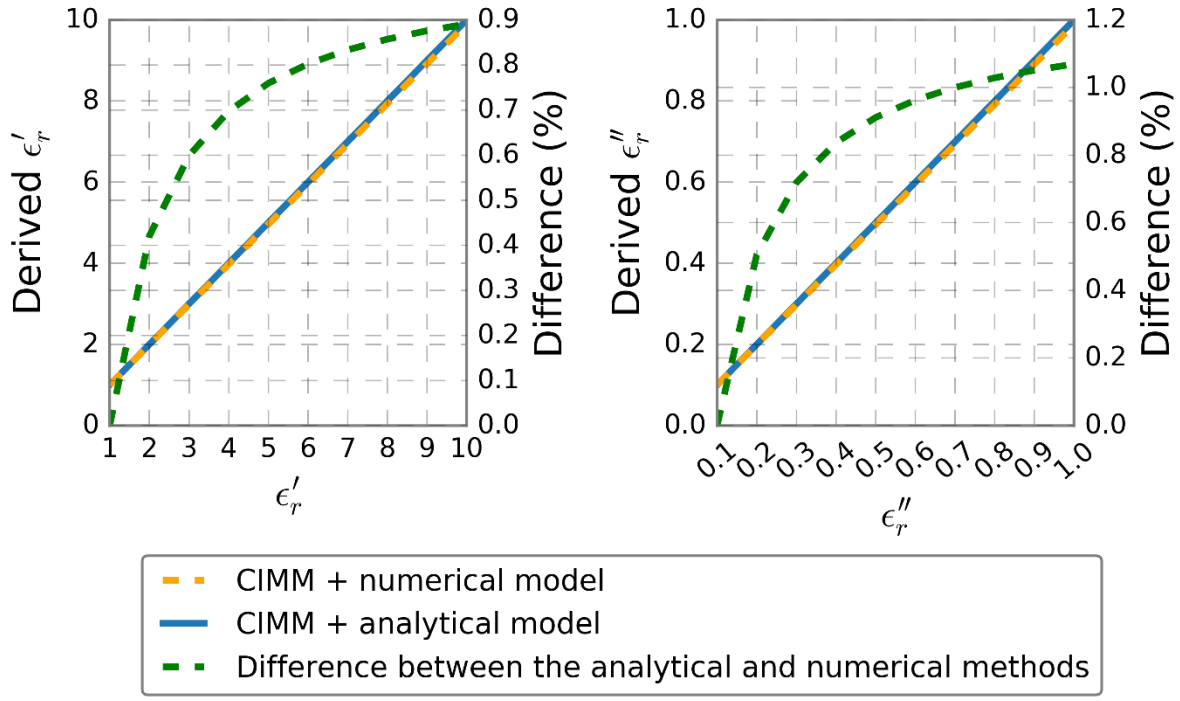

Figure 35: Derived real (right) and imaginary (left) parts of the subsurface complex permittivity as a function of the true real (right) and imaginary (left) parts of the subsurface permittivity using the Capacitance-Influence Matrix Method (CIMM) and numerical models.

Unfortunately, analytical solutions are not available for more complex geometries. Whenever possible, these geometries should be numerically modeled and simulations should be run and compared to measurements performed with a replica in a controlled environment as done for the Philae lander (see Chapter 3, Section 2.3).

4. Exploring the capabilities of the mutual impedance probes

Understanding the capabilities of MIP is important in order to properly design these instruments and plan for their measurements. On Earth, it is easy to change the geometrical configuration of the system and to perform numerous measurements. The constraints associated with a planetary mission limit the number of geometrical configuration possibilities and the amount of measurements to be performed. It is therefore necessary to opt for the best configuration in order to optimize the scientific output.

4.1. Sensitivity of the transmitting electrodes

Understanding how the current injected in the medium evolves as a function of the height above the surface can constrain the subsurface properties in the vicinity of the electrode and/or provide information on the attitude of the electrode with respect to the surface. We modelled a 4-electrode spherical MIP lying over a dielectric surface of relative permittivity ϵ_r and we used the CIMM method combined with numerical models solved with COMSOL Multiphysics© to simulate the theoretical current amplitude injected into the surface using the constraints describes in Table 6, first as a function of the distance to the surface for a fixed $\epsilon_r = 5$ of the subsurface (Figure 36, left), then as a function of the dielectric constant of the subsurface for a fixed distance $h = 1$ cm between the bottom of the electrodes and the surface (Figure 36, right).

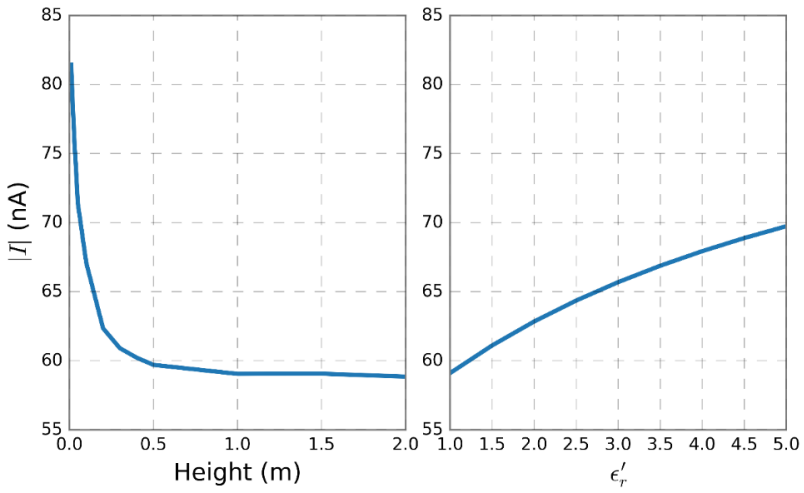

Figure 36: Amplitude of the current injected into the surface as a function of the height of the electrodes above the surface for a fixed $\epsilon_r = 5$ of the subsurface (left) then as a function of the dielectric constant of the subsurface for a fixed separation h=1 cm between the bottom of the electrodes and the surface (right).

Figure 36, left, shows that the current amplitude rapidly decreases with the distance between the electrode and the surface, levelling off at a distance of about 0.4 m. Figure 36, right shows a stable increase of the amplitude with increasing ϵ_r of the subsurface. Therefore, knowing either the relative permittivity of the subsurface or the distance of the electrode to the subsurface enables one to retrieve the other parameter. As we will see in section 4.2, the theoretical sounding depth of a 4-electrode MIP is larger than 0.4 m which means that combining the analysis of current and potential measurements can help reveal heterogeneities at different depths in the subsurface. This example was produced with spherical electrodes; accurate geometrical simulations should be performed for more specific cases. This result is used in Chapter 4, Section Chapter 4:4.3 in order to derive from SESAME-PP current measurements at the surface of 67P/Churyumov-Gerasimenko's nucleus upper limits for the real and imaginary parts of the subsurface permittivity or a lower limit for distance between the electrode and the surface.

4.2. Sounding depth

The sounding depth of MIP is difficult to quantify owing to the fact that the subsurface does not affect the measurement in the same way down to a defined depth, but less and less at larger distances from the probe.

In order to quantify the sounding depth of a 4-electrode MIP, calculations were conducted in which the mutual impedance is estimated while a perfect reflector is progressively moved upward: we consider that the sounding depth corresponds to the distance at which the reflector significantly influences the measurements (i.e., when the difference between the mutual impedance with and without reflector exceeds the accuracy of the measurement, namely about 10%, in the case of the SESAME-PP/Philae). It is possible to solve simple cases analytically; more complex cases require the use of the CIMM and numerical models (see Chapter 3 Section 3 for the application to the SESAME-PP instrument and Chapter 5 Section 3.4 for the PWA-HASI instrument).

Let us consider a quadrupole with two transmitting and two receiving pin point electrodes as shown in Figure 37 where b is the distance separating the receiving and transmitting dipole and a the distance between the two electrodes of the same dipole. All the electrodes are located at a height h above a perfect reflector.

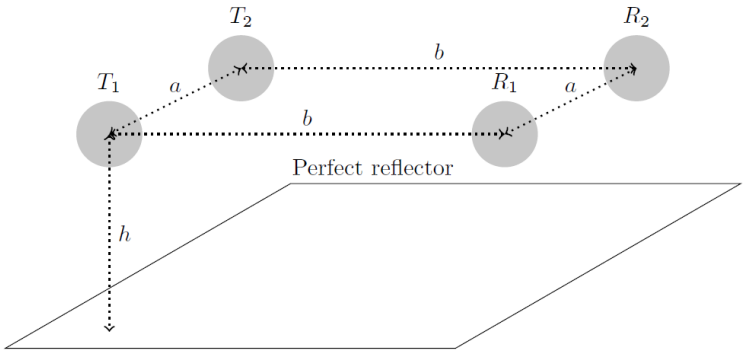

Figure 37: 4-electrode MIP. a is the distance between the transmitting and receiving dipoles. b is the distance between the transmitting electrodes as well as between the receiving electrodes.

Assuming that the injected current is constant (which occurs, as seen in Section 4.1, when the transmitting electrode lies more than ~ 50 cm above a surface), we search the height h over a perfect reflector for which the measured mutual impedance measured is equal to 90% (assuming the measurement error is 10 %) of the vacuum mutual impedance which can be expressed as:

$$Z_m = 0.9Z_0 \tag{83}$$

With a constant current equation (83) becomes:

$$\Delta V_m = 0.9\Delta V_0 \tag{84}$$

$$V_{R_1 m} - V_{R_2 m} = 0.9(V_{R_1 0} - V_{R_2 0}) \tag{85}$$

Using the method of image charges and considering that a charge $Q = \frac{I}{j\omega}$ is applied to the transmitting electrodes, one derives the following relationships for the received potentials:

$$V_{R_1 m} = \frac{Q}{4\pi\epsilon_0}\left(-\frac{1}{a} + \frac{1}{\sqrt{a^2+b^2}} + \frac{1}{\sqrt{4h^2+a^2}} - \frac{1}{\sqrt{a^2+b^2+4h^2}}\right) \tag{86}$$

$$V_{R_2 m} = \frac{Q}{4\pi\epsilon_0}\left(\frac{1}{a} - \frac{1}{\sqrt{a^2+b^2}} - \frac{1}{\sqrt{4h^2+a^2}} + \frac{1}{\sqrt{a^2+b^2+4h^2}}\right) \tag{87}$$

Combining equations (85), (86) and (87) we obtain:

$$-\frac{2}{a} + \frac{2}{\sqrt{a^2+b^2}} + \frac{2}{\sqrt{4h^2+a^2}} - \frac{2}{\sqrt{a^2+b^2+4h^2}} = 0.9\left(\frac{2}{a} + \frac{2}{\sqrt{a^2+b^2}}\right) \tag{88}$$

The sounding depth corresponds to the distance h which verifies equation (88). Solving this equation for different values of a and b results in Figure 38.

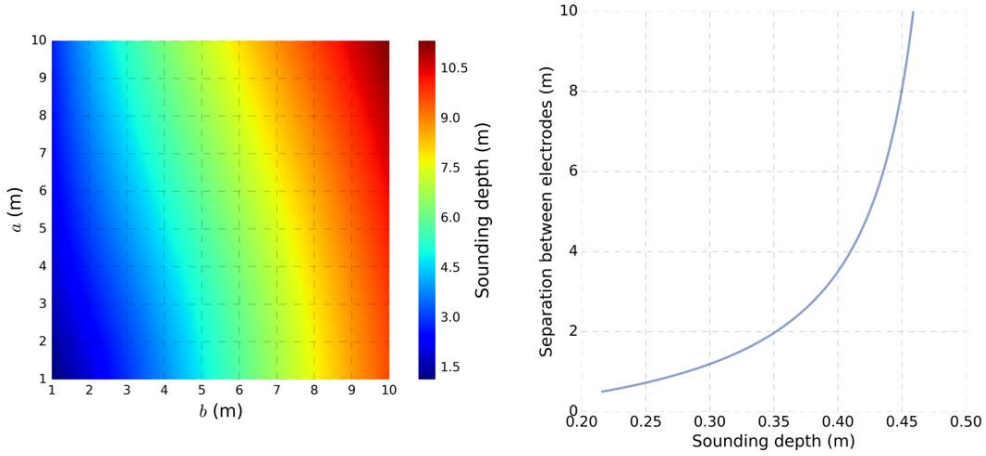

Figure 38: Left: Sounding depth of a 4-electrode MIP as a function of the distance between the receiving and transmitting dipole ($\boldsymbol{b}$) and between the electrodes in a same dipole ($\boldsymbol{a}$). Right: Sounding depth of a self-impedance probe as function of the distance between the electrodes.

Figure 38, left, shows that both the separation between the dipoles and between the electrodes within a same dipole influences the sounding depths: larger separations lead to larger sounding depths, although the distance between dipoles (b) has a greater influence on the sounding depth than the distance between electrodes of a same dipole (a). We also observe that all sounding depths are larger than the sensitivity distance of the transmitting foot justifying the use of a constant current.

For comparison, the same method was used to determine the sounding depth of a self-impedance probe (Figure 38, right). Self-impedance probes have a shallower sounding depth that increases rapidly with the distance between electrodes when this distance is small (less than 4.0 m) but then reaches a maximum of about 0.5 m. In contrast, MIP can sense depths as large as 10 m for an equivalent separation distance between electrodes.

4.3. Heterogeneous subsurfaces

The ability to sound multiple depths by changing the geometrical configuration of MIP is one of the main advantages of the mutual impedance probe technique. It allows us, for example, to assess the heterogeneous nature of the subsurface. To illustrate this fact, we use the Capacitance-Influence Matrix Method combined with numerical simulations to model a quadrupole over a set of heterogeneous subsurfaces.

4.3.1. Study cases

We modelled 5 cases of heterogeneous subsurfaces. We first consider a surface with a constant imaginary part of the complex permittivity ($\epsilon'' = 0.5$) and a heterogeneous dielectric constant. We then fix the dielectric constant ($\epsilon' = 5.0$) and vary the imaginary part of the complex permittivity. The first heterogeneous model is a uniform random distribution of dielectric constant (ranging from 2 to 4) and imaginary part of the permittivity (ranging from 0.2 to 1.0, Figure 39 a). The size of the heterogeneities is controlled by the mesh of the model and have been set to 0.3 m.

The second heterogeneous model is a 2-layer subsurface with a separation interface located at 0.5 m under the surface (Figure 39 b). For this model, we assume a dielectric constant of 4 for the upper layer and 2 for the bottom layer and an imaginary part of 0.8 for the upper layer and 0.4 for the bottom layer.

The third heterogeneous model is a 2-layer model with a separation interface located at 5 m under the surface (Figure 39 c). We use the same values of dielectric constant and imaginary part as we did for the second model.

In the fourth heterogeneous model (Figure 39 d), we set a gradient of the dielectric constant from 4 at the surface to 2 at a depth of 10 m and a gradient of the imaginary part of 1 at the surface to 0 at a depth of 10 m.

Finally, the fifth heterogeneous model presents a spherical object with a radius of 2 m located 0.2 m under the surface (Figure 39 e). The dielectric constant is set to 2 inside the sphere and 4 outside, the imaginary part is set to 0.2 inside the sphere and 0.8 outside.

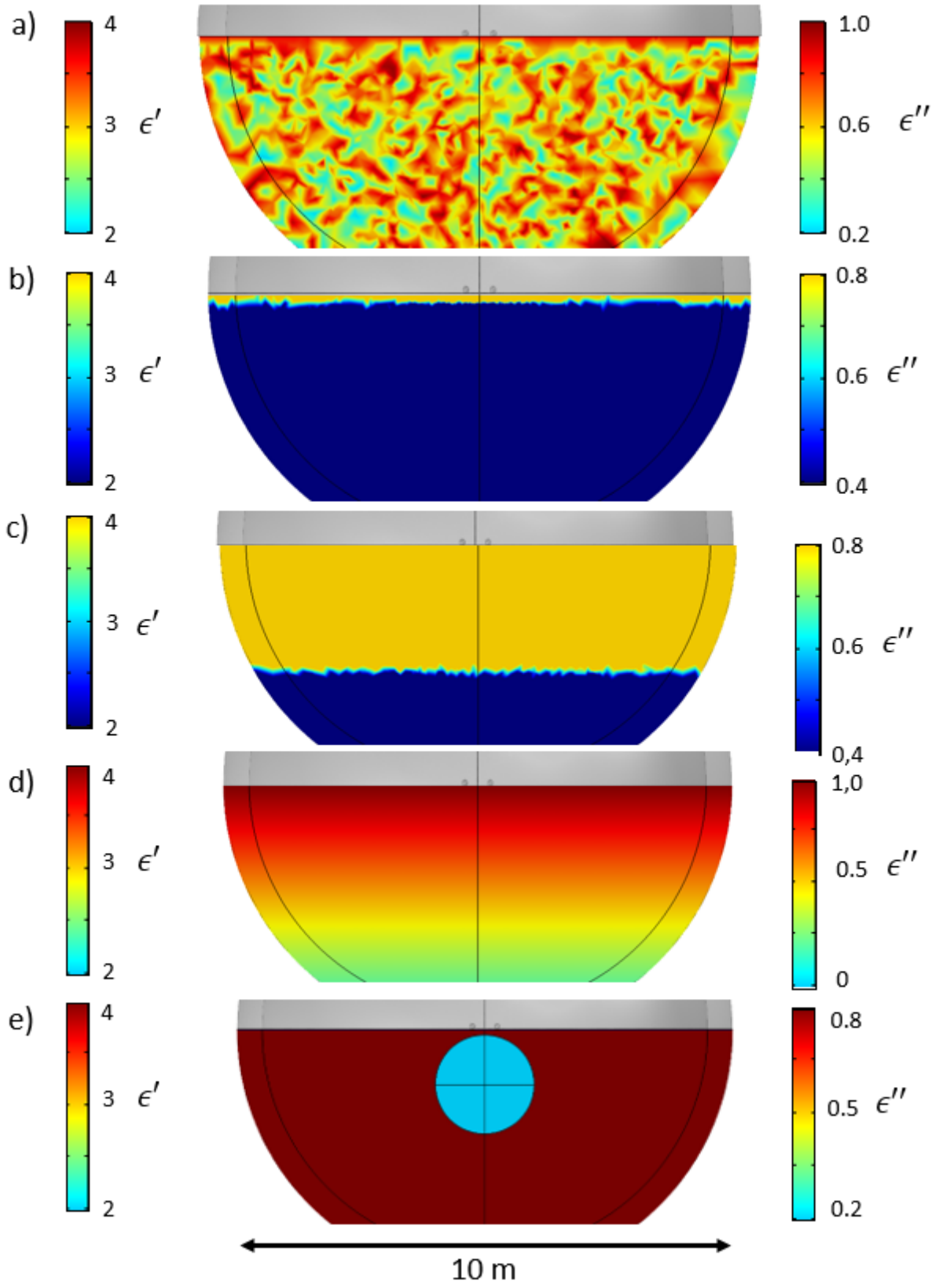

Figure 39: Five investigated heterogeneous subsurface models with the associated real and imaginary scales. (a) random distribution model, the mean size of the particles is 0.5 m. (b) 2-layer model with an interface at a depth of 0.5 m. (c) 2-layer model with an interface at a depth of 5 m. (d) Gradient model. (e) Spherical heterogeneity model.

4.3.2. Derived permittivity

Using a homogeneous subsurface model, we build charts (see section 2.5) giving the expected mutual impedance (in the complex plane) as a function of the dielectric constant and imaginary part of the permittivity. Then for each heterogeneous model we simulate a simple mutual impedance probe (4 pin point electrodes with ideal current generator and voltmeter) located at 1 cm above the surface. These simulations were repeated, progressively increasing the distance between the MIP transmitting and receiving dipoles in order to sound an increasing volume of the subsurface. Using the charts, the complex permittivity of the subsurface can be deduced from the mutual impedances obtained by simulations for different separation distances between the dipoles (which is related to the sounding depth of the MIP, as demonstrated in section 4.2). Figure 40 and Figure 41 show the derived real and imaginary parts of the complex permittivity for each heterogeneous subsurface as function of the separation between the dipoles.

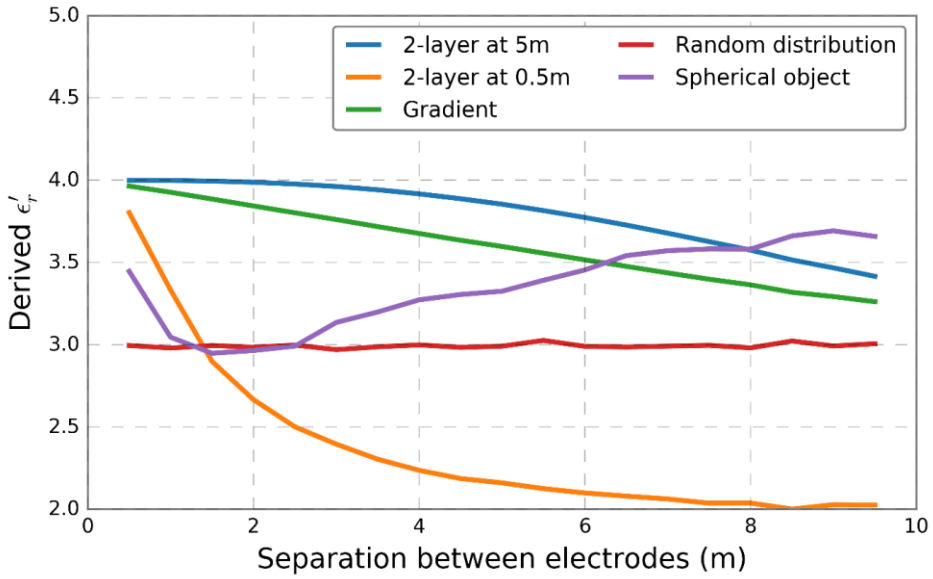

Figure 40: Derived dielectric constant as a function of the separation distance between the dipoles for the 5 investigated heterogeneous subsurface models

For the random distribution model, the derived dielectric constant equals the mean value of the subsurface dielectric constant. In addition, there is no influence of the separation distance between the dipoles. For the 2-layer models, the result depends on the depth of the interface. When the interface is close to the surface, we observe a rapid change (here a drop) in the derived dielectric constant for small separations; then the value converges towards the dielectric constant of the bottom layer. When the interface is deeper, we observe a slower drop of the derived permittivity and we note that the value derived for a small separation is close to the value obtained for large ones. If we could sound both deep and shallow depths, we would obtain a “S” shaped curve which converges towards the upper layer’s dielectric constant for small separations and towards the bottom layer’s dielectric

constant for larger separations. In the case of a gradient the measured dielectric constant linearly varies with depth (i.e., with the separation distance). Lastly, for the buried spherical object we note that the derived dielectric constant is smaller for small separations, and thus small sounding depths, than for large sounding depths, due to the influence of the sphere.

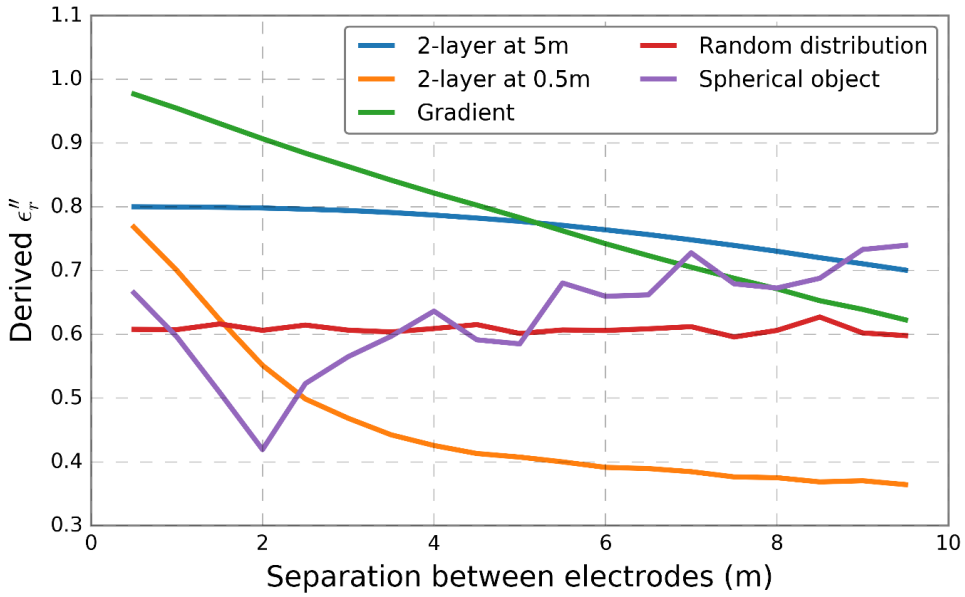

Figure 41: Derived imaginary part of the permittivity as a function of the separation distance between the dipoles for the 5 investigated heterogeneous subsurface models

The results obtained for the imaginary part of the permittivity (Figure 41) are similar to those obtained for the real part. The only notable difference is for the case of a buried spherical object for which the evolution of the derived imaginary part with the sounding depth is more chaotic, illustrating the limits of the method when sounding conductive elements.

This investigation of MIP on heterogeneous subsurfaces illustrate the tendencies that can be expected and demonstrates the need for multiple configurations of operation. MIP operations in at least two geometrical configurations (with a significant difference in terms of sounding depths) allows one to discriminate between the homogeneous/random cases and the 2 layers/gradient/sphere cases. In practice, three geometrical configurations are required to discriminate between these cases. Whenever possible, a maximum possible number of depths should be investigated.

4.4. Maximizing the scientific output

In order to optimize the scientific output from MIP measurements, some operational advice can be formulated:

I. Whenever possible, one should measure both the injected currents and the received potentials.

II. Measurements should be acquired for different and numerous geometrical configurations of operation.
III. When only a few configurations are possible, one should attempt to sound different depths by varying the distance between the transmitting and receiving dipoles, rather than between the electrodes of a same dipole.
IV. Accurate knowledge of the instrument (geometry, electronics etc.…) is important.
V. Accurate numerical simulations of the instrument and its environment are needed to properly assert its capabilities and test interpretative hypotheses.
VI. In the frame of a planetary mission, images of the environment and, if possible of the experimental setup will provide key information about the electrodes geometry, the potential presence of conductors close to the MIP and local surface topography.

5. Concluding remarks

In this chapter we have described the principle and capabilities of the Mutual Impedance Probe technique as a tool to assess the electrical properties of the subsurface. The theoretical background developed by Grard (1990) in order to derive the complex permittivity of the subsurface with a MIP has its limits when applied to realistic configuration of operation (geometry of the electrodes, presence of conductive elements close to the electrodes, electronic circuit) and we have proposed a new approach, called the Capacitance-Influence Matrix Method. This method has been validated against the analytical results and has been used (as well as analytical solutions) to estimate the performances of the MIP. We now have a better understanding of the sounding depth of a 4-electrode MIP and of how using it in different configurations of operation can help characterizing a heterogeneous subsurface. Lastly, we conclude on operational advice to maximize the scientific output from MIP measurements.

Having presented the theory, validation and capabilities of various mutual impedance probe configurations, we will, in the following chapter, apply these principles to a more realistic model, namely the SESAME-PP instrument on board the Philae lander of the Rosetta mission, and validate the method by comparison with laboratory measurements.

Chapter 3: The SESAME-PP/Philae/Rosetta experiment: modelling approaches and performances

The SESAME-PP/Philae/Rosetta is the second mutual impedance probe to have been operated on a planetary surface, after PWA-MIP/HASI/Huygens/Cassini-Huygens on Titan (see Chapter 5). As mentioned in Chapter 2, the retrieval of the complex permittivity of the surface from MIP measurements is straightforward only when the electrodes are pinpoint or spherical and isolated. In practice, this is rarely the case, especially in the frame of a space mission in which technical and operational constraints are numerous. The SESAME-PP measurements are particularly affected by the factors mentioned in Chapter 2: the electrodes have a finite size and are non-spherical, they are located close to a number of conductive elements (the lander body and legs, the ice screws, the harpoons…) and the electronic circuit has a significant influence (see Figure 30 in Chapter 2). To account for these effects, we have built an accurate numerical model of the instrument and its environment which once combined with the Capacitance-Influence Matrix Method (see Chapter 2, Section Chapter 2:2.4) allows us to correctly analyze the data collected at the surface of 67P/C-G's nucleus in the frame of the Rosetta mission. In Chapter 2, numerical models have been validated, but only by comparison to simple analytical models. To further test the numerical approach as well as estimate the SESAME-PP performances, we built, at LATMOS, a laboratory replica of the Philae lander and SESAME-PP instrument.

First, we will present the SESAME-PP instrument in the context of the Rosetta mission. Second, we will describe the numerical model we have developed and the laboratory model. This replica was used to perform measurement campaigns both in a controlled environment (over a perfect reflector) and in a natural setting (in the Dachstein ice caves). Finally, we will assess SESAME-PP capabilities in terms of sounding depths.

1. The SESAME-PP/Philae/Rosetta experiment

The SESAME-PP instrument is part of the ambitious ESA cometary mission Rosetta (Glassmeier et al. 2007). After a brief description of Rosetta's mission objectives and payload, we will explain how SESAME-PP has a much needed role in the general context of cometary exploration.

1.1. Comets and Rosetta's mission objectives

1.1.1. Comets and their scientific interests

Comets (from the Greek *kometes* meaning 'the hairy one') have been observed since ancient history (the oldest records go back as far a -1000 BC in China, Ho 1962) and were generally considered to be bad omens. The first scientific studies of comets were conducted by Paolo Toscanelli, who observed the comet P/Halley in 1456. Later Tycho Brahe studied comet C/1577 V1 and showed that the horizontal parallax was smaller than 15 arcmin, indicating that the comet was located at a distance larger than 4 times the distance Earth-Moon. A parabolic orbital movement of comets was first hypothesized by Georg Dörffel, and Isaac Newton later proved that the comet observed in 1680 has an elliptical orbit based on the theory of gravitation. Later Edmond Halley predicted the orbit of the comet named after him and it was proven true in 1758 by Johann Palitzsch thus demonstrating the validity of the law of gravity up to the distance of the aphelion of the comet, i.e. 35 AU. Further, the study of the periodicity of Encke's comet showed that it returned to perihelion 0.1 days in advance. In 1836 the mathematician Friedrich Bessel hypothesized that this was due to non-gravitational forces, more specifically forces induced by the evaporation of volatile matter.

In the years 1950 and 1951 four major theories on comets were developed. First, Fred Whipple proposed and detailed in 3 papers (Whipple 1950a; Whipple 1950b; Whipple 1955) the icy conglomerate model in which the nucleus of a comet is described as an agglomeration of rocks, dust and ices (including H_2O, NH_3, CH_4, CO_2 and C_2N_2). The sublimation of ices, due to the increasing temperature as the comet approaches the Sun, releases gases and dust grains to form the comet's atmosphere, called the coma. Second, the study of kinematics by Jan Hendrik Oort (1950) led to the prediction of the existence of a vast reservoir of comets located at ~50 000 AU from the Sun. This reservoir was later called the Oort Cloud. Third, in 1951 the astronomer Gerard Kuiper hypothesized the presence of a second cometary reservoir. This belt would have formed at the early ages of the Solar System and would be farther than the known planets, located between 30 and 100 AU from the Sun. Its existence was confirmed when the first trans-Neptunian object was detected (Jewitt & Luu 1993). The orbital period of comets generally depends on their origin: long-period comets (T> 200 years) generally come from the Oort Cloud whereas short period comets (T<200 years) tend to come from the Kuiper Belt. Finally, in 1951 Ludwig Biermann proposed an explanation to the motion of cometary plasma tails by interaction with the solar wind.

Comets are primitive objects with a composition that has barely changed in 4.6 Gyr. As such, they likely hold important clues on the youth and evolution of the Solar System. Comets may have also brought to our planet organic molecules and water on Earth. Up to 80 volatile species were known

in comets in the pre-Rosetta era, all of them are also present in the interstellar medium (except for S_2). The refractories detected on Halley's Comet were mostly silicate based (crystalline and amorphous olivine, pyroxene). The detection of CHON in Halley's Comet filled a gap in the understanding of abundances. When combining these molecules with the volatiles detected one can retrieve solar abundances for most species. Methanol and formaldehyde were also detected. Prior to the arrival of Rosetta at 67P/C-G, a variety of models were proposed including the icy-glue model (Gombosi & Houpis 1986), the icy conglomerate model (Whipple 1950b), the fluffy aggregate model (Donn & Meakin 1989), and the primordial rubble model (Weissman 1986); these models are mainly based on observations collected during the flybys of comet 1P/Halley in the mid-eighties. In these models, as in the most recent layered pile model (Belton et al. 2007), the mantle generally consists of residues that remain on the surface after the sublimation of volatiles. This deposition layer may vary in size and composition (Mendis & Brin 1978; Whipple 1989), but it was found that the uppermost layers of the nucleus of comet 1P/Halley consist of extremely dark, carbon-rich materials (Keller et al. 1987).

Most comets nuclei are generally smaller than 10 km (some are as large as 100 km, C/2002 VQ94 for example), have masses between 10^{14} and 10^{21} g and are dark objects (albedo ranging from 0.02 to 0.06, Festou et al. 2004). They originate from one of the two regions described above, or come from the interstellar medium. Gravitational perturbations (by exterior planets or by the gravitational influence of a star) modify a comet's movement around the Sun by giving it a high eccentricity orbit. When a comet gets sufficiently close to the Sun its surface temperature rises, the ices start to sublimate and take with them dust particles. The atmosphere formed by the gases and dust is called the coma and starts to be visible $\sim$5 AU from the Sun. A hydrogen cloud is also formed by the absorption of ultraviolet radiation that cause the release of hydrogen. During its orbit, the comet will form two tails: the dust tail (type II), up to 10^7 km long, formed by the escaping dust particles accelerated by the solar radiation pressure; and the ion tail (type I) composed of the molecules that were ionized (principally, H2O+, OH+, CO+, CO2+, CH+ and N2+) by the solar wind. This tail is symmetrically opposite to the Sun, generally straight, and can reach sizes up to 10^6 km.

Before the arrival of the Rosetta mission, a total of 9 space missions were dedicated to comets. The first mission was the International Cometary Explorer (ICE) launched in 1978 by NASA, for the first ever comet encounter. ICE passed though Giacobini-Zinner's and Halley's comet tails (7860 km and 31 million km from the nucleus, respectively). In 1986, the visit of Halley's comet motivated a series of missions. The Soviet spacecrafts, Vega-1 and Vega-2, studied and photographed Halley's comet from a distance of respectively 8890 km and 8030 km. Japan launched in 1985 two space probes, named Susei and Sakigake, dedicated to the study of Halley's comet and in particular its interaction with the solar wind, they approached at a distance of 151 000 km and 7 million km respectively. Giotto was the

first ESA cometary mission; it got at a distance of 600 km from Halley's comet and took the closest picture of a comet's nucleus in 1986, showing a dark potato-shaped nucleus with some active regions (Keller et al 1986). Giotto also observed Grigg-Skjellerup in 1992 from a distance of 200 km. In 2001 the NASA Deep Space 1 mission encountered comet Borrelly and gathered scientific measurements and images. The NASA Stardust mission passed into the dust and gas cloud of comet Wild 2 in 2004 and collected dust particles that were returned to Earth. The most recent cometary mission since Rosetta is the NASA Deep Impact mission that encountered comet Tempel 1 in 2005 on which an impactor was launched. The impact excavated material from the subsurface that could then be studied by the orbiter. Deep Impact was then sent to study comet Garradd in 2012. Thought relatively numerous, all of these missions were flybys and only permitted very short studies of comets. This is what motivated the conception of the Rosetta mission, which includes a lander and an orbiter designed to follow the comet and monitor its evolution as it orbits around the Sun.

1.1.2. Scientific objectives and description of the Rosetta mission

Rosetta's initial target was 46 P/Wirtanen but following a postponement of the initial launch 67P/C-G was chosen as the new target. 67P/C-G is a Jupiter-family comet that originated from the Kuiper belt. It was discovered in 1969 by Klim Ivanovych Churyumov and Svetlana Ivanovna Gerasimenko of the Kiev University's Astronomical Observatory. Prior to Rosetta's arrival not much was known of comet 67P/C-G, a light curve was obtained by the Hubble Telescope and its size and shape were estimated (Lamy et al, 2007). The Rosetta's mission objectives are to better understand the composition, formation, structure, and evolution of comets in general, and 67P/C-G in particular. To this end, the payload of the mission includes 11 instruments on-board the orbiter and 10 instruments onboard a lander called Philae. Its main objectives are:

- Characterize the coma of comet 67P/C-G, its composition, its formation, its interaction with the solar wind and its evolution as the comet evolves around the Sun.
- Characterize the nucleus of comet 67P/C-G (its temperature, composition, geology and evolution through time) from remote sensing and *in situ*, at the landing site of the Philae lander.

1.2. Rosetta's and Philae's payload

1.2.1. Rosetta's payload

Rosetta's payload includes 11 instruments (Figure 42):

- **Alice** (Stern et al. 2007) is a UV imaging spectrograph used to measure the abundance of noble gases and atoms such as H, O, C and S in the cometary coma through the observation of

spectral features in the extreme and far UV (70-205 nm). The instrument thus provides clues on the thermal history and therefore on the orbital past of 67P/C-G. Alice can also determine the production rate and variability of water, carbon monoxide, carbon dioxide gas surrounding the nucleus.

- **CONSERT** (COmet Nucleus Sounding Experiment by Radiowave Transmission, Kofman et al. 2007) is a bistatic radar that operates between a module on Philae and another on board the Rosetta orbiter. A radio signal is transmitted from Rosetta, received by the antennas located on Philae after its propagation through the comet nucleus and send back to the orbiter. The amplitude and celerity of propagation of the received signal can be interpreted in terms of composition and structure of the interior of the nucleus (see Chapter 1, Section Chapter 1:4.5).
- **COSIMA** (Cometary Secondary Ion Mass Analyser, Kissel et al. 2007) is a secondary ion mass spectrometer dedicated to the measurement of the composition of dust grain emitted by the comet and collected in the coma. It is equipped with a microscope to detect and characterize the dust grains and is particularly suited for the detection of organics and minerals.
- **GIADA** (Grain Impact Analyser and Dust Accumulator, Colangeli et al. 2007) analyses the number, mass, momentum and velocity distribution of the dust particles in the coma. These particles can either come directly from the nucleus or be grains that were deflected by the solar radiation; their characteristics and number evolve as the comet orbits the Sun. GIADA can therefore contribute to the determination of one of the key parameters characterizing a comet: the dust to gas ratio.
- **MIDAS** (Micro-Imaging Dust Analysis System, Riedler et al. 2007) also investigates the dust environment around the comet by performing a microtextural and statistical analysis of the dust grains. Using an atomic force microscope, the instrument can provide a 3D image of single μm-sized particles with a resolution of 4 nm.
- **MIRO** (Microwave Instrument for the Rosetta Orbiter, Gulkis et al. 2007) is a combined spectrometer and radiometer operating at millimetric and sub-millimetric wavelengths (188 GHz and 562 GHz). In its radiometry mode, MIRO senses the subsurface temperature of the comet nucleus to depths of few centimeters. In its spectrometry mode, it is designed to detect and monitor the abundance of key volatiles species including H_2O (and its isotopes), CO, CH_3OH and NH_3.
- **OSIRIS** (Optical, Spectroscopic and Infrared Remote Imaging System, Keller et al. 2007) is a camera imaging system operating in the visible, near infrared and near UV wavelength domains. It is composed of a wide and a narrow-angle camera to both provide high spatial

resolution images (with resolution as good as two centimeters per pixel 1 km away from the surface) of the nucleus and wide views of the comet and its coma.

- **ROSINA** (Rosetta Orbiter Spectrometer for Ion and Neutral Analysis, Balsiger et al. 2007) is composed of two mass spectrometers and a pressure sensor. The mass spectrometers are designed to study the composition of the comet's atmosphere and ionosphere and measure the temperature and velocity of gas and ions. In particular, ROSINA can measure the deuterium/hydrogen (D/H) ratio which is key to determine whether or not comets have contributed to Earth's water.
- **RPC** (Rosetta Plasma Consortium, Carr et al. 2007) consists in five instruments that share common electronics and software. The Ion Composition Analyzer (ICA) measures the velocity and mass of positive ions. The Ion and Electron Sensor (IES) measures the ion and electron environment around the nucleus. The Langmuir Probe (LAP) measures the electron temperature and density of the surrounding plasma. The Magnetometer experiment (MAG) is used to characterize the magnetic field at the solar wind/coma interface. The Mutual Impedance Probe (MIP) characterizes the electron gas environment (speed, temperature and density).
- **RSI** (Radio Science Investigation, Pätzold et al. 2007) experiment uses the radio communication system of Rosetta and ground stations on Earth to deduce, from frequency shifts in the radio signals, the mass and gravity of the comet nucleus and characteristics of the ionized medium surrounding the probe.
- **VIRTIS** (Visible and Infrared Mapping Spectrometer, Coradini et al. 2007) is a visible and IR imaging spectrometer designed to identify the gaseous species of the coma and the solids of the nucleus surface. It can also measure the temperature of the nucleus and monitor its spatial and temporal variations.

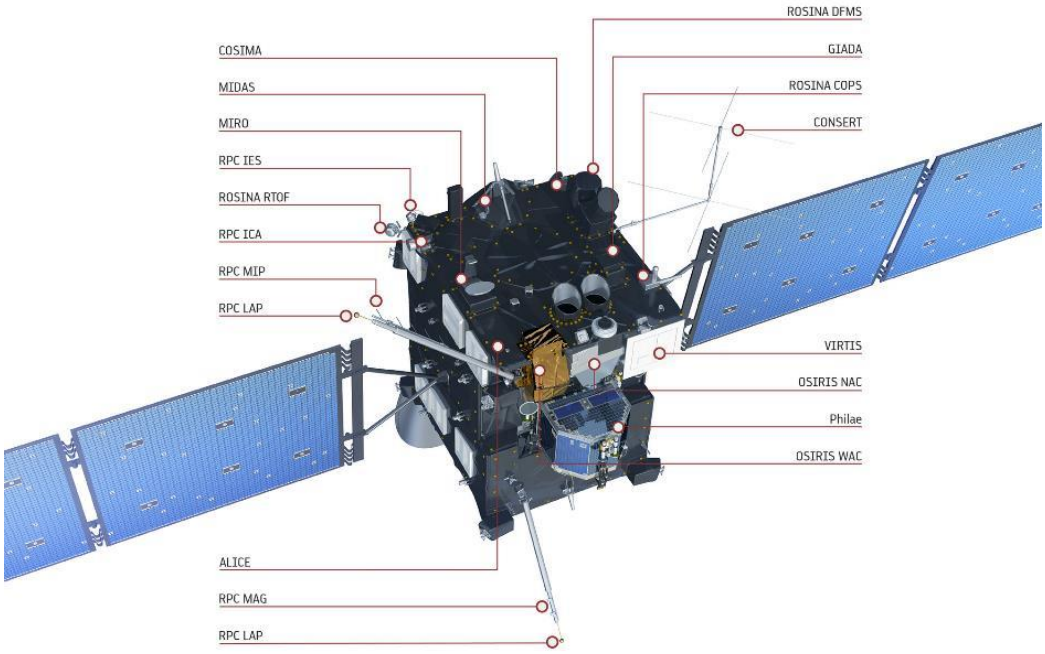

Figure 42: Localization of the instruments onboard the Rosetta orbiter. Credits: ESA/ATG medialab

1.2.2. Philae's payload

In addition to CONSERT Philae includes 9 instruments (Figure 43):

- **CIVA** (Comet Infrared and Visible Analyzer, Bibring et al. 2007) is a set of 7 optical cameras that produced a panoramic image of the close environment of the Philae lander (see Figure 100 in Chapter 4). Two cameras are aligned so as to produce stereoscopic images. It also is a spectrometer designed to investigate the composition, texture and albedo of the surface.
- **ROLIS** (ROsetta Lander Imaging System, Mottola et al. 2007) is a high-resolution CCD camera which primary purpose is to take picture during the descent of Philae towards the nucleus, and below the lander once on the surface.
- **SD2** (Sample Drilling and Distribution, Finzi et al. 2007) is a device containing a drill capable of drilling down to 20 cm in the surface and collecting samples for analysis for COSAC and Ptolemy.
- **COSAC** (COmetary SAmpling and Composition, Goesmann et al. 2007) is a gas analyzer that can detect complex organic molecules in the gas and dust close to the landing site or in a sample delivered by the SD2 system.
- **Ptolemy** (Wright et al. 2007) is also a gas analyzer but aiming at measuring isotopic ratios of light elements (hydrogen, carbon, nitrogen and oxygen).

- **ROMAP** (ROsetta lander Magnetometer And Plasma monitor, Auster et al. 2007) is a combination of a magnetometer and plasma instrument designed to investigate the local magnetic field and the comet/solar-wind interaction.
- **MUPUS** (MUlti PUrpose Sensor for Surface and Subsurface Science, Spohn et al. 2007) consists of a number of temperature sensors located on a 35-cm long penetrator (MUPUS-PEN) and on the harpoons designed to penetrate the subsurface of the nucleus and to measure its thermal and mechanical properties. In addition, MUPUS has a thermal mapper (MUPUS-TM) mounted on the Philae lander to measure the thermal inertia of the surface.
- **APXS** (Alpha-P-X-ray Spectrometer, Klingelhöfer et al. 2007) is an experiment designed to determine the chemical composition of the nucleus at the Philae landing site.
- **SESAME** (Surface Electrical Sounding and Acoustic Monitoring Experiments, (Seidensticker et al. 2007) is an instrumental package composed of 3 instruments, namely PP, CASSE and DIM, designed to measure, respectively, the electrical, mechanical properties of the nucleus as well as the particles emitted from the surface. See section 1.3 for more details.

There is a great synergy between the instruments described above. In particular, some of the instruments collect information that are useful to better analyze and interpret the measurements of the SESAME-PP instrument. These information can give indications on the position of the electrodes and their contact with the ground (CIVA, ROLIS, SESAME-CASSE), on the composition the surface (VIRTIS, COSAC), on the subsurface porosity at different depths especially though the measurement of the thermal inertia (VIRTIS, MIRO, MUPUS-PEN and MUPUS-TM, CONSERT) and on the electromagnetic environment surrounding the lander (RPC, ROMAP).

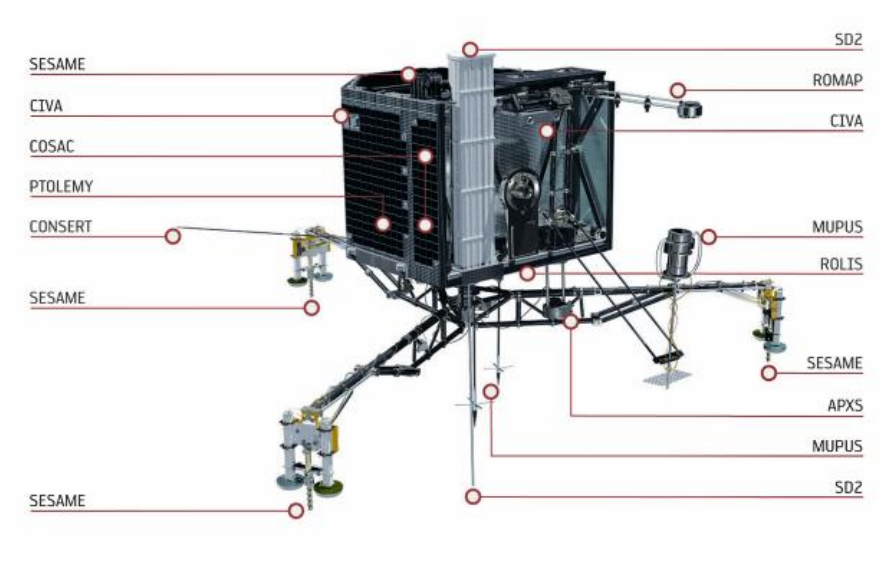

Figure 43: Localization of the instruments onboard the Philae lander. Credits: ESA/ATG medialab

1.2.3. Depth sounded

Among the instruments of the Rosetta and Philae payload, MIRO, CONSERT, MUPUS-PEN, SD2, SESAME-CASSE and SESAME-PP are all designed to sense the subsurface of the nucleus, though with different objectives and at different scales. In particular, MIRO and CONSERT, like SESAME-PP, provide constraints on the electrical properties of the subsurface. However, the respective sounding or penetration depth of these instruments differ from that of SESAME-PP. It can be estimated using Equation (58) in Chapter 1, that CONSERT can probe 100's of meters while MIRO only senses a few centimeters. SESAME-PP's sounding depth was estimated to be about 1 meter (see Chapter 2, Section Chapter 2:4.2) as illustrated by Figure 44, the SESAME-PP experiment thus complements the CONSERT and MIRO experiments in terms of sounding depth.

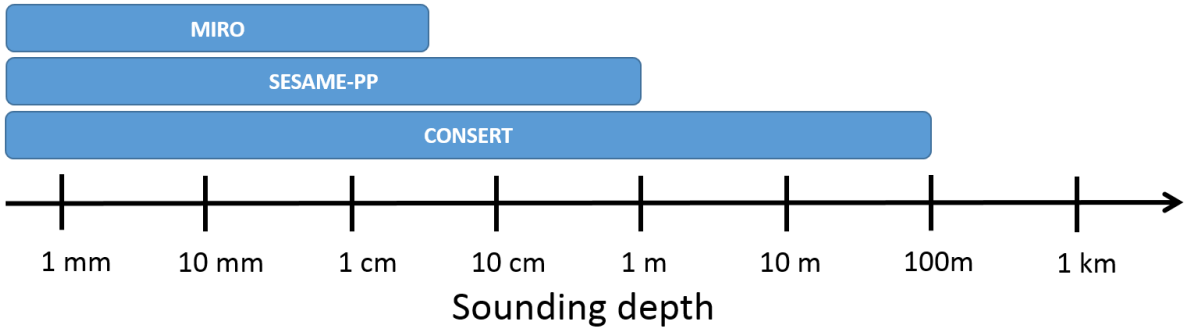

Figure 44 Sounding depth of the three Rosetta instruments capable of measuring the electrical properties of the subsurface.

1.3. The SESAME-PP experiment

1.3.1. The SESAME package

The SESAME-PP instrument is part of the SESAME experiment (Seidensticker et al. 2007) which also includes the Comet Acoustic Surface Sounding Experiment (CASSE, Kochan et al. 2000) and the Dust Impact Monitor (DIM, Flandes et al. 2012).

DIM measures the size and direction of arrival and then derives the mass and velocity of dust or ice particles (with a diameter of a few μm - dm) escaping from the comet's nucleus and detected when impacting a cube-shaped sensor mounted on top side of Philae. These particles are ejected from the surface by the comet's activity and either form the comet's coma or are drawn back to the nucleus by gravity. DIM measurements thus provide information on the erosional/depositional dynamic processes at play at the surface of the nucleus and on their intensity.

The CASSE instrument records the acoustic waves through the comet subsurface. It can operate in an active mode, when the waves are generated by transmitters built into the feet of the lander (see Section 1.3.2 for a more precise localization), or in a passive mode when it listens for noise produced by other instruments (e.g., hammering of MUPUS-PEN) or by thermal or impact induced activity on the comet. Doing so, CASSE can reveal any holes or layering in the subsurface down to a depth of around 2 meters.

Lastly and as mentioned previously, PP was primarily designed to measure the complex permittivity of the first meters of the nucleus' subsurface to help constrain its composition and porosity and monitor potential evolutions with time. More details are given in the next section.

PP, CASSE and DIM share most of their electronics: Each instrument has a dedicated circuit board located inside the body of Philae and linked together by the experiment bus. The instruments also share a microcomputer, 3 different types of memory and 2 different softwares:

- a common flight software, designed to interpret the telecommands, set the operating modes of the instruments, process the science data and transmit them to the lander communication system.
- the Electrical Ground Support Equipment (EGSE) software, called Alibaba (Figure 45), which provides a graphical interface to easily display the scientific data from the 3 experiments.

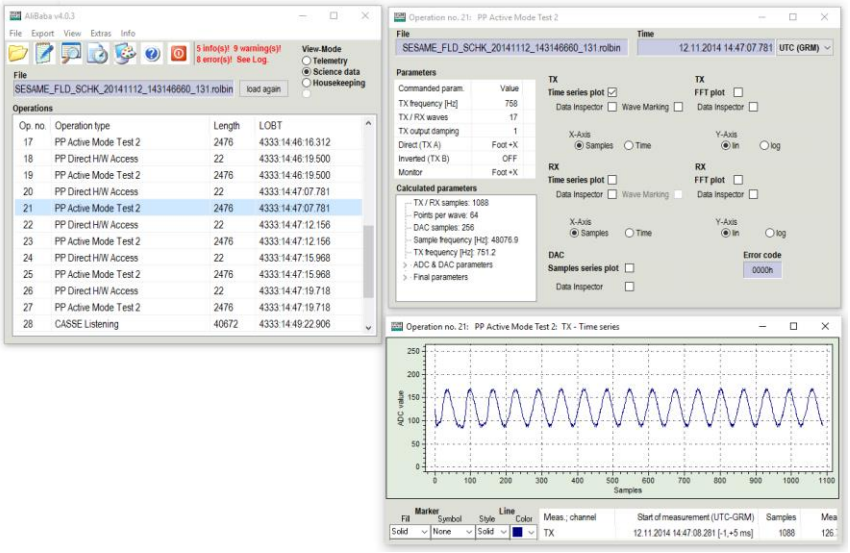

Figure 45 Screenshot of Alibaba, the graphical interface program common to all three SESAME instruments. It allows an easy and quick verification of the data. In particular Alibaba can display SESAME-PP time series data and perform a FFT on them

1.3.2. The SESAME-PP experiment and operation modes

The SESAME-PP experiment is the result of the collaboration of multiple institutes. It has been developed jointly by the FMI (Finnish Meteorological Institute, Helsinki, Finland), the RSSD (Research and Scientific Support Department, Noordwijk, The Netherlands), and the LATMOS (Laboratoire Atmosphères, Milieux, Observations Spatiales, Guyancourt, France). The responsibilities of each institution is as follows: FMI was responsible for the instrument definition, the conception of the main electronics board, the flight software specification, conception of on-board analysis algorithm, the ground support equipment, the instrument simulator, and the flight operation definition. RSSD was responsible for the pre-amplifier design, the pre-amplifier qualification, the integration of the instrument, and its calibration. LATMOS was responsible for the instrument modelling and calibration support. The data analysis was conducted in all three institutions although, the majority was done in LATMOS.

The instrument is composed of:

- The SESAME-PP electronics are located on a separate board of the SESAME electronics itself located inside the body of the lander. Its main features are an external data memory, a digital control circuitry and three analogue modules: injected current generator, received signal measurement module and plasma wave integrator.
- The cables that link the electronics of SESAME-PP to the multiple electrodes
- The electrodes and their guards

SESAME-PP has five electrodes, three transmitting and two receiving ones (see Figure 46). The two receiving electrodes are located on two of the feet of the Philae lander; hereafter called +Y and

−Y electrodes. One of the transmitting electrodes is located on the third foot of the lander hereafter referred to as +X; the two others are co-located with MUPUS-PEN and APXS. Over each electrode is also located a guard to shield it from the influence of the Lander.

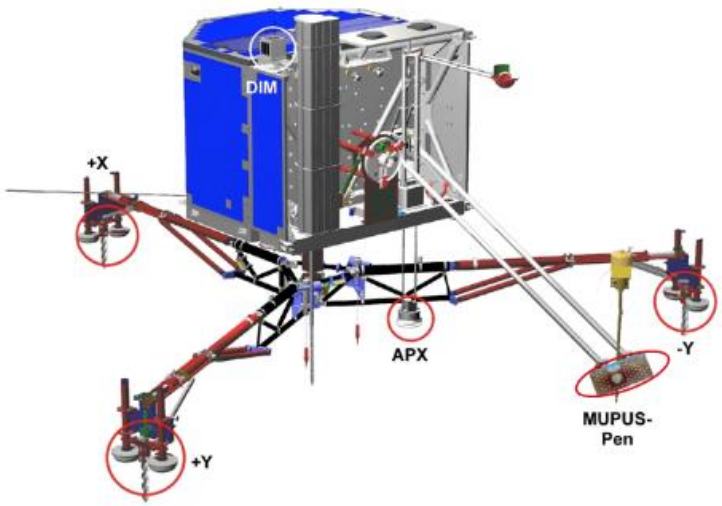

Figure 46 The Rosetta lander Philae with deployed landing gear and appendages showing the locations of the SESAME-PP sensors (red circles). Three electrodes are located on the feet of the lander; each of them is composed of two interconnected soles. The two other electrodes are co-located with the MUPUS-PEN and APXS instruments. Copyright ESA/ATG medialab

The electrodes mounted on the feet of the lander are designed in a similar way. They are made of a thin (thickness of 35 µm) stainless steel mesh (Figure 47a) that is glued on the bottom of the foot soles (the soles are made of glass fiber). Closing each sole is a thin steel lid (the guards, see Figure 47b). Each foot is made of two soles with the electrodes linked by a coaxial cable. A CASSE transmitter (Figure 48b) and a CASSE accelerometer (Figure 48c) are located inside the soles of each foot can be found Additionally, for the two receiving feet, a preamplifier is attached to the lid of the sole containing the CASSE accelerometer (Figure 47b).

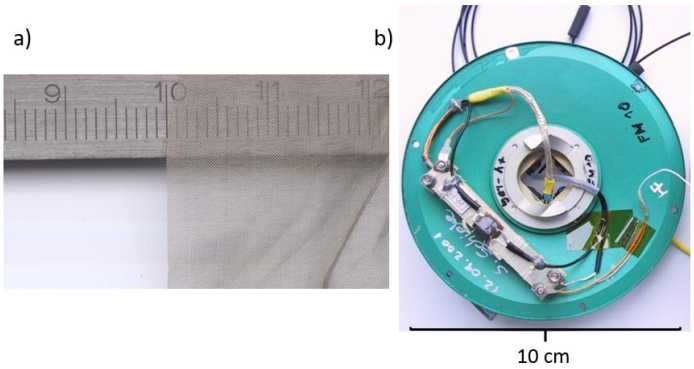

Figure 47 a) Picture of the metallic mesh glued to the bottom of the glass fiber soles that acts as electrodes for SESAME-PP. b) Picture of one of the guards that closes the sole, the rectangular block is one of the two preamplifiers located in the receiving feet.

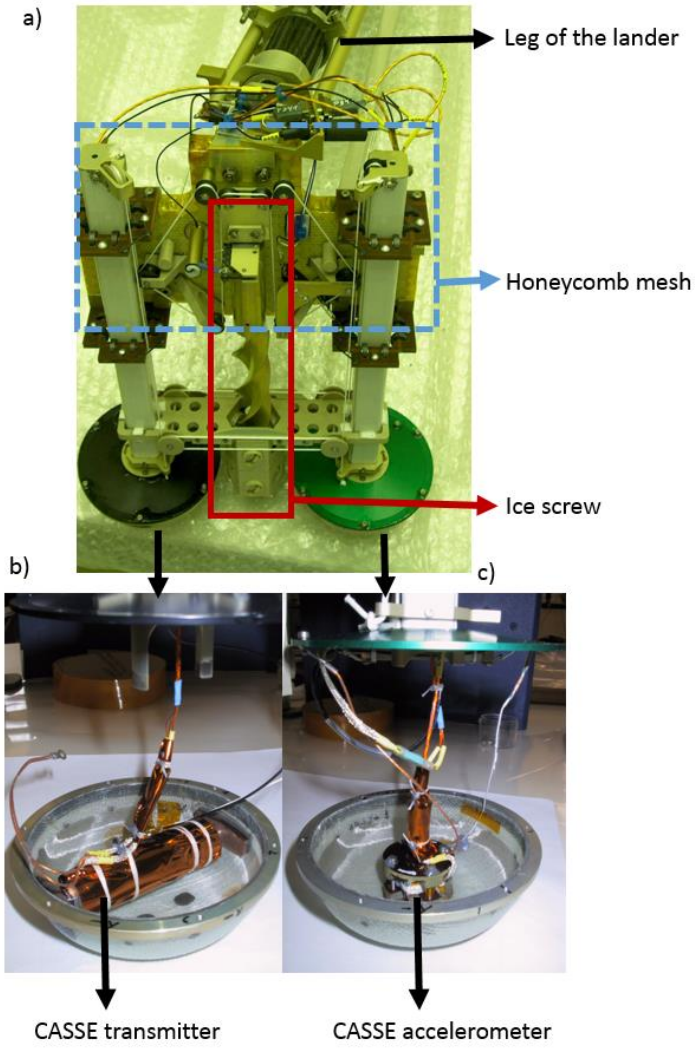

Figure 48: a) Picture of one of the receiving feet of the Philae lander with, indicated by a blue box, the honeycomb structure holding the two soles together and, in red, the ice screw. b) Detail of the inside of one of the soles containing a CASSE transmitter. c) Detail of the inside of one of the soles containing a CASSE accelerometer.

The two soles of one foot are held together by a honeycomb conductive structure and separated by an ice screw (see Figure 48a).

The transmitting electrode mounted on the MUPUS-PEN instrument has a different design. It is made of a flexible mesh (Figure 49a). In principle, it should lie on the ground after the deployment and hammering of the penetrator (Figure 49b). The mesh is multilayered with one layer being the electrode and another begin the guard (each layer is 0.6 mm thick, see Figure 49c). The MUPUS-PEN electrode is designed to be deployed up to 1 m away from the back of the lander's body.

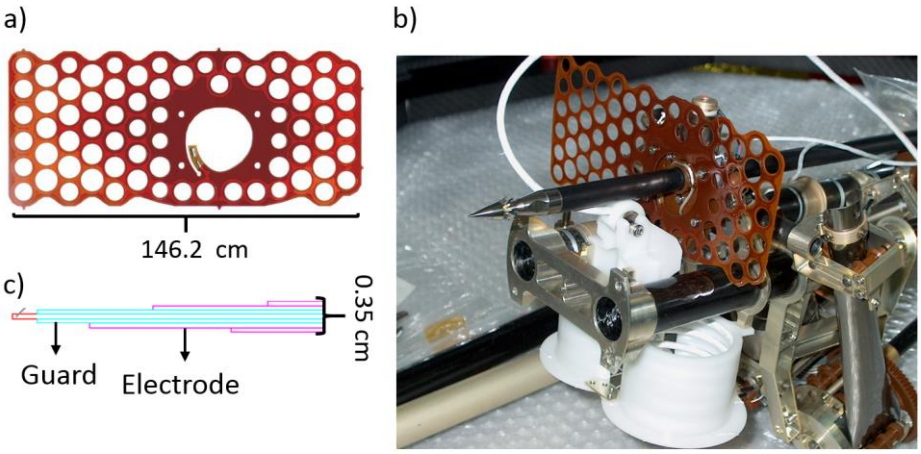

Figure 49: a) MUPUS-PEN transmitting electrode, b) MUPUS-PEN transmitting electrode attached to MUPUS-PEN, c) Side view of the MUPUS-PEN electrode with the layers corresponding to guard and electrode indicated.

The third transmitting electrode is integrated in the lid of the APXS detector. It is made of a multilayered ring (5 layers, the electrode and the guard are copper layers 70 µm thick separated by 35 µm, see Figure 50). When APXS is deployed the ring should touch the cometary surface. The APXS electrode and deployment device are mounted in an opening in the floor of the balcony of the Philae body.

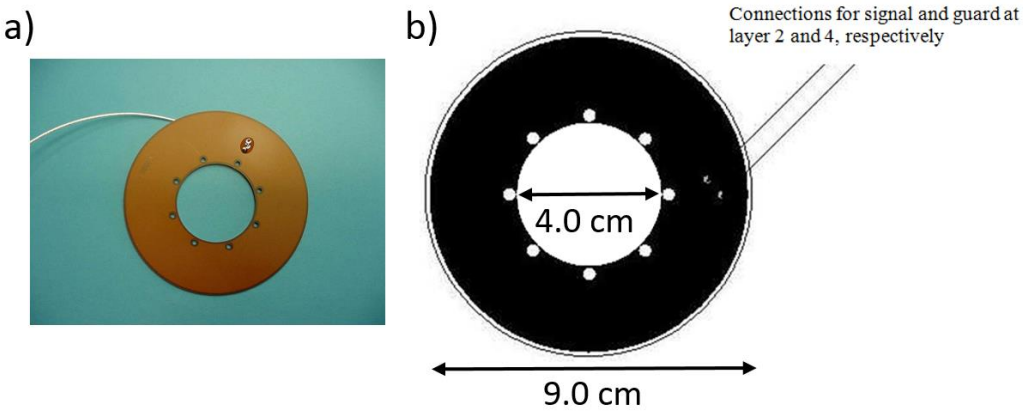

Figure 50: a) APXS electrode. b) Dimensions of the APXS electrode and indication of the layers corresponding to the guard and electrode.

The block diagram of SESAME-PP is shown in Figure 51. Upon command, the Digital-to-Analog-Converter generates voltages between 0 V and +5 V with frequencies between 5 Hz and 20 kHz which is then level-shifted and amplified to -10 V/+10 V analog output. A 50 kHz low-pass filter removes the step transitions from the output signal. The direct output is then connected with the help of a switch-box to either the +X or APXS electrode. The inverted signal (in phase opposition, i.e. with a phase shift of 180° compared to the direct signal) can be connected to either the APXS or MUPUS-PEN electrode (the option of both signals being directed to the APXS electrode is prevented by hardware). If only one

electrode is selected the voltage of that electrode alternates between -10 V/+10 V with regard to the lander's body (i.e. the ground). The signals are sent to the electrodes via triaxial cables, the inner cable transmits the signal to the electrode, the middle cable is at the same voltage as the signal cable, finally the outer cable is connected to the body of the lander (considered to be the ground). The middle cable sets any metallic surface in the vicinity of the transmitter electrodes (like the CASSE transmitters and accelerometers) to the same potential as the electrode therefore allowing a minimum of stray capacitances between the electrode and metallic surfaces located close by. The guards are also set to the potential of the signal reducing the influence of the elements of the feet and legs on the measured current which is measured through a 2250 Ω resistor.

The receiving electronics consist of the electrode, a preamplifier (located in one of the soles) and 2 guards. The preamplifiers input is connected to the electrodes in both soles and has two outputs. One output sets the guards and the CASSE elements to the same potential as the electrodes, shielding them from the influence of the conductive element close by. The second output is connected to the SESAME-PP electronics board and transmits the amplified received signal. On the SESAME-PP electronics board a multiplexer selects the channels to be recorded. The selected signals are then sent to the analog-to-digital converter and processed by the onboard computer.

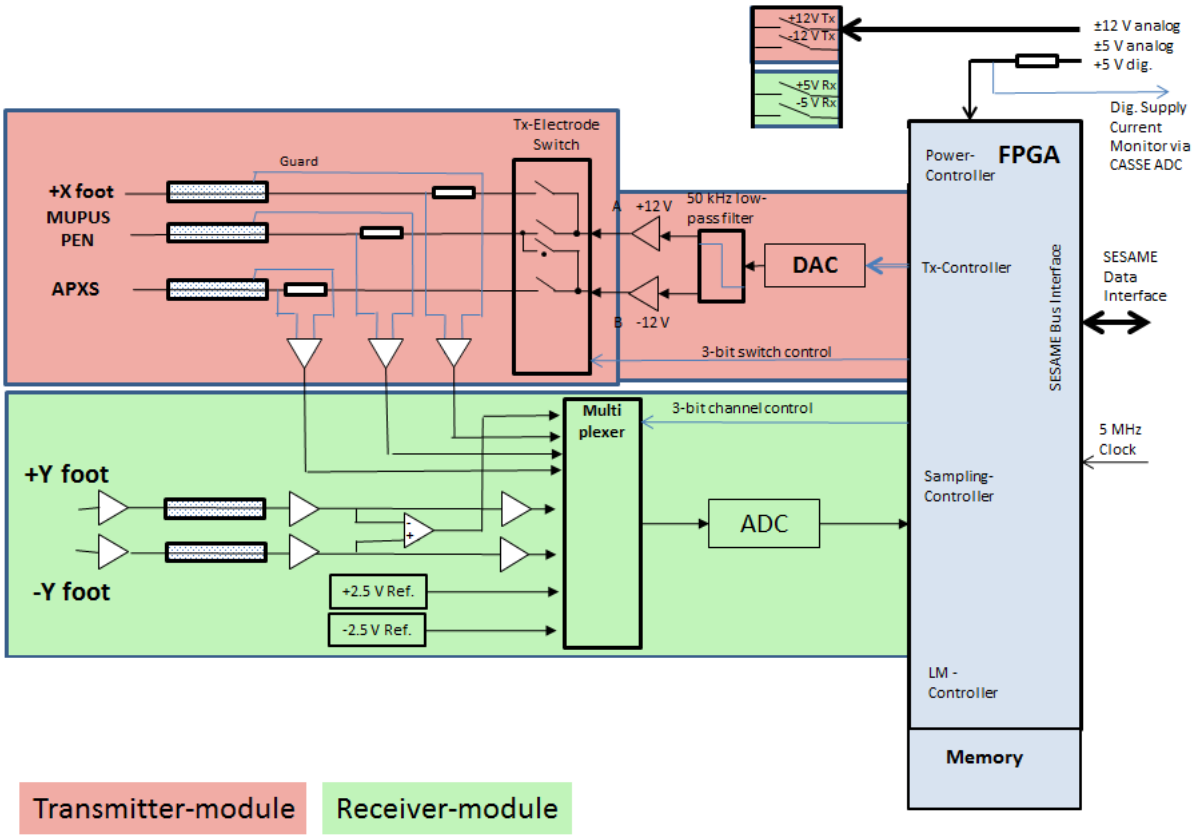

Figure 51: SESAME-PP instrument block-diagram

In the active mode of operation of SESAME-PP, two transmitting electrodes are selected to inject a current into the environment and the induced potential difference between the two receiving electrodes is measured. Additionally, a second signal can be acquired: this signal can either be the current that flows through one of the two transmitting electrodes or the potential sensed by one of the receiving electrodes. The transmitted signal consists in a sinusoidal signal composed of 17 complete waves (the first wave is ignored during the processing phase to avoid setup problems with the preamplifiers) at a chosen frequency and amplitude (the amplitudes peak to peak is defined as $A = 20/2^n$ V, where n is a fixed parameter between 0 and 4). The sampling frequency of both the measured currents and potentials are frequency-dependent: below 1500 Hz, 64 sample points per wave are used; above 3400 Hz, only 16, and in the intermediate range, 32.

The on-board data processing is as follows:

- The data vectors are checked for oversaturation, if this is the case it is indicated in the telemetry packet.
- A wavelet transformation is used to move the frequency domain.
- A low pass and high pass filters are used to remove any frequency higher than twice or lower than half the selected frequency.
- A sine wave is fitted on the data and the amplitude and phase shift are recorded.

Time series (see Figure 52 for an example) can also be recorded. They consist of 17 complete waves with a number of points dependent on the chosen frequency. The data are then processed on Earth at the cost of a larger data volume (2816 bytes for time series against 800 bytes for the on-board processed data).

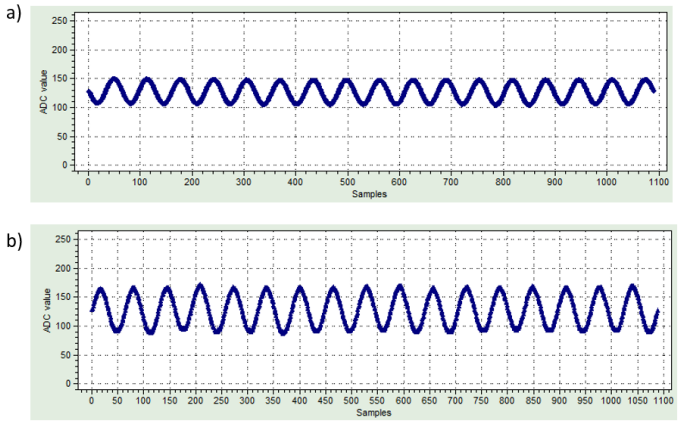

Figure 52: Time series acquired on the surface of 67P/CG for a frequency of 758 Hz, a) Transmitted current on the +X foot, b) Received potential difference between the +Y and -Y feet.

As mentioned previously, the transmitting dipole consists either of +X and MUPUS-PEN, +X and APXS, or MUPUS-PEN and APXS. Though, in principle, only four electrodes are required, the possibility of selecting among three transmitting dipoles and varying the geometry of the quadrupole allows to probe different volumes of material and possibly to detect heterogeneities in the near subsurface (as demonstrated in Chapter 2, Section 4.3). A reduced geometry mode that makes use of the three foot electrodes only (+X as the transmitter and −Y and +Y as the receivers) was also anticipated for in-flight calibration and for the first measurements after landing before the deployments of APXS and MUPUS. In this mode of operation, the body of Philae acts as the second transmitting electrode, which is not optimal. Unfortunately, because of the shortness of the Philae mission, the measurements performed on the surface of 67P/C-G were only acquired in this mode of operation (see Chapter 4 Section 3.3).

The SESAME-PP instrument also includes a passive operation mode that records the potential difference between the two receiving electrodes with a sampling frequency of 20 kHz, without any active transmitting electrode, the data vector is then analyzed with a wavelet algorithm that generates a logarithmic power spectrum for 10 frequency bins. The main objective of this mode is to measure the electric field of the plasma waves generated by the interaction of the solar wind with the charged dust and ionized gases that surround the nucleus, and thus to monitor the activity of the comet.

The SESAME-PP instrument offers three important features. First, its maximum power requirement is 1767 mW, each measurement lasts 6 s and requires 3 mWh of energy (including the power needed by the SESAME computer). Secondly, the required data volume is small: at most, 2816 bytes per measurement for the time series. Thirdly, the total mass of the instrument does not exceed 170 g and, thus, easily meets space mission requirements.

2. Modeling SESAME-PP

2.1. SESAME-PP numerical model

As shown in Chapter 2 Section 3, the Capacitance Influence Matrix Method combined with numerical models offers a way to derive the complex permittivity of a ground from SESAME-PP data while properly accounting for the influence of the conductive environment of the electrodes and of the electronic circuit. In this section, we will describe the numerical geometry model as well as the different steps required for the analysis the SESAME-PP data collected on the surface of the 67P/C-G comet or by the laboratory replica of the instrument built at LATMOS and presented in Section 2.4.

2.2. SESAME-PP lumped element model

In order to apply the Capacitance-Influence Matrix Method, we discretize the conductive environment of SESAME-PP into a set of 19 discrete conducting elements listed in Table 7. Michel Hamelin (LATMOS) built a preliminary, simplified model to verify and evaluate the possibility of an in-flight calibration just before landing, assuming a quasi-vacuum environment. During my thesis, I rebuilt a new model geometrically more accurate and in particular I introduced the presence of an interface with a semi-infinite medium of given permittivity (Figure 53).

The Philae body (element number 13) is the largest of the discrete conducting elements next to SESAME-PP. It is covered with solar panels and can be regarded at low frequencies as a perfect conductor. A close-up of the numerical model constructed for the feet of the lander is shown in Figure 53 B). The transmitting electrodes are elements number 3–4 (+X electrode), 14–15 (MUPUS-PEN electrode) and 16–17 (APXS electrode); the receiving electrodes are elements number 7–8 (−Y electrode) and 11–12 (+Y electrode). All electrodes, guards and ice screws are either made of steel or copper. We emphasize that the ice screws are especially important to model because they are located very close to the electrodes (less than 5 cm away) and the guards only shield their influence partially. The harpoons, designed to anchor the lander to the nucleus, are also metallic. The foot plates are made of an aluminum honeycomb structure. The landing gear is made of carbon fiber but was metal coated and most of the assembling elements are made of steel. Therefore, it is possible to consider that all the elements are perfect conductors in a numerical simulation.

Table 7 Conducting elements of SESAME-PP and its environment.

Element number	**Element**	**Element number**	**Element**	**Element number**	**Element**
1	+X foot plate	**8**	-Y soles	**15**	Electrode APXS
2	+X screw	**9**	+Y foot plate	**16**	Guard MUPUS-PEN
3	+X guard	**10**	+Y screw	**17**	Electrode MUPUS-PEN
4	+X soles	**11**	+Y guard	**18**	Harpoon 1
5	-Y foot plate	**12**	+Y soles	**19**	Harpoon 2
6	-Y screw	**13**	Body of the lander & Landing Gear		
7	-Y guard	**14**	Guard APXS		

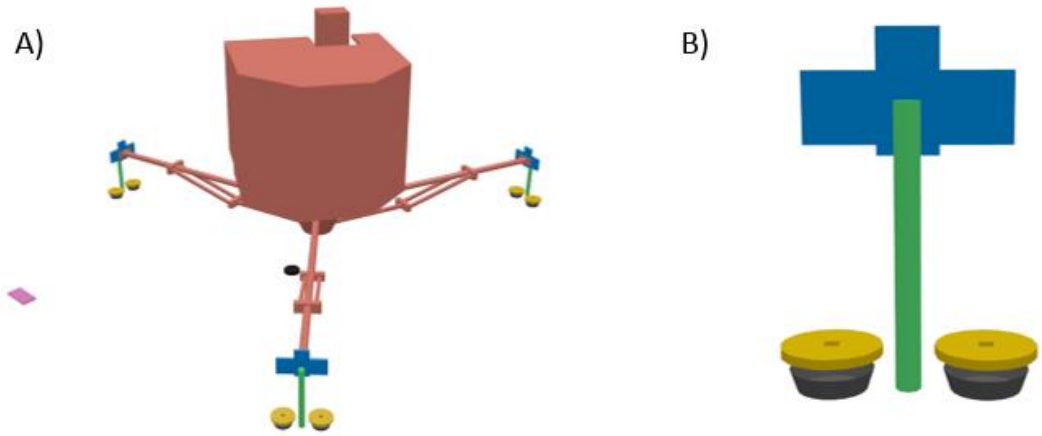

Figure 53: A) Numerical geometry model of the SESAME-PP instrument and its conducting environment. The red shape is the body of the lander combined with the landing gear (element 13). The body is rotated by 11.2 ° with respect to the landing gear. The blue shapes are the conductive plates linking the legs of the lander to the feet (elements 1, 5 and 9). The green shapes are the ice screws on each foot (elements 2, 6 and 10). The yellow shapes are the guards of the electrodes (elements 3, 7 and 11). The dark grey shapes represent the soles of the electrodes (elements 4, 8 and 12). The pink shape is the MUPUS-PEN electrode and guard (elements 16 and 17). Lastly, the black shape is the APXS electrode (elements 14 and 15), once deployed under the balcony. Not represented on this numerical model are the harpoons located under the body of the lander (elements 18 and 19). B) Zoom on one of the feet of the lander.

COMSOL Multiphysics is capable of performing numerical calculations on complex geometries but unnecessary complex geometries will result in too long computation times and, more importantly if not meshed correctly they can induce errors in the results. Therefore, we made certain simplifications:

- The part linking the body to the landing gear has overall a complex geometry (see Figure 54a). However, it is located at a sufficient distance from the electrodes (~ 1 m) to be approximated by a conical section (see Figure 54b). Additionally, it has been verified with numerical models that its influence is small compared to that of the body.

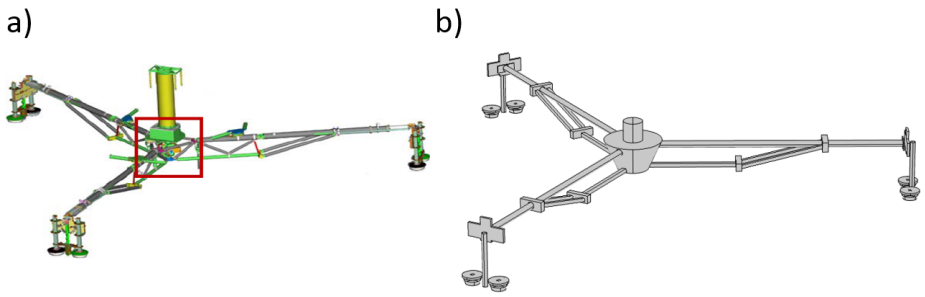

Figure 54: a) Detailed model of the Philae landing gear, outlined in red is the part linking the body to the landing gear, b) Simplified numerical model where the central part is approximated by a conical section.

- The interface between the legs and the feet is simplified by a parallel plate capacitor of equivalent capacitance.
- The geometrical model of the feet omits the presence of the non-conductive elements holding the soles, and the soles themselves (made of glass fiber); the shape of the electrodes is approximated by the section of a cone.
- Two models were built for the guards, a first one was very close to the true geometry of the guards (Figure 55a) and a second one approximated them by cylinders (radius = 5 cm and height 1 cm, Figure 55b). Tests showed that the approximation by the cylinders induced very small differences in the numerical results.

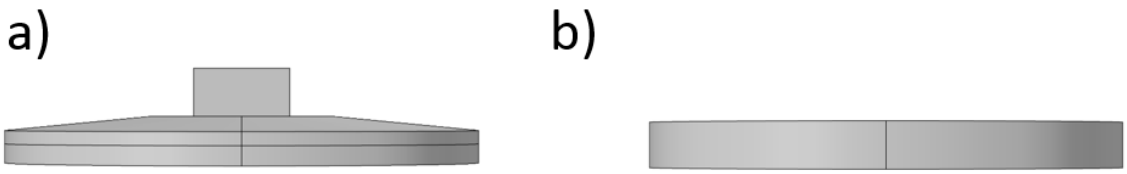

Figure 55: a) Geometrically accurate guard, b) Guard approximated by a cylinder giving similar numerical results

- The screws located between the two soles of a foot are approximated by cylinders with appropriate dimensions (i.e, height = 20 cm and radius = 2 cm).
- The initial model included the CASSE sensors in the soles, but their influence was shown, with the help of numerical models, to be negligible and they were removed (Figure 56), this is due to them being covered by a conductive shield set to the electrode potential.

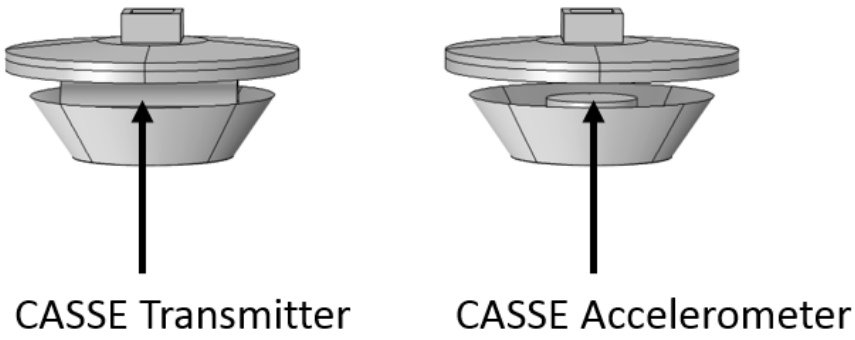

Figure 56: Model of the feet including the CASSE elements

- The MUPUS-PEN electrode and its guard are represented by a single block with appropriate dimensions (146.2 x 64.9 cm). The height of the block must be increased to 0.5 cm (compared

to 0.35 µm) to avoid meshing errors. The holes were not represented as they have dimensions much smaller than the wavelength.

- The APXS electrode and its guard are represented by a ring with appropriate dimensions (see Figure 50b). As for the MUPUS-PEN electrode, the height of the APXS electrode and guard had to be exaggerated (0.5 cm) to avoid meshing errors.

The limitations of these simplifying assumptions have been tested against simulations and are proven to have very little impact on the results. The model also offers the possibility to rotate the body of the lander with regard to the landing gear in order to properly simulate the attitude of Philae during the descent and on the surface.

2.3. Application of the Capacity-Influence Matrix Method

Step 1: Derivation of medium capacitance-influence matrix $[K_m]$

In order to derive $[\boldsymbol{K_m}]$ (see Chapter 2, Section 2.4)**,** we import the numerical model of the lander representative of the flight model (taking into account the approximations described above, see Figure 53) and its attitude with respect to the environment into COMSOL Multiphysics© (https://www.comsol.com). All 19 elements are considered to be perfect conductors. The ground is characterized by its complex permittivity, and morphology (the simplest being a plane but more complex surfaces can be modelled, see Chapter 4, Figure 99). The whole lander with its conducting elements and the environment are then meshed (Figure 57). As explained in Chapter 2 Section 2.4, the code cycles through the 19 elements. A Dirichlet boundary condition potential of 1 V is applied to the active conductor while those of the others are set to 0 V. COMSOL calculates for each cycle the charge Q carried by each element and hence the matrix $[\boldsymbol{K_m}]$. The code is run for a variety of environment models, lander attitudes and electrode positions on the surface.

Figure 57 : Meshed model of the Philae lander.

Step 2: Derivation of the electronic matrix $[K_e]$

The conducting elements are also linked by the electronic circuit. The components of the electronic matrix $[\boldsymbol{K_e}]$ were derived from a combination of measurements performed on the electronics of the laboratory replica of SESAME-PP (see section 2.2) and of simulations on electronic models.

The circuit that connects the DAC output to the coaxial cable is considered to have a gain $G_{Tx} = 1$ (this is true at low frequencies). The transmitter electrodes are connected to their respective guards by a 2.250 kΩ resistor and a capacitor whose value depends of the transmitting electrode (394 pF for the Tx foot, 300 pF for the MUPUS-PEN electrode and 1.1 nF for the APXS electrode). The guards are also linked to the body by a 100 kΩ resistance and a capacitor (1.14 nF for the Tx foot, 965 pF for the MUPUS-PEN electrode and 880 pF for the APXS electrode). The electrodes are linked to the body via a capacitor (26.3 pF for the Tx foot, 24.7 pF for the MUPUS-PEN electrode and 20.4 pF for the APXS electrode). The ice screw and foot plate of the +X foot are linked to the guard through a capacitor (0.2 pF for the ice screw and 15 nF for the foot plate).

The reception electrodes are linked to the body by a 1.47 pF capacitor and to the guards by a 101 pF capacitor. The ice screws are linked to the body by a 0.2 pF capacitor and the foot plates are linked to the guards by a 15 nF capacitor and a 10 mΩ resistor. The guards are linked to the body by a 95 pF capacitor and a 100 kΩ resistor. Finally, the potentials of the guards of the receiving electrodes are equal to the potential of the soles multiplied by the preamplifier transfer factors α_7 and α_{11}. These factors have a well-known frequency and temperature dependence. However, the preamplifiers were exposed to very low temperatures (-165°C) during the FSS (First Science Sequence) on the surface of 67P/C-G while the flight model preamplifiers were tested and qualified at -150°C. After the Philae landing it has therefore been necessary to study the response of the spare preamplifier available at LATMOS in a vacuum down to -170°C between 10 Hz and 51.2 kHz. It was then possible to extrapolate the transfer factors of the flight models at the low temperatures they were exposed to. The resulting electronic matrix of SESAME-PP at a frequency of 758 Hz is given in Table 8.

Table 8 Real (top) and imaginary (bottom) part of the electronic capacitance matrix [K_e] (pF) at an operating frequency of 758 Hz.

El.	1	2	3	4	5	6	7	8	9	10	11	12	13	14	15	16	17	18	19
1	−21	0	21	0	0	0	0	0	0	0	0	0	0	0	0	0	0	0	0
2	0	0	0	0	0	0	0	0	0	0	0	0	0	0	0	0	0	0	0
3	21	0	−95 400	93 300	0	0	0	0	0	0	0	0	2100	0	0	0	0	0	0
4	0	0	93 300	−93 300	0	0	0	0	0	0	0	0	0	0	0	0	0	0	0
5	0	0	0	0	−21	0	21	0	0	0	0	0	0	0	0	0	0	0	0
6	0	0	0	0	0	0	0	0	0	0	0	0	0	0	0	0	0	0	0
7	0	0	0	0	21	0	−2120	0	0	0	0	0	2100	0	0	0	0	0	0
8	0	0	0	0	0	0	0	0	0	0	0	0	0	0	0	0	0	0	0
9	0	0	0	0	0	0	0	0	−21	0	21	0	0	0	0	0	0	0	0
10	0	0	0	0	0	0	0	0	0	0	0	0	0	0	0	0	0	0	0
11	0	0	0	0	0	0	0	0	21	0	−2120	0	2100	0	0	0	0	0	0
12	0	0	0	0	0	0	0	0	0	0	0	0	0	0	0	0	0	0	0
13	0	0	2100	0	0	0	2100	0	0	0	2100	0	−10 500	0	0	2100	0	2100	0
14	0	0	0	0	0	0	0	0	0	0	0	0	0	0	0	0	0	0	0
15	0	0	0	0	0	0	0	0	0	0	0	0	0	0	0	0	0	0	0
16	0	0	0	0	0	0	0	0	0	0	0	0	2100	0	0	−95 400	93 300	0	0
17	0	0	0	0	0	0	0	0	0	0	0	0	0	0	0	93 300	−93 300	0	0
18	0	0	0	0	0	0	0	0	0	0	0	0	2100	0	0	0	0	−95 400	93 300
19	0	0	0	0	0	0	0	0	0	0	0	0	0	0	0	0	0	93 300	−93 300
El.	1	2	3	4	5	6	7	8	9	10	11	12	13	14	15	16	17	18	19
1	15 000	0	−15 000	0	0	0	0	0	0	0	0	0	0	0	0	0	0	0	0
2	0	0.2	−0.2	0	0	0	0	0	0	0	0	0	0	0	0	0	0	0	0
3	−15 000	−0.2	16 100	0	0	0	0	0	0	0	0	0	11 400	0	0	0	0	0	0
4	0	0	0	26.3	0	0	0	0	0	0	0	0	−26.3	0	0	0	0	0	0
5	0	0	0	0	15 000	0	−15 000	0	0	0	0	0	0	0	0	0	0	0	0
6	0	0	0	0	0	0.2	0	0	0	0	0	0	−0.2	0	0	0	0	0	0
7	0	0	0	0	−15 000	0	15 200	−101	0	0	0	0	−95	0	0	0	0	0	0
8	0	0	0	0	0	0	−101	102	0	0	0	0	−1.48	0	0	0	0	0	0
9	0	0	0	0	0	0	0	0	15 000	0	−15 000	0	0	0	0	0	0	0	0
10	0	0	0	0	0	0	0	0	0	0.2	0	0	−0.2	0	0	0	0	0	0
11	0	0	0	0	0	0	0	0	−15 000	0	15 200	−101	−95	0	0	0	0	0	0
12	0	0	0	0	0	0	0	0	0	0	−101	102	−1.47	0	0	0	0	0	0
13	0	0	−1140	−26.3	0	−0.2	−95	−1.48	0	−0.2	−95	1.47	32 500	0	0	880	−20.4	−965	24.7
14	0	0	0	0	0	0	0	0	0	0	0	0	0	0	0	0	0	0	0
15	0	0	0	0	0	0	0	0	0	0	0	0	0	0	0	0	0	0	0
16	0	0	0	0	0	0	0	0	0	0	0	0	−880	0	0	1980	−1100	0	0
17	0	0	0	0	0	0	0	0	0	0	0	0	−20.4	0	0	1100	1120	0	0
18	0	0	0	0	0	0	0	0	0	0	0	0	−965	0	0	0	0	1530	562
19	0	0	0	0	0	0	0	0	0	0	0	0	−24.7	0	0	0	0	−562	587

Step 3: Solving the numerical model

Once $[\boldsymbol{K_m}]$ and $[\boldsymbol{K_e}]$ determined, the injected current and received potentials for a given environment are derived from Equation (77) in Chapter 2 (19 linear equations with 19 unknowns), taking into account the 19 constraints that apply to the potentials and currents. These constraints and their rational are recapitulated in Table 9.

Table 9: Constraints applied to the potentials and currents to solve Chapter 2, Equation (77)

Variable	Constraint	Comments
I_1, I_2, (I_3), I_4, I_5, I_6, I_7, I_8, I_9, I_{10}, I_{11}, I_{12}, (I_{13}), I_{14}, (I_{15}), I_{16}, (I_{17}), I_{18}, I_{19}	0 A	The current injected in a passive conductor is null. The currents in transmitting electrodes (between brackets) are set to 0 only when not used.
$\sum_{k=1}^{19} \boldsymbol{I_k} = \boldsymbol{0}$	0 A	Kirchhoff's law
V_3-V_{13} or V_3-V_{15} or V_3-V_{17} or V_{15}-V_{17}	Amplitude of the transmitted signal	The potential difference between the two transmitting electrodes is set by tele-command.
V_{11}-V_{13}	(V_{12}-V_{13}) *α_{11}	The potentials of the guards of the receiving electrodes are equal to the potential of the soles multiplied by the transfer factors α_7 and α_{11}. The parameters α_7 and α_{11} depend on temperature and frequency and have been measured.
V_7-V_{13}	(V_8-V_{13}) *α_7	

The current $\boldsymbol{I_{meas}}$ flowing thought the transmitting electrodes is measured with a resistance and capacitor in parallel located between the guard and the electrode with the following formula ($\boldsymbol{K}$ is the capacitance influence matrix, that combines the influence of the electronic matrix $\boldsymbol{K_e}$ and the influence of the conductors and environment close to the electrodes $\boldsymbol{K_m}$):

$$\boldsymbol{I_{meas}} = i\omega\left(V_{guard} - V_{electrode}\right)\boldsymbol{K}(guard, electrode) \quad (89)$$

with $[\boldsymbol{K}] = [\boldsymbol{K_e}] + [\boldsymbol{K_m}]$

The potentials on the two receiving electrodes are measured with respect to the Philae body potential (element #13) with the following formulas:

$$V_{+Y} = V_{11} - V_{13} \quad (90)$$

$$V_{-Y} = V_8 - V_{13} \quad (91)$$

Using this model and this method we are able to predict the potential and current measurements for a variety of surface and lander configurations of operation and to compare them with actual measurements.

The numerical approach described above cannot be validated by comparison with simple analytical models. In order to pursue its validation and to test SESAME-PP performances, we have built a laboratory replica of the instrument mounted on the lander using spare models of SESAME-PP electrodes and electronics. This replica was used to perform measurements in both controlled and natural environments.

2.4. SESAME-PP laboratory model

The laboratory model of SESAME-PP was built at LATMOS (France) during the summer 2013 by Sylvain Caujolle-Bert, engineer, and under CNES funding. It includes the electronics of SESAME-PP as well as a replica (scale 1:1) of the Philae lander. In spring-fall 2015 the replica of Philae was refined by the mechanical section of the DT-INSU (Département Technique – Institut National des Sciences de l'Univers) to make it more accurate and robust.

Figure 58: Left: Laboratory replica (Sylvain Caujolle-Bert). Right: Refined replica with a more robust and accurate model built by the mechanical section of the DT-INSU in 2015.

2.4.1. Description of the laboratory replica of SESAME-PP

The laboratory replica of the SESAME-PP experiment is composed of:

- An interface box connected to a computer that simulates the SESAME flight software built by the FMI (Figure 59, right).

- The qualification model's electronic board identical to the flight model and the flight spare, the only difference being that the field-programmable gate array chips were radiation hardened for the flight model (Figure 59, left).
- The MUPUS-PEN electrode is an early prototype that does not have a guard.
- The APXS electrode is a flight spare.
- The glass fiber soles are flight spares provided by the FMI.
- The steel mesh electrodes were rebuilt.
- The 2 guards with preamplifiers and the preamplifiers themselves are flight spares provided by the RSSD.
- The 4 other guards were rebuilt.
- The other elements of the foot were rebuilt.

Figure 59: Left: Qualification model's electronic board. Right: EGSE simulating the SESAME flight software

The differences between the flight model and the laboratory replica mainly affect the electronic matrix due to the use of different cables linking the elements together. The numerical model was therefore adapted to represent the laboratory model. In absence of the MUPUS-PEN guard (the guard of the spare was absent), we removed it from the numerical model and from the capacitance influence matrix. The transfer functions of the preamplifiers were changed to the appropriate models.

Measurements with the replica are performed in a way similar to those of the flight model. When performing a test, we set the measurement frequencies, the amplitude division (the potential difference set between the guard and electrode of the transmitting electrode) of the transmitted signal and chose the receiving electrodes. The on-board processor then applies a Fast Fourier Transform on the time series (on 16 of the 17 waves) of the selected channel, either the current

measured on the transmitting electrode or the induced potential on one of the two receiving feet. Only one parameter can be measured at a time, therefore, in practice 3 measurements are made to measure I_{meas}, V_{+Y} and V_{-Y} and determine their amplitude and phase. We usually perform 3 similar measurements and use their averaged value.

2.4.2. Description of the Lander replica

The Lander replica was built in order to represent the conductive elements that have an influence on the measurements. It is composed of the body, the legs and feet of Philae. The replica of the body has the same dimensions and shape as the actual lander body (Figure 60, left). The only differences are the absence of the CONSERT antennas and of the instruments located on the balcony of the lander (CIVA, MUPUS-TM, DIM, etc.). The body is covered by aluminum sheets and can thus be regarded as a perfect conductor. The legs of the lander are very similar to that of the flight model, in composition (carbon fiber), shape and dimensions. However, contrary to the flight model they were not coated with metal (for simplification purposes we will still assume that they are perfect conductors). The small deviations from the flight model should have no significant influence on the measurements.

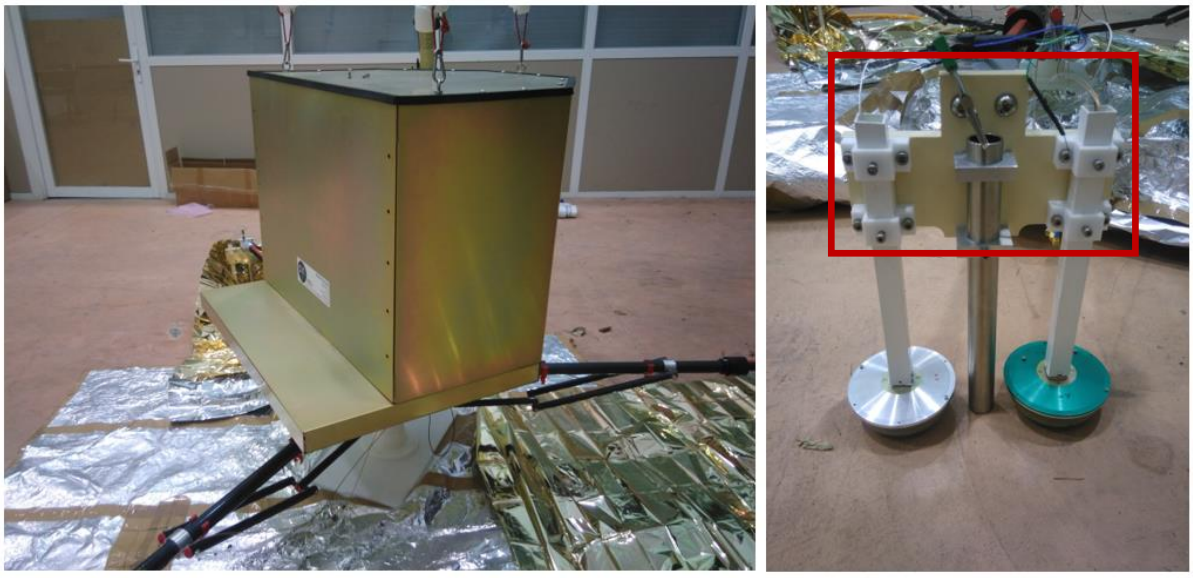

Figure 60: Left: Body of the Philae replica Right: One of the two receiving feet of the lander, indicated in red is the honeycomb structure that holds the two soles together and referred to as the “foot-plate”.

The feet of the lander (Figure 60, right) were built with very similar shapes and dimensions. The main differences are the representation of the ice screws by hollow aluminum cylinders of appropriate dimensions. These differences do not induce any significant measurement differences. Thanks to a rope and pulley system, the lander can be lifted at the desired height above the surface

as well as tilted with respect to the vertical (Figure 69). To simulate a space environment, the replica can be lifted up to 1.6 m (see section 3).

2.5. Experimental tests in a controlled environment and validation of the numerical model

2.5.1. General considerations

For each laboratory measurement, time series are acquired by the EGSE and processed with a Fast Fourier Transform to determine and record the amplitude and phase of the signal. In parallel, the CIMM is used to predict the theoretical emitted current on the transmitting electrodes and the potential on each receiving electrode using Equation (89), (90) and (91).

The error bars associated with this numerical approach were estimated by regenerating a new mesh with the same size parameters. This was done 360 times and provided us with a normal distribution of the phase and amplitude for the current and potentials.

The error bar associated with predicted laboratory measurements were estimated by performing the same measurement 300 times for a given frequency and amplitude of emitted signal.

For both uncertainty estimations, we consider that twice the standard deviation represents the uncertainty of our simulation or measurement. The uncertainty on the mutual impedance of SESAME-PP is calculated using classic uncertainty propagation formulas.

For comparison, measurements and numerical simulations are performed using the same input parameters (frequency, geometry and amplitude of the transmitted signal). We then compare the difference between the measurements to the coverage of the error bar:

$$|X_{meas} - X_{simu}| < k\sqrt{\sigma^2(X_{meas}) + \sigma^2(X_{simu})} \quad (92)$$

Where X can either be the amplitude or phase of the transmitted current on the transmitting electrode I_{meas}, the potential on the receiving electrode or the mutual impedance Z_m, σ is the measured standard deviation and k the coverage factor (for a confidence interval of 95% we take $k = 2$). We consider that the numerical simulations and laboratory measurements give the same result when equation (92) is satisfied.

2.5.2. Three-foot configuration measurements in a controlled environment

The first tests performed in order to validate the numerical model and the Capacitance-Influence Matrix method were with the 3-foot configuration in the integration hall of the LATMOS laboratory over a perfect electrical reflector (Figure 61a). This set up can be readily modeled under

COMSOL Multiphysics by a grounded surface at a distance *h* from the bottom of the lander feet. The boundary conditions are a zero potential at infinity and on the grounded surface (Figure 61b).

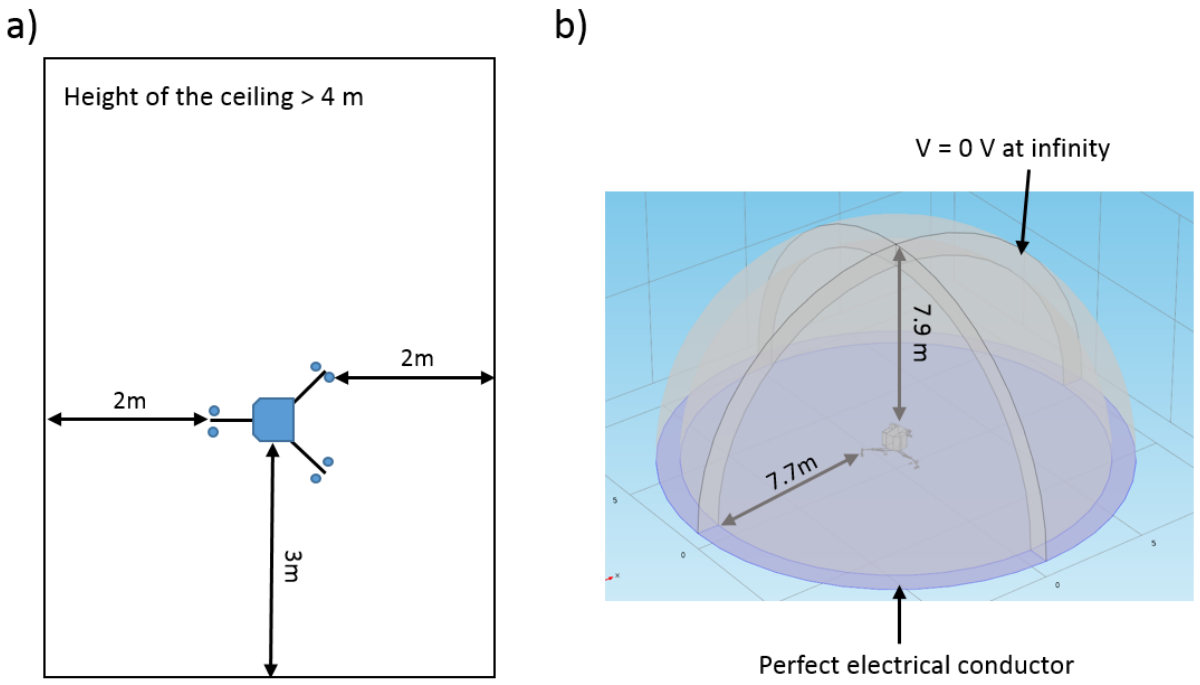

Figure 61: a) Schematic representation of the lander in the laboratory. The lander's electrodes were placed at a distance of at least 2 meters from the walls and the ceiling. A more complex simulation taking into account the walls and ceiling showed no noticeable influence when they were 2 m away from the electrodes. b) 3D geometry model used for the numerical simulations. The lander is lying over a perfect electrical conductor (i.e, a surface where V = 0) and the boundaries of the half sphere were set numerically at infinity with a potential V = 0.

Measurements parallel to the surface

We conducted tests with the 3 feet in a plane parallel to the surface at various frequencies (74 Hz, 146 Hz, 409 Hz, 758 Hz, 2148 Hz, 6510 Hz and 10080 Hz) and heights (40 mm, 54 mm, 115 mm, 238 mm, 305 mm and 1570 mm). The selected frequencies were on the basis of hardware limitations and heights are the thicknesses of the plastic blocks that were used to set precisely the electrodes over the perfect reflector.

Figure 62 shows the comparison between the measured and simulated currents injected in the +X foot as a function of frequency when the feet are 1.6 m above the floor. A linear logarithmic increase is expected from theory (see Chapter 3, Equation (89)) and the phase is expected to increase with frequencies, which is observed only for 3 frequencies (409, 758 and 2148 Hz). The deviation of the simulations from the measurements at low and high frequencies can be explained by a limited documentation and understanding of the electronics behavior at the limits of the instrument operational frequency range (at the highest frequencies for example the gain of the DAC output is probably lower than 1).

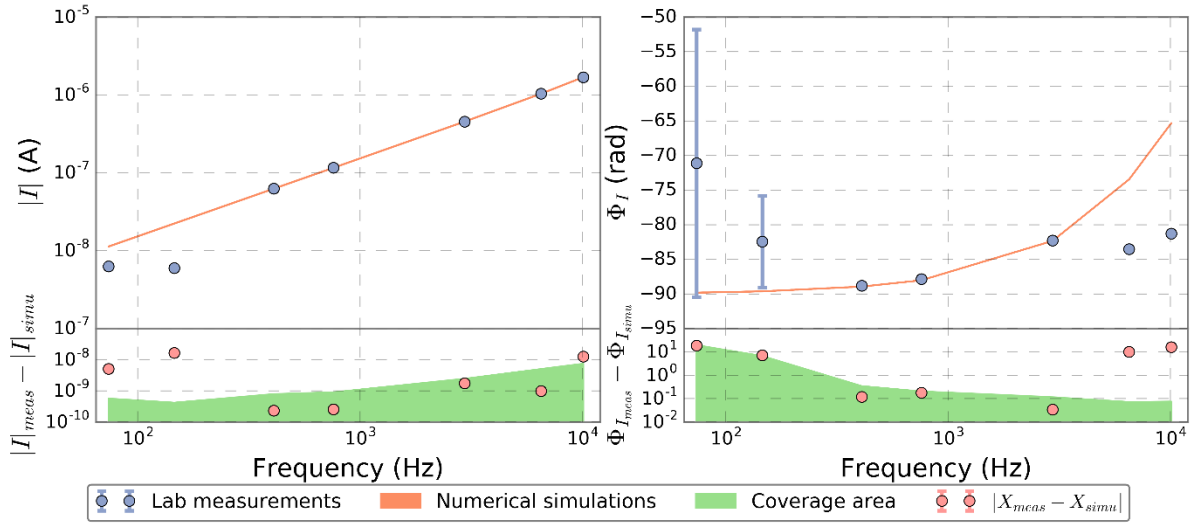

Figure 62: Amplitude and phase of the current on the +X foot as a function of frequency 1.6 m over a perfect electrical reflector, from laboratory measurements (dots with error bars) and numerical simulations (area representing the dispersion of the simulations), in most cases the error bar is too small to be represented. The residuals between the numerical simulations and the laboratory measurements are shown below the plots and compared to the added errors (numerical and experimental uncertainties).

We then compare the measured and simulated currents on the +X foot as a function of height over the perfect reflector at 758 Hz (Figure 63). The amplitude of the current is expected to increase as the electrode gets closer to the perfect reflector, as observed. The numerical simulations and measurements have overlapping error bars for all heights except one (115 mm). Both simulations and measurements also show that the phase slightly increases when the electrodes get closer to the surface (Figure 63, right).

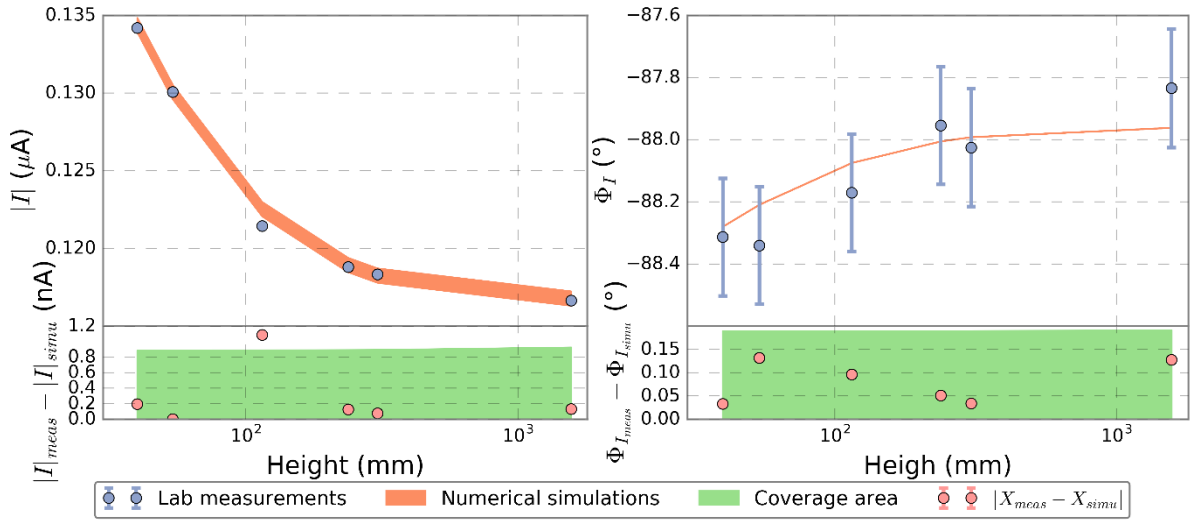

Figure 63: Amplitude and phase of the transmitted current on the +X foot as a function of the height over a perfect electrical reflector at 758 Hz, from laboratory measurements (dots with error bars) and numerical simulations (area representing the

dispersion of the simulations). The residuals between the numerical simulations and the laboratory measurements are shown below the plots and compared to the added errors (numerical and experimental uncertainties).

We then compare the potentials received on the two feet of the lander when they are at the same distance from the perfect reflector. It is important to note that, despite the apparent symmetry of the system, small deviations in geometry and electronics induce a potential difference between the two feet. In an approach, similar to that described for the current, we first compare the simulated and measured potentials as a function of frequency of the transmitted signal in vacuum (e.g., 1.6 m above the ground). Based on numerical simulations, the amplitude of the measured potential should increase rapidly with frequency up to 1000 Hz and then stabilize at higher frequencies (Figure 64, left). However, measurements little decrease in amplitude between 74 Hz and 146 Hz. At higher frequencies, there is a good correlation between measurements and numerical simulations. As predicted, the phase of the receiving signal decreases with frequency (Figure 64, right) but relatively significant differences between simulation and measurements are observed at 74 Hz, 146 and 10080 Hz. As for the current, the deviations of the measurements from predictions are most likely due to our limited documentation and understanding of the receiving electronics behavior at low and high frequencies.

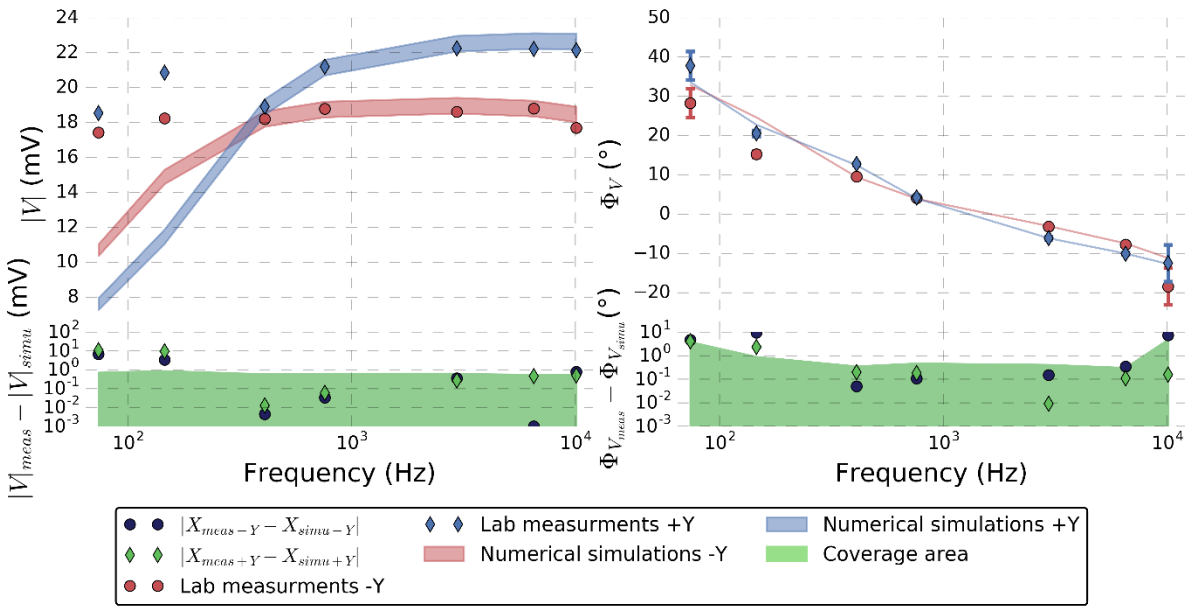

Figure 64: Amplitude (left) and phase (right) of the potential on the +Y foot as a function of frequency 1.6 m over a perfect electrical conductor, from laboratory measurements (dots with error bars, very small error bars are not visible) and numerical simulations (area representing the dispersion of the simulations, when the dispersion is very small the area resemble lines).

We then compare the received potential as a function of height at 758 Hz. The amplitudes of the potentials of the two feet are expected and observed to increase (Figure 65, left) and the phases

to drop (Figure 65, right), as the electrodes get closer to the perfect electrical reflector. The measured and simulated potentials of both feet are in very good agreement at 758 Hz.

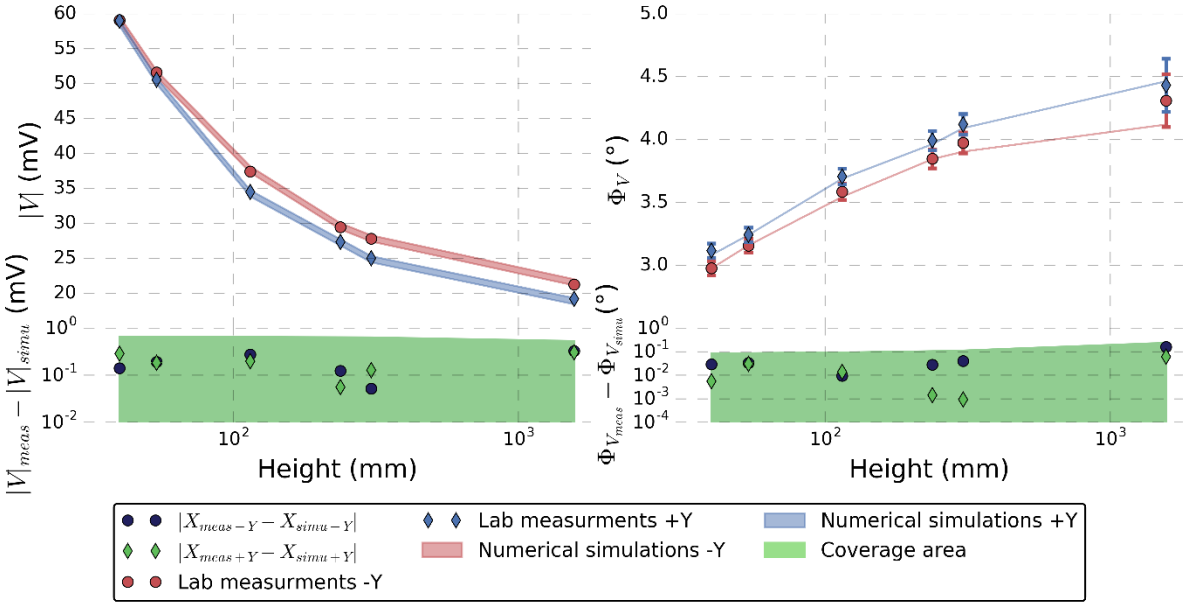

Figure 65: Amplitude (left) and phase (right) of the potentials on the +Y and –Y feet as a function of height over a perfect electrical conductor at 758 Hz, from laboratory measurements and numerical simulations.

Simulations predict that the impedance amplitude and phase should decrease with frequency (Figure 66). This is confirmed by the laboratory measurements at all frequencies except for the smallest and largest (74Hz, 146 Hz and 10080 Hz). This deviation is not surprising as the impedance is the ratio of potential over current.

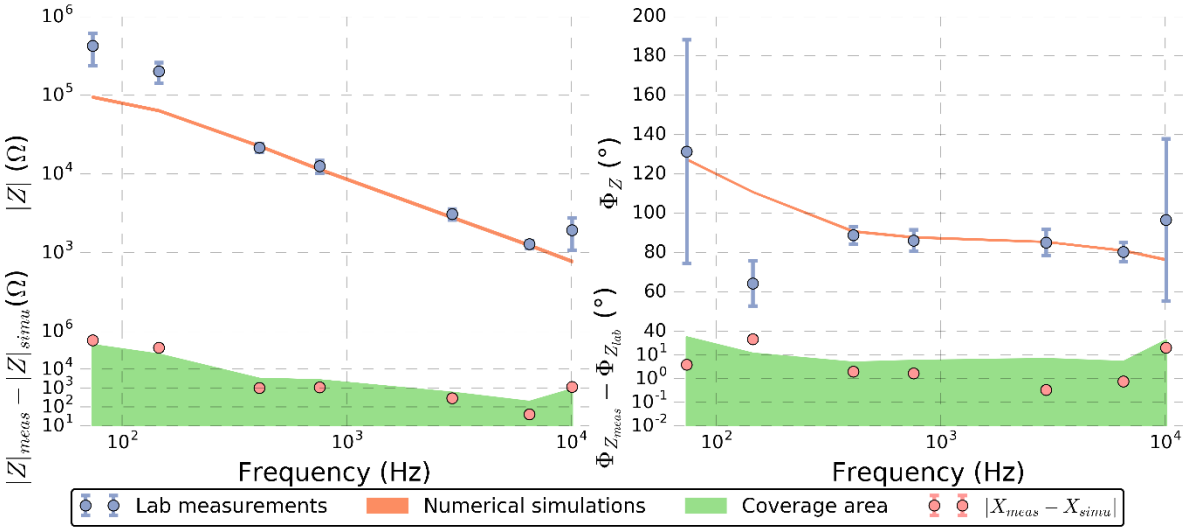

Figure 66: Amplitude (left) and phase (right) of the mutual impedance as a function of frequency 1.6 m over a perfect electrical conductor, from laboratory measurements and numerical simulations.

Further, the amplitude of the impedance is expected to increase, the closer the electrodes are to the perfect reflector; this is also observed in the laboratory measurements at 758 Hz (Figure 67).

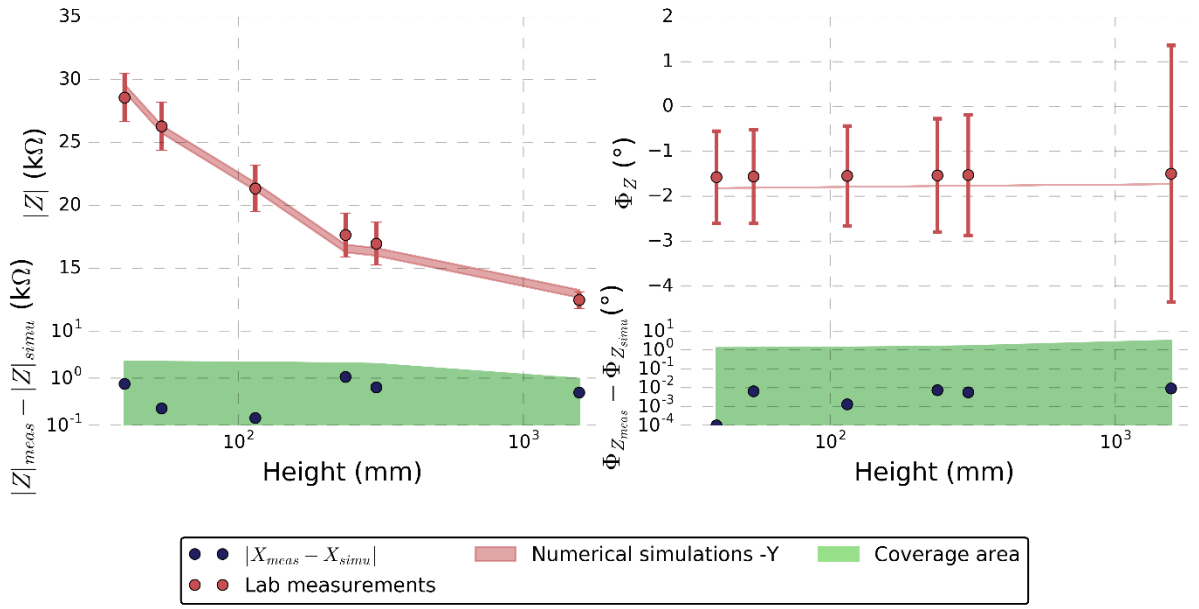

Figure 67: Amplitude and phase of the mutual impedance as a function of height over a perfect electrical conductor at 758 Hz, from laboratory measurements and numerical simulations.

Lastly, in order to retrieve the complex permittivity of the subsurface, we use charts that relate the complex impedance to the relative permittivity (see Chapter 2 Section 3.4). To this end, it is necessary that the mutual impedances obtained from both the CIMM and laboratory measurements be sufficiently close to be considered equal (taking into account the uncertainties on both methods). Figure 68 represents the simulated and measured mutual impedance plotted in the complex as a function of the height over a perfect electrical conductor and for a frequency of 758 Hz. We observe a good agreement between the two methods. This is also verified for three other frequencies (409 Hz, 2948 Hz and 6510 Hz, not represented). This gives us a good confidence in the use of our numerical approach to interpret the SESAME-PP measurements.

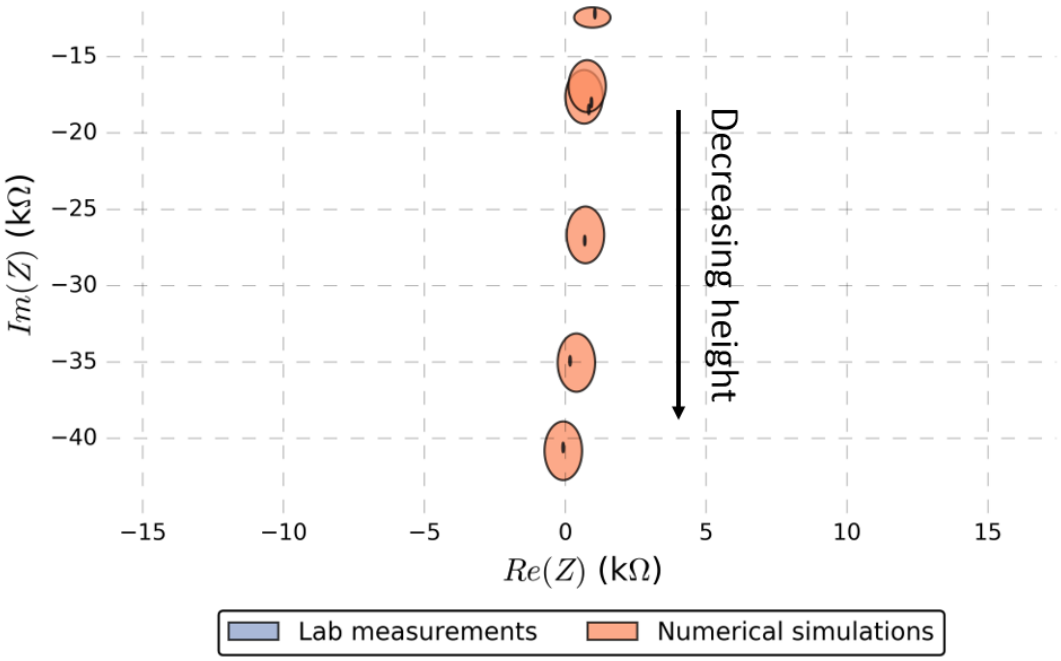

Figure 68: Mutual impedance represented in the complex plane at 758 Hz for 6 different heights (1500 mm, 305 mm, 238 mm, 115 mm, 54 mm, 40 mm), from laboratory measurements and numerical simulations.

In conclusion, laboratory measurements in the 3-foot mode parallel to the surface show a good agreement with the numerical simulations for the two frequencies of interest (409 Hz and 758 Hz, used on the surface of the comet, see Chapter 4, Section 3.3). Further investigation of the electronics could help correct for the discrepancies. In the rest of the chapter we will focus primarily on the intermediate frequency at 758 Hz.

Measurements in a tilted position

Comparing numerical simulations and measurements in a tilted position, where one receiving electrode is closer to the surface than the other is required in order to validate the use of the ratio of the two receiving feet potentials as an investigation method (this will be used in Chapter 4, Section 4.4.2 for the SESAME-PP data analysis). Figure 69 shows a picture of the lander in this tilted position.

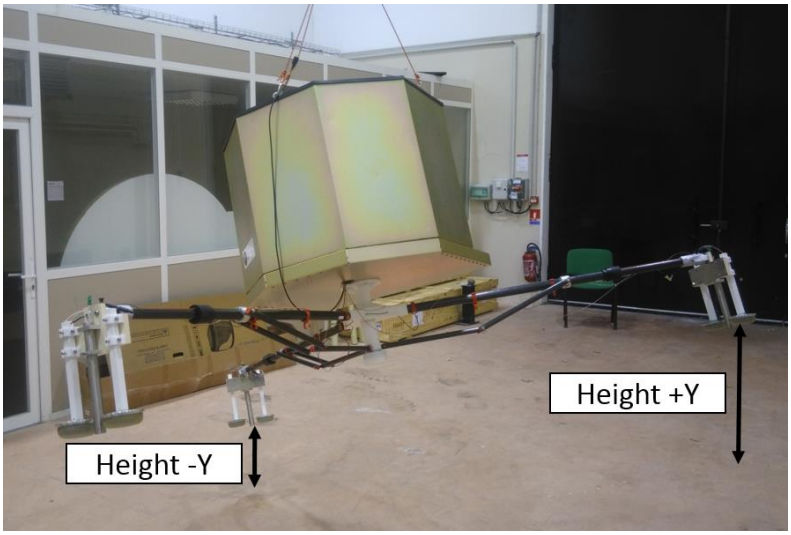

Figure 69: Replica of the Philae lander including SESAME-PP in the "tilted" position. The -Y foot is the closest one to the perfect electrical conducting surface. The height difference between the two receiving feet is about 50 cm.

The measured and simulated ratios between the potentials received on the –Y and +Y feet as a function of their heights above the ground at 758 Hz are displayed in Figure 70.

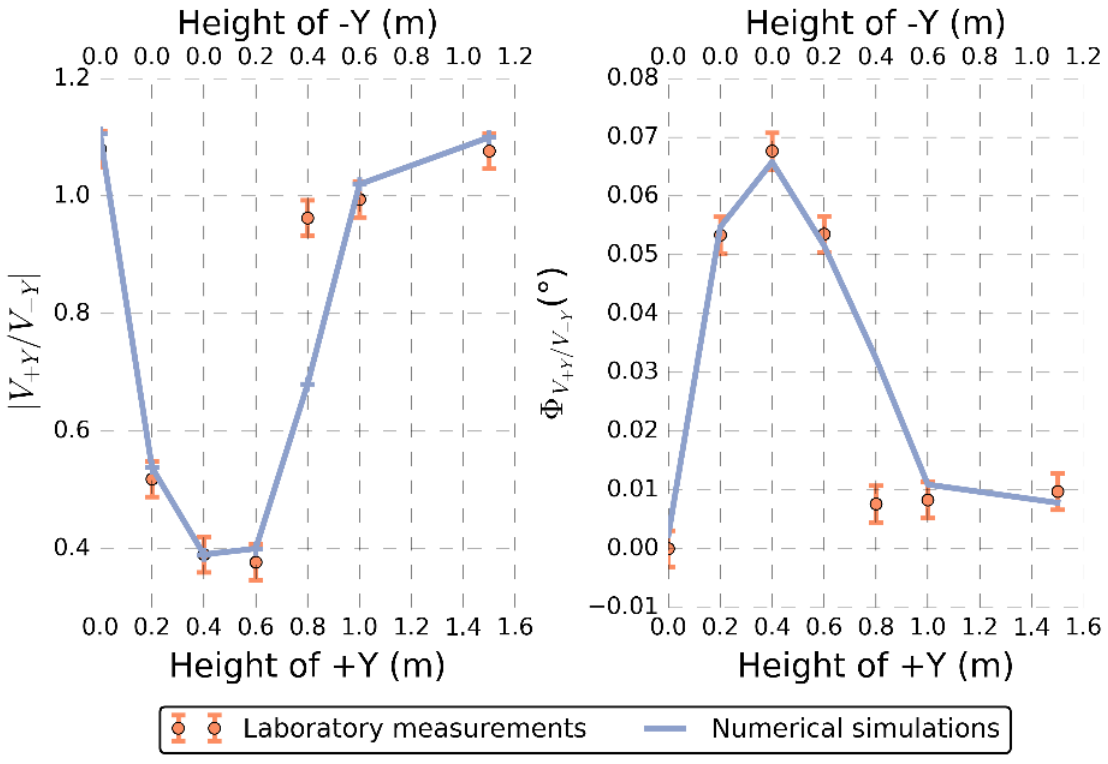

Figure 70: Amplitude (left) and phase (right) of the ratio between the +Y and -Y feet as a function of their heights above the ground at 758 Hz, from laboratory measurements and numerical simulations.

For the measurements performed at the maximum height (i.e., 1.6 m), the ratio is close to 1 as expected since both electrodes can be considered in vacuum (despite -Y being closer to the surface).

When the lander is lowered, the -Y electrode being closer to the surface measures a potential with higher amplitude and lower phase than the +Y electrode. This causes the amplitude of the ratio +Y/-Y to drop and the phase of the ratio to increase. Once the -Y electrode touches the surface, its potential stabilizes whereas the +Y potential continues to increase; this is why the ratio amplitude starts to increase and the ratio phase to decrease. The measurements and simulations both show a return to the original ratio when the two feet touch the surface. The good agreement between the measured and simulated ratios validate the use of the potential ratio as a data analysis method.

2.5.3. Five-electrode configuration in a controlled environment

The five-electrode configuration uses the MUPUS-PEN and APXS electrodes as transmitting electrodes in addition to the +X foot. The main advantage of these electrodes is that they can be deployed around the lander (respectively at 1 m from the body and under the balcony), offering the possibility to sound varying volumes and therefore depths.

We performed measurements with the 5-electrode configuration over a perfect electrical reflector for a number of possible MUPUS-PEN angles around the lander (see Figure 71).

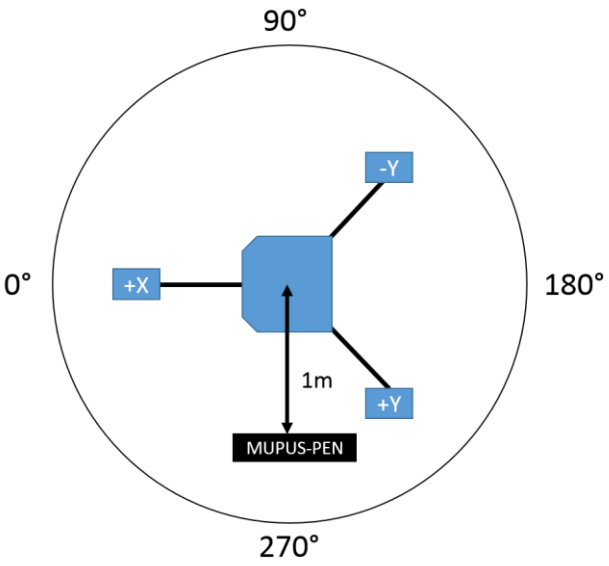

Figure 71: Reference for the angle of deployment of the MUPUS-PEN electrode

The current measured on the MUPUS-PEN electrodes are in good agreement with numerical simulations for both the phase and amplitude regardless of the angle of deployment (Figure 72). The absence of variation with the angle of MUPUS-PEN in the simulations are probably caused by an oversimplification of the numerical model (absence of the influence of the conductive cables linking the MUPUS-PEN electrode to the body) but this approximation has a negligible effect and therefore is not taken in account.

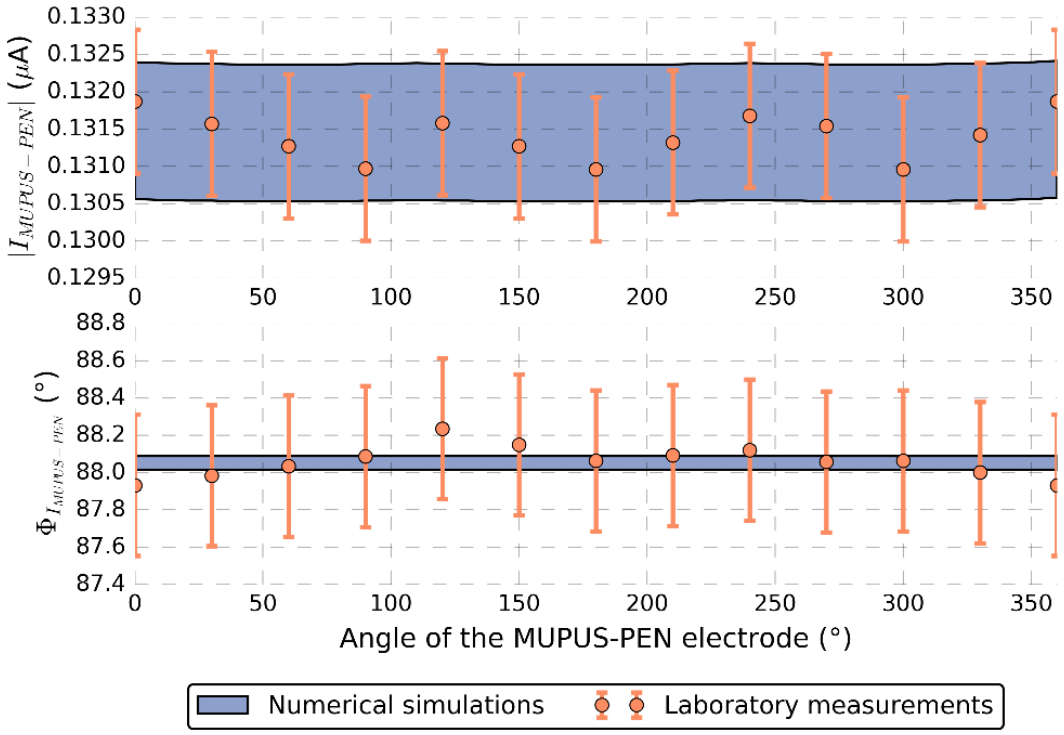

Figure 72: Amplitude (top) and phase (bottom) of the injected current as a function of the angle of deployment of the MUPUS-PEN electrode, from laboratory measurements and numerical simulations. The Areas represent the dispersion of the measurements.

The measured and simulated amplitude and phase of the received potentials are in good agreement for all angles of deployment (Figure 73 and Figure 74). As expected, the amplitude is higher on the receiving electrode that is closer to the transmitting one. At an angle of 120° (respectively, 240°), the MUPUS-PEN electrode is very close to the -Y electrode (respectively, +Y electrode), we observe an increase of the amplitute and a decrease of the phase, this would therefore be an optimal configuration of operation for the MUPUS-PEN electrode as it would provide the highest signal/noise ratio for the mutual impedance. An unexpected result is that the minimum amplitude (resp., maximum phase) for the received potential on both feet is not found when the transmitting electrode is the farthest away from the receiving electrode but rather when it is the closest to the opposite receiving electrode. We attribute this phenomena to the complex geometry of the lander's body and legs; in these positions, the transmitting electrode is very close to the conductive legs of the lander which have a very strong influence on the measured potential.

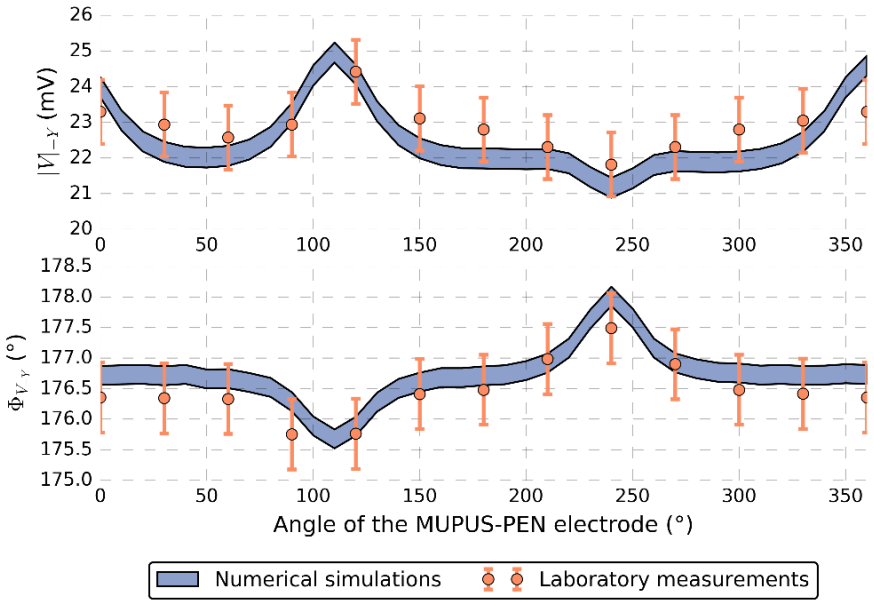

Figure 73: Amplitude (top) and phase (right) of the potential received on the -Y foot as a function of the angle of deployment of the MUPUS-PEN electrode, from laboratory measurements and numerical simulations.

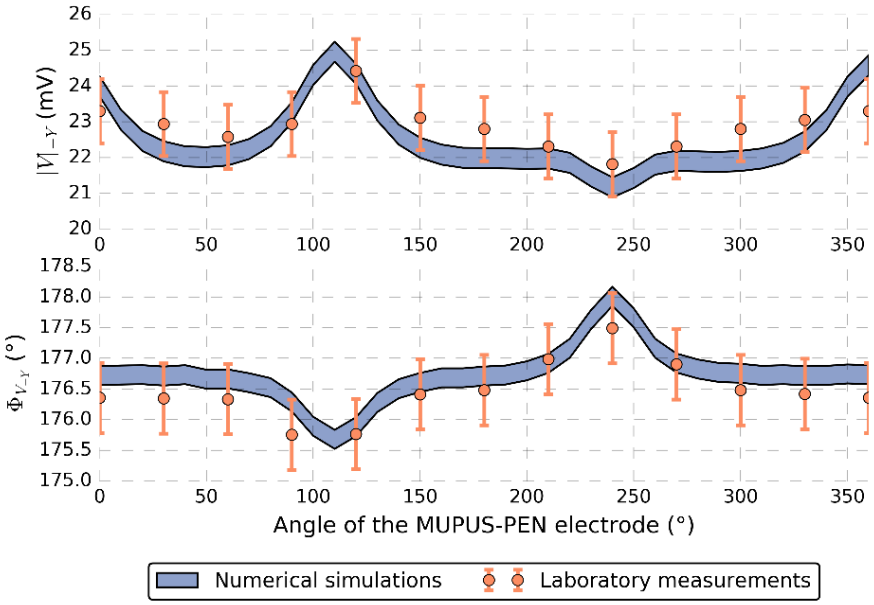

Figure 74: Amplitude (top) and phase (right) of the potential received on the +Y foot as a function of the angle of deployment of the MUPUS-PEN electrode, from laboratory measurements and numerical simulations.

The impedance measurement as a function of the MUPUS-PEN electrode angle of deployment are consistent with numerical simulations (Figure 75). Since the current does not have an important variation with the angle of the transmitting electrode, the maximum of the amplitude and the minimum of the phase are located where the potential difference between the receiving electrodes is maximum (i.e., 120° and 240°).

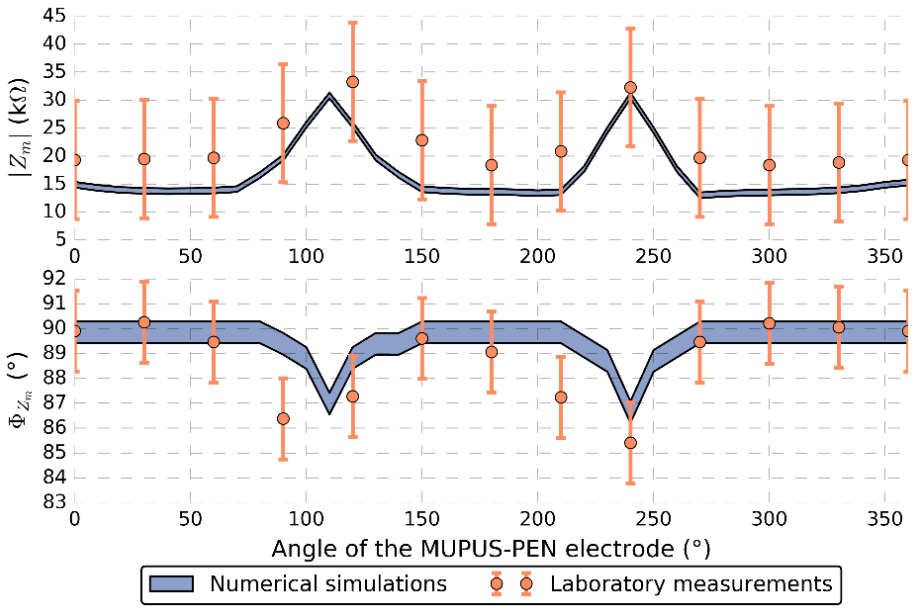

Figure 75: Amplitude (top) and phase (right) of the mutual impedance as a function of the angle of deployment of the MUPUS-PEN electrode, from laboratory measurements and numerical simulations.

With the help of measurements and numerical simulations, we have shown that the Capacitance-Influence Matrix Method enables one to reproduce accurately the measurements of a mutual impedance probe located on a lander with a complex geometry and electronic circuit in a controlled environment. Knowing accurately the close environment of the electrodes and the electronic circuit is required to apply this method. We have also shown that the method can be used at the frequencies at which the SESAME-PP data were collected on the surface of the 67P/C-G nucleus while our partial understanding of the electronics behavior at high and low frequencies might limit our confidence in the results obtained at other possible frequencies (74Hz, 146 Hz, 6510 Hz and 10080 Hz).

In order to further validate the method, measurements and simulations over a natural dielectric surface were conducted in the Dachstein ice caves, in Austria.

2.6. Tests in a natural environment and comparison with the numerical model

Tests in a controlled environment offer a first validation of the Capacitance Influence Matrix Method, but in order to gain a better confidence in the method, field tests are required. Unfortunately, it is difficult to set up lab measurements over natural ground because the technical requirements are high (e.g., a large volume of material is needed). An alternative is to perform field tests with the replica on terrains whose subsurface composition is relatively well known. For that purpose, we selected the Daschstein ice caves, in Austria. As seen in Chapter 1 Section 2.1, water ice has well defined electrical characteristics. It also has the advantage of being one of the main constituents of comets for which the SESAME-PP instrument was designed.

2.6.1. Dachstein field campaign

The Dachstein ice cave complex is located in the Northern Calcareous, in the center of Austria. The caves formed about 10 million years ago (5 million for the youngest) and were filled with water ice for most of that time. The measurements were performed in the Giant Ice Cave (Rieseneishöhle) at the end of a 2.7 km long tunnel. The elevation above sea level is 1460 m and the cave is composed of multiple halls linked by passageways. The caves offer a protected icy surface that is at least 2 meters thick and up to 15 m thick (a thickness larger than the sounding depth of SESAME-PP, see section 2.7). The Dachstein ice caves have already been used to study the past climate of Earth (May et al. 2011) and for testing instruments that could be used for the detection of present or past life on Mars (Groemer 2012). Included in these instruments was a ground penetrating radar (Dorizon et al. 2016) that confirmed that the depth of the bedrock was more than 2 meters deep in the area studied.

Figure 76: Partial map of the Dachstein ice caves extracted from Groemer et al (2012). The area circled in blue is the location where measurements with the SESAME-PP were performed.

The field campaign involved a team of 5 people, Alice Le Gall, Hamelin Michel, Sylvain Caujolle-Bert, Guillaume Lorgeoux and myself. During four days, we conducted measurements over the icy surface of the cave system with the replica of the SESAME-PP instrument in varying configurations. The measurements performed and problems encountered are presented hereafter.

2.6.2. Description of the area studied

The measurements were performed in the Tristandom hall (see Figure 77), the first cavity encountered when entering into the Giant Ice Cave. It offers (1) a high ceiling (necessary for the set-up, see Figure 77), (2) a large surface area necessary for the deployment of the lander in order to reduce interferences caused by conductive elements (human bodies and metallic structures for example) and (3) a thickness of ice (between 2 m and 15 m depending on the location) much larger

than the sounding depth of the SESAME-PP instrument (see Figure 77). The ice at Tristandom hall has a rugged surface, a slightly blue color and a wet aspect. The thin film of liquid water on the surface was wiped out before the measurements.

Figure 77: Replica of the SESAME-PP instrument over the icy surface of the Tristandom hall. Left: general view of the set-up and underlying ice. Right: close up of the lander resting on the surface.

2.6.3. Three-foot configuration measurements over an icy surface

The first tests were performed with the 3-foot configuration. We measured the potential on the two receiving feet and the current transmitted with the +X foot. When comparing the measurements at two frequencies (409 Hz and 758 Hz) in amplitude and phase to those performed over a perfect electrical reflector in LATMOS (see section 2.3.1), we note that they are similar (taking into account error bars) at heights higher than 20 cm (see Figure 78 and Figure 79). However, at the 3 smallest heights, we observe a divergence: the amplitude and phase increase at a slower rate over the surface of Tristandom hall indicating that the surface is not a perfect reflector.

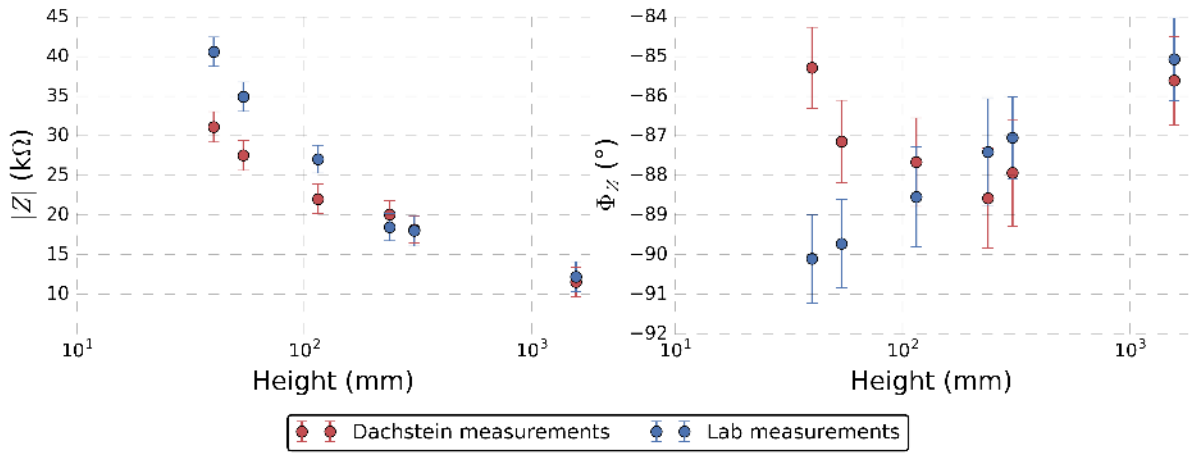

Figure 78: Amplitude (left) and phase (right) of the mutual impedance measured at LATMOS over a perfect electrical reflector and in the Dachstein ice caves at 409 Hz.

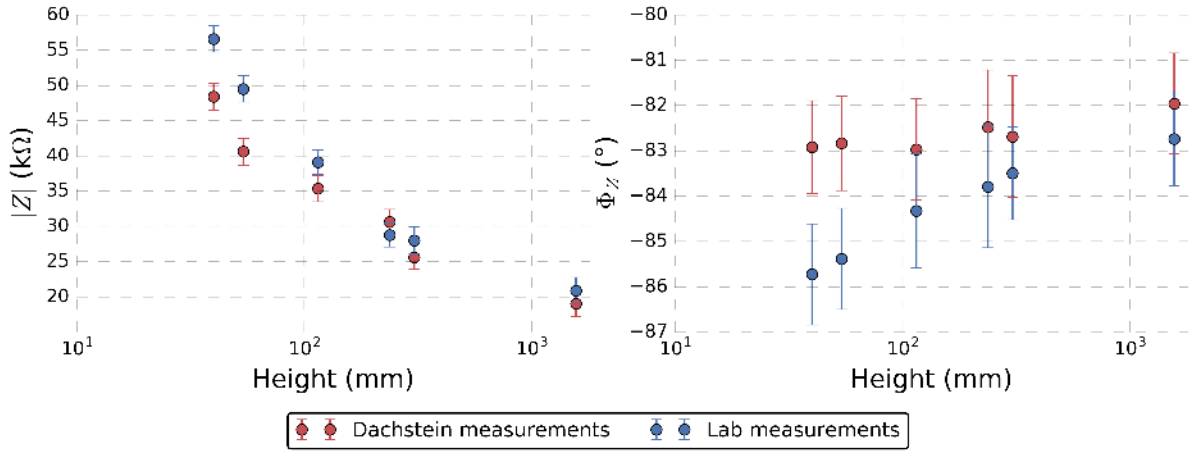

Figure 79: Amplitude (left) and phase (right) of the mutual impedance measured at LATMOS over a perfect electrical reflector and in the Dachstein ice caves at 758 Hz.

In order to constrain the complex permittivity of the icy subsurface, we built charts of complex impedance values for a range of complex permittivity of the subsurface and for a height over the surface of 40 mm (Figure 80). We then overlay the measured complex impedances at 409 Hz and 758 Hz and observe that they all fall in areas of high permittivity/conductivity.

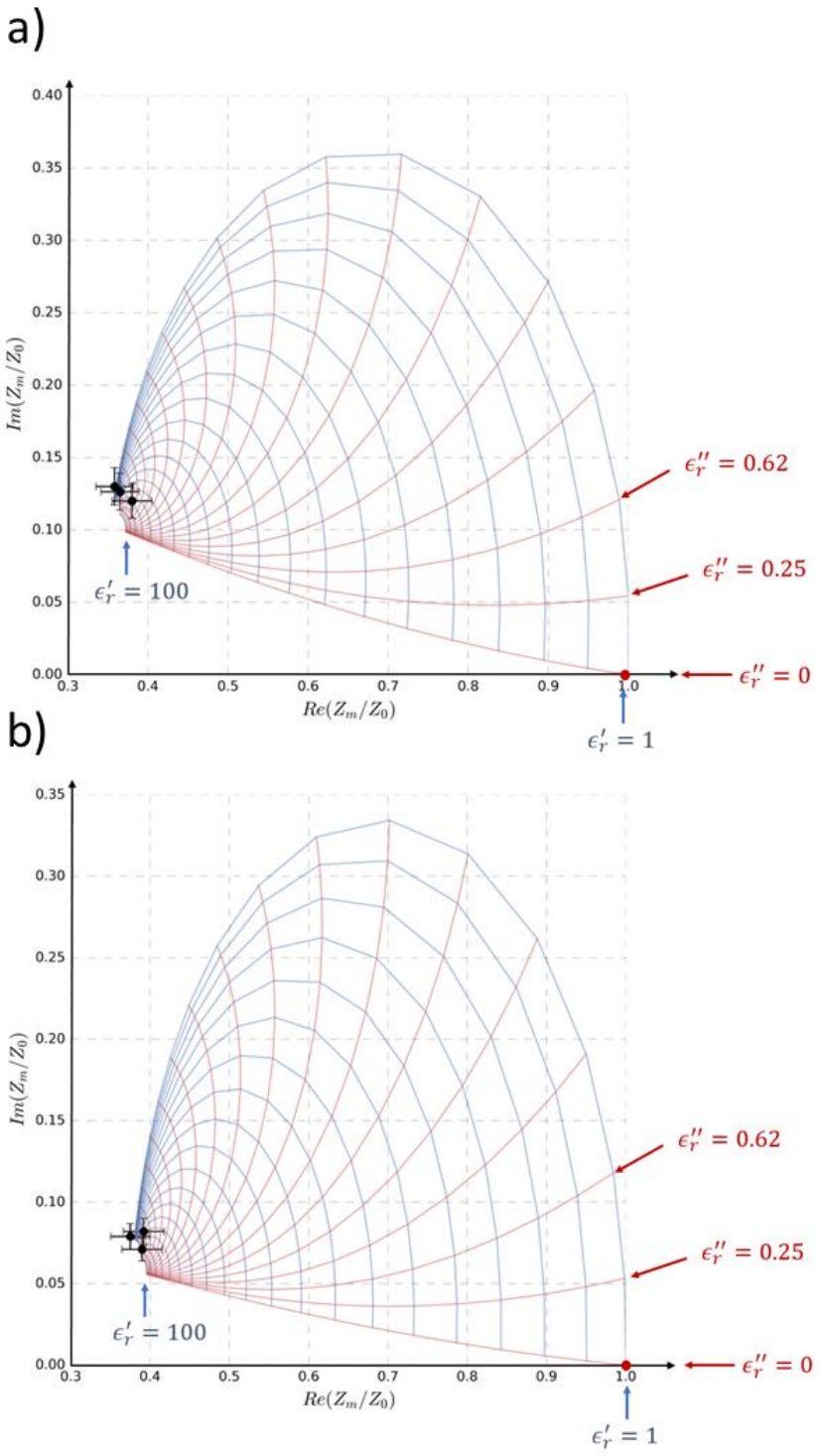

Figure 80: Predicted normalized mutual impedance of the SESAME-PP numerical model lying over a horizontal surface. The expected mutual impedance is shown in the complex plane as a function of the real and imaginary parts of the relative permittivity of the near-surface (for a frequency of operation of a) 409 Hz b) 758 Hz). The dielectric constant of the subsurface ranges from 1 to 100 on a logarithmic scale and the imaginary part ranges from 0 to 100 also on a logarithmic scale. The red dot indicates the vacuum relative permittivity. The black dots represent the measurements performed in the Dachstein ice caves, they are located in the area of high dielectric constant/ high conductivity and due the accuracy of the measurements it is not possible to retrieve the electrical characteristics of the subsurface.

The accuracy of the measurements is not high enough to characterize subsurfaces with high dielectric constant and/or conductivity (see Chapter 2 Section 3.4). Fortunately, the measurements made on the surface of the comet are made at very low temperatures (-165°C) and water ice can be regarded as an almost pure dielectric (see Chapter 1 Section Chapter 1:2.1).

2.7. Sounding depth of SESAME-PP

The Capacitance-Influence Matrix Method can also be used to estimate SESAME-PP performances and, in particular, its sounding depth. The approach is the same as that described in Chapter 2 Section 4.2: Numerical simulations are performed with a perfect reflector that is progressively moved near the lander and we considere that the sounding depth corresponds to the distance at which the reflector significantly influences the measurements. More specifically, the sounding depth can be defined as the distance at which the difference between the mutual impedance with and without reflector exceeds the error made on the impedance measurement, namely $\sim$ 7%.

We first applied this method to the three-foot configuration (+X and the Philae body as transmitting electrodes) assuming that the ground over the perfect electrical reflector has a complex permittivity (ϵ_r' , ϵ_r'') and that the electrodes are located 1 cm above the surface. Figure 81 shows that the sounding depth increases with the real and imaginary parts of the subsurface complex permittivity and tends towards $\sim$ 1.8 m when ϵ_r' and ϵ_r'' are both larger than 5. We note that the sounding depth slightly exceeds the distance between the electrodes (about 1 m).

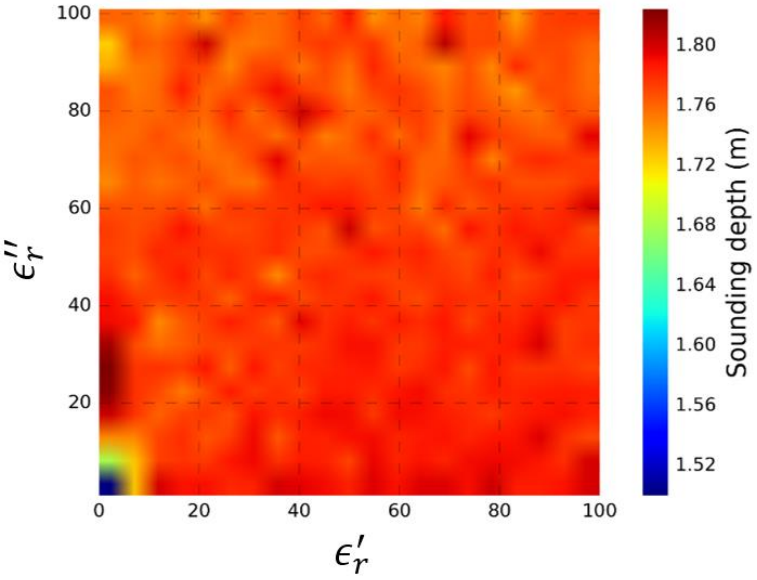

Figure 81: SESAME-PP sounding depth as a function of the real and imaginary parts of the complex permittivity of the subsurface.

We then evaluate the sounding depth for the four-electrode configuration (+X and MUPUS-PEN as the transmitting electrodes). We set to 2.4 and 0 the subsurface dielectric constant and conductivity, respectively (values found for the near-surface of the 67P/C-G's nucleus, see Chapter 4, Section 5.4.2). For each position of the MUPUS-PEN, we estimate the sounding depth with the method described above. Figure 81 shows that the SESAME-PP sounding depth varies with the position of the MUPUS-PEN transmitting electrode, ranging from 0.4 to 1.6 m. By using SESAME-PP with different configurations of operation, different depths below the surface (down to 1.6 m) can be sounded and the instrument can therefore detect possible layers in the subsurface. When SESAME-PP is operated with +X and APXS as transmitting electrodes the theoretical sounding is reduced to 1.0 m.

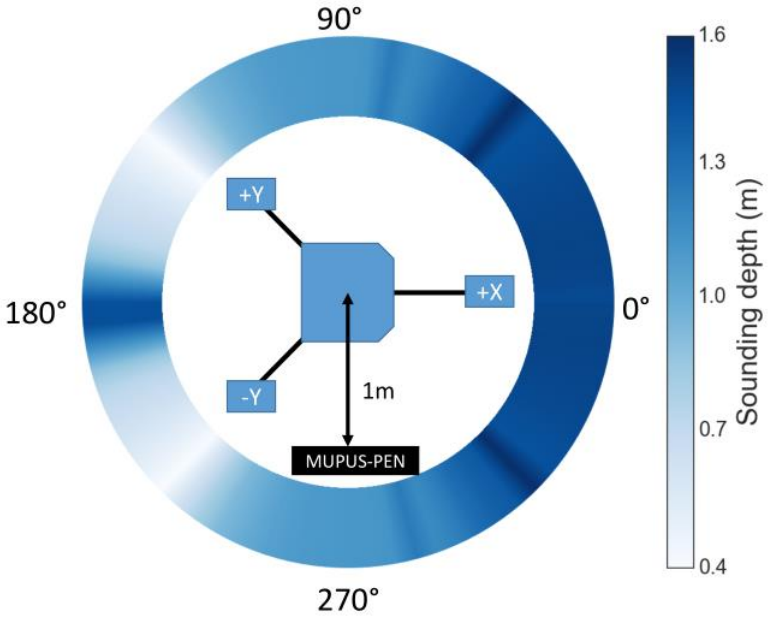

Figure 82: Theoretical sounding depth of SESAME-PP as a function of the MUPUS-PEN position (in degree with respect to the +X leg direction) when the transmitting electrodes are +X and MUPUS-PEN. The distance of 1 m indicated for the MUPUS-PEN electrode is the maximum theoretical deployment distance.

3. Concluding remarks

In this Chapter we described the context of the SESAME-PP instrument as part of the Rosetta mission and as a main component of the SESAME experiment. We presented the payload of both the orbiter and Philae lander and highlighted the complementarily of the instruments that can help interpret the SESAME-PP data collected on the surface of the cometary nucleus.

We then described the numerical model developed for the SESAME-PP instrument and the Philae lander and the constraints on the equations used to apply the Capacitance-Influence Matrix Method. In order to validate our numerical approach for complex and realistic geometries, we compared predictions from simulations to measurements made in a controlled environment with a

replica of the instrument. We demonstrated that for mid-range frequencies (between 409 Hz and 2148 Hz) the method is accurate.

This work provided us with a first order confirmation of our approach. In an effort to gain a better confidence in the method, we also conducted field tests in a natural icy setting with the aim of retrieving the complex permittivity of water ice at relatively warm temperature (∼-3° C). However, this turned out to be impossible and we demonstrated that SESAME-PP is not designed to measure the complex relative permittivity when the dielectric constant or conductivity is high. Finally, we used the Capacitance-Influence Matrix Method to show that the theoretical sounding depth of the SESAME-PP instrument is in the range 0.5-2 m.

Chapter 4: Electrical properties and porosity of the first meter of 67P/Churyumov-Gerasimenko's nucleus as constrained by SESAME-PP/Philae/Rosetta

Since its arrival at 67P/C-G in June 2014, the Rosetta probe and the Philae lander have collected a wealth of scientific data that will require years to analyze. The orbiter has been observing the nucleus, coma, dust and gas trails of the comet for 2 years offering a global picture of the comet and of its evolution as it orbits the Sun. On the other hand, the Philae lander, despite an acrobatic landing on November 12, 2014, collected observations during 3 days, providing a local view of the nucleus, a "ground truth".

First, we will describe the Rosetta's spacecraft travel towards 67P/C-G, the multiple landings of Philae on the surface of the comet, the orbiters mission continuation up to and past perihelion (August 19, 2015), and the scenario of end-of-mission in September 2016 (section 2).

We will then present the main discoveries that have been made on the nucleus and coma thanks to the Rosetta mission and put them in the context of the scientific objectives of the SESAME-PP experiment (section 3).

Section 4 will be dedicated to the description of the SESAME-PP measurements during the cruise phase, descent towards the nucleus and on the surface. We will explain the calibration of the collected data and the difficulty in interpreting the measurements due to the unexpected attitude and environment of the lander at its final landing site.

In Section 5, we will present our 3D model we built using most of the available information on the attitude and environment of Philae. This model is then used to derive constraints on the electrical properties of the subsurface. These constraints are compared in Section 6 to other data to help understand the composition and porosity of the subsurface of the nucleus. These results have been published in an A&A paper: "Electrical properties and porosity of the first meter of the nucleus of 67P/Churyumov-Gerasimenko. As constrained by the Permittivity Probe SESAME-PP/Philae/Rosetta", Lethuillier et al., Astronomy & Astrophysics, vol. 591,2016.

1. RDV, landing and escort

The Rosetta mission can be divided into three phases: the cruise phase, up to the rendez-vous with 67P/C-G (March 2004-June 2014), the Philae landing phase (November 2014) and the escort phase (December 2004-September 2016).

1.1. The cruise phase and Rosetta "rendez-vous "with 67P/C-G

The Rosetta spacecraft was launched in March 2004 from Kourou, French Guyana. From there it entered a cruise phase, with the help of three gravitational assists, two from the Earth and one from Mars (Montagnon & Ferri 2006; Ferri et al. 2008).

During the cruise, the main operations were orbit determinations and health-checks (performed by the instruments and main systems to detect potential anomalies). Rosetta also performed fly-bys of two asteroids: asteroid (2867) Steins was encountered in September 2008 (Accomazzo et al. 2010) and asteroid 21 Lutetia on July 10, 2010. During both flybys many of the instruments of the orbiter gathered scientific data.

Steins is a class E diamond shaped asteroid (i.e., with a surface made primarily of enstatite, $MgSiO_3$). Its dimensions were found to be 6.67 × 5.81 × 4.47 km^3 (Jorda et al. 2012) but the asteroid was probably part of a differentiated object that broke up. Its surface exhibits many craters, including one 2-km wide (its surface was dated by crater counting and found to be ~ 150 million years old, Keller et al. 2010). MIRO and VIRTIS observations both point towards a high thermal inertia, strongly suggesting a rock-dominated regolith (Gulkis et al. 2010; Leyrat et al. 2011).

Lutetia is a M-type (metallic) asteroid with dimensions much larger than Steins, namely 121 x 101 x 75 km^3. Its surface was dated by crater counting and found to be 3.6 billion years' old (Sierks et al. 2011). The bulk density was determined to be very high (3.4 g/cm^3 whereas asteroids usually have bulk densities in the range 1.2 to 2.7 g/cm^3 (Pätzold et al. 2011). A geological map was produced showing a diverse set of surface features (Thomas et al. 2012) and a surface composition likely chondritic in nature (Tosi et al. 2012). Contrary to the Steins asteroid, Lutetia's crust was found to have a very low thermal inertia consistent with a lunar-like regolith (Gulkis et al. 2012). It is also believed that Lutetia could be partially differentiated with a metallic-rich core surrounded by a chondritic crust (Weiss et al. 2012).

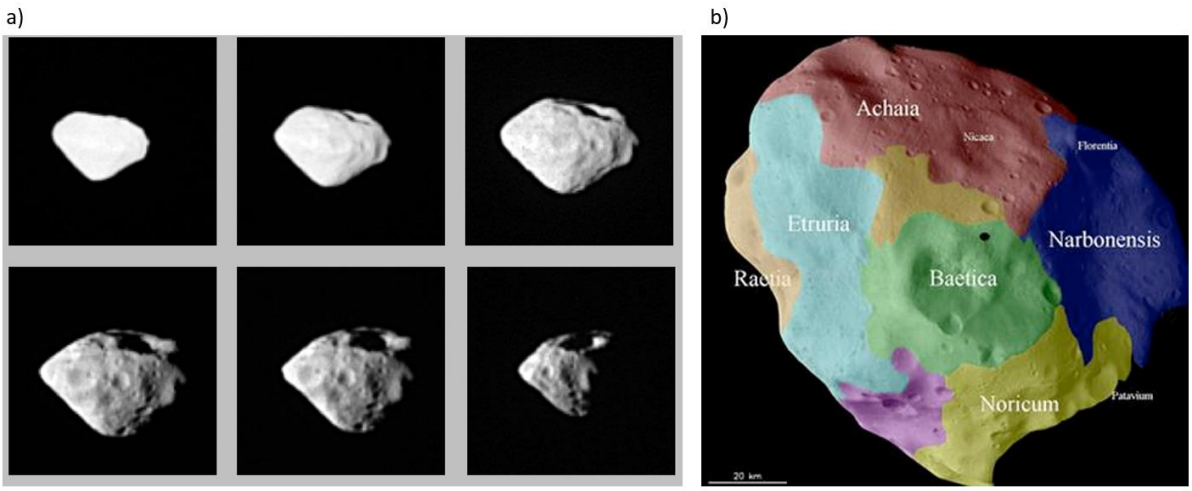

Figure 83: a) Steins asteroid as observed by the OSIRIS instrument. At closest approach the Rosetta spacecraft was at a distance of 800 km Credits: ESA/MPS/UPM/LAM/IAA/RSSD/INTA/UFM/DASP/IDA. b) Main geological regions observed on the Lutetia asteroid, from Thomas et al (2012).

Operating on solar energy alone, the spacecraft was placed into a deep space hibernation for 31 months in June 2011 as it cruised out to a distance of nearly 800 million km from the warmth of the Sun, beyond the orbit of Jupiter. It woke up successfully on January 20th 2014 (see Figure 84b for the wake up confirmation signal) and the "rendez-vous" phase began.

After the wake-up from hibernation the navigation activities resumed as planned. The comet position and speed relative to the spacecraft were calculated and Rosetta started its approach phase towards the nucleus of 67P/C-G (Morlay et al. 2015). Up to ten orbital corrections were performed between the 7th of May and the 6th of August 2014 to reduce Rosetta's velocity relative to the comet. The spacecraft nominally arrived at 67P/C-G on August 6th 2014, as it was at a distance of 3.7 AU from the Sun (Taylor et al. 2015), progressively revealing a bi-lobal nucleus (Figure 84c and d) with very low albedo (Taylor et al. 2015).

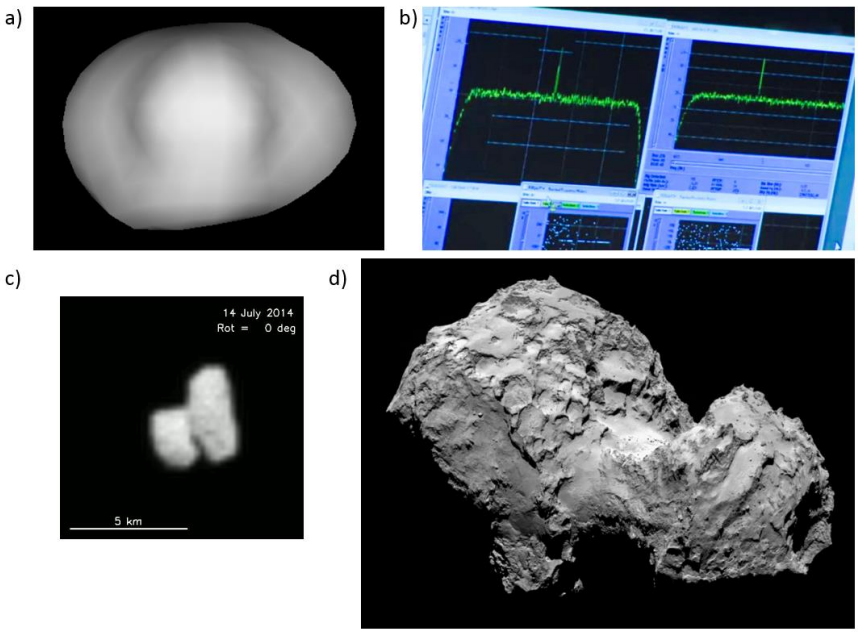

Figure 84: a) Original shape model of 67P/C-G derived from the light curve captured by the Hubble space telescope. Credit: NASA, ESA and Philippe Lamy, b) wake up signal received on the 20th January 2014. Credit: ESA, c) Photo of 67P/C-G comet's nucleus taken by the OSIRIS camera on the 14th of July 2014. Credit: ESA/Rosetta/MPS for OSIRIS Team MPS/UPD/LAM/IAA/SSO/INTA/UPM/DASP/IDA, d) Photo of 67P/C-G comet's nucleus taken by the OSIRIS camera on the 6th of August 2014. Credit: ESA/Rosetta/NAVCAM.

1.2. Philae separation and landing at Abydos

The landing site selection was performed in less than 6 weeks, during which an intense investigation and assessment of the comet nucleus was performed. The landing had to take place before the activity became too intense but also at a time where sunlight is generous enough to recharge Philae's batteries by the solar cells. It was decided that the landing would take place when the comet was around 3 AU from the sun. The landing site had to satisfy a number of criteria and constraints

- Dynamic constraints: The landing site had to be dynamically reachable.
- Safety constraints: The slope of its surface had to be moderate as well as to account for the presence of boulders and crevasses.
- Communication constraints: The visibility of the landing site from the Orbiter had to be high for periodic communication.
- Illumination constraint: The landing site had to benefit from at least 7 hours of solar illumination to recharge the Philae batteries but also at least 1-2h of night to avoid overheating.
- Scientific constraints: The landing site has to be of great scientific interest.

This lead to the selection of 10 possible landing sites which was then narrowed down to 5 (A, B, C, I and J, see Figure 85). Finally, on the 13-14 September 2014, the site J (located on the smaller lobe of the nucleus), later renamed Agilkia, was selected as primary site and site C (located on the larger lobe of the nucleus) as the backup site.

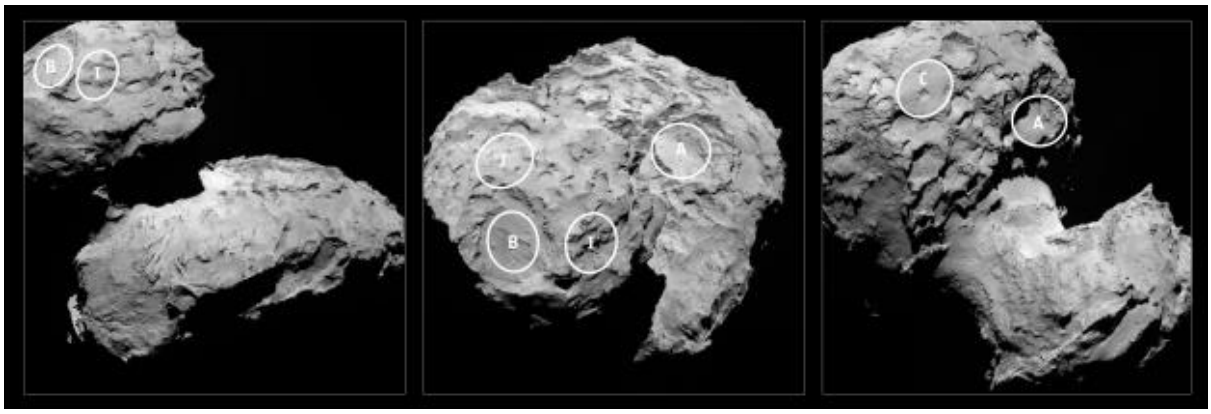

Figure 85: Five candidate landing sites selected for detailed investigation. Credits: *ESA/Rosetta/MPS for OSIRIS Team MPS/UPD/LAM/IAA/SSO/INTA/UPM/DASP/IDA*

The Rosetta spacecraft started the Philae separation manoeuver on November 12 2014 by changing its orbit to a hyperbolic trajectory towards the nucleus. Philae separated on November 12, 08:35:00 at a distance of 20.5 km above the nucleus. The descent took 7 hours, and Philae touched the surface at 15:34:03 at Agilkia. The first touchdown (TD1, see Figure 86) was detected both by the SESAME-CASSE instrument and the landing gear damper sensors. Unfortunately, the harpoons located under the body of the lander did not fire and the cold gas system intended to push down the lander on the surface did not work. This led the lander to bounce off the surface and continue to move (this was seen on the solar generator data and on the first CIVA images). The lander touched the surface with a vertical movement two more times (named TD2 and TD3, see Figure 86) and had a possible collision with a cliff (no vertical deceleration, Biele et al. 2015). The times and locations of each event can be found in Table 10 and Figure 86, respectively. After TD3, Philae came to a rest at its final landing site baptized Abydos. This is where the lander made most of its scientific measurements during a phase called the First Science Sequence (FSS). Three days later, on November 15 2014 at 00:07 Philae's batteries run out, halting scientific operations and forcing the lander to enter a hibernation mode (Biele et al. 2015). To date, the final position of Philae has not been officially determined, although it has been narrowed down to an area by the analysis of CONSERT observations (Kofman et al. 2015; Herique et al. 2015, see Figure 87) and may have been identified on OSIRIS images (https://cnes.fr/fr/web/CNES-fr/11853-gp-la-camera-osiris-localise-le-lieu-d-atterrissage-final-de-philae.php).

Table 10: Time of the different recorded events of the Philae lander (Biele et al. 2015).

Event	Time (UTC) 12/11/2014
TD1	15:34:04
Collision	16:20:00
TD2	17:25:26
TD3	17:31:17

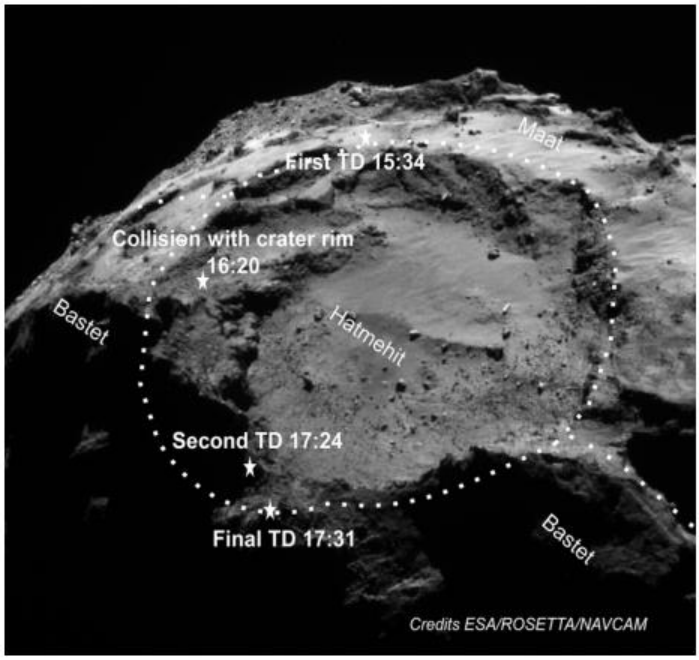

Figure 86 Location of different events as estimated by the SONC overlaid on a OSIRIS image (Biele et al., 2015)

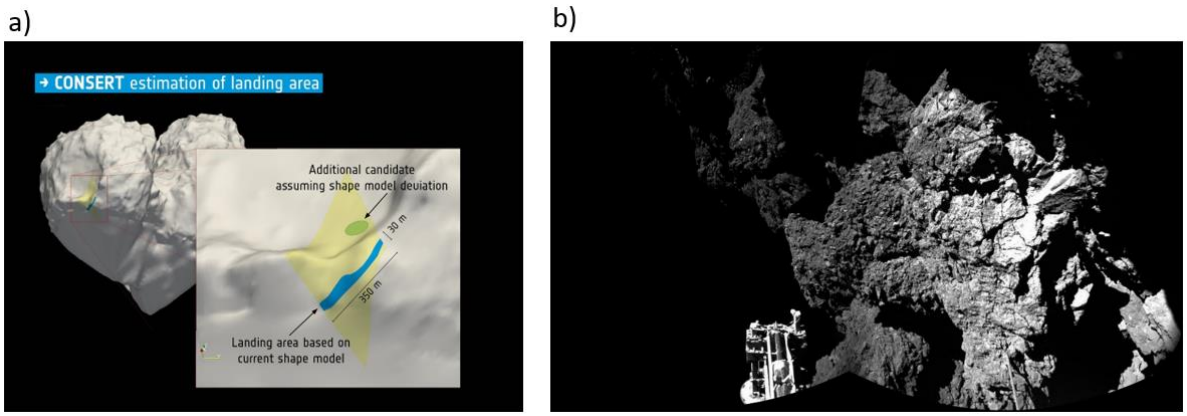

Figure 87: a) Landing site area as constrained by CONSERT. The blue area shows the most probable landing site regions; the green area represents another possibility assuming shape model deviation Credits: ESA/Rosetta/Philae/CONSERT. b) Image made from the pictures taken by 2 of the CIVA cameras at the final landing site. Credits: ESA/Rosetta/Philae/CIVA.

The characteristics and, in particular, the topography of the final landing site are also not well known. The only thing for sure is that Philae is now resting in a non-horizontal attitude (based on the CIVA images, see Figure 87b) in a location that is very poorly illuminated which shortened the duration of the FSS and prevented the lander from waking up from hibernation for a long enough period to perform new science operations. Section 4.4.1 provides a detailed list of most of the available constraints on the attitude and environment of Philae at Abydos.

1.3. Escort phase

After Philae's FSS, the Rosetta orbiter resumed its normal observations. The landing occurred when the comet was 3 AU from the Sun and since then Rosetta has been continually escorting and analyzing the coma and the nucleus of the comet up to and past perihelion at varying distances from the object. No major problems have been reported, with the exception of a navigation issue that occurred in March 2015 when the primary star trackers failed in locking on to stars due to the comet activity. After this event, the spacecraft trajectories were replanned in order to ensure that the instruments can operate safely, as the comet activity is high around perihelion and Rosetta spent summer 2015 at more than 150 km from the nucleus. The initial end-of-mission date was December 2015 but the Rosetta mission has been extended until September 30, 2016 where the orbiter is expected to land on the surface of the nucleus granting the instruments a unique opportunity to take a close look at the nucleus.

2. Main results from the Rosetta mission

The Rosetta mission has provided us with a wealth of information on the 67P/C-G comet enabling scientists to study in details its coma, nucleus and activity. It has already profoundly enriched our view of this primitive object. Despite the close ending of the mission, the amount of data collected will keep busy scientists for years. In the next section, we will briefly describe our current understanding of the comet, focusing on available information on the near-surface of its nucleus in relation with the scientific objectives of the surface mode of SESAME-PP.

2.1. Nucleus

The nucleus represents the solid part of a comet from which the coma, hydrogen cloud, gas and dust trails find their origin. It is also the most difficult part of the comet to observe and study. As such it has been the target of most instruments of the Rosetta mission.

Main properties

The global shape, density and rotation of 67P/C-G was mainly investigated by the OSIRIS instrument (Sierks et al. 2015). Its mass was determined by the RSI experiment (Pätzold et al. 2015).

The rotation period was estimated to be ~12 h (Mottola et al. 2014). The main properties are listed in Table 11. From the mass and volume, its density was found to be ~ 532 kg/m^3 (Sierks et al. 2015; Jorda et al. 2016), consistent with a very porous nucleus (70-80% porosity).

Table 11: Main properties of the 67P/C-G comet

Size of the nucleus	Small lobe: 2.5 km x 2.5 km x 2.0 km Large lobe: 4.1 km x 3.2 km x 1.3 km
Mass	10^{13} kg
Volume	25 km^3
Density	532 ± 7 kg/m^3
Rotation period	12.4043 ± 0.0007 h
Orbital period	6.55 years
Orbital eccentricity	0.640

Morphology

Most of the information relative to the morphological aspect of the nucleus comes from the OSIRIS, ROLIS and CIVA instruments. The surface of the nucleus presents many heterogeneities: 19 regions (see Figure 88) with different morphological aspects have been defined (Thomas et al. 2015). These regions can be divided into 3 main groups: 1) consolidated regions that display many fractures at different scales, indicative a low bulk density and heterogeneities in terms of composition and/or porosity, 2) smooth regions that are suspected to be regions of past and present prolonged activity and, 3) depressions remnants of outbursts of past activity (El-Maarry et al. 2015).

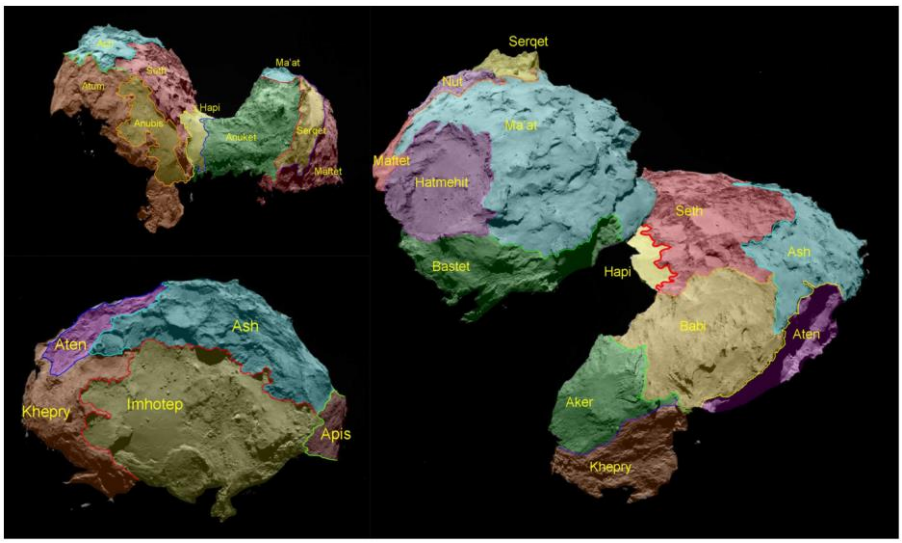

Figure 88: The 19 geomorphological regions of 67P/C-G as defined by the Osiris team (Thomas et al. 2015).

The observed geomorphologic structures and slopes are reminiscent of those found on Earth which can be explained by the fact that that the strength-to-gravity ratio on 67P/C-G is similar to that of weak rocks on Earth (Groussin et al. 2015). The presence of fractures and polygonal networks on the surface have been identified on OSIRIS and CIVA images and are thought to be the result of thermal stresses (El-Maarry et al. 2015; Bibring et al. 2015). The polygonal features identified could be an indication of shallow subsurface ice (El-Maarry et al. 2015). The presence of pits on the surface, source of some of the observed dust jets, has been linked to a mechanism of sinkhole collapse (Vincent et al. 2015). The pits diameter ranges between 10 and 100 m and extend up to 210 m below the surface. These pits are formed by the collapse of the surface overlying a cavity, this exposes more fractured surfaces and therefore allows more volatiles to sublimate. The origin of the cavities is still unsure but 3 hypotheses have been proposed:

- These cavities were present since the low-velocity accretion of the comet, and the weakening of the surface by volatile sublimation causes the collapse.
- They could have formed after the sublimation of pockets of CO and CO_2 ice (which sublimate a much higher temperature compared to water ice).
- The transition of pockets of water ice from an amorphous to a crystalline structure could warm up volatiles, the gas would then escape through the pores forming a cavity.

The presence of smooth surface and consolidated cliffs are indications of erosion and transport processes on the surface (Keller et al. 2015).

Composition of the surface

One of the unexpected results is the lack of surface ice exposed on the surface. The presence of bright spots by the OSIRIS camera (Sierks et al. 2015; Pommerol et al. 2015; Filacchione et al. 2016) is indicative of its presence in some very localized regions and on boulders (El-Maarry et al. 2015) but the VIRTIS spectrometer has constrained to a maximum of 1% the surface water ice coverage (Capaccioni et al. 2015).

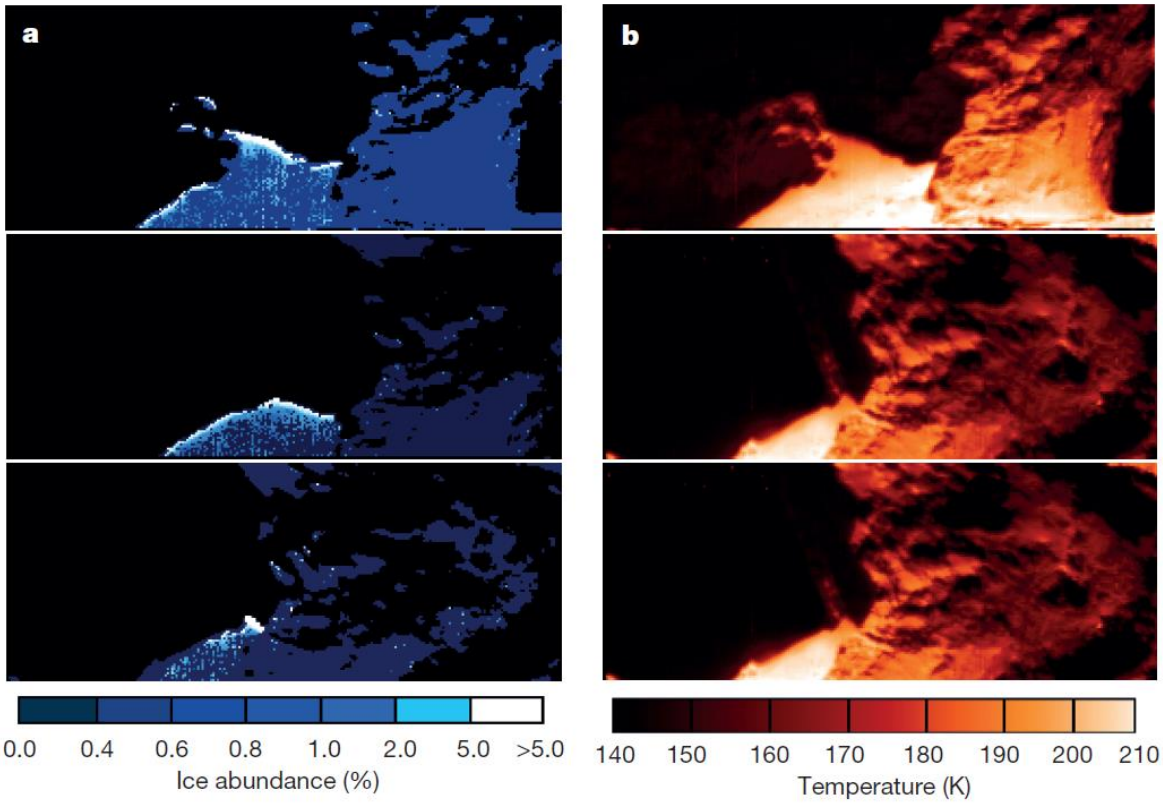

Figure 89: a) Water ice abundance as inferred by VIRTIS. b) Temperature measured on the same area. It can be observed that the maximum ice abundance is located near the shadows in the newly heated (i.e., newly illuminated areas) (De Sanctis et al. 2015)

A water ice cycle was identified on the surface by measurements from the VIRTIS instrument (De Sanctis et al. 2015, Figure 89), it was observed that the maximum water ice abundance is located in the areas newly exposed to the sun, the cycle hypothesized is as follows: during the local day the subsurface (a few cm below the surface) is heated by sunlight, the water ice present sublimates and escapes. During the following local night, the surface rapidly cools while the deeper layers remain warm, therefore the subsurface ice sublimates and freezes once it gets to the surface. Finally, during the next comet day the newly formed layer of ice sublimates thus closing the cycle.

The presence of CO_2 has also been identified by the VIRTIS instrument in the Anhur region with abundance reaching up to 1.6% (Filacchione et al. 2016). The presence of the CO_2 ice has only been measured for short period of time bringing the authors to the conclusion that its presence has a seasonal nature.

Most of the illuminated surface has been observed by the VIRTIS instrument and found to have a very low albedo. This combined with the reddish slope of its spectrum has been interpreted as due to the presence of opaque minerals associated with non-volatile organic macromolecular materials (carbon-hydrogen and oxygen-hydrogen chemical groups, Capaccioni et al. 2015). The

presence of carboxylic acids and NH_4^+ ions is also compatible with VIRTIS data and the absence of hydrated minerals indicate a lack of genetic link with primitive chondrites (Quirico et al. 2016).

After the first landing of Philae, the COSAC instrument measured the composition of the dust brought up. It detected complex molecules, precursors of amino acids. The list of detected compounds can be found in Goesmann et al. (2015) but it includes Alcohols, Carbonyls, Amines, Nitriles, Amides and Isocynates, some of the components were detected for the first time in comets (Ethanamides, Isocyanatomethane, Propanal and Propanone).

Thermal properties

The thermal properties of the comet's surface have mainly been investigated by the MIRO, VIRTIS and MUPUS instruments. The surface temperatures were measured by the VIRTIS instrument (an example of the temperature variations inferred from data obtained in July and August 2014 is presented in Figure 90, Capaccioni et al. 2014).

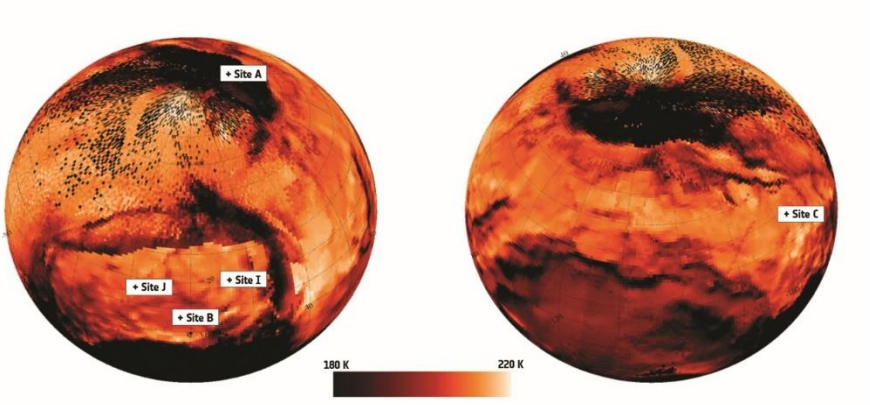

Figure 90 Temperature map of the 67P/C-G comet in an orthographic projection. The data was acquired in July and August 2014 when the comet was between 3.6 AU to 3.45 AU from the sun. The 5 selected landing sites are indicated. The map shows an important temperature variation on the surface linked with insolation (Capaccioni et al. 2014).

The subsurface thermal properties were estimated by MIRO data in the sub-millimetric and millimetric domain. MIRO points towards a thermal inertia of 10 to 50 $J.K^{-1}m^{-2}s^{-0.5}$, consistent with a thermally insulating powdered surface a few centimeters thick (Gulkis et al. 2015). The southern regions of the nucleus were determined to be much colder having been in darkness for extended periods of time (subsurface temperatures in the range 25-50 K were measured, Choukroun et al. 2015). The MIRO data also exhibits strong diurnal variations indicating that the thermal emission comes mainly from the upper centimeters of the surface (Schloerb et al. 2015).

At Abydos, The MUPUS instrument measured temperatures varying between 90 K and 130 K confirming that Abydos was faintly illuminated and estimated the thermal inertia to be 85±35 $J.K^{-1}m^{-}$

$^{2}s^{-0.5}$ (Spohn et al. 2015), a value higher than the one measured by MIRO that could be indicative of a thinner layer of dust at Philae's landing site than on the rest of the nucleus.

Origin

One of the main features of 67P/C-G is its bi-lobal shape, that was also observed on other comets (e.g., comet Halley) and is compatible with accretion models (Jutzi et al. 2015). Although there seems to be no major difference in the composition of the two lobes nor in their thermal properties (Choukroun et al. 2015), it is theorized that the comet acquired this shape after the collision at low velocity and accretion of two smaller bodies (Rickman et al. 2015). Massironi et al. (2015) studied OSIRIS images and observed that the stratifications observed on one lobe are independent from the stratified structures on the other lobe (for example, the stratifications are inclined in opposite directions close to the comet's neck). It was also observed that comparing the orientation of terraces (flattened areas) on the surface presented a better fit to gravity vectors (gravity vectors represent the local direction of the gravitational force; terraces should form at right angles to the gravity vectors) computed for the two different lobes than for gravity vectors computed for the whole comet pointing to the theory of accretion of two separate objects.

Activity

The activity on the nucleus is at the source of the coma and it is therefore key to understanding the mechanisms at play.

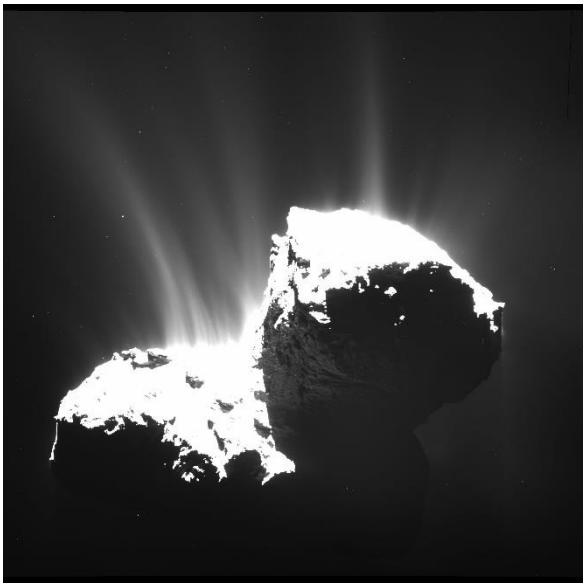

Figure 91 Observed outgassing of comet 67P/C-G Credits: ESA/Rosetta/NAVCAM.

The outgassing of the comet (see Figure 91) comes mainly from the neck region (i.e between the two lobes) of the comet (Bockelée-Morvan et al. 2015; Migliorini et al. 2016) with a measured

water column density higher by 1 or 2 orders of magnitude than elsewhere as measured by MIRO (Biver et al. 2015). This led to the hypothesis that the outgassing is not only correlated to illumination but also to the local topography and to a heterogeneous distribution of water ice in the subsurface (Biver et al. 2015; Lee et al. 2015; Lara et al. 2015). The sublimation of H_2O ice is correlated to the diurnal cycle indicating that the water ice is located in the diurnal thermal layer that is in the range 1-2 cm for the MIRO instrument (Lee et al. 2015). The detection by VIRTIS of CO_2 outgassing from illuminated and non-illuminated areas suggests that the CO_2 ice is located at a depth below the diurnal skin depth (Bockelée-Morvan et al. 2015; Schloerb et al. 2015).

2.2. Coma

The coma is composed of the volatiles that have sublimated from the surface of the nucleus, but also of refractory materials, namely dust particles that the sublimating volatiles have taken with them.

Gases

The coma has been determined to be water dominated (Hässig et al. 2015), with a strong CO and CO_2 presence except in the winter hemisphere where CO and CO_2 sometimes become the main constituents (Le Roy et al. 2015). The night-side contribution to the total water column density was determined to be very low (less than 10% as measured by the MIRO instrument, Biver, N. et al. 2015). The difference of water production between the summer and winter hemisphere ($H_2O_{summer}/H_2O_{winter}$ = 16) can only be explained by temperature differences and it has been hypothesized that the northern hemisphere has been processed much more during the last orbit when it was the summer hemisphere and therefore is depleted in volatiles (Le Roy et al. 2015).

The main constituents that have been detected by Rosina are: water, carbon monoxide, carbon dioxide, amonia, methane, methanol, formaldehyde, hydrogen sulphide, hydrogen cyanide, sulphur dioxide and carbon disulphide (Le Roy et al. 2015). So far the only amino-acid (a key ingredient to life) that has been detected in the coma by Rosina is glycine. This amino-acid is the only one that can form in the absence of liquid water and is probably the only one present in comets. Rosina also detected phosphorous which is a constituent of DNA and RNA and is also present in cell membranes (Altwegg et al. 2016).

Further, Rosina detected molecular oxygen, a highly reactive constituent, in the coma. It was determined to have an abundance of 1–10% relative to H_2O, a value higher than predicted by the Solar System formation models. It is hypothesized that the molecular oxygen was incorporated into the water ice in the early protosolar nebula stage of our Solar System which would require rapid cooling

(Bieler et al. 2015). In agreement with this idea the molecular nitrogen, as measured by Rosina, is about 25 times less abundant than the expected protosolar value indicating that the ice was formed at very low temperatures in the protosolar nebula (Rubin et al. 2015).

The ratio of Deuterium with regard to Hydrogen (D/H) in water is an important indicator of its origin (theoretical simulations show that its value is dependent on the distance from the Sun at which the water formation took place). The origin of Earth's ocean water can be investigated with this method: previous measurements on asteroids have shown a good agreement with Earth water (see Figure 92). The D/H ratio measured on 67P/C-G is 3 times the ratio measured in Earth's oceans, suggesting that Jupiter family comets are not the source of Earth ocean–like water (see Figure 92, Altwegg et al. 2015).

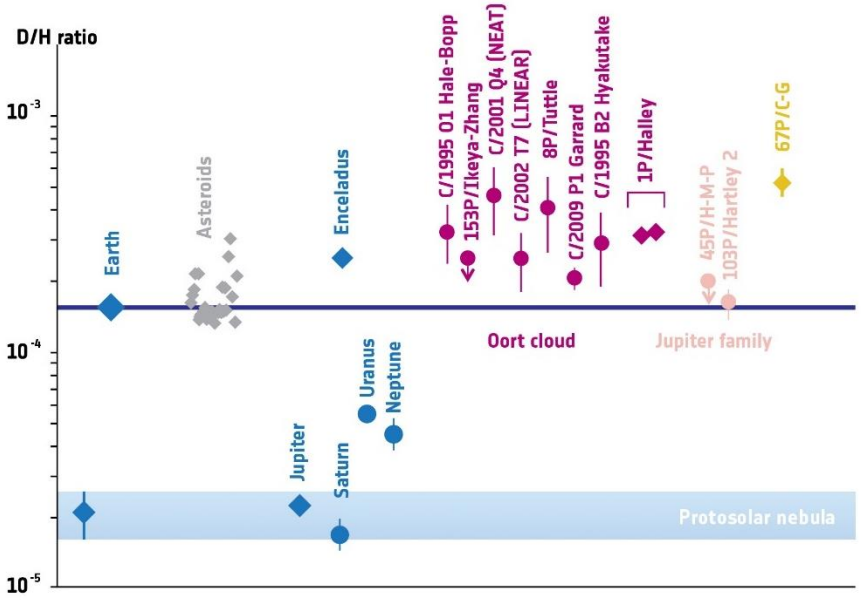

Figure 92 D/H ratio in the Solar System. Credits: Data from Altwegg et al. 2015 and references therein

The coma appeared to be heterogeneous in composition (Feldman et al. 2015) with diurnal and seasonal variations (Hässig et al. 2015). The Rosina measurements first showed that H_2O, CO and CO_2 have a heterogeneous distribution (Altwegg et al. 2015) and later that C_2H_6, HCN, CH_3OH and CH_4 also are heterogeneously distributed (Luspay-Kuti et al. 2015). These heterogeneities are probably related to composition heterogeneities in the subsurface of the southern hemisphere of the nucleus. It could also be indicative of the presence of 2 different types of ices in the subsurface (H_2O vs CO_2, Luspay-Kuti, A. et al. 2015).

Dust

The dust particles present in the coma have been studied extensively by the GIADA team. It was found that the dust to gas mass ratio is 4 ± 2 (Rotundi et al. 2015) and the dust to ice volume ratio is 2 (Pätzold et al. 2015). The dust activity increased by a factor 6 from 3.36 to 2.43 AU from the Sun (Della Corte et al. 2015).

The size of the dust particles measured by the COSIMA instrument range from 1 to 100 µm. The low albedo and the presence of a connecting matrix indicate that carbonaceous matter is one of the main constituent of these grains (Langevin et al. 2016). The dust particles are sodium-rich and the dust layer may have formed while the comet was far from the Sun (when the flow of gas is no longer sufficient to remove the dust grains from the surface, a dust layer is formed as the volatiles continue to depleted slowly (Schulz et al. 2015).

2.3. Context of the SESAME-PP measurements

The refractory dehydrated layer most likely covers the water ice, the depth of which is variable (Groussin et al. 2015; Choukroun et al. 2015). This would explain the strong presence of water in the coma and its absence on the surface of the nucleus. A vertical heterogeneity of the thermal properties indicates a heterogeneity in the physical property of the material at least up to a few centimeters deep (Schloerb et al. 2015). At larger scale (10s of meter), the CONSERT data are consistent with a gradient in the dielectric constant with depth (Ciarletti et al. 2015) that could be due to a decreasing dust-to-ice ratio or an increasing porosity. The SESAME-PP instrument measures electrical properties up to a depth of about 1 m. Its sounding depth is thus between that of MIRO (sounded depth of a few centimeters) and CONSERT (sounded depth of a few hundred meters, see Chapter 3, Section Chapter 3:1.2.3)

3. SESAME-PP observations during the cruise, descent and landing

3.1. Cruise

The SESAME-PP instrument was activated on several occasions (a dozen times) during the cruise phase of the Rosetta mission, essentially for payload checkouts and functional tests. House-keeping and science data were collected to check the instrument health, confirm that commands were successfully executed, and test new or revised flight procedures.

The typical SESAME-PP health check generates telemetry on internal electronics reference voltages, the potentials at the two receiving sensors (i.e., V_8 and V_{12}, see Chapter 3, Section 2.3), their difference (ΔV), and the currents flowing through the three transmitter electrodes (I_4 at the +X sole, I_{17} at the MUPUS-PEN hammering device and I_{15} on the lid of the APXS sensor housing) to verify that

these signals are not disturbed by noise and remain within the expected limits. These measurements were performed at various sounding and sampling frequencies. Because the landing gear is folded, the potentials measured during the cruise phase cannot be used for science nor reference purposes.

Tests were also conducted to examine the level of the interferences generated by CONSERT soundings and by Philae's flywheel during the SESAME-PP operations. It was discovered that the CONSERT signal strongly affects both SESAME-PP passive and active observations. CONSERT transmits an RF signal of 0.2 s every 2.5 s, and it was first assumed that SESAME-PP could be operated between the radar pulses, which was later proven to be wrong (Section 3.2). It was recommended to operate the flywheel with the lowest possible rotation rate after the separation of Philae from Rosetta to limit electrical noise.

The only notable change in the SESAME-PP performance during the cruise was observed after the flyby of asteroid (2867) Steins (September 5, 2008): the level of the transmitted current in +X changed slightly at all frequencies (see Figure 93). This is probably due to of a change of stray parasite capacitances when the Rosetta spacecraft was rotated to examine the asteroid, thus exposing the Philae module to the Sun for about half an hour and likely changing the position of the electrode slightly with respect to the grounded structures. The transmitted current then remained stable until the end of cruise. The standard deviation of the currents measured before and after the Steins flyby gives a useful indication on the precision of the SESAME-PP measurements, namely, 28 nA on the amplitude and 0.9°on the phase.

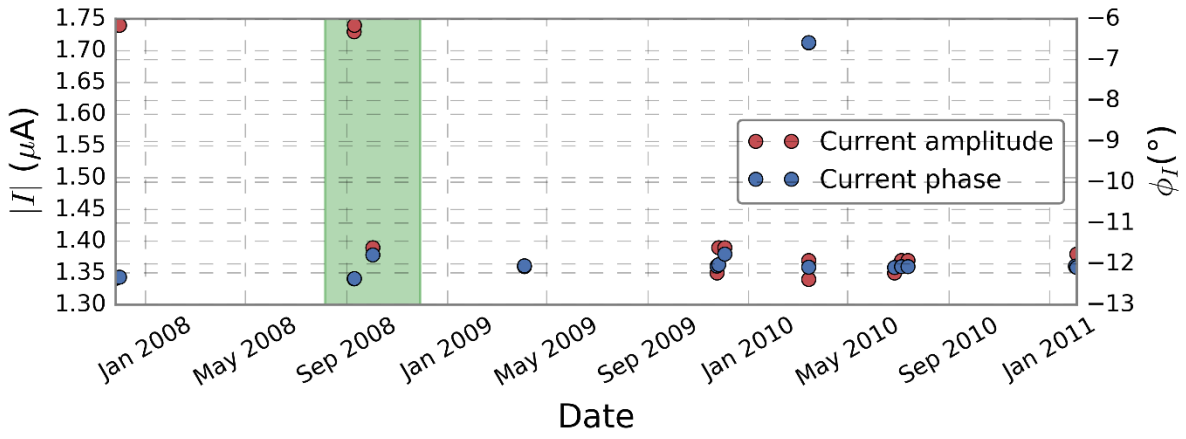

Figure 93 Current amplitude and phase at 758 Hz during the Rosetta cruise, indicated in green is the flyby of the Steins asteroid

The post-hibernation tests in March 2014 showed that all SESAME hardware and software had successfully survived the 31 months of hibernation of the Rosetta probe. It was also discovered that

the RF link disturbed SESAME-PP, but it was anticipated that this interference would fade away after separation.

Lastly, only passive measurements were performed during the pre-delivery phase in October 2014 in order to monitor the plasma environment over one full rotation of the comet and to look for possible variations of the comet activities. These observations were conducted in cooperation with the Rosetta Plasma Consortium instruments RPC-MIP and RPC-LAP (Langmuir Probe). The passive measurements performed by SESAME-PP during the whole cruise show no significant variation (Figure 94) except for those performed during this pre-delivery phase (October 16th & 17th): SESAME-PP detected 4 possible events (one major one at 14:51:27 UTC and 3 minor ones a few hours later). The main caveats in the interpretation of these events is the fact that Philae was in stowed position during these measurements and that the conductive body of Philae, the Rosetta spacecraft and the other functioning instruments could have induced these perturbations. However, at the time of the strongest event, on October 17, 2014, RPC-MIP recorded a drop to lower frequencies (Lebreton, personal communication, 2016) that could indicate that this event is not an artefact. Bearing this in mind it is only possible to give a qualitative explanation to these measurements at the time of this manuscript. These events could indicate plasma wave activities at the distances indicated in Table 12. A more in depth comparison with the RPC data is necessary to properly understand these measurements.

Table 12: Time, signal/noise ratio and distance of Rosetta to the comet for all 4 events recorded by the SESAME-PP passive measurements on October 17, 2014

Time of the event (UTC)	**Signal/Noise (for the 58.5 Hz center band frequency)**	**Distance to the comet (km)**
14:51:27	~14	10.05
16:01:04	~1	10.04
17:10:54	~2.5	10.02
17:11:10	~2.5	10.02

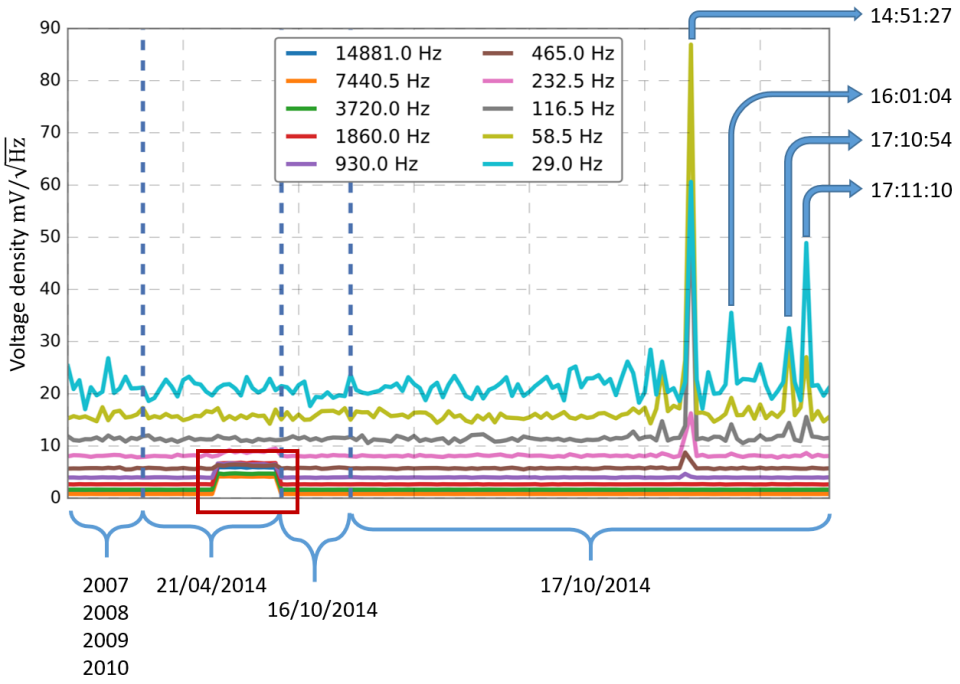

Figure 94 Passive measurements of the SESAME-PP instrument during the cruise and the pre-delivery phase. One major and 3 minor events were detected on the 17/10/2014. All times are indicated in UTC. The reported frequencies are the center of the frequency bin. The red square indicated interference measurements that were performed during the cruise.

3.2. Separation, Descent, Landing (SDL)

Four data blocks were acquired throughout the SDL phase that started on November 12, 2014 at 08:35:00 UTC (Table 13):

I. before separation,
II. immediately after separation with the landing gear deployed,
III. outside the Rosetta spacecraft zone of influence, and
IV. shortly before nominal touchdown.

The SESAME-PP measurements acquired during the first sequence are in line with those performed during cruise. Only passive measurements were conducted during the second block for a joint RPC/SESAME-PP plasma environment monitoring. The third and fourth blocks were primarily dedicated to the calibration of the instrument in a near-vacuum environment. I_4 , V_8 , V_{12} and ΔV were measured and acquired in the form of time series at 409 Hz and 758 Hz and processed onboard data (i.e., the phase and amplitude of I_4 and ΔV) were acquired at these same frequencies and five additional frequencies, namely, 74, 146, 2946, 6510, and 10080 Hz. These measurements were all the more crucial as no calibration could be performed with the flight model of Philae with deployed landing gear before launch.

Table 13: SESAME-PP active measurements during the SDL and FSS phases

Measurement block	Date	Start-End (UTC)	Frequency (Hz)	Foot temperatures (°C) +Y (top) –Y (bottom)
SDL1	2014-Nov-12	07:41:01-07:41:57	TS:758, 409	-135.0 - 140.8
SDL3	2014-Nov-12	09:05:04-09:11:21	TS:758, 409	-133.9 - 138.8
SDL4	2014-Nov-12	14:47:23-14:48:30	TS: 758, 409	-124.3 - 125.2
FSS1	2014-Nov-13	08:10:49-08:13:07	TS: 758, 409 PD:10080,6510, 2948, 146, 74	-131.8 - 161.8
FSS2	2014-Nov-13	10:12:47-10:15:07	TS: 758, 409 PD:10080, 6510, 2948, 146, 74	-145.7 - 162.1
FSS3	2014-Nov-13	12:14:09-12:17:09	TS: 758, 409 PD:10080, 6510, 2948, 146, 74	-156.8 - 163.4
FSS4	2014-Nov-13	14:16:51-14:19:11	TS: 758, 409 PD:10080, 6510, 2948, 146, 74	-161.9 - 164.1

Notes. (a) The SDL2 block was only dedicated to passive measurements and is therefore not shown here (b) TS stands for "time series" and PD for "onboard processed data". (c) as measured by SESAME-CASSE PT1000 temperature sensors

Unfortunately, all potential measurements performed during the second, third and fourth block of the SDL phase were saturated (see Figure 95 for an example). The observed disturbances are undoubtedly due to interferences generated by CONSERT sounding operations that stopped only three minutes after SESAME-PP's last measurement block during the SDL phase. As a consequence, we do not have an in-flight calibration data from the instrument and, in particular, we are working under the assumption that the receiving electrodes and, specifically, the embedded preamplifiers have evolved similarly during Rosetta's ten-year journey to the comet. This assumption is supported by the identical amplifier design and preselection of individual models with highly similar characteristics, as well as uniform exposure of both flight models to temperature, radiation, and vacuum. The transmitted currents on the +X foot, fortunately, were not perturbed and can be used for comparison to the currents measured at the surface of the comet during the FSS phase (see Section 4.3).

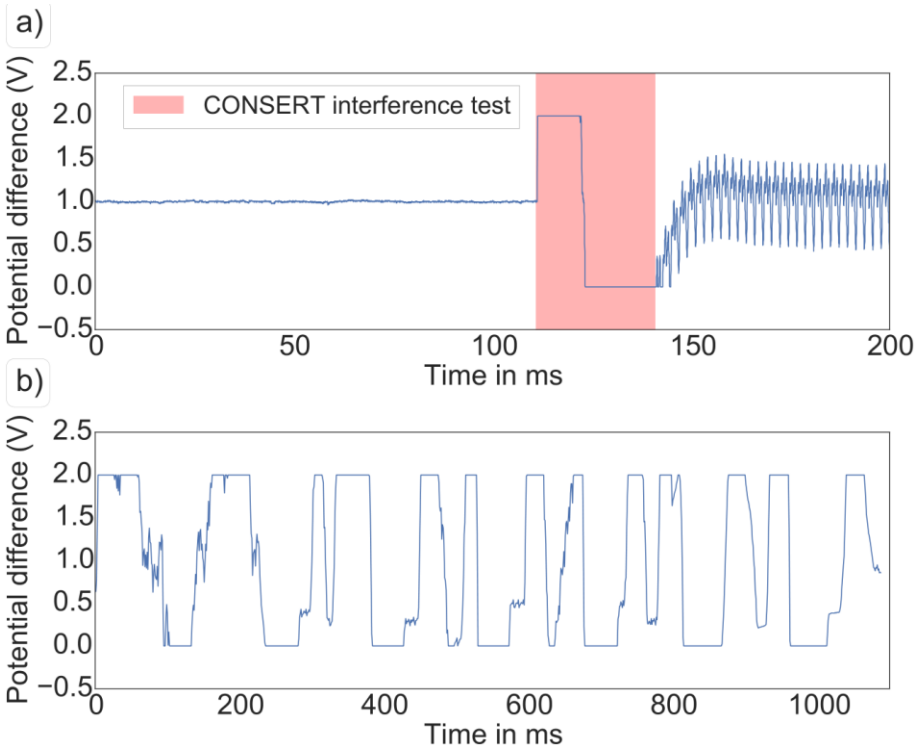

Figure 95: Top panel: time series of the potential difference between the receiving electrodes during an interference test between SESAME-PP and CONSERT conducted in 2010. CONSERT operations clearly saturate the SESAME-PP receiving channels at 132 ms. Bottom panel: time series of the potential difference between the receiving electrodes during the descent of the Philae lander toward the comet. The saturation pattern is similar to that observed during the SESAME-PP/CONSERT interference test

3.3. First Science Sequence (FSS) on the surface

On November 12, 2014, at 15:34:06 UTC, the harpoon ejection failed during the first touchdown of Philae on comet 67P/C-G. The lander bounced away from the surface before eventually coming down to a rest at its final landing site, Abydos, about two hours later (see more detailed description above). The Philae module was then commanded to enter a "safe mode" that consists of four measurement blocks that require no mechanical activity e.g., DIM, COSAC and PTOLEMY sniffing, ROMAP, and MUPUS-TM (Thermal Mapper). These included SESAME-PP in a reduced geometry mode that only uses the three foot electrodes (+X as transmitter and –Y and +Y as receivers). The MUPUS-PEN and APXS were deployed on November 14, 2014, but could not be used as transmitters for SESAME-PP because of the constraints on Philae's operations time.

As a consequence, SESAME-PP did not operate in a nominal quadrupolar configuration during FSS. Instead, it performed four identical measurement blocks using the three foot electrodes; the lander body played the role of the fourth electrode. The measurement blocks were performed on November 13, 2014 at two-hour intervals, starting shortly after local sunset and continuing into local night (Table 13). Each block consisted of one health check, two passive measurements and 11 active measurements. In the active mode, I_4 , V_8 , V_{12} , and ΔV were measured and collected in the form of

time series at 409 Hz and 758 Hz, while only the phase and amplitude of I_4 and ΔV were acquired at 74, 146, 2946, 6510, and 10080 Hz. The active measurements of each block lasted for about 2 min.

The first measurement block (FSS1) started shortly after the end of the sunlit period with +X and +Y feet at a temperature of about −120° C, while the –Y foot temperature, permanently in shadow, was at −165° C. By the time of the fourth measurement block (FSS4), all three feet had reached the same temperature of about −165°C, which enables the temperature variation effects to be monitored. The quoted temperatures were measured by the PT1000 thermal sensors attached to the SESAME-CASSE sensors and may differ from the real temperatures of the +Y and –Y preamplifiers. In particular, the PT1000 sensors are insulated from the close environment with a guarding kapton-aluminium foil, while the SESAME-PP receivers are in good thermal contact with the lid of the soles. As a consequence, it is likely that SESAME-PP receivers cooled faster after sunset than indicated by the SESAME-CASSE temperature sensors. Moreover, while the accuracy of the SESAME-CASSE temperature sensors is ±2°C at −100° C, it is ±10° C around and below −160° C. Lastly, we note that, prior to the launch of the Rosetta probe, SESAME-PP preamplifiers had not been calibrated for temperatures below −150° C. Additional tests have been conducted at LATMOS after the Philae landing on ground models of the preamplifiers in a cryogenic room for temperatures down to −175° C to provide a more reliable calibration of the data against temperature.

As shown in Figure 96a, a drop in potential was observed throughout the night at the +Y foot, while the potential measured on –Y remained constant. The data were corrected for the temperature dependence of the preamplifier gain using the latest calibration and temperatures indicated by SESAME-CASSE sensors. However, we cannot rule out that this drop could be due to an incomplete correction of the temperature dependence of the electronics. As a matter of fact, if the +Y receiver was 10°C cooler than indicated by the SESAME-CASSE temperature sensor during the fourth block and if the –Y foot was 10°C cooler during the entire FSS, which is possible given the accuracy of the thermal sensors below −150° C and the measurements of the MUPUS-TM instrument with reference to temperatures in the range −183° C to −143° C (Spohn et al. 2015), then the trend would have disappeared once the appropriate calibration correction had been applied (Figure 96b). As a further argument, the electrical properties of water ice and other potential candidates for the surface material of the nucleus are not expected to vary at such low temperatures (see Chapter 1, Section 3.1.1).

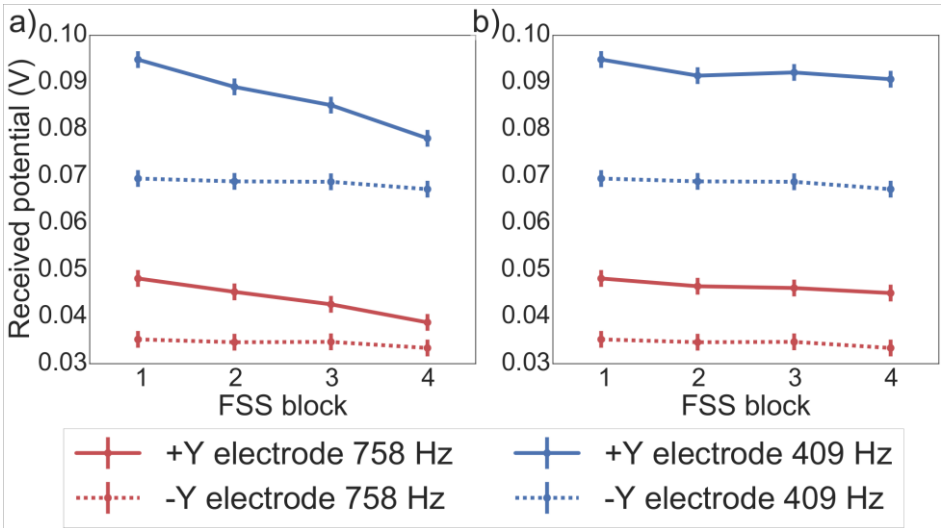

Figure 96: Calibrated measured potentials on the SESAME-PP receiving electrodes –Y and +Y for the four measurement blocks of the FSS. a) The temperatures used for calibration are those measured by the SESAME-CASSE PT1000 sensors. The potential of the +Y electrode decreases with time. b) The temperatures used for the calibration for the –Y electrode and the FSS4 measurements of the +Y electrode are those measured by the SESAME-CASSE PT1000 temperature sensors, minus 10° C. The drop in potential of the +Y electrode has now disappeared.

The most interesting feature shown in Figure 96 is the significant potential difference measured between the two receiving electrodes: the potential of +Y is significantly larger than that of –Y with a ratio V_{12}/V_8 of 1.35 ± 0.03. In a homogeneous environment, the potential of the two feet are expected to be nearly identical (i.e., a ratio V_{12}/V_8 of 1.08 would be expected owing to the slight asymmetry induced by the body rotation of 11.2° relative to the landing gear). The potential difference was observed both at 409 and 758 Hz. We estimate that this feature is genuine and not an effect of any hypothetical temperature gradient since it was still present at the end of the night (i.e., during FSS4) when both feet were at the same temperature. Strictly speaking, in the absence of any calibration during the SDL, we cannot completely rule out a drift of one of the receiving channels with respect to the other during the long journey to the comet. There is however no direct evidence for such a drift, and given the identical preamplifier and electronics design, near-identical prelaunch characteristics, and identical environment during cruise, an identical drift, if any, can be assumed. In addition, we recall that no drift was observed on PWA-HASI/Huygens after the seven-year cruise of the Cassini–Huygens probe to the Saturnian system. The difference between the potentials of the –Y and +Y electrodes is further analyzed and compared to numerical simulations in Section 4.4.

Lastly, the amplitude of transmitted current on foot +X is analyzed in light of the current measured during the descent phase in Section 4.3.

4. Analysis of the SESAME-PP surface data

4.1. Approach

As described earlier, the most interesting observation at Abydos is the significant potential difference measured between the two receiving electrodes. Although the absence of calibration during the descent phase leaves a theoretically possible drift of one channel with respect to the other, we assume that both receiving electronic circuits aged in the same way and we investigate the implications of this observation in terms of electrical properties and distribution of the matter around the SESAME-PP electrodes, assuming a homogenous composition.

Our approach consists in comparing the flight model measurements to a number of numerical simulations based on realistic models, using the Capacity-Influence Matrix Method described in Chapter 2, Section 2.4. This method requires a good knowledge of the configuration of operation at Abydos which was far from nominal. As a matter of fact, the landing of Philae did not take place as planned. Philae bounced several times until it reached Abydos where it came to a rest in what looks like a cavity just slightly larger than the size of the lander, and partially shadowed by nearby boulders or cliffs with the +Y foot pointing upward, the –Y foot pointing downward, and the +X foot close to or resting on a Sun-illuminated surface (Bibring et al. 2015).

Section 4.4.1 is dedicated to the reconstruction of the attitude and environment of SESAME-PP at Abydos using almost all available constraints, including those provided by the measurements of the current transmitted on the +X foot (analyzed in Section 4.3). We emphasize that if Philae had come to a rest in a nominal horizontal position, resting on its three legs, in the absence of measurements that employed the other transmitting electrodes, we would have most likely observed no meaningful difference of potential between the two receiving electrodes because the configuration of operation would have been almost perfectly symmetrical (hence, $\Delta V \sim 0$). In this regard, the acrobatic attitude of Philae at Abydos offers an opportunity for SESAME-PP to provide insights into the near surface of 67P/C-G at this location.

4.2. FSS passive measurements

Two passive measurements were made at each FSS sequence, one at the beginning and one at the end. The measurements show no significant signal over the noise for the two first FSS. A peak is observed in the voltage spectral density at the beginning of the third FSS that drops at the end of the sequence. This peak is observed for two central frequency bands (118.5 Hz and 236.5 Hz) and no parasite inducing activities were undertaken at that time. The ROLIS MUPUS measurements operated during all of the SESAME-PP passive measurements on the surface making them unlikely candidates

as source of the disturbance. This event could be interpreted as electromagnetic surface activity. At the same time RPC-MIP registered an increase in its low frequency components (Lebreton et al, personal communication) that could be linked to this event, although the distance between the instruments at this time makes this hypothesis unlikely. The possibility of electromagnetic surface activity is supported by the absence of a magnetic field (Auster et al. 2015) and by the detection of solar wind sputtering on the surface of the comet (Wurz et al. 2015).

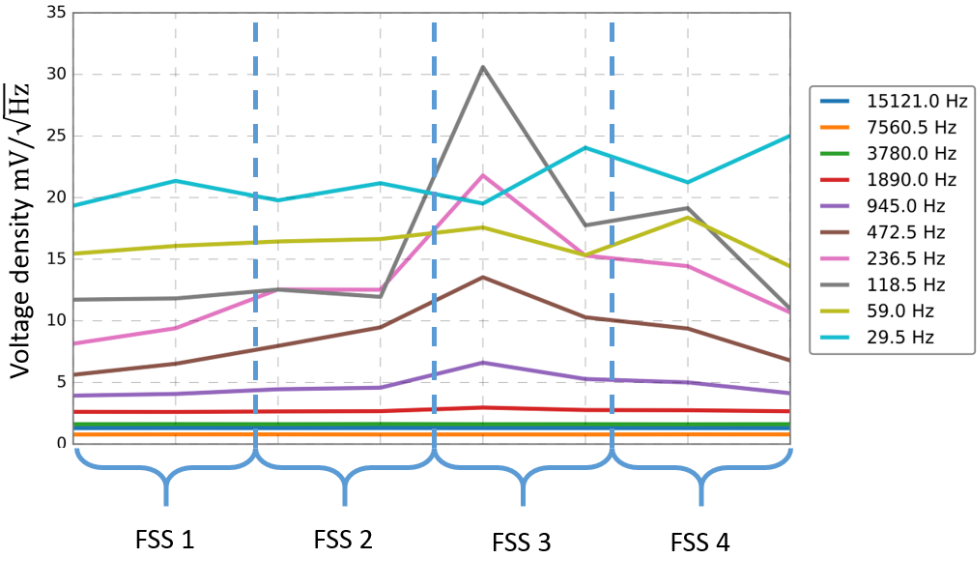

Figure 97: Passive measurements of the SESAME-PP instrument during the FSS. The reported frequencies are the center band frequencies of each bin. The event recorded at the beginning of FSS3 could be indicative of electromagnetic activity.

4.3. Transmitted currents

A potential difference is applied between the sole of the transmitting electrode and the body, generating a current that depends upon the electrical properties of the environment around the transmitting electrode. The current injected through the +X electrode was measured (amplitude and phase) both during the SDL phase, in a near-vacuum environment, and at the beginning of the FSS phase, on the surface of 67P/C-G nucleus. No significant difference (within the error bars) is noted between these two sets of measurements. Figure 98 also shows that both SDL and FSS are close to the value expected in vacuum from numerical simulations. This observation suggests that, during FSS, the transmitting electrode (+X) was not in contact with the nucleus surface and/or that the material under the transmitting electrode has very low dielectric constant and conductivity.

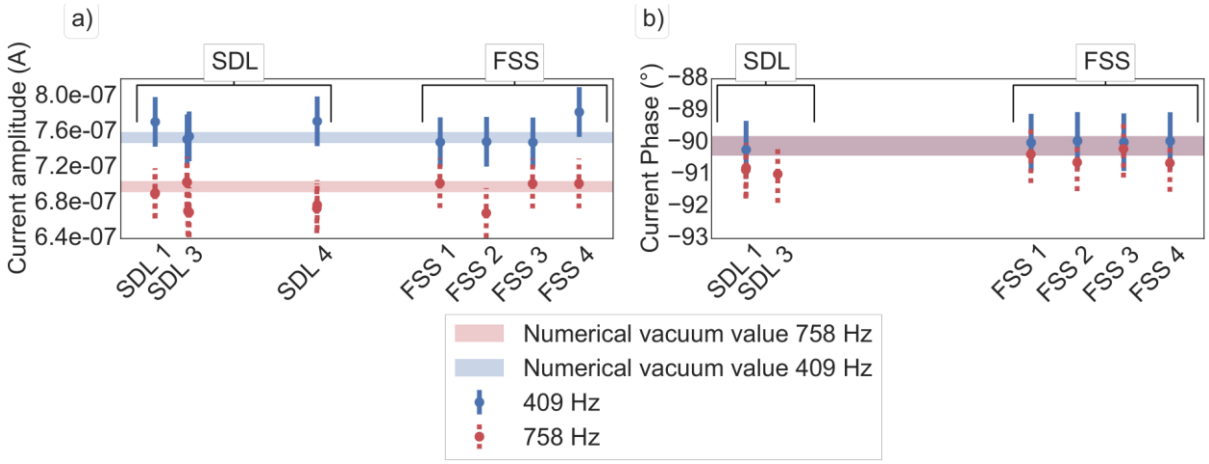

Figure 98: Amplitude (a) and phase (b) of the currents measured during the SDL and FSS phases at 409 Hz and 758 Hz. The phase of the currents measured during SDL4 could not be retrieved because of disturbances in the signal. The blue (resp., red) shaded lines indicates the expected amplitude of the current and phases at 409 Hz (resp., 758 Hz) in vacuum obtained from numerical simulations and the associated error due to the mesh approximation. The potential difference used to generate the current at 758 Hz is half of that used at 409 Hz.

The SESAME-CASSE data recorded during the hammering of MUPUS-PEN contain information on the quality of the contact between the Philae feet (where CASSE sensors are also located) and the surface. They show that, at the beginning of the hammering session, only the +Y foot reliably recorded MUPUS-PEN strokes; the sensors in the +X and –Y feet detected them at a later stage (Knapmeyer et al. 2016). This suggests that Philae moved during the initial phase of the session, eventually settling in an attitude that improved the coupling between the foot sensors and the surface. Because SESAME-PP measurements were performed before the deployment of the MUPUS boom, this would imply that the contact between the transmitting +X electrode and the surface was bad or even nonexistent when the transmitted currents shown on Figure 98 were measured. More specifically, a distance of only 1 cm between the +X foot and the surface would be sufficient to explain the absence of a significant difference between the currents measured during SDL and FSS.

However, if we assume that the +X foot was close to the surface (< 1 cm), SESAME-PP current measurements place a constraint on the upper limit of the dielectric constant and conductivity of the surrounding material. Comparison with numerical simulations yields a maximum dielectric constant of 3 and a maximum conductivity of $4 \cdot 10^{-8}$ S/m. With such a low conductivity, the surface material of the nucleus could be regarded as a pure dielectric.

4.4. Received potentials

As mentioned earlier to retrieve the permittivity of the surface from the comparison of the measured received potentials and the numerical simulations derived from the Capacity-Influence Matrix Method, a good knowledge of the configuration and environment of SESAME-PP operations is required. Almost all available constraints were thus gathered to build a suite of realistic and reliable

geometry models of the environment and attitude of Philae at Abydos. These models were first constructed, using the free and open-source Blender software, and then imported into COMSOL Multiphysics to simulate the SESAME-PP operations numerically. Unfortunately, the uncertainties on the phases of the received potentials are too large to estimate the electrical conductivity of the near surface; the dielectric constant can however be retrieved.

4.4.1. Reconstruction of Philae attitude and environment at Abydos

In order to reconstruct the attitude and environment of Philae at its final landing site, we took into account constraints from various origins:

I. CIVA images (Bibring et al. 2015): The CIVA panorama at Abydos consists of a set of seven images around the Philae body taken by cameras with well-known positions and fields of view (Figure 99 and Figure 100) and provides a wealth of constraints for the reconstruction of the attitude and surroundings of the lander. Revealing that one of the 693 mm long CONSERT antenna is touching the surface, camera 3 even gives a quantitative indication of the distance of the "walls" of the hole in which Philae rested. In addition, a pair of stereo images taken by cameras 5 and 6 in the direction of the lander balcony allows us to evaluate distances (in the range 80cm-7m) and reconstruct the 3D environment in this direction.

II. ROLIS images (S. Mottola, personal communication) Pointing under the lander, the ROLIS instrument provides two additional images as well as distance information by stereography.

III. MUPUS (Spohn et al. 2015): Additional constraints can be obtained from two of the three MUPUS instruments. First, MUPUS-TM detected direct illumination behind the lander in the direction of the PEN deployment, which completes information from the solar array telemetry (these are not takeninto account in the present model). Second, the MUPUS-PEN probe was nominally deployed and started the hammering sequence. While it is not clear whether or not the probe hit an obstacle during its 58.5 cm long deployment, the 30 mm long MUPUS-PEN probe most likely touched the surface without fully penetrating it.

IV. SESAME-CASSE (Knapmeyer et al. 2016): As mentioned previously SESAME-CASSE recorded the hammering of the MUPUS-PEN and the clear signal that was measured by the +Y accelerometers strongly suggests that this foot was in good contact with the surface. On the –Y and +X feet, the signal was weak at the beginning of the hammering sequence and then increased as if the lander had slightly moved, thereby enhancing the contact between this foot and the "ground". We note that SESAME-PP operation occurred

before the MUPUS-PEN hammering and therefore at a time when the contact of the +X and –Y electrodes with the sur- face was possibly poor, even nonexistent.

V. SESAME-PP: Though not very constraining, SESAME-PP current measurements suggest that the +X foot is not necessary resting on the surface (see Section 4.3); this is consistent with SESAME-CASSE first measurements on the +X accelerometer. Further, the ratio between the potentials measured on the +Y and –Y feet (i.e., $\frac{V_{12}}{V_8} = = 1.35 \pm 0.03$) suggests that the +Y foot may be surrounded by and/or closer to a greater amount of cometary material than the –Y foot.

The geometry model of Philae attitude and environment at Abydos has two main degrees of freedom. First, the amount of matter located under the +Y foot in the blind spot of the CIVA and ROLIS cameras. If a small amount of matter is present there, then a high subsurface dielectric constant is required to reconcile simulations with SESAME-PP data and, in particular, to retrieve the measured ratio V_{12}/V_8. Second, the quality of the contact between SESAME-PP receiving electrodes and the surface controls the measured potentials. The better this contact is, the higher the received potential.

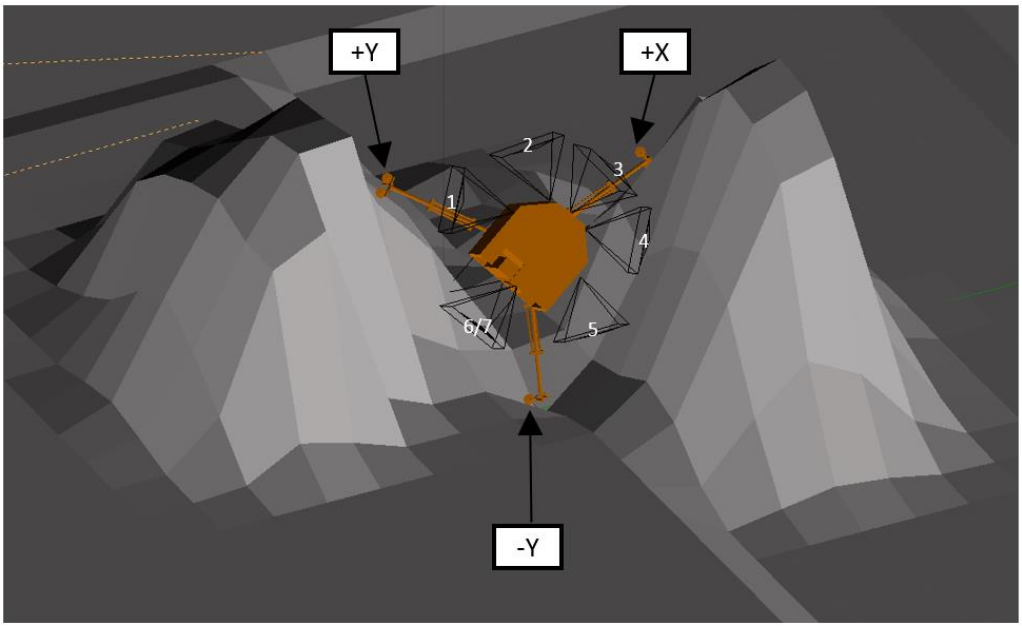

Figure 99: Possible 3D model of the Philae attitude and environment at Abydos. The fields of view and numbers of the CIVA cameras are indicated with black triangles. The model was built using the Blender software (http://www.blender.org/)

Figure 99 shows a possible 3D model of the Philae lander attitude and environment at Abydos. This model satisfies all of the constraints previously listed and was built to provide a lower bound for the subsurface dielectric constant. This was carried out by adding as much cometary material as possible under the +Y foot, and giving +Y (respectively, –Y) a good (respectively, bad) contact with the

surface. The simulated CIVA panorama obtained with this 3D model is compared to the actual panorama taken by CIVA in Figure 100.

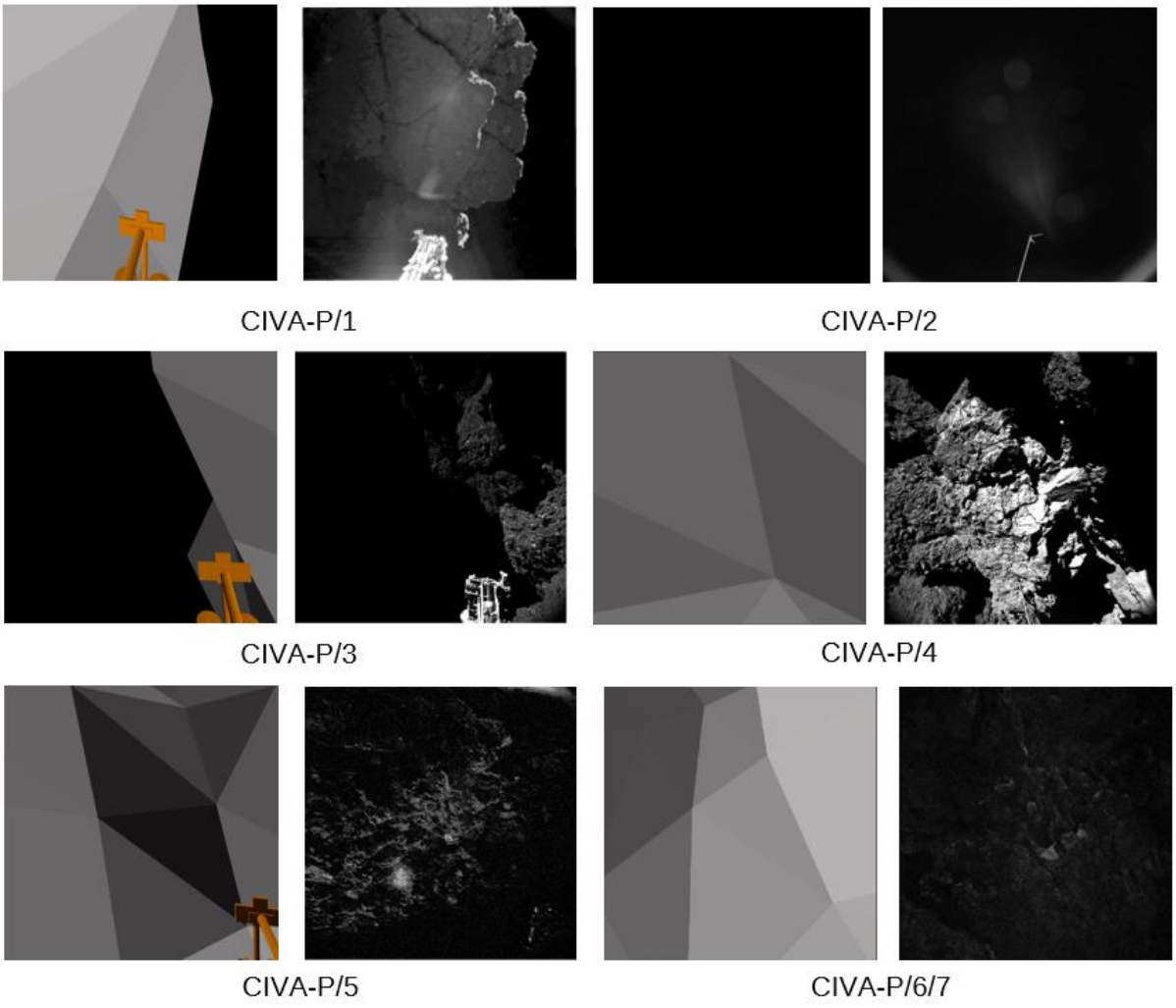

Figure 100: Comparison between the CIVA images (credits: ESA/Rosetta/Philae/CIVA) taken at Abydos and the corresponding camera views in the model of Philae environment and attitude built under Blender

4.4.2. Retrieval of the dielectric constant of the near surface of Abydos

The model of the Philae lander attitude and environment at Abydos presented in Figure 99 was found after varying the two degrees of freedom mentioned in Section 4.4.1 to retrieve the lowest possible dielectric constant of the subsurface. Applying the Capacity-Influence Matrix Method to this model, we compute the ratio between the potential amplitude of the two receiving feet (i.e., V_{12}/V_8) varying the dielectric constant of the subsurface around Philae from 1 to 5 and setting the conductivity to zero. We find that the value for which simulation best reproduces SESAME-PP observations is 2.45 ± 0.20. We emphasize that this value is a strict lower limit: any other geometrical model satisfying the constraints listed in Section 4.4.1, but with less material around +Y and/or a better contact between the -Y electrode and the surface, requires a higher dielectric constant to be reconciled with SESAME-

PP observations at Abydos. Furthermore, we verify that including a non-null conductivity results in a higher lower limit for the dielectric constant.

5. Implications for the composition and porosity of the first meter of 67P/C-G's nucleus

The SESAME-PP measurements at the surface of 67P/C-G provide a lower limit for the dielectric constant of the near surface of the nucleus at Abydos in the frequency band of 409 Hz to 758 Hz. The inferred value of 2.45±0.20 applies to the first meter of the nucleus (see Chapter 3, Section 2.7). This result can be compared to investigations of the electrical properties of the nucleus with radars (Kamoun et al. 2014; Kofman et al. 2015) and to laboratory measurements on putative cometary analogs (Heggy et al. 2012). It thus can bring new constraints on the porosity and composition of subsurface of the 67P/C-G nucleus and on their variations with depth.

Based on observations with the radar system of the Arecibo Observatory (2.38 GHz) during a close encounter of the comet with the Earth, Kamoun et al. (2014) constrain the dielectric constant of the top ~2.5m of the subsurface of 67P/C-G to be in the range 1.9−2.1 at that frequency. We emphasize that this value is an average for the whole surface of the nucleus. More recently, using the propagation time of the CONSERT signals in the upper part of the smaller lobe of 67P/C-G, Wlodek Kofman et al. (2015) find that the average dielectric constant of the interior is very small, namely 1.27, at the CONSERT operation frequency of 90 MHz.

Assuming that the surface material consists of a ternary mixture composed of a dust phase, an ice phase, and vacuum, and using a mixing law, the Arecibo, CONSERT, and SESAME-PP inferred dielectric constant can be used to invert the volumetric fraction of each of these phases at their respective sounding depths. Using the Hashin-Shtrikman bounds (see Chapter 1 Section 3) derived from Maxwell Garnett mixing formula, Wlodek Kofman et al. (2015) thus estimate that their result is consistent with a volumetric dust/ice ratio of 0.4 to 2.6 and a porosity of 75 to 85% (even higher for ordinary chondrites), while Kamoun et al. (2014) constrain the porosity of the first meters to be ~ 70%. We follow strictly the same approach as in Kofman et al. (2015) for the inversion of the SESAME-PP derived dielectric constant.

For their analysis, Wlodek Kofman et al. (2015) consider that the dust phase must be chondritic in nature. In absence of information on the dielectric constant of carbonaceous and ordinary chrondrites at the low frequencies of SESAME-PP, we use the same values as in Wlodek Kofman et al. (2015), namely values in the range 2.6−2.9 for carbonaceous chondrites and 4.8–5.6 for ordinary chrondrites as measured by Heggy et al. (2012) on meteoritic samples. To support this assumption,

we note that geological materials at very low temperature (the temperature at Abydos during SESAME-PP measurements ranges between −165°C and −130°C; see Table 13) have relatively little variation in the real part of the permittivity with frequency. In practice, we only use the upper bounds of these ranges (2.9 for carbonaceous chondrites and 5.6 for ordinary chrondrites) since SESAME-PP observations provide a constraint only on the lower bound of the dielectric constant. We further note that the dielectric constant of chrondrites was measured for pellets with a porosity of 30% so that the dust volumetric fraction contains 30% of vacuum, which has to be taken into account. Regarding the ice phase, we use the highest value assumed by (Kofman et al. 2015), namely 3.1, which corresponds to 100% water ice. We emphasize that there is no approximation in using this value at low frequencies since, as previously mentioned in Chapter 1, Section 3.1.2, the dielectric constant of water ice at cryogenic temperatures loses its frequency dependence.

The constraints, in terms of dust-to-ice ratio and porosity, derived from SESAME-PP are presented on the ternary diagram in Figure 101 (blue domain) next to CONSERT results (red domain). We note that SESAME-PP-derived constraints apply to the first meter of the near surface, while CONSERT-derived constraints apply to hundreds of meters below the surface.

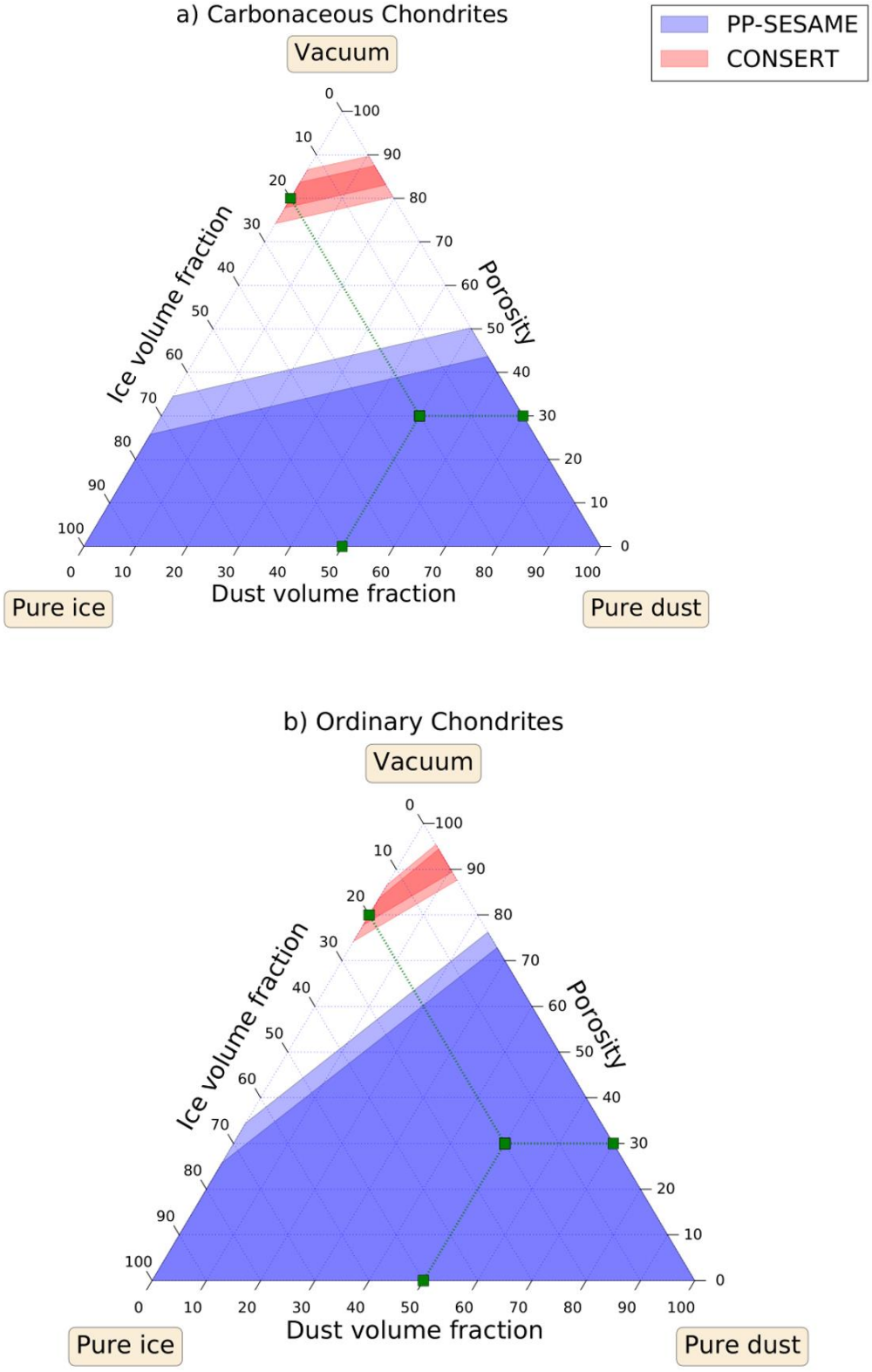

Figure 101: Ternary diagram of dust, ice, and porosity volumetric fraction as derived from SESAME-PP (blue domain) and CONSERT (red domain) observations for carbonaceous (a) and ordinary (b) chondrites. The results from SESAME-PP are representative of the composition and porosity of the first meter of the 67P/C-G nucleus, while the results from CONSERT is an average for the first hundreds of meters of the interior of the small lobe of the comet. To help read this diagram, an example is shown (green squares) on the figure, corresponding to 30% porosity, 50% dust, and 20% ice. The region with a lighter blue or red colour show the error on the inferred dielectric constants.

The SESAME-PP results suggest that the first meter of the nucleus is more compacted with a porosity below 50% for carbonaceous chondrites and below 75% in the case of less primitive ordinary chondrites, than its interior as sensed by CONSERT. Though less constrained, a comparison between SESAME-PP and Arecibo results further suggests that there may also be a gradient in porosity in the first meters of the cometary mantle.

The presence of a relatively resistant "shell" is supported by observations from the MUPUS instrument package that reveal that both the thermal inertia and surface strength at Abydos are larger than expected (Spohn et al. 2015). As mentioned before (Section 4.4.1), the MUPUS-PEN thermal probe could barely penetrate the near surface, pointing to a local resistance of at least 2 MPa, and the thermal inertia was found to be 85 ± 35 Jm -2 K -1 s -1/2, which is consistent with a near-surface porosity in the range 30−65% and most likely in the range 40−55%. At a larger scale (>10m), the idea of enhanced compaction near the surface (consequent to an increasing porosity with depth) is supported by the CONSERT data acquired at grazing angles that are consistent with a decreasing dielectric constant with depth (Ciarletti et al. 2015), although this latter result could also be attributed to a decreasing dust-to-ice ratio. SESAME-PP observations place no constraint on the dust-to-ice ratio in the first meter below the surface.

However, the dust abundance relative to ice is most likely much larger near the surface than deeper. Most geological models (Belton et al. 2007) even predict a desiccated outer dust layer, possibly few meters thick, as a by-product of ice sublimation. If proven to be true, this would imply that the first meter of the subsurface consists of 55% of dust and 45% of porosity in the case of carbonaceous chondrites and 25% of dust and 75% of porosity in the case of ordinary chondrites (see Figure 101).

On the other hand, MUPUS results suggest that the desiccated dust layer is thin at Abydos and, together with the SESAME-PP finding of an enhanced compaction of the near surface of the comet, suggest that some cementing processes are at play. These processes most likely involve ice that may sinter at each perihelion and refreeze as soon as the comet is receding from the Sun. The landing site of Philae was poorly illuminated in November 2014 and frozen ice was probably still present in the upper layers of the surface.

As a further argument, the appearance of Abydos is consolidated as defined by (El-Maarry et al. 2015) and the network of fractures revealed by CIVA images on the walls of the cavity in which Philae settled (see Figure 100), which are also seen at a larger scale by the OSIRIS Rosetta camera, is often an indication of the contraction of ice below the surface (El-Maarry et al. 2015). In addition, CIVA

images show variations in the surface reflectance at cm down to mm scale; the brighter spots in the observed granular grains could be ice-rich (Bibring et al. 2015).

6. Concluding remarks

In this chapter I described the global context of the Rosetta mission, from its launch to its end on the surface of the comet this September. We then gave a brief summary of the major discoveries that were made on the coma and nucleus of the 67P/C-G comet, this was done in order to put in context the measurements and interpretations of the SESAME-PP instrument on the surface of the comet. We then proceeded to describe in detail all the measurements that were acquired by SESAME-PP during the cruise, the descent towards the nucleus and on the surface. We presented the problems encountered, most notably the saturation of the receiving channels during descent that prevented us from acquiring calibration measurements. The acrobatic landing of Philae also presented us with a challenge as the derivation of the dielectric constant depends on our knowledge of the attitude of the lander and its close environment. We then proceeded with the description of the 3D model of the lander attitude in its environment I built using most of the available constraints. This model allowed us to derive a lower bound for the value of the dielectric constant, and compare the result to other instruments findings, in particular that of the bistatic radar CONSERT. We conclude that there is a dielectric constant gradient in the subsurface of the comet, this gradient is probably linked to a porosity gradient, the comet having a solid outer crust and a very porous interior. These analysis and results have been published published in June 2016 in Astronomy and Astrophysics (Lethuillier et al. 2016).

Chapter 5: The PWA-MIP/HASI/Huygens instrument, revisiting the data collected on the surface of Titan

On January 14, 2005, the Huygens probe (Lebreton & Matson 2002), a module of the Cassini/Huygens mission (NASA/ESA/ASI), landed on the surface of Titan, Saturn's biggest moon (Lebreton et al. 2005). Huygens fortunately landed on a solid surface "whose properties are analogous to wet clay, lightly packed snow and wet or dry sand" (Zarnecki et al. 2005). Among the instrument on board the probe, there was a mutual impedance probe called PWA-MIP/HASI (Permittivity Wave Altimetry-Mutual Impedance Probe/Huygens Atmospheric Structure Instrument) designed to measure the electrical properties of Titan's atmosphere and of surface. This chapter presents the re-analysis of the surface data acquired by PWA-MIP/HASI.

From the PWA-MIP/HASI data acquired at the Huygens landing side, a first very preliminary estimate of the ground dielectric constant (~2) was published in (Fulchignoni et al. 2005). Grard et al. (2016) later constrained the dielectric constant in the range 2-3 and provided a rough estimate of the conductivity of ~0.4 nS/m. In this chapter, we describe the work done to pursue and refine the analysis of this data set, accounting, in particular, for new insights on the final resting position of the Huygens capsule. Grard et al. (2016) also reported a sudden change in the PWA-HASI-MIP measurements, recorded about 11 min after the Huygens landing, probably related to a variation of electrical properties of the surface but no detailed scenario was brought forward.

After a brief description of the scientific context (section 2), we describe the PWA-MIP/HASI descent and surface observations (section 4), and the numerical models that have been developed for their analysis (section 3). More reliable estimates of both the dielectric constant and the electrical conductivity are derived (section 5). In section 6, these findings are compared to laboratory measurements of the electrical properties of tholins that are potential analogs of the organic materials that cover most of Titan's surface. The laboratory measurements have been performed at LATMOS, at PWA-MIP/HASI frequencies of operation and over a wide range of temperatures, covering that of Titan's surface (i.e., -180°C). This work enables us to constrain the composition of Titan's first meters at the Huygens landing site and to advance an explanation for the sudden change of permittivity recorded ~11 min after the landing. Parts of these results have been published in: "The electrical properties of Titan's surface at the Huygens landing site measured with the PWA-HASI Mutual Impedance Probe. New approach and new findings", Hamelin et al., Icarus, vol. 270, 2016.

1. The Cassini/Huygens mission and Titan

1.1. The Cassini/Huygens mission in brief

The Cassini spacecraft, launched on the 15th of October 1997, is a NASA/ESA/ASI joint endeavor composed of an orbiter (Cassini, NASA) and a surface probe (Huygens, ESA). It was designed to explore the environment of the Saturn system, its atmosphere, its rings and its moons, in particular, the biggest one: Titan.

The mission scientific objectives include:

- Characterize the atmosphere of Saturn (composition, density temperature) and its motions (waves, eddies and storms)
- Monitor its diurnal and seasonal variations,
- Study the plasma and magnetic environment of Saturn,
- Characterize the composition and size of the materials constituting the rings,
- Study the dynamic processes responsible for their structure,
- Study the relationship between the moons and rings,
- Map and study the geology and composition of Saturn's moons, in particular, Titan.

After a journey of 7 years, the Cassini spacecraft reached Saturn in July 2004 and has been orbiting the giant planet since then. The Huygens probe was separated from the Cassini spacecraft on December 25, 2004 and landed on Titan less than one month later, on January 14, 2005. After a 2.5 h of descent through its atmosphere, the probe reached the surface that turned out to be solid. Data were collected during more than 1 hour until the Cassini spacecraft disappeared behind the horizon. After 2 extensions (2008-2010 for the Equinox Extended Mission and 2010-2017 for the Solstice Extended Mission), the Cassini mission will end in September 2017 with a plunge into Saturn's atmosphere. By then, the orbiter will have flown by Titan 127 times.

1.2. Titan after Cassini-Huygens

Titan was discovered on the 25th of March 1655 by Christian Huygens; it was later given its name by John Herschel. In 1908 Josep Comas i Solà observed a limb darkening on Titan, it was attributed to the presence of an atmosphere which was later confirmed by Gerard Kuiper who also detected the presence of methane by spectroscopic analysis (Kuiper 1944).

Table 14: Main physical characteristics of Titan

Orbital period	15.95 days
Mean radius	2575.5 Km

Mass	1.345 x 10^{23} kg
Mean density	1.8798 g/cm^3
Gravity	1.354 m/s^2

Titan is Saturn's largest moon and the second largest satellite in the Solar System after Ganymede, its main characteristics are summarized in Table 14. It is also the only satellite to possess a dense atmosphere. The composition of this atmosphere is dominated by nitrogen (95%) with a few percent of methane (2% in the upper atmosphere) and hosts an intense photochemistry responsible for the synthesis of solid organic aerosols (Niemann et al. 2005). These organic hazes are optically thick and are the reason why Titan's surface remained mysterious before the arrival of the Cassini spacecraft. It was, however, speculated that this surface could be at least partially covered by organic aerosols falling from the atmosphere and that liquid hydrocarbons (methane, ethane) could flow on it. More than ten years after Cassini arrival at Saturn**,** the scientific context has significantly evolved. On board the Cassini orbiter, a RADAR was specially designed to observe (in the microwave domain) the surface of Titan though the veil of its opaque atmosphere (Elachi et al. 2005). The Cassini VIMS (Visual and Infrared Mapping Spectrometer, Capaccioni et al. 1998) and ISS (Imaging Science Sub-system, Porco et al. 2004) are also able to map the surface through 7 narrow atmospheric windows in the near IR. These instruments have revealed the wealth of Titan's geology: hydrocarbon lakes and seas in high latitude regions, dune fields in the equatorial belt, mountains, channel networks (Stofan et al. 2007; Jaumann et al. 2008; Lopes et al. 2010; Radebaugh et al. 2011; Le Gall et al. 2016). In the atmosphere and at the surface, there is evidence for a carbon cycle on Titan, similar to the water cycle on Earth (Choukroun & Sotin 2012). There is also hints of a subsurface ocean (Baland et al. 2011) and cryovolcanism (Lopes et al. 2007).

Furthermore, the in-situ measurements performed at the Huygens landing site, although they cannot be regarded as representative of the entire surface, provided an invaluable ground truth for Cassini remote measurements. Because it is useful for the PWA-MIP/HASI data analysis in section 6, we recall that the main instrument sensors on board the Huygens probe were (Figure 102): i) the HASI sensors on two deployable booms system and on the stub, ii) the Gas Chromatograph and Mass Spectrometer (GCMS), iii) the Aerosol Collector and Pyroliser (ACP), iv) the Surface Science Package (SSP), v) the Descent Imager/Spectral Radiometer (DISR), vi) the accelerometer located close to the probe center of mass. The detailed description of these instruments can be found in Lebreton & Matson (2002).

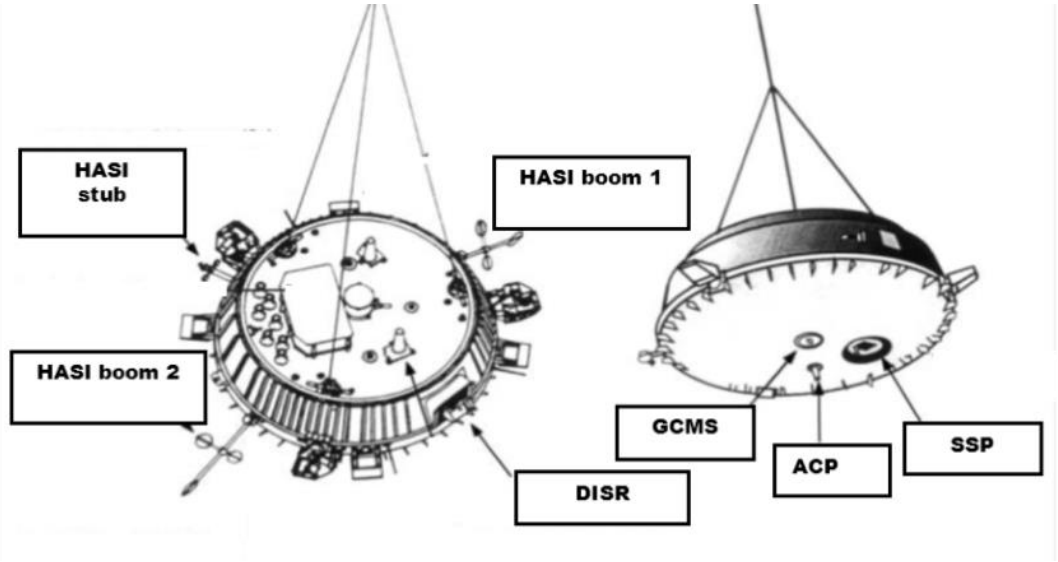

Figure 102: Locations of the main payload sensors and PWA booms (Lebreton & Matson 2002).

The probe landed at a latitude of 10.3° S and a longitude of 167.6° E (Karkoschka et al. 2007). The temperature and pressure measured at the surface by HASI were 93.65±0.25 K and 1471±1 hPa (Fulchignoni et al. 2005). In such conditions, both methane and ethane can exist in their three forms (solid, liquid and gas). As shown on the photo taken by DISR (Figure 103b), the landing site appears to be relatively flat and strewn with 2-20-cm sized, likely water ice mixed with organics cobbles lying on a dry river bed (Tomasko et al. 2005). The presence of at least some liquid hydrocarbons in the close subsurface was indicated unambiguously by the detection of CH_4 and C_2H_6 by the GCMS during its operation on the ground, where its heated inlet caused the release of hydrocarbons on board Huygens (Niemann et al. 2005; Niemann et al. 2010). Additional evidence of dampness was provided by the temperature evolution of the inlet (Lorenz et al. 2006), the possible formation of a dewdrop on the camera baffle (Karkoschka & Tomasko 2009), and the suppression of ultrasound propagation in a SSP instrument, probably by the evolution of absorbing vapors (Lorenz et al. 2014). SSP was mostly dedicated to the physical characteristics of the surface, either solid or liquid (Zarnecki et al. 2002; Zarnecki et al. 2005; Leese et al. 2012): close remote sensing of the surface was performed by the active SSP Acoustic Properties sensor (API-S) that detected specular properties compatible with a wet and smooth surface (Towner et al. 2006) as well as by the HASI Radar Altimeter Extension (RAE) which is part of the Permittivity, Waves and Altimetry (PWA) instrument (Fulchignoni et al. 2002; Fulchignoni et al. 2005).

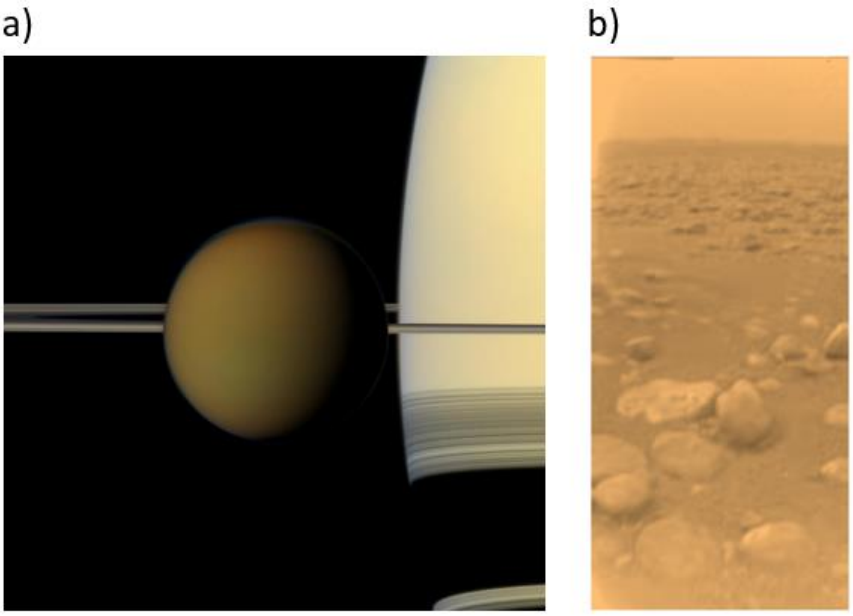

Figure 103: a) Image of Titan in front of Saturn in true colors Credits: JPL/NASA. b) Image of Titan's surface taken by the Huygens probe on 14/01/2015. Credits: ESA/NASA/JPL/University of Arizona

2. The PWA-MIP/HASI instrument

2.1. Description

The PWA analyzer (Grard et al. 1995) is a unit of the HASI instrument (Fulchignoni et al. 2002) designed for investigating the electric properties and other related physical characteristics of the atmosphere of Titan, from an altitude of around 140 km down to the surface. It includes: i) two Relaxation Probes (Rp1 and Rp2 in Figure 104) initially set at a DC potential with respect to the lander structure and then allowed to return to their equilibrium potential due to the collection of charged particles from the environment and, ii) a Mutual Impedance Probe (PWA-MIP/HASI) that measures the voltage difference (ΔV) between two receiving electrodes, Rx1 and Rx2, induced by the current flowing between two transmitting electrodes, Tx1 and Tx2. The four electrodes of the MIP and the two electrodes of the RP were installed on the deployable booms of the lander (Figure 104).

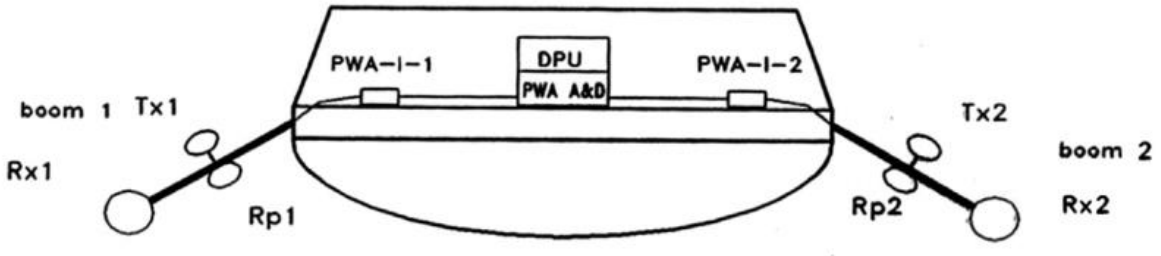

Figure 104: Schematic representation of the HASI-PWA-MIP and HASI-PWA-RP instruments with the electrodes indicated

In a similar way to SESAME-PP/Philae, the PWA-MIP/HASI instrument can be operated in two modes: a passive mode dedicated to study electrostatic natural waves, and an active mode designed to determine the complex permittivity of the atmosphere and surface of Titan. The instrument was designed to operate at a frequency of 45 Hz in the atmosphere and at four additional frequencies on the ground, namely 90 Hz, 360 Hz, 1440 Hz and 5760 Hz.

2.1.1. Transmitting circuit

The transmitting electrodes of PWA-MIP/HASI are 65 mm diameter rings (Figure 105) which have a capacitance of 1.85 pF in vacuum. An active measurement consists in applying a sinusoidal voltage of known amplitude to the Tx_1 and Tx_2 electrodes through small coupling capacitances of 0.43 pF ± 20% (Trautner & Falkner 2000). Contrary to the SESAME-PP instrument, the current injected into the environment is not measured and recorded. The consequence is that the current has to be assumed constant. This assumption, however, is supported by the location of the transmitting electrodes on the boom: they are high enough with respect to the surface plane so that the influence of this latter is minimal (see chapter 2 section 4.1). This is also supported by the electronic design that minimize the influence of the environment on the electrodes (Hamelin et al. 2007).

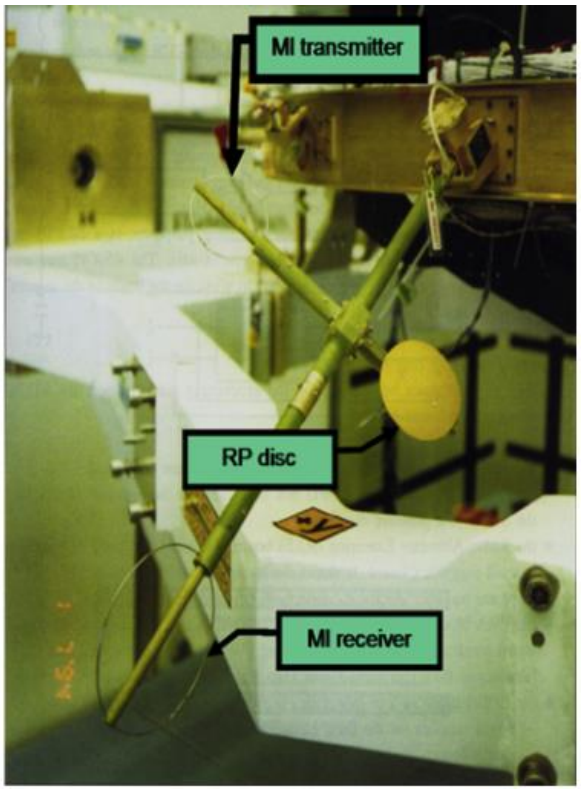

Figure 105: Photo of one of the Huygens booms. The MIP and RP electrodes are indicated.

2.1.2. Receiving circuit

The receiving electrodes of PWA-MIP/HASI consist of two 100 mm diameter rings (Figure 105) which both have a capacitance of 2.64 pF in vacuum. The receiving circuits are connected to the preamplifiers located inside the Huygens body and therefore are at a temperature higher and better known than that of the electrodes mounted outside.

2.2. Numerical geometry model

As done for the analysis of the SESAME-PP data (Chapter 3, section 2.1), a geometrical model of PWA-MIP/HASI was built using the COMSOL Multiphysics™ software. This model takes into account 7 conductors (against 19 for the SESAME-PP model), namely the 4 electrodes of PWA-MIP (Tx1, Tx2, Rx1, Rx2), the relaxation probes Rp1 and Rp2, and the Huygens capsule.

A first finite element model to solve the Laplace equations was built by Cadène (1995) to estimate the influence of the body on the passive and active measurements. A first analysis of the electronic circuit was also performed to estimate the performances of the instrument. Later, another model was built to provide a first interpretation of the data collected during descent and on the surface (Grard et al. 2006). In 2007 the data collected during the descent was reanalyzed with the CIMM using concurrent determinations of the capacity- influence matrix: finite element methods and charge methods (Hamelin et al.2007) The main perturbating effect on the measurements was found to be a velocity effect which was finally taken into account. First attempts to model the electric coupling between MIP electrodes on Huygens and the ground were done by Fernando Simões (Grard et al. 2006; Simões et al 2007). This study demonstrated that the current measurement was not necessary.

For a more in depth study, we built a more geometrically accurate model with both a better representation of the electrodes (not approximated by spheres) and a better representation of possible positions of the lander at the surface of Titan (with the possibility of electrodes penetrating the surface, see Section 4.2).

In this model, the thin disk- and ring- electrodes (respectively, RP and MIP electrodes) are approximated by geometrical elements (spheres or cylinders) of same capacitance and, for the sake of simplicity, the Huygens capsule is represented by a body with a cylindrical symmetry. All the model parameters are reported in Table 15.

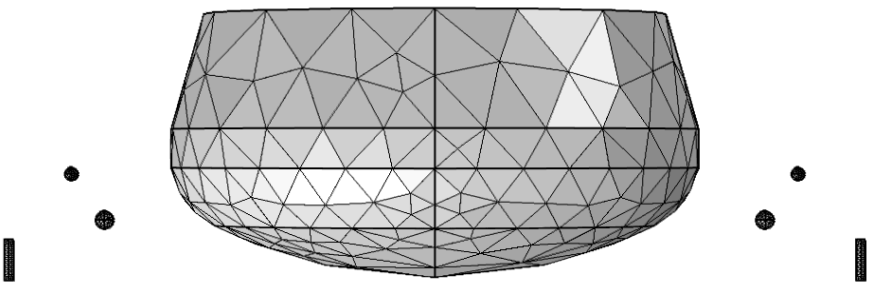

Figure 106: Meshed model of the Huygens lander and the PWA-MIP/HASI electrodes

Later (in Section 4.2), a ground with a given complex permittivity is added to this model in order to compute the medium capacitance-influence matrix $[\boldsymbol{K_m}]$ (see Chapter 2, Section 3.2) and apply the CIMM.

Table 15: Geometrical model of the Huygens probe and the PWA-MIP/HASI electrodes

Name	**Geometry**	**Dimensions**	**Capacitance (pF)**	**Model geometry**	**Coordinates (m)**		
					x	Y	z
Huygens body	See Figure 104	1.3 x 0.7 m	62.83	Simplified	Origin of the referential: Bottom of the probe		
Tx_1	Ring 1.2 mm	65 mm	1.85	Sphere r = 16.6 mm	0.252	-0.885	-0.070
Tx_2	Ring 1.2 mm	65 mm	1.85	Sphere r = 16.6 mm	0.252	0.885	-0.070
Rx_1	Ring 1.2 mm	100 mm	2.64	Cylinder h = 100 mm r = 11.4 mm	0.042	-1.043	0
Rx_2	Ring 1.2 mm	100 mm	2.64	Cylinder h = 100 mm r = 11.4 mm	0.042	1.043	0
Rp_1	Disk	70 mm	2.50	Sphere r = 22.8 mm	0.139	-0.811	0.04
Rp_2	Disk	70 mm	2.50	Sphere r = 22.8 mm	0.139	0.811	0.04

2.3. Electronic model

In order to apply the CIMM, the electronic matric $[\boldsymbol{K_e}]$ must also be determined. The transmitter circuit applies a 10 V voltage to the transmitting electrodes through a low-pass filter and a coupling capacitor (C_T = 0.425 pF). The transmitting electrodes are also connected to the reference ground (i.e., the Huygens body) by a coupling capacitor (C_S = 0.3 pF). These values are known with a 20 % accuracy. We note that the calibrations were performed at room temperature; the capacitances

located outside the Huygens body are thus probably smaller than estimated, due to temperature shrinking.

The receiving electrodes are connected to a preamplifier located inside the Huygens body by a coupling capacitor located inside the boom. The electronic characteristics were estimated based on nominal component values or derived from calibration measurements.

Lastly, the relaxation probe electrodes are considered to be floating conductors and only Rp_2 is connected to the Huygens body by a capacitor C_{RP} = 352 pF.

A more in depth discussion on the electronics characterization is out of the scope of this work but can be found in Trautner & Falkner (2000); Jernej & Falkner (2004); Hamelin et al. (2007); Hamelin et al. (2016). The derivation method of the 45 Hz electronic matrix $[\boldsymbol{K_e}]$ can be found in Hamelin et al. (2007).

2.4. Sounding depth

The PWA-MIP/HASI instrument has only one geometrical configuration. Additionally, the current is not measured. This implies that the instrument is only able to probe a single depth. In order to assess this sounding depth, we followed the same approach as for SESAME-PP (Chapter 3, Section 3) using numerical models with the Capacitance-Influence Matrix Method.

We first consider that the lander with the PWA-MIP/HASI instrument lies on a surface with a dielectric constant of 2.50 and an imaginary part of the complex relative permittivity of 0.5 (a value close to the inferred value of the subsurface of Titan, see section 4.3). We then record the potential difference measured between the receiving electrodes (the current is considered to be constant) while a perfect reflector is progressively moved up to the surface: we consider that the sounding depth corresponds to the distance at which the reflector significantly influences the measurements (i.e., when the difference between the potential difference with and without reflector exceeds the error on the potential difference measurement, namely 2%).

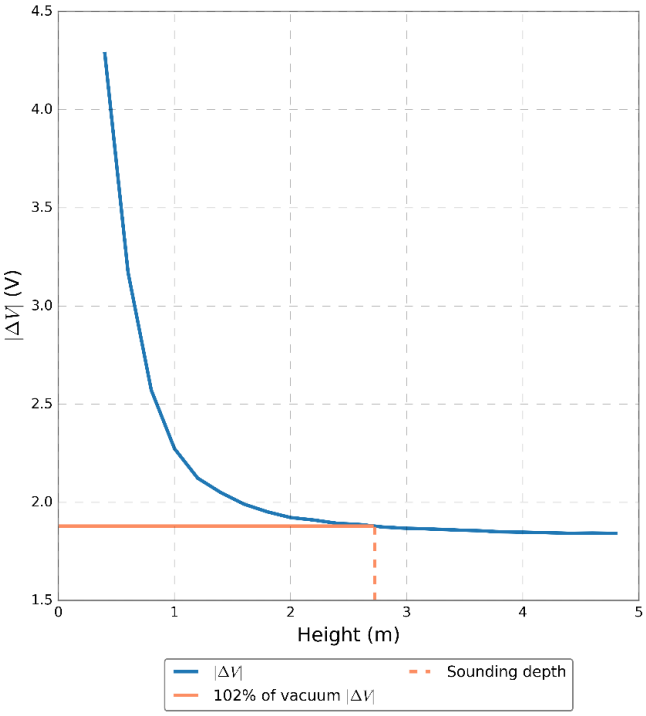

Figure 107: Simulated potential difference measured by the PWA-MIP/HASI instrument as a function of the distance to a perfect electrical reflector buried in a subsurface of dielectric constant 2.5 and permittivity imaginary part 0.5. The orange line indicates the depth at which the perfect electrical reflector affects the measured potential difference by 2%. This depth is a good proxy for the sounding depth of the instrument.

As shown on Figure 107, the PWA-MIP/HASI sounding depth is about 2.7 m; it is larger than the sounding depth of the SESAME-PP instrument in its 3-foot configuration (see chapter 3 section 3) due in part to the better accuracy of the instrument (made possible because the current is constant)

3. Data collected during descent and on the surface

On January 14, 2005, PWA-MIP/HASI collected data both during the descent of the Huygens probe and on the surface of Titan. During the descent, PWA-MIP and PWA-RP measurements led to the discovery of electron and ion density layers in the lower atmosphere (Fulchignoni et al. 2005; Grard et al. 2006; Simões et al. 2007; Hamelin et al. 2007; López-Moreno et al. 2008) and revealed the existence of an atypical Schumann resonance that implies the presence of a subsurface water ocean (Béghin et al. 2010). Following the successful landing of Huygens, the operation of PWA was extended for approximately 32 min measuring the electrical properties of the ground until the end of the HASI measurement cycle, recording also the weak 36 Hz signal of the Schumann resonance (Béghin 2014), while the data link to the orbiter lasted for 40 min more (Pérez-Ayúcar et al. 2006).

The PWA-MIP/HASI data consist in successive measurements of the voltage difference ΔV between the two receiving electrodes Rx1 and Rx2. The signals from each electrode are fed into a differential amplifier before being processed by an Analog to Digital Converter (ADC). The numerical

waveforms are analyzed by a digital signal processor (DSP) which provides, through the telemetry, the complex voltage (real and imaginary parts) at ADC level.

3.1. Descent measurements

The PWA-MIP/HASI measurements performed during the Huygens descent, just before the landing in a neutral atmosphere (i.e., close to vacuum), can be used as a reference both to estimate the atmosphere conductivity at higher altitudes (Hamelin et al. 2007) and to calibrate surface data.

These reference measurements are shown by green lines in Figure 108. In this vacuum-like environment, an average potential difference of $\Delta V_{vac} = 1.842$ V was measured consistent with measurements recorded at an altitude of 99.7 ± 1.3 km where PWA-RP/HASI registered a plateau indicative of the absence of free electrons (López-Moreno et al. 2008). Unfortunately, these "vacuum measurements" were performed only at 45 Hz so that a correction has to be performed for higher frequencies (Section 4.1).

3.2. Surface measurements

On the surface, PWA-MIP/HASI measurements were acquired every 2 seconds during 32 min at 5 frequencies, namely 45 Hz, 90 Hz, 360 Hz, 1440 Hz and 5760 Hz (see Figure 108). Interestingly, at all frequencies except 5760 Hz, a sharp discontinuity was recorded about 11 min after landing. This discontinuity is hypothesized to be due to a sudden change in the subsurface material composition as further developed in section 7.

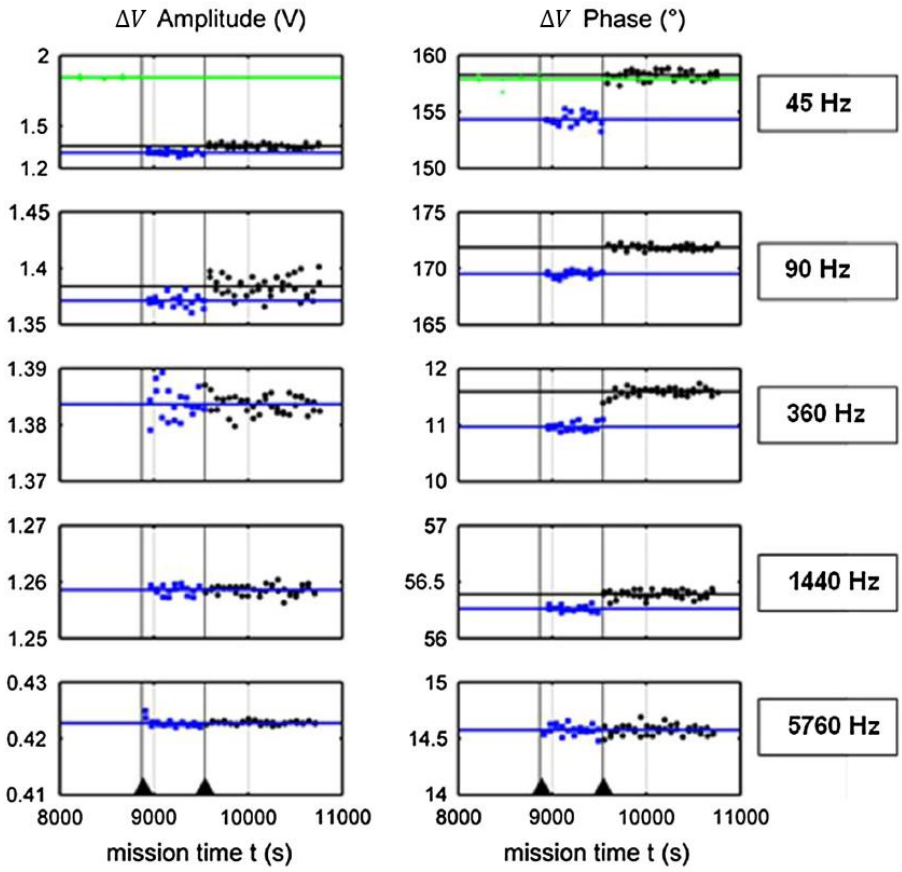

Figure 108: PWA-MIP/HASI measured $\mathbf{\Delta V}$ vs. mission time: (a) Amplitude (left) and phase (right) of $\mathbf{\Delta V}$ for the 5 operation frequencies 45, 90, 360, 1440, and 5760 Hz (from top to bottom). The green dots in the upper panels are the last measurements at 45 Hz before touch-down (indicated by a black vertical line at t = 8870 s). The average amplitude and phase (green lines) serve as references for the calibration of the surface data. The discontinuity at 9539 s mission time is also indicated. Horizontal lines show the mean values of amplitude of phase, before (blue) and after (black) that time. (b) Zoom on the landing event. The PWA-MIP/HASI instrument performed two consecutive measurements (separated by 2 seconds) every 192 s for the atmospheric mode (only at 45 Hz) and every 64 s for the surface mode (at all frequencies).

4. Data calibration and analysis

In this section, we apply the CIMM (described in Chapter 2) to the PWA-MIP/HASI data collected on Titan's surface. We first proceed to some adjustment on the electronic matrix $[\boldsymbol{K_e}]$ based on vacuum calibration at 45 Hz and then determine the possible configurations of operation of PWA-MIP at the surface of Titan in order to realistically simulate the medium capacity-influence matrix $[\boldsymbol{K_m}]$. Measurements are then compared to simulations in order to infer the ground complex permittivity and reliable associated uncertainty.

4.1. Data calibration and electronic matrix

Reference measurements in a pseudo-vacuum environment that are required for calibration were only performed at 45 Hz. For that frequency, the calibration of ΔV should thus be straightforward. However, using the Capacitance-Influence Matrix combined with the numerical model described in section 2.2, we noted a small difference between the expected voltage in vacuum

and the measured one (possiblt due to a non-neutral atmosphere): the predicted amplitude is $|\Delta V_{vac}|$= 1.790 V instead of 1.842 V and the predicted phase is $\phi(\Delta V_{vac}) = -153.44°$ instead of $-158.04°$.

This difference is most likely due to the uncertainty on certain elements of the electronic matrix $[\boldsymbol{K_e}]$, namely the coupling capacitor linking the electronic board to the transmitting electrodes and the capacitance of the connection between the receiving electrodes and the Huygens capsule. By slightly adjusting the electronic matrix while still staying in the bounds of the error bars, it is possible to retrieve the vacuum measurements. An additional correction of 4.60° has to be applied to the phase, this difference can be explained by slight modifications of the electronics during the Cassini cruise.

At frequencies greater than 45 Hz, there is no reference measurements and the calibration of these data then relies on the analytical model of the electronic circuit (see, Hamelin et al. 2016, Table 2). Unfortunately, the use of these analytical model for 5760 Hz results in unrealistic complex permittivity values. Additionally, using these models the ratio of the voltage amplitudes measured on the Titan surface at 1440 Hz and 5760 Hz differ by about $\sim$ 3 dB which cannot be ascribed to a frequency dependence of the subsurface (most materials, like water ice, loose their frequency dependence at the low temperature of Titan's surface). This anomaly together with the unexplained phase shift at 45 Hz probably results from a drift of the amplifier characteristics, possibly due to capacitor losses induced by radiations during the Cassini cruise, other parts of the electronics could have also been affected (capacitances, cables etc…). We therefore discard the measurements performed at the two highest frequencies, namely 1440 and 5760 Hz but keep the measurements collected at 90 Hz and 360 Hz.

4.2. PWA-MIP/HASI configuration of operation at the Huygens landing site

The next step of the CIMM consists in determining the medium capacity-influence matrix $[\boldsymbol{K_m}]$ (see chapter 2 section 3.2) which requires a good knowledge of the configuration of operation of the permittivity probe and, in particular, of the position of the lander with respect to the surface.

The Huygens lander survived the landing but little is known on the final position of the PWA-MIP/HASI and on the integrity of the booms. In its nominal attitude, the Huygens capsule is standing upright on a flat surface, the transmitting electrodes remain above the interface and the lower parts of the receiving electrode rims are buried, a few mm below the surface. In reality, the surface of the ground was probably altered by the impact, and the contact area between the Huygens capsule and the ground, as well as the location of the PWA-MIP electrodes with respect to the interface, depend on the lander penetration depth and its attitude.

Grard et al. (2006) first addressed the effect of the geometry of operation on the estimation of the ground complex permittivity but with a preliminary scenario for the Huygens landing. Since then, thanks to a synergy between various Huygens experiments, such as HASI-ACC (accelerometers), DISR (image) and SSP (attitude), more reliable scenarios for the landing have been proposed (Figure 6, Schröder et al. 2012). In these scenarios, the Huygens capsule dug a 12-cm deep depression by hitting the surface. It then bounced off the depression to return to the original ground level and slid on the surface over a distance of 50 cm, perhaps wobbling before coming to a rest in a field covered with pebbles of diameter ~2-20 cm, as seen in the DISR images (Tomasko et al. 2005).

Given the inferred mechanical strength of the surface material ($K = 50$ kPa, (Bettanini et al. 2008) and $K = 34$ kPa, (Hamelin et al. 2016)), if the surface on which the Huygens Probe landed is flat, it then must have penetrated it by less than a 1 mm. However, if the Huygens Probe ended on pebbles, it must be standing slightly above the ground level. This later hypothesis is supported by parallax in the camera system and the sharpness of focus of features on the surface that suggests that the base of the probe is located 1±2 cm above ground level (Karkoschka et al. 2007). The multipath interference pattern seen in the probe radio signal further indicates that the base of the probe was 1 ± 5 cm above ground level (Pérez-Ayúcar et al. 2006).

We therefore studied (i.e., built numerical simulations) two extreme configurations (in accordance with the measurements made by Schröder et al. 2012):

- The Huygens probe is lying over pebbles with the bottom located 3 cm over the surface
- The probe penetrated a flat surface by 1 cm

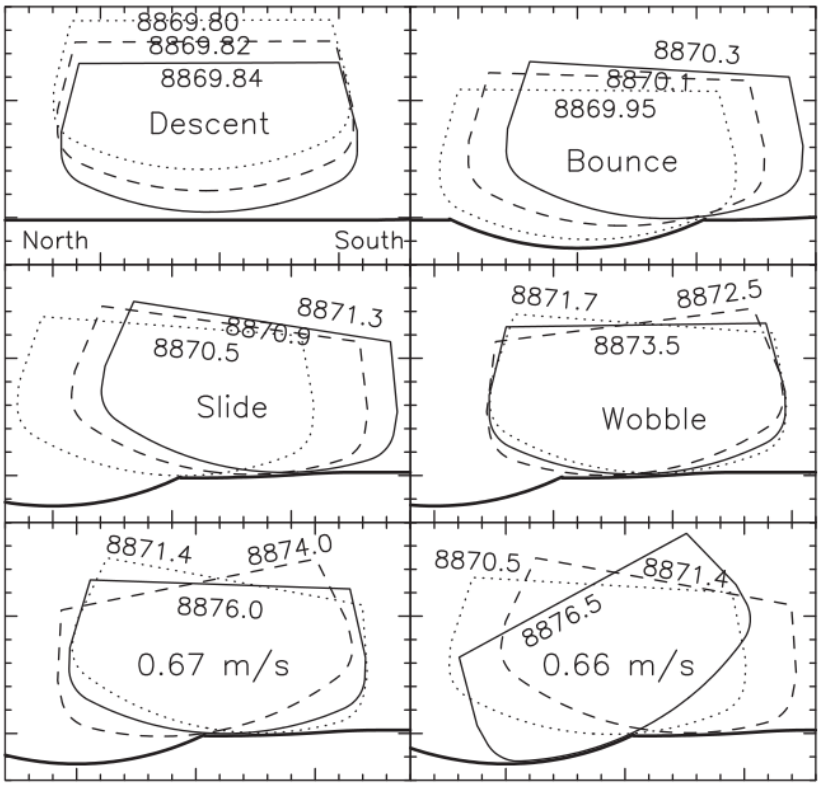

Figure 109: Possible landing scenario of the Huygens probe indicating the location of the probe for three mission times (in chronological order: dotted, dashed, and solid outlines). The two bottom panels illustrate two possible landing scenarios in the case where the impact speed was slower than 1 m/s. Small tick marks are spaced by 10 cm; large tick marks by 50 cm. This figure is from Schröder et al. 2012.

According to Schröder et al. (2012) there is also a distinct possibility that the Huygens lander could have stabilized in a tilted position. This could have a strong effect on our measurements as one of the receiving electrodes could potentially be buried while the other is not. To account for this we considered the two following extreme cases:

- Without tilt: the two receiving electrodes are parallel to the surface
- With tilt: one of the receiving electrodes is inserted into the ground and the other one is located above the ground

The 4 investigated configurations are shown in Figure 110 ; the actual positions of the Huygens lander and the PWA-MIP/HASI are probably bracketed by these extreme cases.

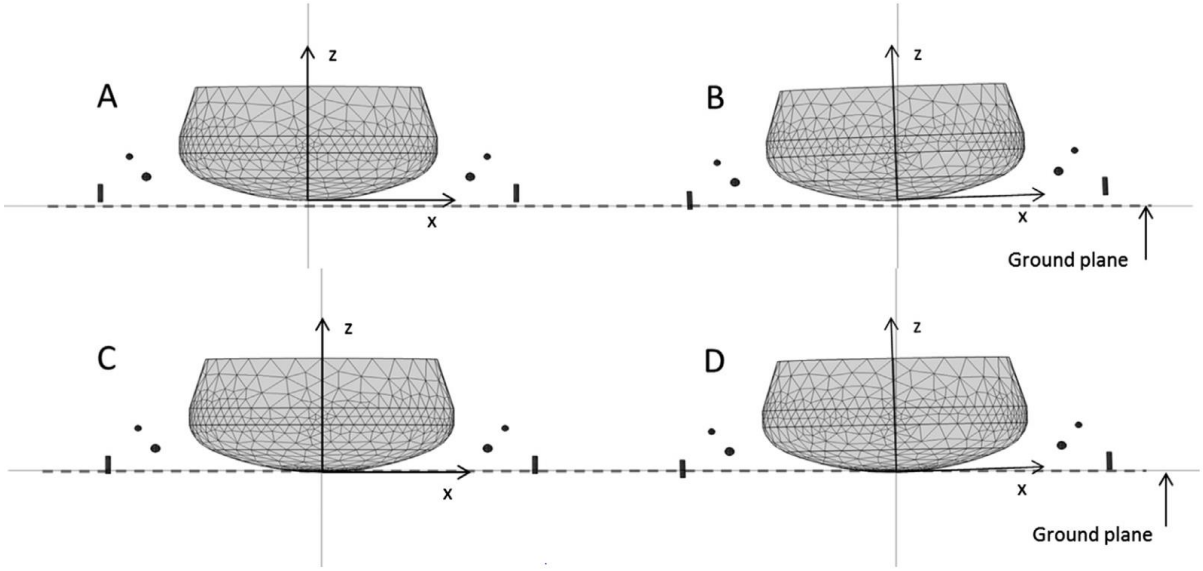

Figure 110: Four investigated model configurations: Huygens capsule on pebbles, above the ground (A and B), or slightly buried into the ground (C and D), in an upright position (A and C) or tilted, with one receiving electrode above the ground (B and D).

4.3. Derived permittivity

We applied the Capacitance-Influence Matrix Method using the model described above and varying the real and imaginary parts of the complex permittivity of Titan's surface. Hence we obtain the charts of the complex normalized voltage: $\Delta V_n = \Delta V / \Delta V_{vac}$ shown in Figure 111 and Figure 112. The measured normalized voltages were superimposed on these charts for the 4 tested geometrical configurations of operation, separating measurements acquired before (Figure 111) and after (Figure 112) $\sim$ 11 min after landing (mission time: t=9539 s) where Grard et al. (2006) reported a sudden change.

The left panels represent the grids derived from the non-tilted models (A & C in Figure 110) and the right panels represent the tilted positions (B & D). The red square is the average value of the measured complex normalized voltages ΔV_n from which we derive the average complex permittivity of the subsurface. We obtain relatively different results for the two non-tilted models ($\epsilon_r \sim 2.7 - 0.6i$ for model A and $\epsilon_r \sim 2.3 - 0.3i$ for model C) while the difference is less pronounced between the two tilted models ($\epsilon_r \sim 2.5 - 0.4i$ for model A and $\epsilon_r \sim 2.35 - 0.3i$ for model C). It thus appears that the derived complex permittivity is mainly sensitive to the height of the electrodes above the surface.

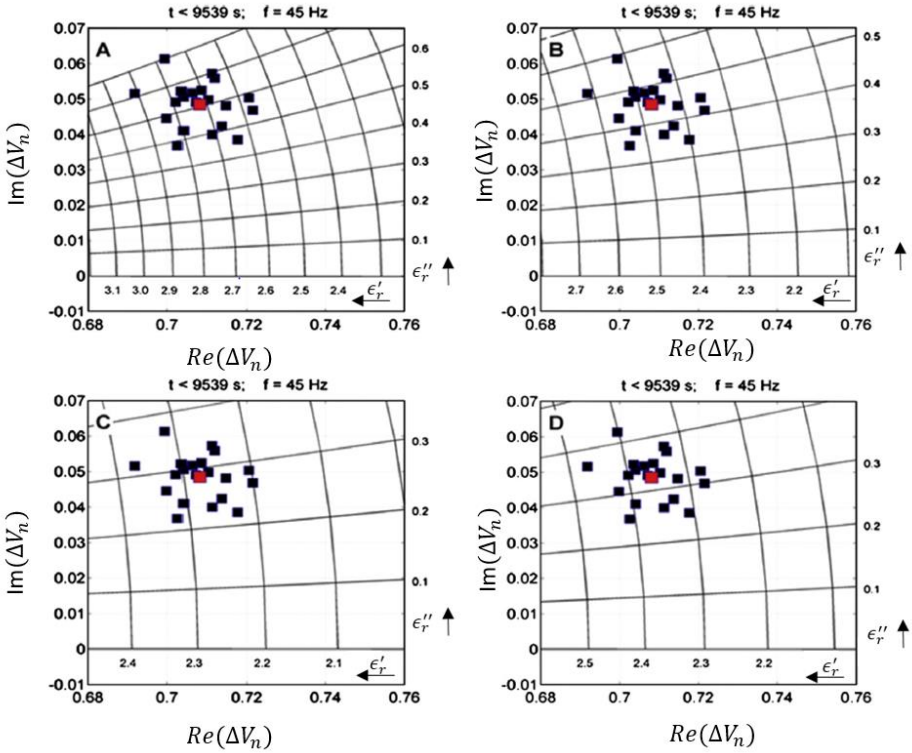

Figure 111: Analysis of the PWA-MIP/HASI data collected at 45 Hz on the surface of Titan, less than 11 min after landing. The panels show the vacuum-normalized voltages $\boldsymbol{\Delta V_n}$ in the complex plane (square dots) superimposed on 4 grids, built with the four geometries defined in section 4.2, that give access to the complex permittivity ($\boldsymbol{\epsilon_r'}$ and $\boldsymbol{\epsilon_r''}$) corresponding to each PWA-MIP measurement. The red square represents the average value of the measurements.

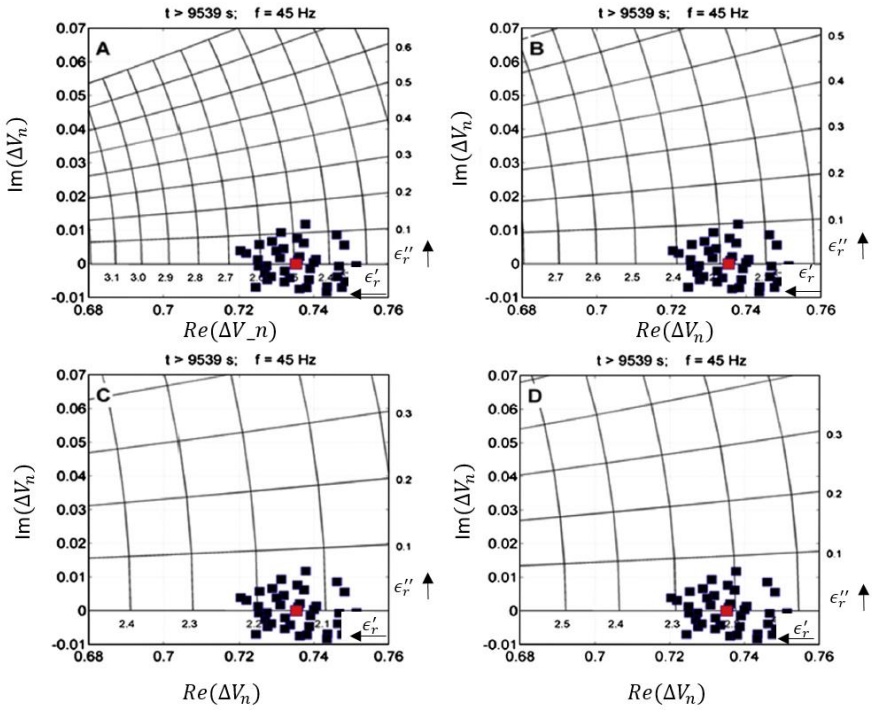

Figure 112: Analysis of the PWA-MIP/HASI data collected at 45 Hz on the surface of Titan, more than 11 min after landing. The panels show the vacuum-normalized voltages $\boldsymbol{\Delta V_n}$ in the complex plane (square dots) superimposed on 4 grids, built with the four geometries defined in section 4.2, that give access to the complex permittivity ($\boldsymbol{\epsilon_r'}$ and $\boldsymbol{\epsilon_r''}$) corresponding to each PWA-MIP measurement. The red square represents the average value of the measurements.

This approach was repeated for the frequencies 90 Hz and 360 Hz. Results are shown in Figure 113. The red triangles represent the average values inferred for ϵ_r and the red dotted circles the dispersion around these values. Each circle centered on a triangle is associated to one of the four investigated models.

We note that the results associated to models A and C bound the results from the two other models; these cases can therefore be regarded as the most extreme cases. We also note that the uncertainty related to the configuration of operation is larger than the uncertainty due to the measurement dispersion.

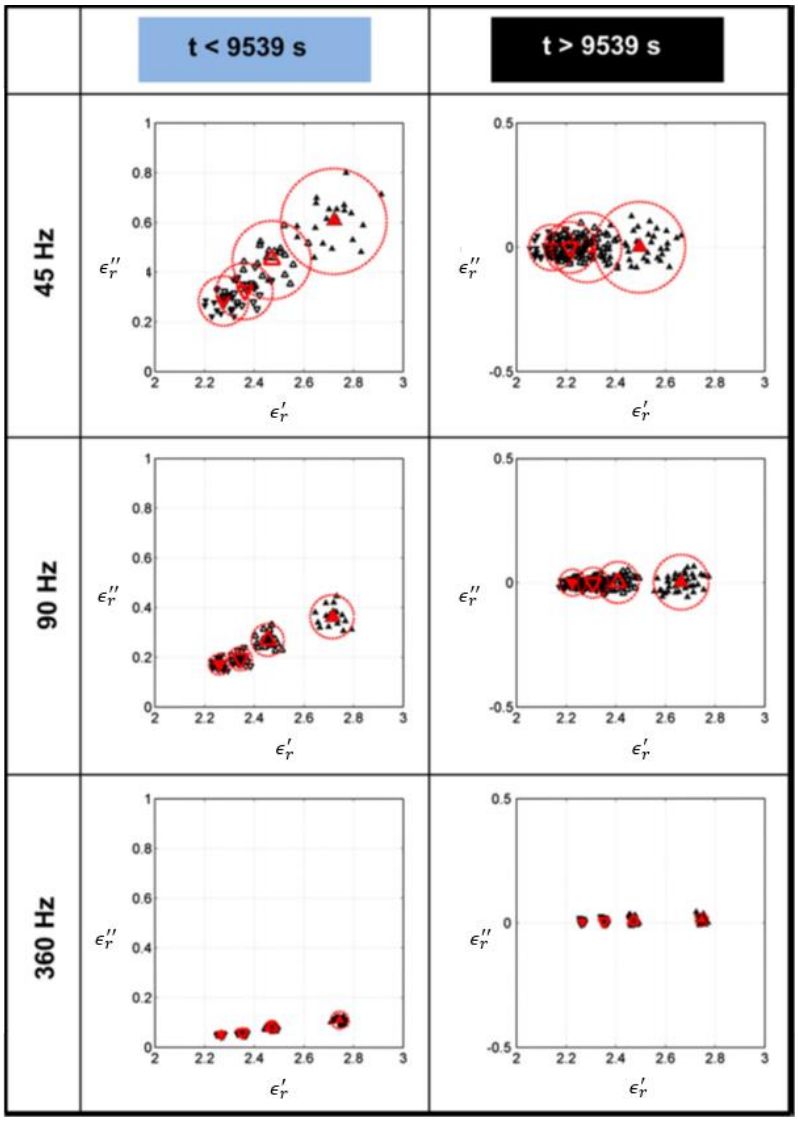

Figure 113: Summary of the relative permittivity deduced from the charts for all geometries, namely A (full upward triangles), B (empty upward triangles), C (full downward triangles) and D (empty downward triangles). The red triangles show the mean values for each geometry and the red circles indicate the experimental dispersion (2r). Left panels are for t < 9539 s and right panels are for t > 9539 s. From top to bottom: frequencies 45, 90 and 360 Hz.

The inferred values of the subsurface complex permittivity for the frequencies 45 Hz, 90 Hz and 360 Hz, before and after the 9539 s event are reported in Figure 114. The interpretation in term of composition of these results is discussed below. Meanwhile, we note a drop of both the dielectric constant (mostly at 45 Hz, negligible at other frequencies) and of the imaginary part of the permittivity (observed at all frequencies) around the mission time 9539 s. More specifically, at 45 Hz the dielectric constant drops from 2.5 ± 0.4 to 2.4 ± 0.3 and the imaginary part drops from 0.5± 0.3 to 0.0± 0.2. The drop of the dielectric constant can be explained by the measurement uncertainty but the drop of the imaginary part is significant enough to be indicative of a change in the electrical properties of the first meters of Titan's surface after the Huygens landing.

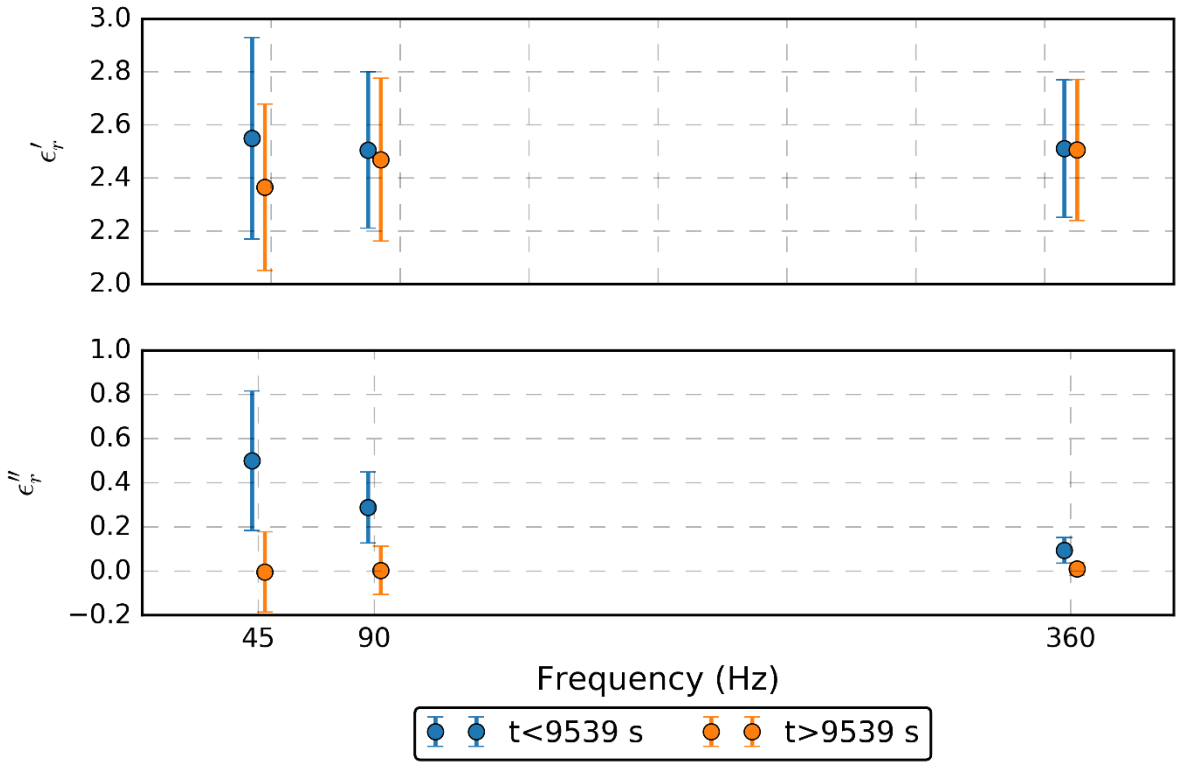

Figure 114: Summary of the results obtained at 45, 90 and 360 Hz. Upper panel: Inferred average dielectric constants and associated error bars at the 3 frequencies considering the uncertainty on the configuration of operation, before (blue lines) and after (orange lines) t = 9539 s. Lower panel: Same as above for the imaginary part of the complex subsurface permittivity.

4.4. Titan's first meter surface composition

We find that the first meters of Titan's surface at the Huygens landing site has a dielectric constant of 2.5±0.3 and an imaginary part of the complex permittivity of 0.5±0.3 at frequencies between 45-360 Hz. Though not very constraining on the composition, these values are consistent with the complex permittivity of materials expected on Titan. With PWA-MIP/HASI well calibrated measurements at the five frequencies it would have been possible to derive some Cole-Cole model

from the results but unfortunately the relatively large error bars relative to the only three validated frequencies would remove credit to such analysis.

Prior to Cassini, the composition of Titan's surface was thought to be that of its bulk crust i.e., primarily made of water ice (Tobie et al. 2005). This was supported by the detection of water ice by Griffith et al. (2003) from telescope infrared spectroscopy measurements. Water ice at 94 K has a dielectric constant of 3.15 independent of the PWA-MIP/HASI working low frequency (e.g. Mattei et al. 2014); this compound could be present in small to moderate abundance or in a porous form in the subsurface.

However, Cassini observations have shown that water ice is not the major component of Titan's surface (Clark et al. 2010; Janssen et al. 2016). Water ice is only exposed at some locations and the surface seems to be elsewhere covered by a layer of organic materials. As mentioned before, the atmosphere of Titan is the host of an intense and complex photochemistry that produces a wealth of solid organic particles (or aerosols) by photodissociation (mainly by solar UV rays) and recombination of the molecules of N_2 and CH_4 (Lorenz & Mitton 2002; Waite et al. 2007). The heaviest of these particles are eventually deposited on the surface, forming a likely thick sedimentary layer of organics (Tomasko, et al. 2005). With time, surface processes (e.g., eolian/pluvial/fluvial erosions, impacts… Lopes et al 2007, Soderblom et al 2007) erode this layer and/or mix organics with water ice. In the frame of this work, the electrical properties at PWA-MIP/HASI frequencies (10 Hz-10 kHz) of analogues of Titan's organic aerosols (also called "tholins") were investigated for the first time; the laboratory measurements conducted at LATMOS and their results are presented in section 6. At a higher frequency (14 GHz) but a low temperature (77 K), Paillou et al. (2008) measure dielectric constants in the range 2.0-2.4 depending on the degree of compaction of the tholin samples. At low frequencies (100 Hz), slightly higher values (2.85-2.95) were found for nitrile-rich organic compounds, which are also plausible candidates for Titan's surface (Le Gall et al., 2016).

Furthermore, liquid hydrocarbons (methane, ethane) are present at the surface of Titan, in the form of lakes and seas (Stofan et al., 2007) and may be trapped in the pores of the subsurface (Lorenz et al 2008). In Titan's equatorial regions such as the Huygens landing site, methane rainfalls are most likely rare (except for storms around the Equinox,(Charnay et al. 2015)) but liquid could be brought in the subsurface by fluvial action or by the circulation of an underground alkanofer. In that regards, the Huygens landing site was interpreted as a dry riverbed (Tomasko et al., 2005). At 14 GHz, Mitchell et al. (2015) measured a dielectric constant of 1.7 for liquid methane and 2.0 for liquid ethane.

The composition of Titan's surface at the Huygens landing site is further discussed in section 6 in light of new constrains on the electrical properties of analogues of Titan's tholins.

4.5. The 9539 s event

The sudden change of electrical properties at 9539 s cannot be explained solely by the uncertainty of the measurements. In about 4 s, the imaginary part of the complex permittivity of the subsurface of Titan dropped from 0.5±0.3 (corresponding a conductivity of 1.2±0.6 nS/m at 45 Hz) to zero (i.e. <0.2, corresponding to a conductivity < 0.5 nS/m at 45Hz) while no significant change in the inferred dielectric constant was recorded.

There is no indication of motion around 9539 s in the data acquired by either the SSP tilt sensor, the accelerometer or the DISR camera. The 9539 s even thus cannot be ascribed to a change in the probe position or attitude. The GCMS instrument did detect a continuous increase of the ambient atmospheric content of methane after landing, likely a consequence of outgassing of the ground heated by the Huygens probe (Niemann et al., 2010, see also Lorenz et al., 2014), but this evolution was continuous and shows no sudden change at 9539 s. The most relevant observation for the 9359 s event was obtained by the HASI temperature sensor: a 0.2 K drop of temperature was measured at exactly the same time (Figure 115). Since the HASI temperature sensors are ~1 m away from the PWA-MIP/HASI electrodes, the detected event, if correlated, must be characterized by a relatively large scale. While an abrupt change of the electrical properties of the ground volume under the Huygens Probe (a few meters deep) is excluded, a change in a superficial layer could explain these observations.

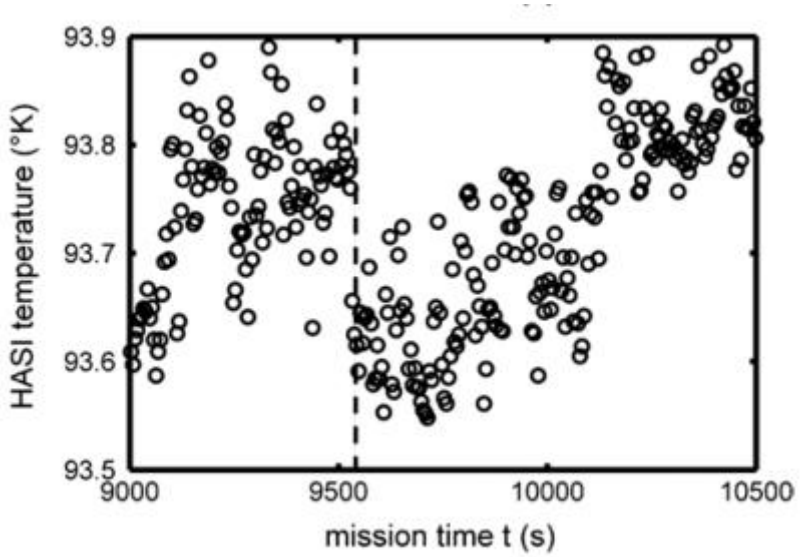

Figure 115: HASI temperature observed at around 9539 s (from Fulchignoni et al. 2005)

More specifically, a possible explanation for both PWA-MIP/HASI observations and the temperature jump is the sudden release of gas from the subsurface after the sublimation of liquid inclusions beneath the capsule. Heat from the probe could have, in 11 minutes, altered the surface

material temperature down to a depth of ~10 cm (estimate from Hamelin et al., 2016, Section 7.2.2. based on assumption on the thermal properties of Titan's surface) and triggered this outgassing.

In theory, such an event in which vacuum substitutes for liquid in the pores of the uppermost layer of the subsurface would indeed decrease both the real and imaginary parts of the subsurface complex permittivity. In absence of information on the conductivity of liquid relevant to Titan at PWA-MIP/HASI frequencies, it is difficult to estimate the degree to which the inferred conductivity would be affected. However, in the following section, we further investigate the composition of Titan's surface at the Huygens landing site assuming that it consists of a mixture of organics, water ice and pores filled of liquid (pre-event) or vacuum (post-event).

Another plausible explanation is that the evaporation of liquids could have removed a thin conductive layer located on the surface. The decrease of both the real and imaginary parts of the subsurface complex permittivity could be explained by both the removal of the thin layer and the substitution of the liquids by vacuum. The properties and composition of this layer are discussed further in Section 7.3.

5. Electrical properties of analogues of Titan's organic materials

In 2015, LATMOS obtained funding from the French Space Agency CNES (20 k€) and the program DIM-ACAV (Domaine d'Interet Majeur – Astrophysique et Condition d'Apparition de la Vie, 30 k€) of the Region d'Ile-de-France for a project called PAP (Permittivity d'Analogues Planétaires). The objective of this project was to set up, at LATMOS, a measurement bench to measure the complex permittivity of materials relevant to planetary or cometary surfaces, at low frequencies (10 Hz-10 kHz) and low temperatures (from 20°C down to -180°C). The method used was that of a capacitive cell where an alternative current produces an electric field between the electrodes. The capacitance of the capacitor formed by the two electrodes is then proportional to the dielectric constant of the material located in between the electrodes. The PAP measurement bench was set up in 2016 and used for the first time for the electrical characterization of tholins, potential analogues for Titan's organics.

5.1. Tholins

The term tholins (from the greek Θὸλος, muddy; but also Θολὸς, vault or dome) was first used by Sagan & Khare (1979) to name a "brown, sometimes sticky, residue" they produced at Cornell university by irradiating with various sources a mixture of the cosmically abundant gases CH_4, C_2H_6, NH_3, H_2O, HCHO, and H_2S. The definition was expanded to include many other components produced from different mixtures and even irradiation of ices. Tholins now defines an "abiotic complex organic solid that formed by chemistry from energy input into simple, cosmically relevant gases or solids" and

has been hypothesized to be present in many bodies of the Solar System, for example on Pluto (Grundy et al. 2016), Charon (Grundy et al. 2016), comets (McDonald et al. 1996), Triton (Khare et al. 1994) and Titan.

As photons are the main source of energy in Titan's atmosphere (Sagan & Thompson 1984) light source have been used in conjunction with gas mixtures to try and reproduce the complex photochemistry in Titan's atmosphere and its products, this type of setup could induce a bias in their properties due to the presence of solid surfaces that could be a catalyst for tholins' formation. To overcome this the PAMPRE (French acronym for Production d'Aérosols en Microgravité par Plasma REactifs – Aerosols Production in Microgravity by REactive, Szopa et al. 2006) experiment was set up at the Service d'Aéronomie (which later became part of LATMOS) in 2000. The experiment is able to reproduce the UV photolysis of N_2 and CH_4 and the induced photochemistry, for this a Capacitively Coupled Plasma (RF-CCP) discharge is applied to a mixture of and N_2 and CH_4. The inelastic electrons' impacts dissociate N_2 and CH_4 (Szopa et al. 2006), the resulting neutral atoms and radicals react in a similar way as in photochemistry and it is therefore considered to be a way to simulate Titan's aerosols (Carrasco et al. 2012). The advantage of using a capacitive coupled RF plasma discharges is that the particles produced are in levitation between the two electrodes due to electrostatic force and only deposit once their weight is high enough, this prevents them from interacting with the reactors wall (Szopa et al. 2006). The particles produced are known as Titan's tholins, and we will refer to them as Tholins for the remainder of the manuscript. The percentage of CH_4 in the chamber can be adjusted and is located for the PAMPRE experiment between 1% and 10%. The tholins produced are small spherical particles (in the range 0.2 -2.5 µm with a gaussian distribution with a mean diameter of 0.8 µm, diameters in agreement with Titan's aerosols Szopa et al. 2006). They form aggregates which can be observed microscopically (see Figure 116a) and have a macroscopic appearance of an orange powder Figure 116b).

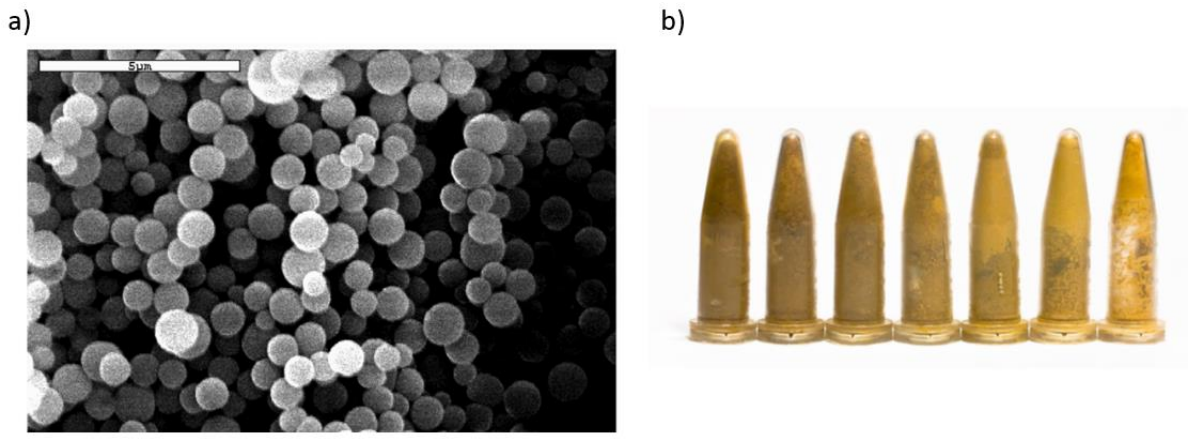

Figure 116: a) SEM observation of the aggregates of tholins produced by PAMPRE (Szopa et al. 2006) b) Tholins synthetized by the PAMPRE experiment in powder form. The colour variation is due to different methane fractions (ranging from 10 % on the left to 1% on the right) in the gas mixture used to produce these samples. Credits PAMPRE/LATMOS

The composition of the Tholins was studied by pyrolysis-gas chromatography-mass spectrometry analysis which consists in heating the tholins up to 650°C and studying the composition of the gases released, the species detected for a sample produced from a mixture of 90% N_2 and 10% CH_4 are indicated in Table 16.

Table 16: Species detected in a tholins sample produced with a gas mixture consisting of 95% N_2 and 5% CH_4 by pyrolysis-gas chromatography-mass spectrometry analysis (Szopa et al. 2006).

Species	Gross formula	Relative abundance (%)	Species	Gross formula	Relative abundance (%)
Helium, methane, C2 hydrocarbons, hydrogen cyanide, others?	He, CH_4, C_2H_y, HCN, others	17.1	Benzene	C_6H_6	1
Ethanedinitrile	C_2N_2	1.1	Butanenitrile	C_4H_8N	1.4
Propene	C_3H_6	1.9	Butenenitrile	$C4H_5N$	0.75
Butene	C_4H_8	0.75	Toluene	C_7H_8	3
Butadiene	C_4H_6	0.75	Unidentified species (several)	$C_xH_yN_z$	6.5
Acetonitrile a +unidentified species	CH_3CN +others	37	Unidentified species (one)	$C_xH_yN_z$	3.8
Butene	C_4H_8	0.9	Ethylbenzene	C_8H_{10}	3.6
Propenenitrile	C_3H_3N	7.8	Dimethylbenzene b	C_8H_{10}	2.9
Pentadiene	C_5H_8	3.5	Dimethylbenzene	C_8H_{10}	0.9
Pentadiene	C_5H_8	1.4			

For a first approach we used Tholins produced with 5% of CH_4, this value was chosen for two reasons, the first is that it is a possible composition of Titan's atmosphere, the second more practical reason is that PAMPRE produces very small amounts of tholins and 5% of CH_4 is the composition that produces the most aerosols, allowing us to study more samples (Carrasco et al. 2012). We measured the electrical properties of 8 of these samples.

5.2. Description of the measurement bench

The key instrument of the PAP measurement bench is a spectral analyzer (Solartron Modulab Material Test System). The objective of a spectral analyzer is to measure an input and output signal over a range of frequencies. In our case the input is a sinusoidal current of given frequency and the output is a voltage, this gives us access to a complex impedance. If this measurement is done between two electrodes separated by a material, then the complex impedance can be related to the complex permittivity of the material (see Section 5.3). Our spectra analyzer is connected to two 10 mm wide cylindrical electrodes via coaxial cables. The frequency of the signal spans a range between 1 Hz and 1 MHz. An additional module was installed in order to measure currents down to the Femto-Ampère which is necessary for materials with low dielectric constant and/or conductivity.

The PAP measurement bench is also composed of:

- A press to produce samples of varying density. Samples are shaped in cylinders of 10 mm diameter. A pressure up to 9 T/cm^2 can be applied to them.
- A sample holder composed of a top and bottom part. The sample is placed between two cylindrical electrodes (Figure 118, right).
- A cryostat to perform measurements at low temperatures (as low as -180°C). Cryogenic temperatures are reached by passive cooling, filling up with liquid nitrogen the reservoir in which the sample holder is placed. The temperature is recorded on both electrodes by PT100 temperature sensors. Figure 117 shows an example of temperature variations with time during a typical measurement cycle. The temperature rapidly reaches -175°C (after about 1 hour) and remains low during about 10 hours until all the liquid nitrogen has evaporated. It then increases back to room temperature in about 10 hours. We note that the temperatures recorded on the two electrodes are very close and we use the average of these two measurements to estimate the sample temperature.
- A vacuum pump to create vacuum (minimum 10^{-2} mbar) in the sample holder in order to prevent the contamination by water ice (formed by condensation of the water in the air) of the sample when the temperature drops.

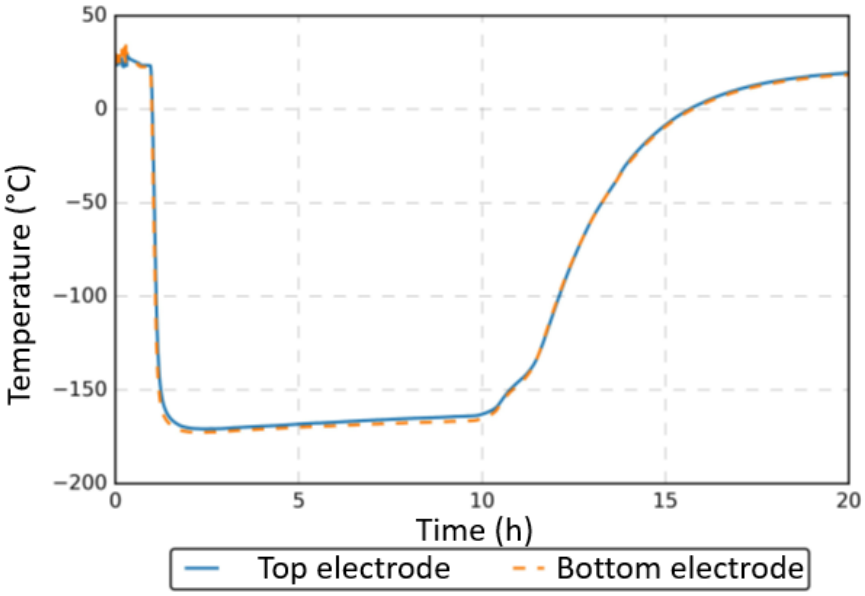

Figure 117: Temperature variations during a typical measurement cycle (20 h). The temperature is recorded both on the top and bottom electrodes.

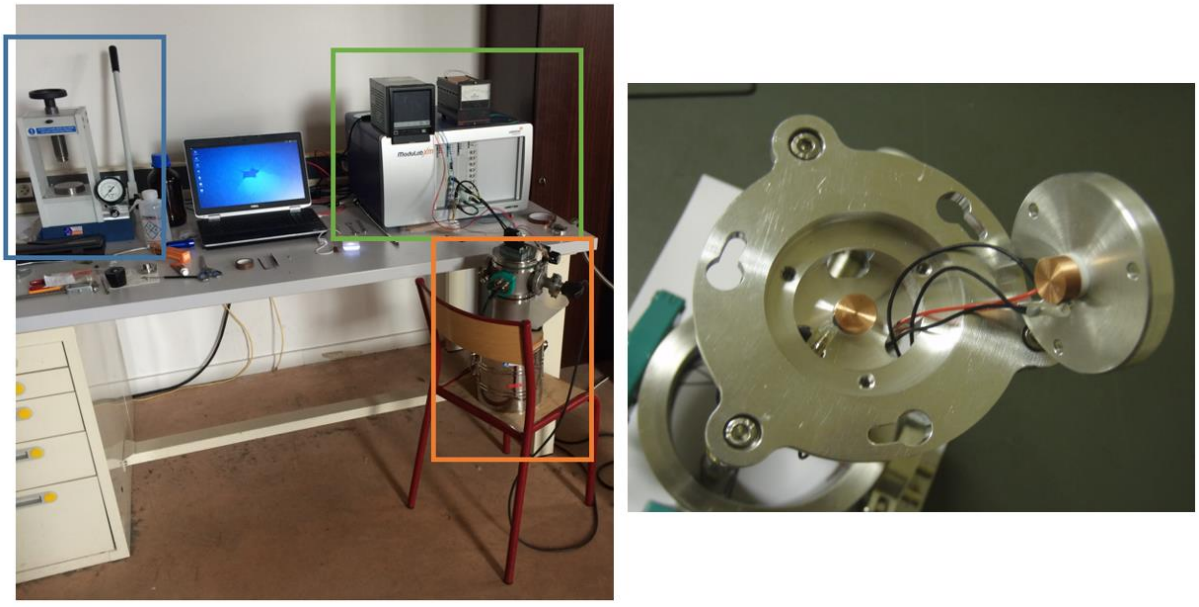

Figure 118: Left: PAP measurement bench with the press (in blue), the Solartron ModuLab Material Test System spectral analyser (in green) and, the cryostat (in orange) where the sample holder is placed. Right: Sample holder with the 10-mm diameter capacitive electrodes used to inject the current thought the sample and measure the potential induced.

5.3. Measurement and derivation of the sample complex permittivity

The spectrum analyzer measures the complex impedance of the sample between the electrodes sweeping the frequency range 1 Hz – 1 MHz. For a given frequency, the same measurement is repeated 3 times and the average value is recorded. It takes about 22 s to measure the complex

impedance over a full frequency spectrum. At the end of a typical measurement cycle which lasts about 20 h (see Figure 13), 3000 to 4000 spectrums have been collected.

The measured complex impedance Z (in Ω) is related to the capacitance C (in F) of the parallel plate electrodes by:

$$C = \frac{1}{i\omega Z} \tag{93}$$

where ω [rad^{-1}] is the angular frequency of the input signal.

The complex capacitance of a parallel-plate capacitor is itself related to the complex relative permittivity of the medium between the parallel electrodes (as represented in Figure 119) by:

$$\epsilon_r = \frac{Cd}{A\epsilon_0} \tag{94}$$

where A [m^2] is the surface area of the electrodes and d [m] the distance between the electrodes.

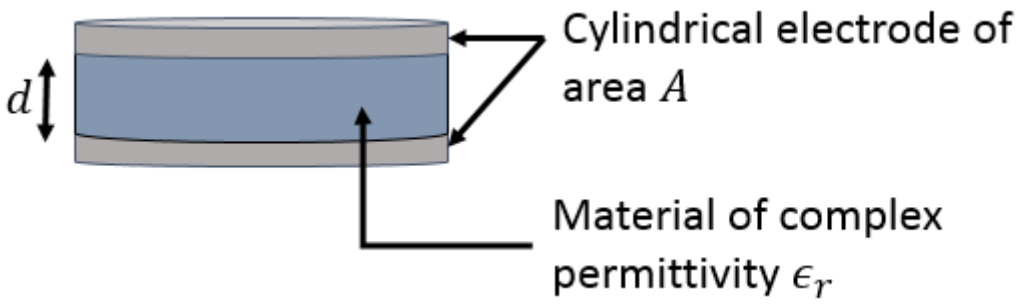

Figure 119: Schematic representation of a cylindrical parallel plate capacitor

However, Equation (2) applies well as long as the distance between the electrodes remains much smaller than their dimensions. In addition, it assumes that the electrical field is entirely concentrated in the dielectric medium between the plates and thus neglects edge effects which induce parasitic capacitances as well as the cables and electronics of the set up.

In order to correct measurements performed on samples from parasitic effects, we calibrate them by measurements made with an empty cell i.e., measurements performed after removing the sample from the sample holder but without changing the distance d between the electrodes. Equation (2) thus becomes:

$$\epsilon_r = \frac{C_c d}{A\epsilon_0} \tag{95}$$

with C_c the corrected complex capacitance:

$$C_c = C_{sample} + \frac{\epsilon_0 A}{d} - C_{empty} \tag{96}$$

The effects of the electronics were evaluated and found to be negligible and can therefore be discarded.

6. Description of the samples

We investigated 8 samples of tholins that were provided by the PAMPRE team in the form of an orange dust (see Figure 116b) and then shaped as cylindrical samples with the press (Figure 120).

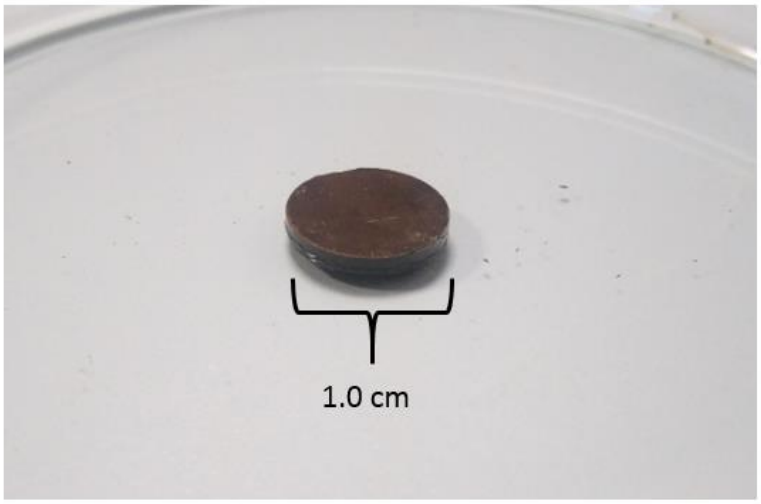

Figure 120: Tholin sample #5 (see Table 17).

Table 17 lists the height, mass, bulk density and porosity of the investigated samples. The porosity was estimated by dividing the bulk density of the sample by the bulk density of the tholins as measured by Brouet et al (2016) using helium pycnometer (Upyc-1200e-V5.04) which evaluates the true density of a sample based on the measured drop in pressure when a known amount of gas is allowed to expand into a chamber containing the sample ($\rho_{tholins}$ =1.44).

Table 17: Characteristics of the 8 investigated tholin samples.

Sample	**1**	**2**	**3**	**4**	**5**	**6**	**7**	**8**
% CH_4	5%	5%	5%	5%	5%	5%	5%	5%
Mass (g)	0.0857	0.1146	0.1233	0.1145	0.0944	0.1171	0.0771	0.0900
Height (cm)	0.087	0.113	0.123	0.115	0.117	0.122	0.078	0.095
ρ	1.254	1.291	1.276	1.270	1.027	1.220	1.259	1.270
$\Delta\rho$	0.032	0.025	0.023	0.024	0.020	0.022	0.036	0.03
Porosity ($\rho_{tholins} = 1.44$)	0.13	0.10	0.11	0.12	0.29	0.15	0.13	0.12
Observations					Loose sample	No proper vacuum	No proper vacuum	No proper vacuum

Three among the eight investigated samples were produced while vacuum was not properly reached in the sample holder. The results showed unexpected behaviors when compared to the other samples and therefore were discarded.

The porosities of our samples are in the range 0.1-0.3, with the actual experimental set up it is not possible for us to produce samples out of this range. Samples of higher porosities would be too loose to be handled and measured correctly (see Section 6.3 for an example) and we are limited by the press to a maximum pressure applied (7T) and therefore cannot obtain samples with lower porosities.

6.1. Frequency and temperature dependence

Figure 121 shows the variations of the real and imaginary parts of the complex permittivity of a tholin sample with frequency. As expected (see Chapter 1, Section 3), the dielectric constant increases with decreasing frequency. Indeed, charge carriers in the material have more time to polarize when the applied electric field is slowly oscillating (i.e., at low frequencies) resulting in higher a dielectric constant, up to 3.9 for the sample shown on Figure 121 at -10°C. As also expected, the frequency dependence tends to disappear at very low temperature; the dielectric constant then tends towards its static limit i.e., about 3.0 in the case shown in Figure 121.

The curves of the imaginary part of the complex permittivity as a function of the frequency display a peak at a frequency of relaxation (a relaxation process, that may me a Maxwell-Wagner effect, appears when the frequency is low enough for a new polarization process to take place and contribute significantly to the complex permittivity, see Chapter 1, Section 2.2) that moves towards lower frequencies when the temperature decreases (1000 Hz at -10°C, 100 Hz at -60°C, 1 Hz at -100°C). At very low temperatures (see -155°C in Figure 121), the peak is not visible in the curve. At the warmest temperature (i.e., -10°C in Figure 121), a second relaxation frequency appears at low frequency. Lastly, we note that the imaginary part can vary by an order of magnitude in the frequency range 1 Hz – 100 kHz and the temperature range -155°C—10°C.

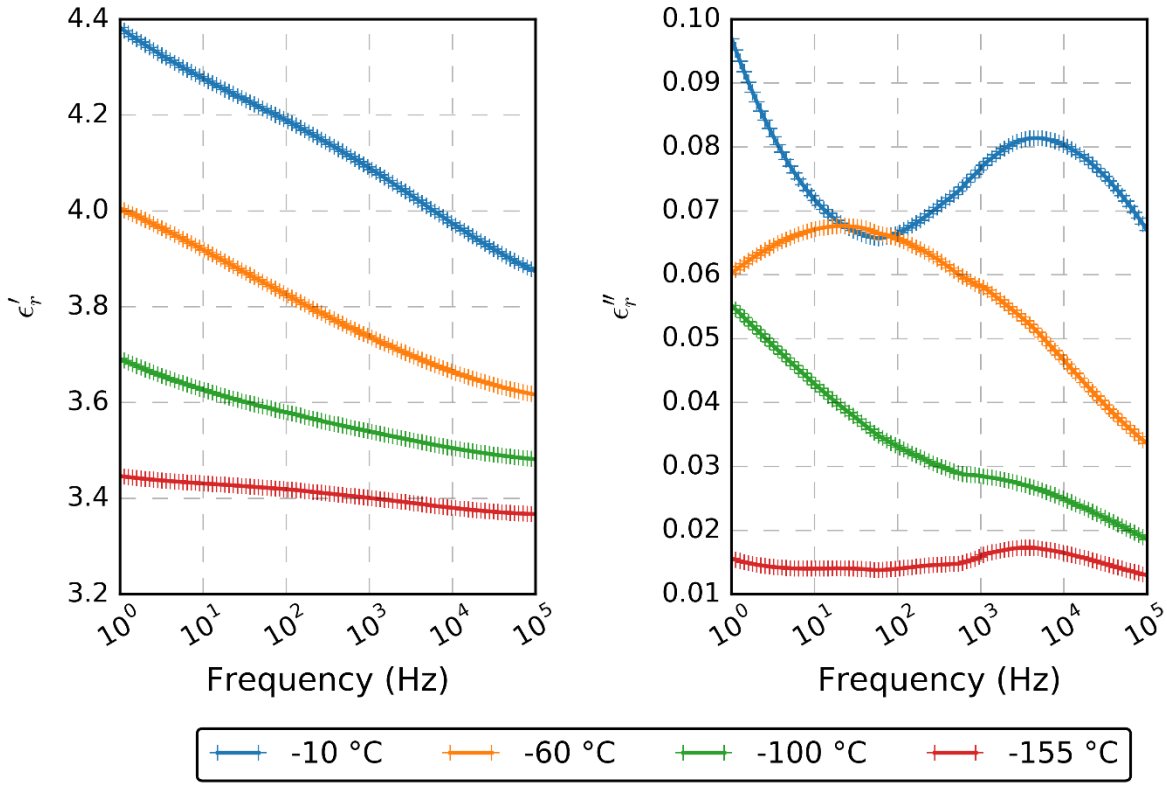

Figure 121: Dielectric constant (left) and imaginary part of the relative complex permittivity (right) of tholin sample #3 see Table 17) as a function of frequency for 4 different temperatures.

Figure 122 shows the temperature dependence of the real and imaginary parts of the permittivity of a tholin sample at various frequencies. As expected, both the dielectric constant and imaginary parts decrease with decreasing temperatures. This is due to the slowing down of the motion of charged particles with lower temperatures which in turn leads to less stored (dielectric constant) and dissipated energy (imaginary part).

More specifically, the dielectric constant steeply decreases between 0° C and -140 °C and then seems to reach an asymptotic plateau tending towards its static value (2.9 in the case shown in Figure 121 and Figure 122). The imaginary part generally decreases with decreasing temperatures but displays a peak that moves towards higher temperatures when the frequency increases (e.g. -80°C at 45 Hz, -40°C at 360 Hz). This illustrates the temperature dependence of the relaxation frequency of the material.

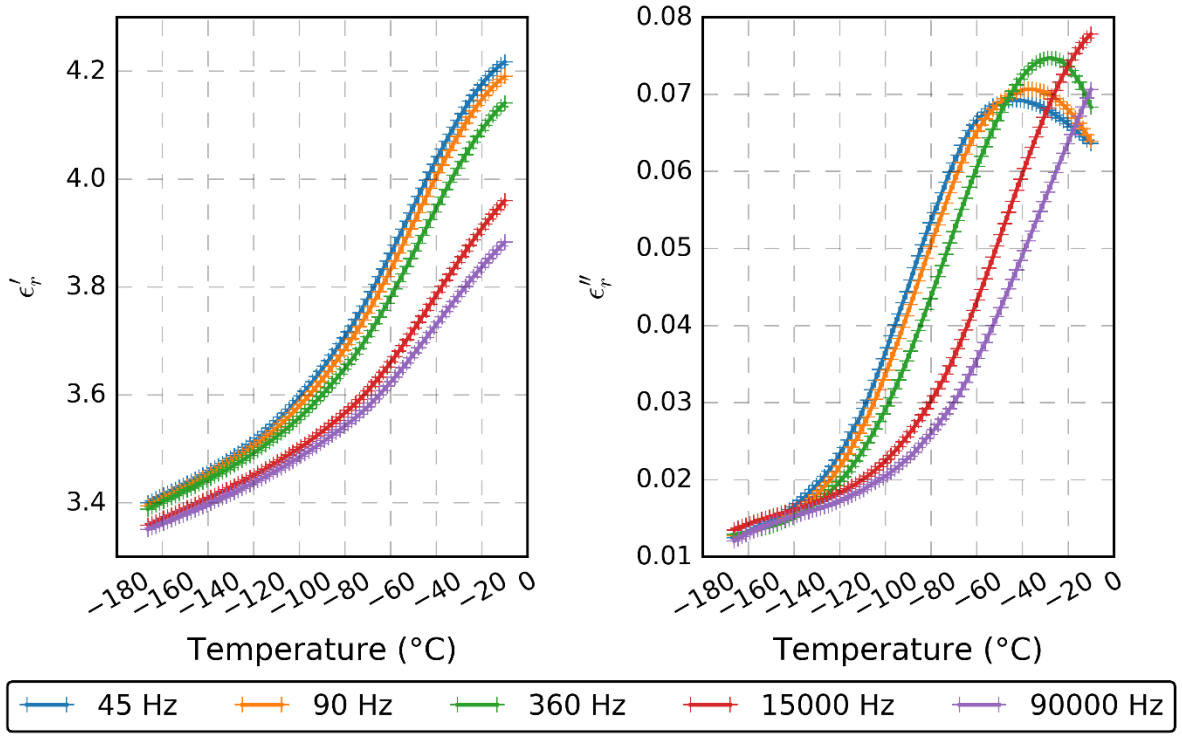

Figure 122: Dielectric constant (left) and imaginary part of the relative complex permittivity (right) of tholin sample #4 see Table 17) as a function of temperature for 5 different frequencies, including the frequencies of operation of the PWA-MIP/HASI instrument.

Similar behaviors of the electrical properties with frequency and temperature were observed on all investigated samples which exhibit different values of dielectric constant and imaginary part of the relative permittivity, depending on their porosity as further developed below.

6.2. Porosity dependence

The investigated tholin samples have porosities in the range 10-30%. Figure 123 shows the effect of this parameter on their electrical properties. Only 5 of samples were considered here because the three samples for which the vacuum was not properly established presented unexpected behaviors that we attributed to the presence of water ice that condenses on the sample and electrodes. Among these samples, 4 have very close and very low porosity and thus undistinguishable electrical properties. However, overall and as expected, both the real and the imaginary parts of the permittivity decreases when the porosity increases (vacuum having the lowest possible values of dielectric constant and conductivity namely: $\epsilon_r' = 1$ and $\epsilon_r'' = 0$).

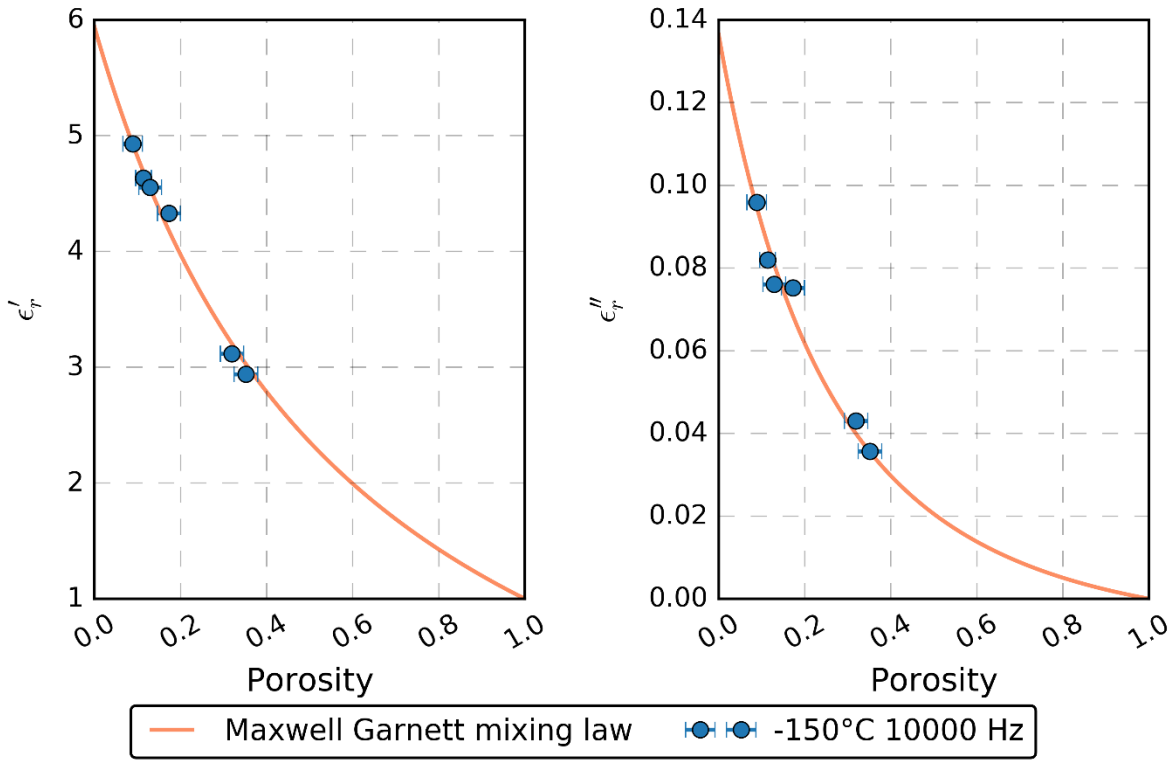

Figure 123: Dielectric constant (left) and imaginary part of the relative complex permittivity (right) of tholin samples as a function of their porosity for 1 temperature/frequency combination. Both the real and imaginary parts decrease with increasing porosity. Also represented is the fitted Maxwell Garnett mixing law. Only one combination is shown for clarity but this was verified for a number of combinations.

6.3. Derivation of the complex permittivity of bulk tholins

Our objective is now to determine the complex permittivity of bulk tholins. This can be achieved following 2 approaches: 1) by measuring the electrical properties of a very compacted tholin sample (i.e., a tholin sample with a porosity of 0%), or 2) by using a mixing law to "correct" the electrical properties of the investigated tholin samples for the contribution of vacuum.

The first approach was not possible with our experimental set-up as the minimum sample porosity we can produce is 0.1. Additionally, if we compressed the tholins sample down to zero porosity it could potentially change its physical properties (for example by fusion due to the compression)

For the second approach, we used the Maxwell-Garnett mixing law (see chapter 1, equation 34) regarding the tholin samples as a matrix of vacuum with spherical inclusions of tholins (i.e. the mixing law that best fits the data points presented in Figure 123). The permittivity of the bulk tholins can then be obtained by solving the second-degree equation (derived from equation 34):

$$2\epsilon_{r_{thol}}^{2}(\phi-1)+\epsilon_{r_{thol}}\left(\phi\epsilon_{r_{samp}}-2\phi\epsilon_{r_{air}}+2\epsilon_{r_{samp}}-\epsilon_{r_{air}}\right)+\epsilon_{r_{samp}}\epsilon_{r_{air}}(1-\phi)=0 \quad (97)$$

Figure 124 shows the results as a function of temperature and frequency. The line represents the average and the shaded area represents the measurements error bar at 1σ. We note that the results barely change within the range of PWA-MIP/HASI operation frequency. The electrical properties of bulk tholins at these frequencies and -180°C i.e., Titan's surface temperature is reported in Table 19. In the following sections, we use these values for the analysis of the PWA-MIP/HASI observations. It is important to note that these values were obtained from tholins samples produced by a gaseous mixture made of 95% N_2 and 5% CH_4. Preliminary tests have shown that the methane percentage is known to influence the electrical properties. Unfortunately, due to time and technical constraints (5% of CH_4 leads to a maximum of tholins produced) this was not investigated further; future studies with other quantities of CH_4 in the original gas mixture are planned.

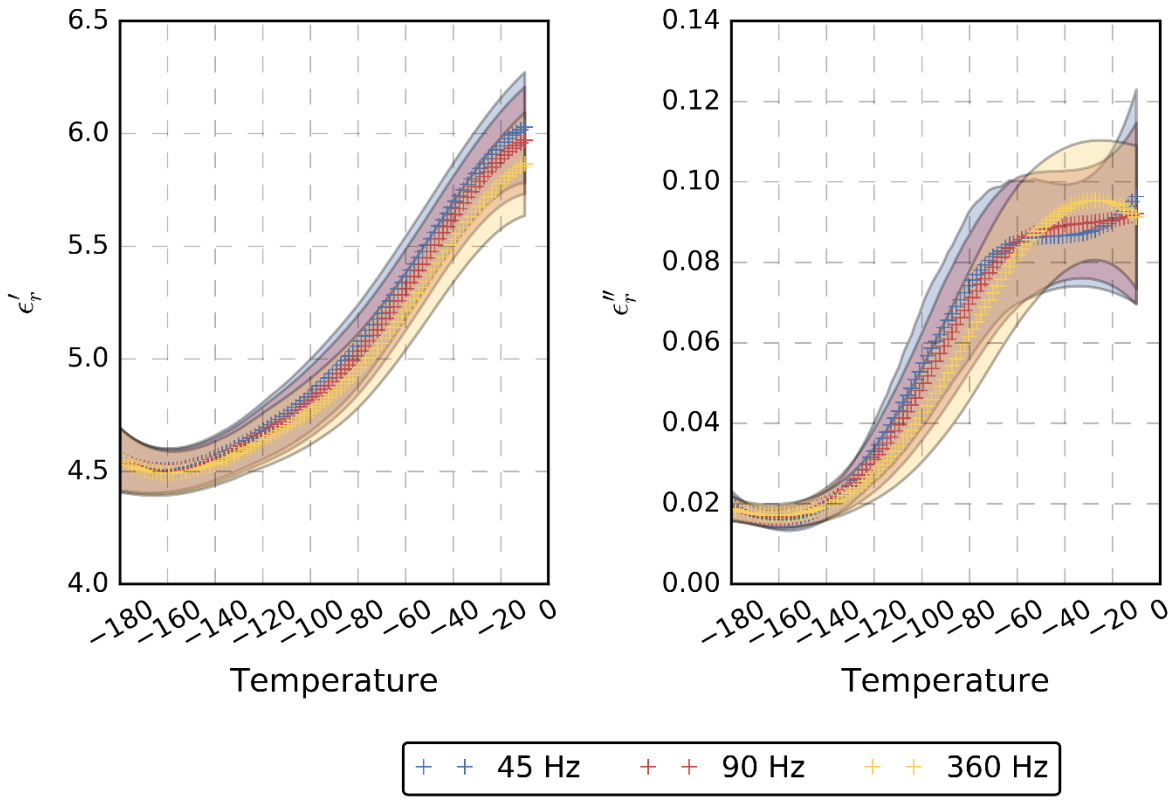

Figure 124: Inferred real and imaginary parts of the relative complex permittivity of bulk tholins as a function of temperature and at PWA-MIP/HASI frequencies of operation. The shaded areas represent the dispersion of the measurements.

Table 18: Dielectric constant and imaginary part of the relative permittivity of bulk tholins at -180°C and for frequencies between 45 Hz and 360 Hz as inferred from Figure 124.

ϵ_r'	ϵ_r''
4.55 ± 0.13	0.02 ± 0.004

7. Constrains on Titan's subsurface composition

Knowing the complex permittivity of water ice and bulk tholins, and the dielectric constant of liquid methane and liquid ethane (see Table 19), and using a mixing law, we can derive new constrains on the composition of Titan's first meters at the Huygens landing site from PWA-MIP/HASI observations and test our explanation scenarios for the 9539 s event (see section 5.5). As the dielectric constant is known for all the constituents we are able to derive the constraints using the real part of the complex permittivity. The constraint provided by the imaginary part of the relative permittivity provide much less information. The ϵ_r'' of liquid ethane/methane is only known at high frequencies (GHz range) and cryogenic temperatures. Unlike the dielectric constant, we are unable to extrapolate the value of ϵ_r'' at lower frequencies (see for example water ice) due to its possible lack of frequency dependence loss at low temperatures. The ϵ_r'' of tholins is known at low frequencies and -180°C (this work) and for water ice can be extrapolated from Mattei et al (2015). Unfortunately, in this case it is the accuracy of the PWA-MIP measurement that prevent us from extracting any constraints. Indeed, the measured $\epsilon_r'' = 0 \pm 0.2$ could be compatible with a matrix entirely composed of water ice, tholins or vacuum (tholins and water ice having $\epsilon_r'' < 0.2$). One important caveat of these models is that the whole subsurface is assume to change due to heating by the probe, but it reality only a superficial layer (around 10 cm deep) would be affected. This superficial layer is the part that has the greater influence on the measurements due to its proximity and so for a first order analysis the assumption that the totality of the subsurface (down too maximum 2.7 m) changes can be made. More complex numerical models taking into account the actual depth heated by the probe are planned for the near future.

Table 19: Electric properties of material relevant to Titan's surface at the PWA-MIP/HASI operation frequencies and -180° C.

Frequencies	**45 Hz**		**90 Hz**		**360 Hz**	
	ϵ_r'	ϵ_r''	ϵ_r'	ϵ_r''	ϵ_r'	ϵ_r''
Water ice[a]	3.15	0.004	3.15	0.002	3.15	0.0004
Tholins[b]	4.55	0.02	4.55	0.02	4.55	0.02
Liquid ethane[c]	2.01	N/A	2.01	N/A	2.01	N/A
Liquid methane[c]	1.74	N/A	1.74	N/A	1.74	N/A

a. Extrapolated from Mattei et al. (2014) b. This work c. Extrapolated from Mitchell et al. (2015)

6.2 The liquid inclusion model

In this scenario, the first meters of Titan consist of a mixture of water ice, tholins and inclusions filled of liquid hydrocarbons (either methane or ethane) during the 11 min that followed the Huygens landing and then filled of vacuum (with the accuracy of PWA-MIP/HASI measurements we consider Titan's atmosphere to be equivalent to vacuum in terms of electric properties) after the outgassing triggered by the heating of the capsule (Figure 125). To derive the constraints, we used the Maxwell Garnett mixing formula.

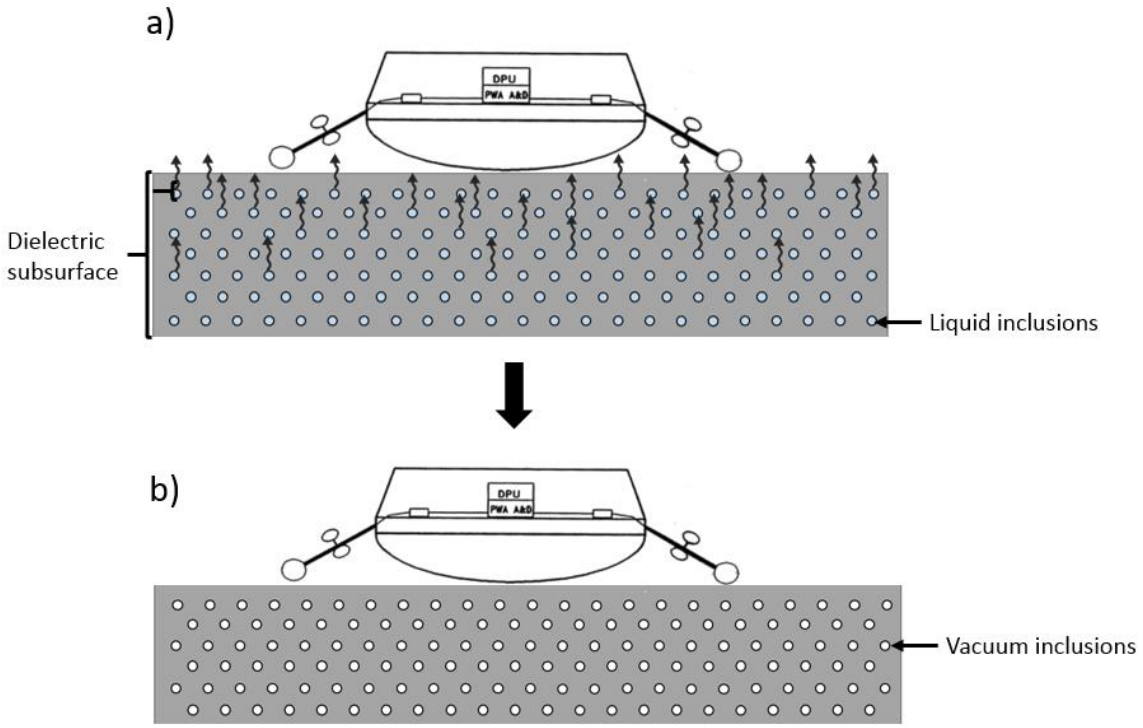

Figure 125: Liquid inclusion model, a) Before the 11 min event the inclusions are filled with liquid hydrocarbons (either methane or ethane) b) Due to heating by the probe the liquid inclusions evaporate and are replaced by vacuum.

Figure 126 presents the constraints on the composition derived from the dielectric constant measured by PWA-MIP/HASI (see Table 20), assuming that the inclusions are filled with liquid methane that evaporates 11 minutes after landing. The blue area represents the constraints before the 11-minute event when the first meters of Titan's surface consists in a 3-phase mixture water ice/tholins /liquid methane while the red area corresponds to the constraints after the 11-minute event (3-phase mixture water ice/tholins/vacuum).

Table 20: Dielectric constant and imaginary part of the complex permittivity of the subsurface measured PWA-MIP/HASI before and after the 9539 s at a frequency of 45 Hz

	ϵ_r'	ϵ_r''
t < 9539 s	2.5±0.3	0.5±0.3
t > 9539 s	2.4±0.3	0.0±0.2

The blue and red areas overlap which implies that the proposed scenario is plausible. Furthermore, the overlap area (in purple) indicates that, if this scenario is proven to be true, then the porosity of the first meters of Titan should be in the range 20-55%. No constraint on the tholins to water ice ratio can be placed.

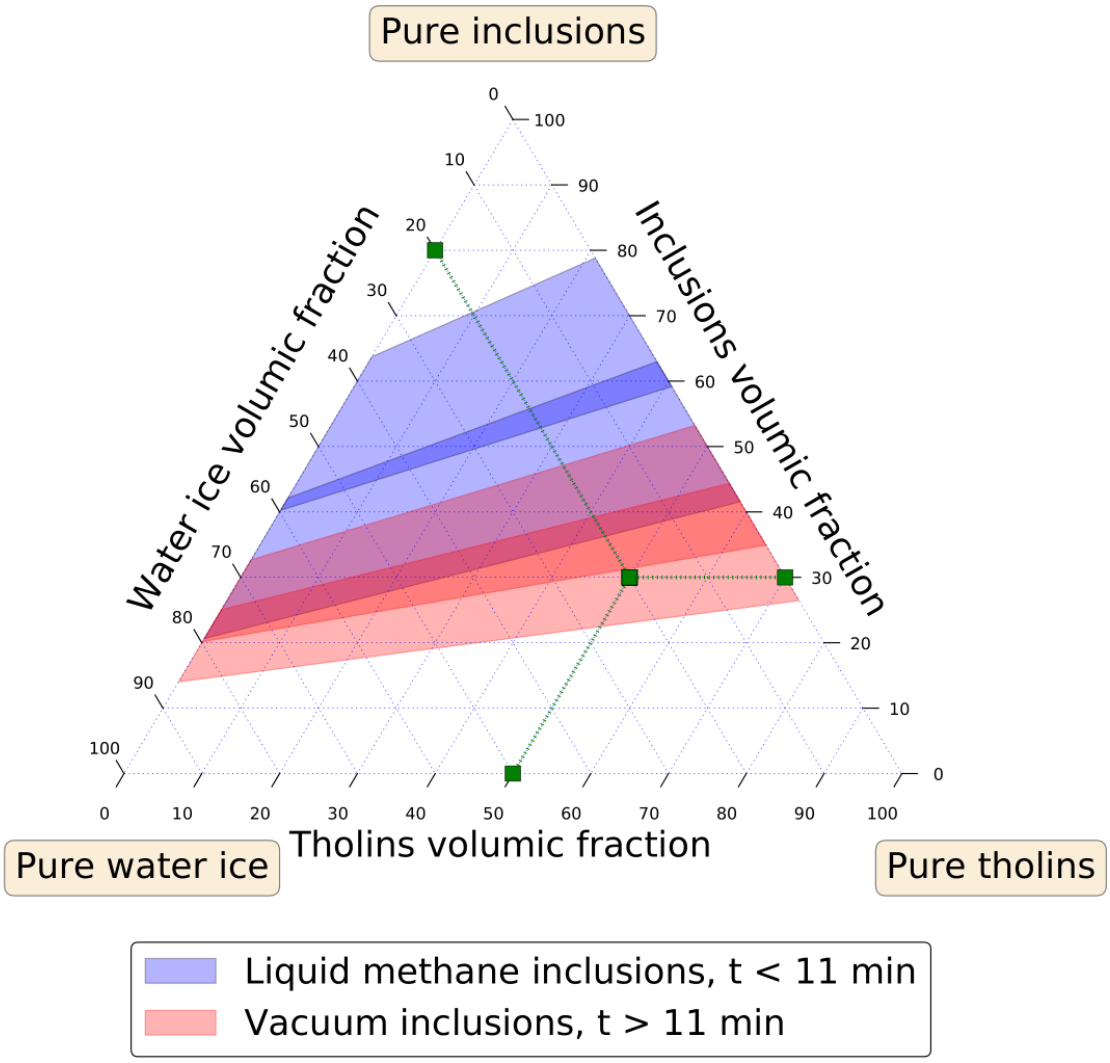

Figure 126: Ternary diagram of tholins, water ice, and inclusions (blue for liquid methane and red for vacuum) volumetric fraction as derived from PWA-MIP/HASI observations. The results are representative of the composition and porosity of the first meters of Titan. To help read this diagram, an example is shown (green squares) on the figure, corresponding to 30% porosity, 50% tholins, and 20% water ice. The regions with a lighter blue or red colour account for the error on the inferred dielectric constants.

Following the same approach but assuming that the pores are initially filled with liquid ethane instead of methane, we obtain Figure 127. This scenario is also plausible (there is an overlap between the blue and red areas) and points to a subsurface porosity of 28 to 55%. Again, no constraints on the tholins to water ice ratio can be placed.

In conclusion, we note that in the case of methane inclusions, the overlap (purple) area is wider which could suggest that this scenario is more likely than the ethane inclusions one (though a mixture of both liquids could also be possible).

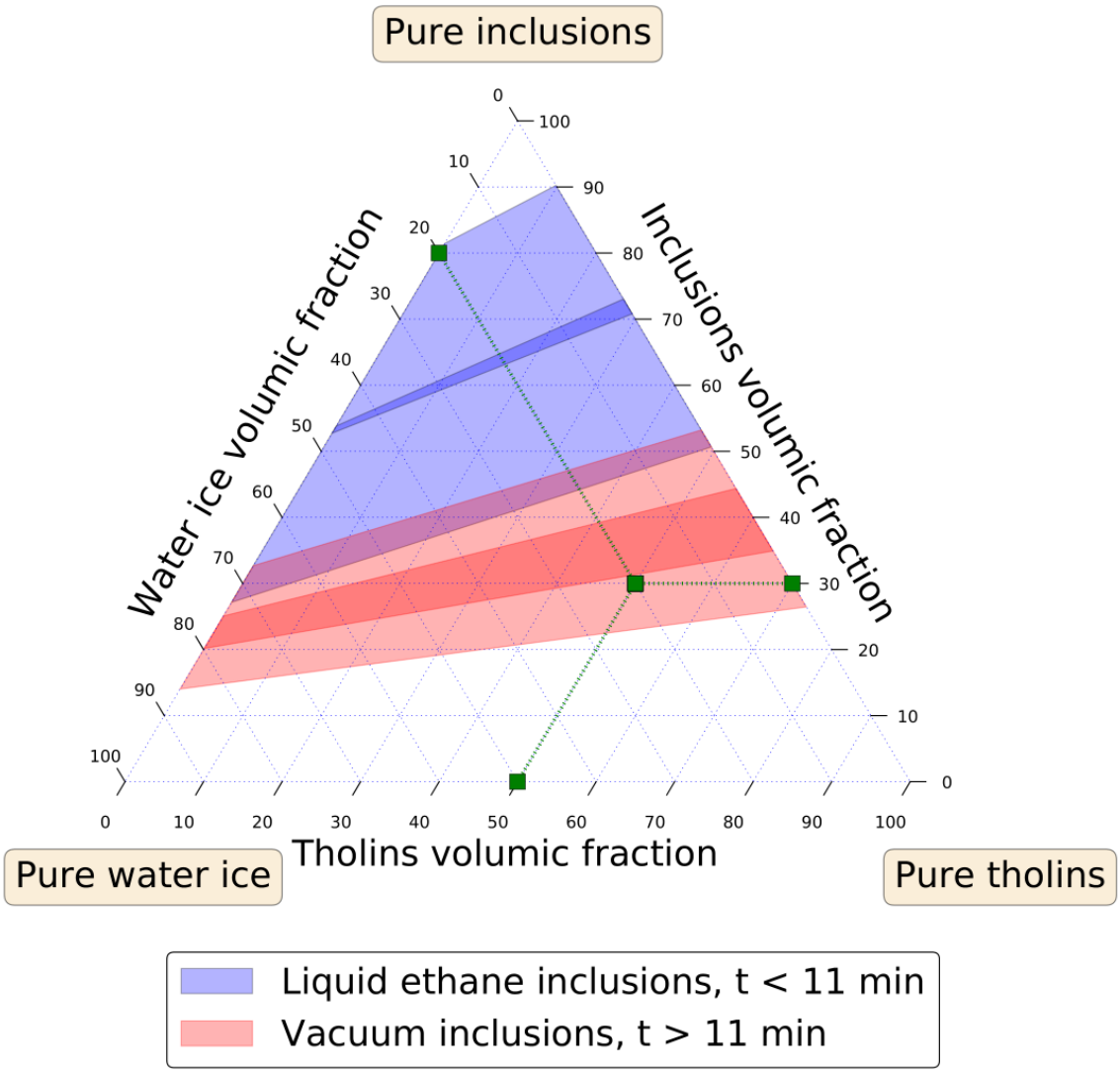

Figure 127: Ternary diagram of tholins, water ice, and inclusions (blue for liquid ethane and red for vacuum) volumetric fraction as derived from PWA-MIP/HASI observations. The results are representative of the composition and porosity of the first meters of Titan. To help read this diagram, an example is shown (green squares) on the figure, corresponding to 30% porosity, 50% tholins, and 20% water ice. The regions with a lighter blue or red color account for the error on the inferred dielectric constants.

7.1. Thin conductive surface layer model

An alternative explanation for the drop of conductivity observed by PWA-MIP/HASI could be the removal of a thin layer of conductive material by the evaporation of the volatile material located in the uppermost layer of the surface of Titan. We investigated the electrical characteristics of this conductive layer using numerical simulations combined with the CCIM method.

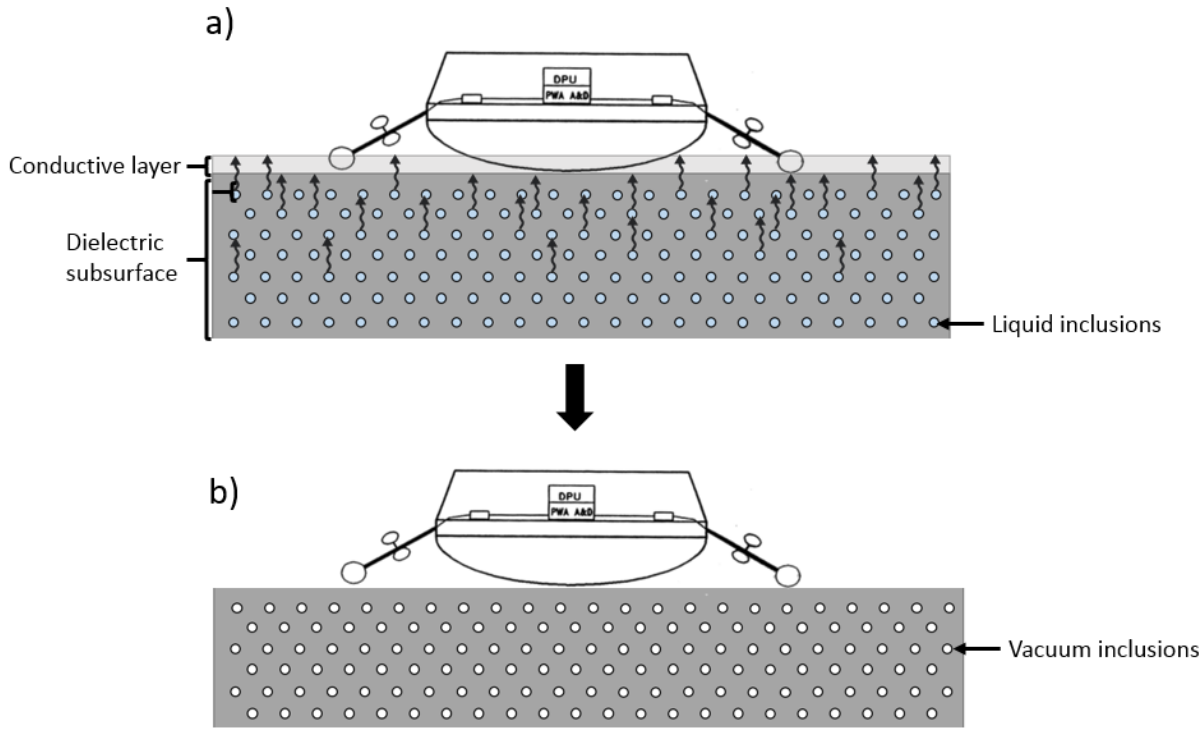

Figure 128: Two-layer model where: a) an upper conductive layer is removed by the evaporation of liquid inclusions located in the second layer b) the inclusions are then filled with vacuum

We built a model consisting of a 2-layer subsurface, the bottom layer consisting of a water ice/tholins matrix with liquid inclusions of methane or ethane ($\epsilon'_{r\,bottom} = 2.5$and $\epsilon''_{r\,bottom} = 0.009$, with 0.009 the tholins imaginary relative permittivity, being the highest known imaginary part of the possible constituents) and a top layer of unknown composition ($\epsilon'_{r\,top} = 2.5$ and $\epsilon''_{r\,top}$ unknown). We estimated the imaginary part of the relative permittivity of the top layer as a function of the thickness of the layer using the charts built with the CIMM (Figure 129). In this approach, we used the numerical model A and C described in Section 4.2) as they provide respectively the maximum and minimum possible permittivity values.

We find (Figure 129) that the observed drop of conductivity after 11 min can be only explained by the removal of layer with a relatively high conductivity, namely between 0.4 and 2.8 (corresponding to a conductivity between 1.0 and 7.0 nS/m) for a layer thickness varying between 4 and 15 cm. According to the data collected by the penetrator of the Surface Science Package, the presence of a thin layer (~7 mm thick, Atkinson et al. 2010) with mechanical properties similar to terrestrial snow is possible. Unfortunately layers thinner than 4 cm are difficult to model. On the other the hand, we performed calculations for thicknesses up to 15 cm but the removal of a layer more than 10-cm thick seems implausible and would probably have been detected by other instruments.

In order to further appraise the plausibility of this scenario we are unfortunately stopped by the lack of information in literature on the conductivity of materials relevant to Titan's at low temperatures and low frequencies. Some polymers, like polyacetylene, have semiconductor properties (Thompson and Squyres, 1990, $\epsilon_r'' = 7.0\times10^{-3}$) and may be present in Titan surface materials but this is still too low to explain the drop in the imaginary part. Other polymers, like polyaniline (which contains nitrogen, similarly to tholins) can have much higher imaginary part, unfortunately no low frequency/cryogenic measurements have been performed on such materials. Lastly, according to Le Gall et al. (2016), some nitrile-rich organics may be especially conductive ($\epsilon_r'' > 0.03$ or $\sigma_{eff} > 0.075$ nS/m at 45 Hz) but no accurate measurements were performed.

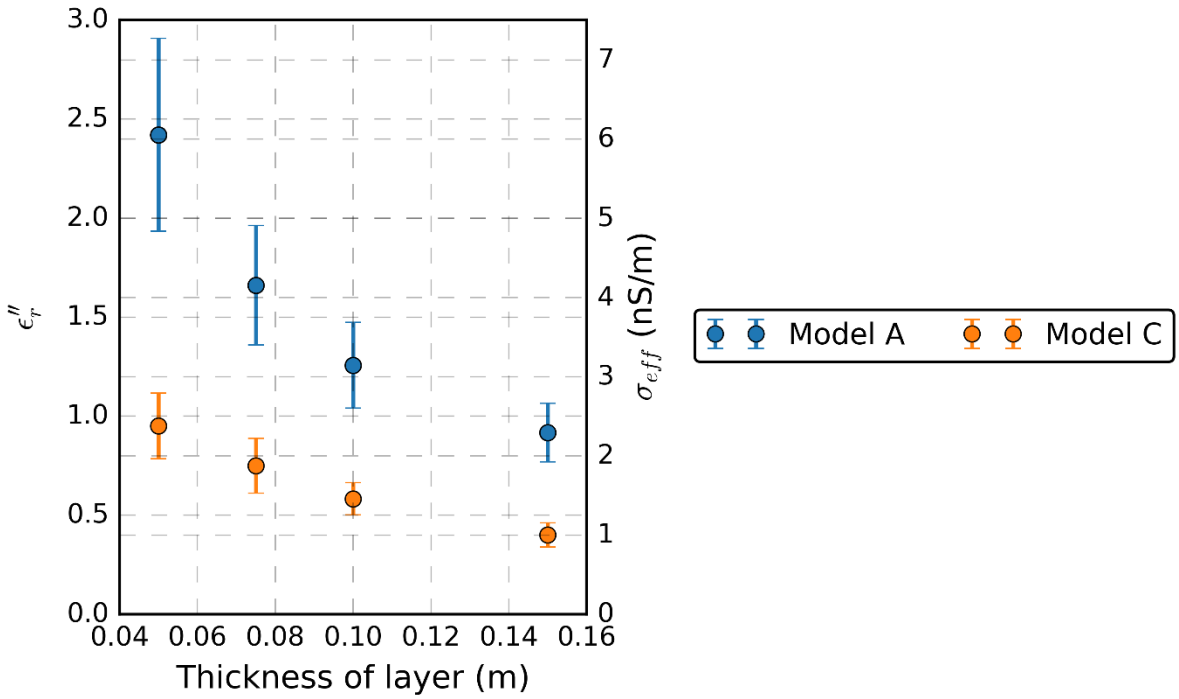

Figure 129: Required imaginary part of the relative permittivity of a hypothetical thin surface layer as a function of the thickness of the layer to explain PWA-MIP/HASI observations (i.e., drop of the conductivity 11 min after landing).

Another possibility is that the conductivity after the event is not null but equal to the maximum allowed by the accuracy of the measurements (i.e. $\epsilon_{r_{bottom}}'' = 0.2$). In this case the conductivity values of the upper layer would be lower than those presented in Figure 129. The simulations for such a model are still being performed and are not available at this time.

Table 21 Possible scenarios explaining the drop of complex permittivity observed 11 min after landing

Scenario	For	Against	Comments
Evaporation of conductive liquid inclusions in the subsurface.	Compatible with the measurements performed before and after the event. Evaporation of liquids has been detected by other instruments.	The event was very brief and the volume of subsurface heated would be important (distance between the electrodes and the temperature sensors > 1m).	The lack of knowledge of low temperature / low frequency complex permittivity of possible hydrocarbons permittivity prevents us from going further.
Removal of a conductive layer by evaporation of liquids inclusions in the subsurface.	Compatible layer detected by the SSP penetrator. Evaporation of liquids has been detected by other instruments.	A 7 mm thick layer would have a very high conductivity and most material's conductivity is low at Titan's surface temperature.	The lack of knowledge of low temperature / low frequency complex permittivity of nitriles (or other Titan analogues) prevents us from going further.
Loss of contact between the electrodes and the surface	Compatible with the brief transition.	No movement detected by other instruments	The loss of contact would have to be simultaneous on the two receiving electrode.

In conclusions Table 21 presents the two possible explanations for the abrupt change of electrical properties 11 minutes after the landing. An additional scenario, in which the change is explained by a change in position of the electrodes is also presented although not very plausible given the available information. Given the temperatures of Titan's surface and the fact that most material's imaginary part of the complex permittivity drops when the temperature is low, the most likely scenario is the removal of a conductive layer by evaporation of liquids inclusions in the subsurface. This is the scenario in which the required imaginary part of the complex permittivity of the liquid inclusions and of the overlying material is the lowest.

8. Concluding remarks

The objective of the Huygens probe mission was to better understand Saturn's largest moon Titan. The results obtained with the PWA-MIP instrument, part of the HASI package, have contributed to this objective by measuring the electrical properties of the first meters of the surface.

In light of new information on the Huygens landing scenarios we have revisited the analysis of PWA-MIP/HASI dataset using a new method based on numerical models and the CIMM. Doing so, we have obtained better constraints on the complex permittivity of the subsurface ($\epsilon_r' = 2.5 \pm 0.3$ and

$\epsilon_r'' = 0.5 \pm 0.3$ for 45 Hz). The drop of the complex permittivity 11 min after the landing, that had already been identified by Gard et al (2006), was also investigated and the complex permittivity of the subsurface was also better constrained after the event ($\epsilon_r' = 2.4 \pm 0.3$ and $\epsilon_r'' = 0.0 \pm 0.2$).

We also performed electrical characterization of potential analogs to Titan's organic materials called tholins. Based on these measurements, we were able to test our proposed interpretation scenarios of the 11-min event. To date, the most likely scenario is the methane inclusions model with a thin conductive top layer (Figure 128) but further numerical models and laboratory investigation of the electrical properties of material relevant to Titan (in particular liquid hydrocarbons and nitrile-rich organics) at low frequencies and temperatures is required to confirm this hypothesis.

Conclusion

Mutual Impedance Probes are non-destructive, light, easily accommodated on a small lander that aim at characterizing the shallow subsurface of celestial bodies. These probes give access to the complex permittivity of ground down to a few meters below the surface, thus providing insights into its composition and structure (in particular on its porosity). The meter-scale depth investigated by MIP is of interest because it gives information that is essential to understand the formation of the body as well as the processes that take place near the surface. It also complements information on the surface and/or deeper subsurface inferred from optical, infrared and microwave observations. When accommodated on a lander that is equipped with a robotic arm or has any kind of even limited mobility, MIP can map the horizontal and vertical variations of the subsurface electrical properties and thus detect buried layers and/or heterogeneities.

So far, two MIP instruments have been operated on very different planetary surfaces: PWA-MIP/HASI/Huygens of the Cassini-Huygens mission on Titan and SESAME-PP/Philae of the Rosetta mission on the nucleus of comet 67P/CG. The analysis of the data collected during the operations of these probes and presented in this manuscript has provided important and new constraints on the near subsurface of these celestial objects.

We have developed a numerical approach based on a method called the Capacitance-Influence Matrix Method in combination with accurate numerical models of the instrument configuration of operation and environment. This approach has been validated by comparison with analytical models (in the case of simple configurations) as well as measurements performed with a replica of the SESAME-PP/Philae in controlled or natural environments.

This model was then adapted to the landing site of SESAME-PP on Philae and PWA-MIP/HASI on Huygens.

In the case of SESAME-PP, this approach enables us to constrain the porosity of the first meter of the cometary nucleus despite the absence of calibration measurement and the attitude far from nominal of Philae on the surface. It is found that the shallow subsurface of the nucleus is significantly more compacted than its interior, possibly due to the sintering of the near-surface water ice.

In the case of PWA-MIP/HASI, we find that the surface of Titan at the landing site has a dielectric constant of 2.5 ± 0.3 and a conductivity of 1.2 ± 0.6 nS/m, in agreement with previously published results but with much more reliable error estimates. These values support a photochemical origin of the material in the first meter of the subsurface. We also propose an original scenarii for the sudden

change observed by PWA-MIP/HASI about 11 min after landing: this phenomenon could result from a drop in the ground conductivity, probably due to the removal of a superficial conductive layer in association with the release of volatile materials warmed by the Huygens Probe.

Both PWA-MIP/HASI and SESAME-PP results were published in international peer-reviewed journals (Hamelin et al., 2016; Lethuillier et al., 2016).

Lastly, in support to the interpretation of PWA-MIP/HASI results, we conducted laboratory measurements on tholin samples. Tholins are potential analogs of the organic materials that cover Titan's surface whose electrical properties at low frequencies (<10 KHz) and low temperatures (down to -180°C, Titan's surface temperature) were unknown. This study was performed at LATMOS and supported by CNES and Région Ile-de-France fundings.

The scientific return of MIP experiments relies on our knowledge of the electrical properties at low frequencies of materials found on planetary subsurfaces. Unfortunately, the literature on this topic in poor and much remains to be done. In particular, our interpretation of the PWA-MIP/HASI results would be greatly helped if we knew the electrical properties of liquid hydrocarbons (methane, ethane) at MIP frequencies. In the future, we envision additional laboratory measurements on solids as well as liquids in collaborations with other laboratories (our present experimental bench is not adapted to liquids).

Besides, the analysis of SESAME-PP data could soon be refined if new insights on the Philae attitude at Abydos were provided, by the OSIRIS camera in particular, when Rosetta approaches the nucleus to eventually land on it, at the end of the mission (planned on the 30th of September 2016). Additionally, the analysis of SESAME-PP passive measurements, and comparison with the RPC observations from the Rosetta orbiter, are still on-going.

This work shows that information on the electrical properties of a planetary subsurface can be derived even if the position of the MIP electrodes with respect to the surface is not well constrained and the configuration of operation is far from nominal. This work also provides recommendations about the optimal configurations of operation, design and accommodation of future planetary permittivity probes. In particular, the choice of the frequency range has to be adapted to the expected materials and anticipated temperature range. The separation between electrodes and their possible capacity to move must be adapted to the targeted investigation depth. A precise knowledge on the actual position of the electrodes with respect to the surface and the conductive elements of the lander is required. Finally, for the interpretation of the derived permittivity in terms of the composition, a database of low frequency/low temperature electrical properties of planetary analogs has to be collected.

No planetary surface Mutual Impedance Probes is presently planned on upcoming missions. This will hopefully change in the future as this technique of investigation possesses many advantages and

have provided first-hand information about the shallow subsurface that would otherwise have requested drilling operation and samples analysis.

As already mentioned, permittivity probes can be easily adapted to landers and even rovers as they have small space and energy requirements. They can provide constraints of the subsurface in a non-destructive way and combine well with other electromagnetic sounding methods such as radars or instruments like neutrons spectrometers that constrain the hydrogen content in the first meter. Three potential targets of MIP are anticipated.:

- Mars has been the target of many missions and it would be possible to adapt a mutual impedance probe to be pulled on the ground behind a rover (e.g. the MIP present on the Beagle lander and the one proposed in the first version of the WISDOM package for the ExoMars mission), thus providing not only a vertical sounding but also a horizontal one (MIP can also monitor temporal variations linked to temperature). Additionally, it could help detect and characterize water ice and organic compounds located under the surface.
- Europa is an object of great interest for exobiology due to the possible presence of a subsurface ocean. A lander equipped with a mutual impedance probe could constrain the structure of the subsurface and help detect the presence of other materials mixed with the water-ice crust.
- Finally, the study of asteroids with mutual impedance probes could help compare them to comets and detect any difference in the top layers. Additionally, this kind of instrument could help detect and measure the ratio of water ice /organic matter present in the subsurface.

Bibliography

Accomazzo, A. et al., 2010. The flyby of Rosetta at asteroid Šteins – mission and science operations. *Planetary and Space Science*, 58(9), pp.1058–1065.

Adams, J. & Hinze, W., 1990. The Gravity-Geologic Technique of Mapping Buried Bedrock Topography. In *Geotechnical an Environmental Geophysics*. pp. 99–106.

Allen, C.C. et al., 1979. Jsc Mars-1: Martian Regolith Simulant. *J. Geophys. Res. Geochim. Cosmochim. Acta Geophys. Res. Lett. J. Geophys. Res. J. Geophys. Res. J. Geophys. Res*, 87168(87), pp.159–10.

Altwegg, K. et al., 2015. 67P/Churyumov-Gerasimenko, a Jupiter family comet with a high D/H ratio. *Science*, 347(6220).

Altwegg, K. et al., 2016. Prebiotic chemicals—amino acid and phosphorus—in the coma of comet 67P/Churyumov-Gerasimenko. *Science Advances*, 2(5).

Atkinson, K.R. et al., 2010. Penetrometry of granular and moist planetary surface materials: Application to the Huygens landing site on Titan. *Icarus*, 210(2), pp.843–851.

Auster, H.U. et al., 2007. ROMAP: Rosetta magnetometer and plasma monitor. *Space Science Reviews*, 128(1), pp.221–240.

Auster, H.-U. et al., 2015. The nonmagnetic nucleus of comet 67P/Churyumov-Gerasimenko. *Science*, 349(6247).

Auty, R.P. & Cole, R.H., 1952. Dielectric Properties of Ice and Solid D2O. *The Journal of Chemical Physics*, 20(8), p.1309.

Baland, R.-M. et al., 2011. Titan's obliquity as evidence of a subsurface ocean? *Astronomy & Astrophysics*, 530(A141).

Balsiger, H. et al., 2007. Rosina - Rosetta orbiter spectrometer for ion and neutral analysis. *Space Science Reviews*, 128(1), pp.745–801.

Barker, R.D., 1997. Electrical imaging and its application in engineering investigations. *Geological Society, London, Engineering Geology Special Publications*, 12(1), pp.37–43.

Barrocu, G. & Ranieri, G., 2000. TDEM: A Useful Tool for Identifying and Monitoring the Fresh-Saltwater Interface. *Engineering*, 12, pp.25–32.

Béghin, C., 2014. The atypical generation mechanism of Titan's Schumann resonance. *Journal of Geophysical Research: Planets*, 119(3), pp.520–531.

Béghin, C., Sotin, C. & Hamelin, M., 2010. Titan's native ocean revealed beneath some 45km of ice by a Schumann-like resonance. *Comptes Rendus Geoscience*, 342(6), pp.425–433.

Belton, M.J.S. et al., 2007. The internal structure of Jupiter family cometary nuclei from Deep Impact observations: The "talps" or "layered pile" model. *Icarus*, 187(1), pp.332–344.

Bettanini, C., Zaccariotto, M. & Angrilli, F., 2008. Analysis of the HASI accelerometers data measured during the impact phase of the Huygens probe on the surface of Titan by means of a simulation with a finite-element model. *Planetary and Space Science*, 56(5), pp.715–727.

Bibring, J.P. et al., 2007. CIVA. *Space Science Reviews*, 128(1), pp.397–412.

Bibring, J.-P. et al., 2015. 67P/Churyumov-Gerasimenko surface properties as derived from CIVA panoramic images. *Science*, 349(6247).

Biele, J. et al., 2015. The landing(s) of Philae and inferences about comet surface mechanical properties. *Science*, 349(6247).

Bieler, A. et al., 2015. Abundant molecular oxygen in the coma of comet 67P/Churyumov–Gerasimenko. *Nature*, 526(7575), pp.678–681.

Birchark, J.R. et al., 1974. High Dielectric Constant Microwave Probes for Sensing Soil Moisture. *Proceedings of the IEEE*, 62(1), pp.93–98.

Biver, N. et al., 2015. Distribution of water around the nucleus of comet 67P/Churyumov-Gerasimenko at 3.4 AU from the Sun as seen by the MIRO instrument on Rosetta. *Astronomy & Astrophysics*, 583(A3).

Bockelée-Morvan, D. et al., 2015. First observations of H2O and CO2 vapor in comet 67P/Churyumov-Gerasimenko made by VIRTIS onboard Rosetta. *Astronomy & Astrophysics*, 583(A6).

Bohren, C.F. & Huffman, D.R., 1998. *Absorption and Scattering of Light by Small Particles* C. F. Bohren & D. R. Huffman, eds., Weinheim, Germany: Wiley-VCH Verlag GmbH.

Bussey, H.E., 1978. Dielectric Measurements of Lunar Soil. *Lunar and Planetary Science*, 9, pp.140–142.

Cadène, F., 1995. *Méthodologie de mesure de conductivité d'atmosphères planétaires*. Univ. Paris VII.

Capaccioni, F. et al., 1998. Imaging spectroscopy of Saturn and its satellites : vims-v onboard Cassini. *Planetary and Space Science*, 46(9-10), pp.1263–1276.

Capaccioni, F. et al., 2014. The composition and thermal properties of the nucleus and coma of the comet 67P/Churyumov-Gerasimenko as seen by VIRTIS, the infrared and thermal imaging spectrometer on-board the Rosetta/ESA probe. In *EGU General Assembly*.

Capaccioni, F. et al., 2015. The organic-rich surface of comet 67P/Churyumov-Gerasimenko as seen by VIRTIS/Rosetta. *Science*, 347(6220).

Carr, C. et al., 2007. RPC: The Rosetta plasma consortium. *Space Science Reviews*, 128(1), pp.629–647.

Carrasco, N. et al., 2012. Volatile products controlling Titan's tholins production. *Icarus*, 219(1), pp.230–240.

Charnay, B. et al., 2015. Methane Storms as a Driver of Titan's Dune Orientation. *Nature Geoscience*, 8, pp.362–366.

Chasseriaux, J.M., Debrie, R. & Renard, C., 1972. Electron density and temperature measurements in the lower ionosphere as deduced from the warm plasma theory of the h.f. quadrupole probe. *Journal of Plasma Physics*, 8(02), pp.231–253.

Choukroun, M. et al., 2015. Dark side of comet 67P/Churyumov-Gerasimenko in Aug.–Oct. 2014. *Astronomy & Astrophysics*, 583(A28).

Choukroun, M. & Sotin, C., 2012. Is Titan's shape caused by its meteorology and carbon cycle? *Geophysical Research Letters*, 39(4).

Chung, D.H., Westphal, W.B. & Olhoeft, G.R., 1972. Dielectric properties of Apollo 14 lunar samples. In *Proceedings of the Lunar Science Conference*. pp. 3161–3172.

Ciarletti, V. et al., 2015. CONSERT suggests a change in local properties of 67P/Churyumov-Gerasimenko's nucleus at depth. *Astronomy & Astrophysics*, 583(A40).

Clark, R.N. et al., 2010. Detection and mapping of hydrocarbon deposits on Titan. *Journal of Geophysical Research*, 115(E10).

Clark, S.P., 1966. *Handbook of physical constants* Rev. ed., Geological Society of America [New York].

Colangeli, L. et al., 2007. The Grain Impact Analyser and Dust Accumulator (GIADA) experiment for the Rosetta mission: Design, performances and first results. *Space Science Reviews*, 128(1), pp.803–821.

Coradini, A. et al., 2007. Virtis: An imaging spectrometer for the Rosetta mission. *Space Science Reviews*, 128(1), pp.529–559.

Della Corte, V. et al., 2015. GIADA: shining a light on the monitoring of the comet dust production from the nucleus of 67P/Churyumov-Gerasimenko. *Astronomy & Astrophysics*, 583(A13).

Dabas, M., Camerlynck, C. & Camps, P.F. i, 2000. Simultaneous use of electrostatic quadrupole and GPR in urban context: Investigation of the basement of the Cathedral of Girona (Catalunya, Spain). *Geophysics*, 65(2), pp.526–532.

Davis, J.L.L. & Annan, A.P.P., 1989. Ground-Penetrating Radar for High-Resolution Mapping of Soil and Rock Stratigraphy. *Geophysical Prospecting*, 37(5), pp.531–551.

Debye, P.J.W., 1929. *Polar molecules*, Chemical Catalog Company, Incorporated.

Décréau, P.M.E. et al., 1987. Plasma probing by active wave experiments on the Viking satellite. *European Geophysical Society*, 5, pp.181–185.

Décréau, P.M.E., Béghin, C. & Parrot, M., 1982. Global Characteristics of the Cold Plasma in the Equatorial Plasmapause Region as Deduced from the Geos 1 Mutual Impedance Probe. *Journal of Geophysical Research*, 87(A2), pp.695–712.

Donn, B. & Meakin, P., 1989. Collisions of macroscopic fluffy aggregates in the primordial solar nebula and the formation of planetesimals. In *Proceedings of the 19th Lunar and Planetary Science Conference*. pp. 577–580.

Dorizon, S. et al., 2016. Performance validation of the ExoMars 2018 WISDOM GPR in ice caves, Austria. *Planetary and Space Science*, 120, pp.1–14.

Durand, E., 1953. *Électrostatique Et Magnétostatique*, Masson.

Elachi, C. et al., 2005. Radar: The Cassini Titan RADAR mapper. *Space Science Reviews*, 115(1-4), pp.71–110.

El-Maarry, M.R. et al., 2015. Regional surface morphology of comet 67P/Churyumov-Gerasimenko from Rosetta/OSIRIS images⋆. *Astronomy & Astrophysics*, 583(A26).

Elshafie, A. & Heggy, E., 2013. Dielectric and hardness measurements of planetary analog rocks in support of in-situ subsurface sampling. *Planetary and Space Science*, 86, pp.150–154.

Feldman, P.D. et al., 2015. Measurements of the near-nucleus coma of comet 67P/Churyumov-Gerasimenko with the Alice far-ultraviolet spectrograph on Rosetta. *Astronomy & Astrophysics*, 583(A8).

Fensler, W.E. et al., 1962. The Electromagnetic Parameters of Selected Terrestrial and Extraterrestrial Rocks and Glasses. In *Symposium-International Astronomical Union*. Cambridge University Press, pp. 545–565.

Ferri, P. et al., 2008. Rosetta in the year of the swing-bys. *Acta Astronautica*, 63(1-4), pp.102–109.

Festou, M., Keller, H. & Weaver, H., 2004. *Comets II*, Tucson: University of Arizona Press.

Filacchione, G. et al., 2016. Exposed water ice on the nucleus of comet 67P/Churyumov–Gerasimenko. *Nature*, 529(7586), pp.368–372.

Filippini, R. et al., 2003. TDEM for Martian in situ resource prospecting missions. *Annals of Geophysics*, 46(3), pp.513–523.

Finzi, A.E. et al., 2007. SD2 - How to sample a comet. *Space Science Reviews*, 128(1), pp.281–299.

Flandes, A. et al., 2013. Dust Impact Monitor (DIM) onboard Rosetta/Philae: Comparison of experimental results and the theory behind the experiment. *Plane*, 84, pp.122–130.

Fujita, S., Mae, S. & Matsuoka, T., 1993. Dielectric anisotropy in ice Ih at 9.7 GHz. *Annals of Glaciology*, 17(1), pp.276–280.

Fulchignoni, M. et al., 2005. In situ measurements of the physical characteristics of Titan's environment. *Nature*, 438(7069), pp.785–791.

Fulchignoni, M. et al., 2002. The characterisation of Titan's atmospheric physical properties by the Huygens Atmospheric Structure Instrument (HASI). *Space Science Reviews*, 104(1), pp.395–431.

Le Gall, A. et al., 2016. Composition, seasonal change, and bathymetry of Ligeia Mare, Titan, derived from its microwave thermal emission. *Journal of Geophysical Research: Planets*, 121(2), pp.233–251.

Glassmeier, K.H. et al., 2007. The Rosetta mission: Flying towards the origin of the solar system. *Space Science Reviews*, 128(1), pp.1–21.

Goesmann, F. et al., 2007. COSAC, the cometary sampling and composition experiment on Philae. *Space Science Reviews*, 128(1), pp.257–280.

Goesmann, F. et al., 2015. Organic compounds on comet 67P/Churyumov-Gerasimenko revealed by COSAC mass spectrometry. *Science*, 349(6247).

Gombosi, T.I. & Houpis, H.L.F., 1986. An icy-glue model of cometary nuclei. *Nature*, 324(6092), pp.43–44.

Gough, S.R., 1972. A Low Temperature Dielectric Cell and the Permittivity of Hexagonal Ice to 2 K. *Canadian Journal of Chemistry*, 50(18), pp.3046–3051.

Grard, R., 1990. A quadrupole system for measuring in situ the complex permittivity of materials: application to penetrators and landers for planetary exploration. *Measurement Science and Technology*, 1(8), pp.801–806.

Grard, R. et al., 1995. An experimental investigation of atmospheric electricity and lightning activity to be performed during the descent of the Huygens Probe onto Titan. *Journal of Atmospheric and Terrestrial Physics*, 57(5), pp.575–585.

Grard, R. et al., 2006. Electric properties and related physical characteristics of the atmosphere and surface of Titan. *Planetary and Space Science*, 54(12), pp.1124–1136.

Grard, R. & Tabbagh, A., 1991. A mobile four-electrode array and its application to the electrical survey of planetary grounds at shallow depths. *Journal of Geophysical Research*, 96(B3), pp.4117–4123.

Griffith, C.A. et al., 2003. Evidence for the exposure of water ice on Titan's surface. *Science*, 300(5619), pp.628–630.

Griffiths, D., 1999. *Introduction to electrodynamics*, Prentice Hall.

Grimm, R.E., 2003. A comparison of time domain electromagnetic and surface nuclear magnetic resonance sounding for subsurface water on Mars. *Journal of Geophysical Research*, 108(E4), pp.1–10.

Groemer, G., 2012. *Mission Report*,

Groussin, O. et al., 2015. Gravitational slopes, geomorphology, and material strengths of the nucleus of comet 67P/Churyumov-Gerasimenko from OSIRIS observations. *Astronomy & Astrophysics*, 583(A32).

Grundy, W.M. et al., 2016. Surface compositions across Pluto and Charon. *Science*, 351(6279).

Gulkis, S. et al., 2012. Continuum and spectroscopic observations of asteroid (21) Lutetia at millimeter and submillimeter wavelengths with the MIRO instrument on the Rosetta spacecraft. *Planetary and Space Science*, 66(1), pp.31–42.

Gulkis, S. et al., 2010. Millimeter and submillimeter measurements of asteroid (2867) Steins during the Rosetta fly-by. *Planetary and Space Science*, 58(9), pp.1077–1087.

Gulkis, S. et al., 2007. MIRO: Microwave instrument for Rosetta orbiter. *Space Science Reviews*, 128(1), pp.561–597.

Gulkis, S. et al., 2015. Subsurface properties and early activity of comet 67P/Churyumov-Gerasimenko. *Science*, 347(6220).

Hamelin, M. et al., 2007. Electron conductivity and density profiles derived from the mutual impedance probe measurements performed during the descent of Huygens through the atmosphere of Titan. *Planetary and Space Science*, 55(13), pp.1964–1977.

Hamelin, M. et al., 2016. The electrical properties of Titan's surface at the Huygens landing site measured with the PWA-HASI Mutual Impedance Probe. New approach and new findings. *Icarus*, 270, pp.272–290.

Hamelin, M., Trautner, R. & R Grard, 2003. Detection of near-surface ice on Mars with electromagnetic techniques on board future surface vehicles. *Journal of Geophysical Research*, 108(E4), pp.1–11.

Hashin, Z. & Shtrikman, S., 1962. A Variational approach to the theory of the effective magnetic permeability of multiphase materials. *Journal of Applied Physics*, 33(10), pp.3125–3131.

Hässig, M. et al., 2015. Time variability and heterogeneity in the coma of 67P/Churyumov-Gerasimenko. *Science*, 347(6220).

Heggy, E. et al., 2001. On Water Detection in the Martian Subsurface Using Sounding Radar. *Icarus*, 154(2), pp.244–257.

Heggy, E. et al., 2012. Radar properties of comets: Parametric dielectric modeling of Comet 67P/Churyumov-Gerasimenko. *Icarus*, 221(2), pp.925–939.

Herique, A. et al., 2015. *Philae localization from CONSERT/Rosetta measurement*,

Ingvaldsen, J.E., Özgöbek, Ö. & Gulla, J.A., 2015. Context-aware user-driven news recommendation. In *RECSYS*. pp. 33–36.

Janssen, M.A. et al., 2009. Titan's surface at 2.2-cm wavelength imaged by the Cassini RADAR radiometer: Calibration and first results. *Icarus*, 200(1), pp.222–239.

Janssen, M.A.A. et al., 2016. Titan's surface at 2.18-cm wavelength imaged by the Cassini RADAR radiometer: Results and interpretations through the first ten years of observation. *Icarus*, 270, pp.443–459.

Jaumann, R. et al., 2008. Fluvial erosion and post-erosional processes on Titan. *Icarus*, 197(2), pp.526–538.

Jernej, I. & Falkner, P., 2004. *HASI-PWA Calibration Document. HASI-PWA-FM-DOC-41*, Graz.

Jewitt, D. & Luu, J., 1993. Discovery of the candidate Kuiper belt object 1992 QB1. *Nature*, 362(6422), pp.730–732.

Johari, G.P. & Jones, S.J., 1978. The orientation polarization in hexagonal ice parallel and perpendicular to the c-axis. *Journal of Glaciology*, 21(85), pp.259–276.

Jorda, L. et al., 2012. Asteroid (2867) Steins: Shape, topography and global physical properties from OSIRIS observations. *Icarus*, 221(2), pp.1089–1100.

Jorda, L. et al., 2016. The global shape, density and rotation of Comet 67P/Churyumov-Gerasimenko from preperihelion Rosetta/OSIRIS observations. *Icarus*, 277, pp.257–278.

Jutzi, M. et al., 2015. The shape and structure of cometary nuclei as a result of low-velocity accretion. *Science*, 348(6241), pp.1355–1358.

Kallemeyn, G.W. et al., 1989. Ordinary chondrites: Bulk compositions, classification, lithophile-element fractionations and composition-petrographic type relationships. *Geochimica et Cosmochimica Acta*, 53(10), pp.2747–2767.

Kamoun, P. et al., 2014. Constraints on the subsurface structure and density of the nucleus of Comet 67P/Churyumov-Gerasimenko from Arecibo radar observations. *Astronomy & Astrophysics*, 568(A21), p.17.

Karkoschka, E. et al., 2007. DISR imaging and the geometry of the descent of the Huygens probe within Titan's atmosphere. *Planetary and Space Science*, 55(13), pp.1896–1935.

Karkoschka, E. & Tomasko, M.G., 2009. Rain and dewdrops on titan based on in situ imaging. *Icarus*, 199(2), pp.442–448.

Kearey, P., Brooks, M. & Hill, I., 2013. *An introduction to Geophysical Exploration*, Blackwell Science.

Keller, H. et al., 2010. E-type asteroid (2867) Steins as imaged by OSIRIS on board Rosetta. *Science*, 327(5962).

Keller, H.U. et al., 1987. Comet P/Halley's nucleus and its activity. In *Exploration of Halley's Comet*. Springer Berlin Heidelberg, pp. 807–823.

Keller, H.U. et al., 2015. Insolation, erosion, and morphology of comet 67P/Churyumov-Gerasimenko. *Astronomy & Astrophysics*, 583(A34).

Keller, H.U. et al., 2007. OSIRIS - The scientific camera system onboard Rosetta. *Space Science Reviews*, 128(1), pp.433–506.

Khare, B.N. et al., 1994. Optical Constants of Triton Tholin: Preliminary Results. In *American Astronomical Society, DPS Meeting*. p. 1176.

Kingery, W.D., 1976. *Introduction to Ceramics*, Wiley.

Kissel, J. et al., 2007. Cosima - High resolution time-of-flight secondary ion mass spectrometer for the analysis of cometary dust particles onboard Rosetta. *Space Science Reviews*, 128(1), pp.823–867.

Klingelhöfer, G. et al., 2007. The Rosetta Alpha Particle X-ray Spectrometer (APXS). *Space Science Reviews*, 128(1), pp.383–396.

Knapmeyer, M. et al., 2016. The SESAME/CASSE instrument listening to the MUPUS PEN insertion phase on comet 67P/Churyumov–Gerasimenko. *Acta Astronautica*, 125, pp.234–249.

Kochan, H. et al., 2000. CASSE — The ROSETTA Lander Comet Acoustic Surface Sounding Experiment — status of some aspects, the technical realisation and laboratory simulations. *Planetary and Space Science*, 48(5), pp.385–399.

Kofman, W. et al., 2015. Properties of the 67P/Churyumov-Gerasimenko interior revealed by CONSERT radar. *Science*, 349(6247).

Kofman, W. et al., 2007. The comet nucleus sounding experiment by radiowave transmission (CONSERT): A short description of the instrument and of the commissioning stages. *Space Science Reviews*, 128(1), pp.413–432.

Kovach, R.L. & Chyba, C.F., 2001. Seismic Detectability of a Subsurface Ocean on Europa. *Icarus*, 150(2), pp.279–287.

Kuiper, G.P., 1944. Titan: a Satellite with an Atmosphere. *The Astrophysical Journal*, 100, p.378.

Kumbharkhane, C. et al., 1996. Structural study of aqueous solutions of tetrahydrofuran and acetone mixtures using dielectric relaxation technique. *Pramana*, 46(2), pp.91–98.

Landau, L.D. & Lifshitz, E.M., 1984. Electrostatics of Dielectrics. In *Electrodynamics of Continuous Media*. pp. 34–85.

Langevin, Y. et al., 2016. Typology of dust particles collected by the COSIMA mass spectrometer in the inner coma of 67P/Churyumov Gerasimenko. *Icarus*, 271, pp.76–97.

Lara, L.M. et al., 2015. Large-scale dust jets in the coma of 67P/Churyumov-Gerasimenko as seen by the OSIRIS instrument onboard Rosetta. *Astronomy & Astrophysics*, 583(A9).

Lebreton, J.-P. et al., 2005. An overview of the descent and landing of the Huygens probe on Titan. *Nature*, 438(7069), pp.758–764.

Lebreton, J.-P. & Matson, D.L., 2002. The Huygens Probe: Science, Payload and Mission Overview. *Space Science Reviews*, 104(1), pp.59–100.

Lee, S. et al., 2015. Spatial and diurnal variation of water outgassing on comet 67P/Churyumov-Gerasimenko observed from Rosetta/MIRO in August 2014. *Astronomy & Astrophysics*, 583(A5).

Leese, M.R. et al., 2012. The Huygens surface science package (SSP): Flight performance review and lessons learned. *Planetary and Space Science*, 70(1), pp.28–45.

Lethuillier, A. et al., 2016. Electrical properties and porosity of the first meter of the nucleus of 67P/Churyumov-Gerasimenko. As constrained by the Permittivity Probe SESAME-PP/Philae/Rosetta. *Astronomy & Astrophysics*, 591(A32).

Leyrat, C. et al., 2011. Thermal properties of the asteroid (2867) Steins as observed by VIRTIS/Rosetta. *Astronomy & Astrophysics*, 531(A168).

Liebe, H.J., Hufford, G.A. & Manabe, T., 1991. A model for the complex permittivity of water at frequencies below 1 THz. *International Journal of Infrared and Millimeter Waves*, 12(7), pp.659–675.

Lopes, R.M.C. et al., 2007. Cryovolcanic features on Titan's surface as revealed by the Cassini Titan Radar Mapper. *Icarus*, 186(2), pp.395–412.

Lopes, R.M.C. et al., 2010. Distribution and interplay of geologic processes on Titan from Cassini radar data. *Icarus*, 205(2), pp.540–558.

López-Moreno, J.J. et al., 2008. Structure of Titan's low altitude ionized layer from the Relaxation Probe onboard HUYGENS. *Geophysical Research Letters*, 35(22).

Lorenz, R. & Mitton, J., 2002. *Lifting Titan's Veil: Exploring the Giant Moon of Saturn*, Kluwer Academic Publishers.

Lorenz, R.D. et al., 2014. A radar map of Titan Seas: Tidal dissipation and ocean mixing through the throat of Kraken. *Icarus*, 237, pp.9–15.

Lorenz, R.D. et al., 2006. Titan's damp ground: Constraints on Titan surface thermal properties from the temperature evolution of the Huygens GCMS inlet. *Meteoritics & Planetary Science*, 41(11), pp.1705–1714.

Lowrie, W., 2007. *Fundamentals of Geophysics*, Cambridge University Press.

Luspay-Kuti, A. et al., 2015. Composition-dependent outgassing of comet 67P/Churyumov-Gerasimenko from ROSINA/DFMS. *Astronomy & Astrophysics*, 583(A4).

Massironi, M. et al., 2015. Two independent and primitive envelopes of the bilobate nucleus of comet 67P. *Nature*, 526(7573), pp.402–405.

Mastrogiuseppe, M. et al., 2014. The bathymetry of a Titan sea. *Geophysical Research Letters*, 41(5), pp.1432–1437.

Mattei, E. et al., 2014. Dielectric measurements and radar attenuation estimation of ice/basalt sand mixtures as martian Polar Caps analogues. *Icarus*, 229, pp.428–433.

May, B. et al., 2011. First investigations of an ice core from Eisriesenwelt cave (Austria). *The Cryosphere*, 5(1), pp.81–93.

McDonald, G.D. et al., 1996. Production and Chemical Analysis of Cometary Ice Tholins. *Icarus*, 122(1), pp.107–117.

Mcsween, H.Y., 1977. Petrographic variations among carbonaceous chondrites of the Vigarano type. *Geochimica et Cosmochimica Acta*, 41(12), pp.1777–1790.

Mendis, D.A. & Brin, G.D., 1978. On the monochromatic brightness variations of comets. *The Moon and the Planets*, 18(1), pp.77–89.

Merkel, R., 1972. The use of resistivity techniques to delineate acid mine drainage in ground water. *Ground water*, 10(5), pp.38–42.

Migliorini, A. et al., 2016. Water and carbon dioxide distribution in the 67P/Churyumov-Gerasimenko coma from VIRTIS-M infrared observations. *Astronomy & Astrophysics*, 589(A45).

Montagnon, E. & Ferri, P., 2006. Rosetta on its way to the outer solar system. *Acta Astronautica*, 59(1-5), pp.301–309.

Morlay, T. et al., 2015. Rosetta Navigation from Reactivation until Arrival at Comet 67P/Churyumov-Gerasimenko. In *Proceedings of the 25 th International Symposium on Space Flight Dynamics (ISSFD)*. Munich, Germany.

Mottola, S. et al., 2007. The ROLIS experiment on the Rosetta Lander. *Space Science Reviews*, 128(1), pp.241–255.

Mottola, S. et al., 2014. The rotation state of 67P/Churyumov-Gerasimenko from approach observations with the OSIRIS cameras on Rosetta. *Astronomy & Astrophysics*, 569(L2).

Mouginot, J. et al., 2012. Dielectric map of the Martian northern hemisphere and the nature of plain filling materials. *Geophysical Research Letters*, 39(2).

Nakamura, N., 1974. Determination of REE, Ba, Fe, Mg, Na and K in carbonaceous and ordinary chondrites. *Geochimica et Cosmochimica Acta*, 38(5), pp.757–775.

Niemann, H.B. et al., 2010. Composition of Titan's lower atmosphere and simple surface volatiles as measured by the Cassini-Huygens probe gas chromatograph mass spectrometer experiment. *Journal of Geophysical Research*, 115(E12).

Niemann, H.B. et al., 2005. The abundances of constituents of Titan's atmosphere from the GCMS instrument on the Huygens probe. *Nature*, 438(7069), pp.779–784.

Olhoeft, G.R. & Strangway, D.W., 1975. Dielectric properties of the first 100 meters of the Moon. *Earth and Planetary Science Letters*, 24(3), pp.394–404.

Paillou, P. et al., 2008. Microwave dielectric constant of Titan-relevant materials. *Geophysical Research Letters*, 35(18).

Paillou, P. et al., 2001. Performances of ground penetrating radars in arid volcanic regions: Consequences for Mars subsurface exploration. *Geophysical Research Letters*, 28(5), pp.911–914.

Pätzold, M. et al., 2011. Asteroid 21 Lutetia: low mass, high density. *Science*, 334(6055), pp.491–492.

Pätzold, M. et al., 2007. Rosetta Radio Science Investigations (RSI). *Space Science Reviews*, 128(1), pp.599–627.

Pätzold, M. et al., 2015. Size-frequency distribution of boulders ≥7 m on comet 67P/Churyumov-Gerasimenko. *Astronomy & Astrophysics*, 583(A37).

Pérez-Ayúcar, M. et al., 2006. Bistatic observations of Titan's surface with the Huygens probe radio signal. *Journal of Geophysical Research*, 111(E7).

Petrenko, V.F. & Whitworth, R.W., 1999. *Physics of ice*, Oxford University Press.

Pettinelli, E. et al., 2016. *Dielectric characterization of ice/MgSO4.11H2O mixtures as Jovian icy moon crust analogues*,

Pommerol, A. et al., 2015. OSIRIS observations of meter-sized exposures of H2O ice at the surface of 67P/Churyumov-Gerasimenko and interpretation using laboratory experiments. *Astronomy & Astrophysics*, 583(A25).

Porco, C.C. et al., 2004. Cassini Imaging Science: Instrument Characteristics And Anticipated Scientific Investigations At Saturn. *Space Science Reviews*, 115(1), pp.363–497.

Porsani, J.L. et al., 2012. TDEM survey in urban environmental for hydrogeological study at USP campus in São Paulo city, Brazil. *Journal of Applied Geophysics*, 76, pp.102–108.

Quirico, E. et al., 2016. Refractory and semi-volatile organics at the surface of comet 67P/Churyumov-Gerasimenko: Insights from the VIRTIS/Rosetta imaging spectrometer. *Icarus*, 272, pp.32–47.

Radebaugh, J. et al., 2011. Regional geomorphology and history of Titan's Xanadu province. *Icarus*, 211(1), pp.672–685.

Rickman, H. et al., 2015. Comet 67P/Churyumov-Gerasimenko: Constraints on its origin from OSIRIS observations. *Astronomy & Astrophysics*, 583(A44).

Riedler, W. et al., 2007. MIDAS - The micro-imaging dust analysis system for the Rosetta mission. *Space Science Reviews*, 128(1), pp.869–904.

Rotundi, A. et al., 2015. Dust measurements in the coma of comet 67P/Churyumov-Gerasimenko inbound to the Sun. *Science*,

347(6220).

Le Roy, L. et al., 2015. Inventory of the volatiles on comet 67P/Churyumov-Gerasimenko from Rosetta/ROSINA. *Astronomy & Astrophysics*, 583(A1).

Rubin, M. et al., 2015. Molecular nitrogen in comet 67P/Churyumov-Gerasimenko indicates a low formation temperature. *Science*, 348(6231), pp.232–235.

Sagan, C. & Khare, B.N., 1979. Tholins: Organic chemistry of interstellar grains and gas. *Nature*, 727, pp.102–107.

Sagan, C. & Thompson, W., 1984. Production and condensation of organic gases in the atmosphere of Titan. *Icarus*, 59(2), pp.133–161.

De Sanctis, M.C. et al., 2015. The diurnal cycle of water ice on comet 67P/Churyumov–Gerasimenko. *Nature*, 525(7570), pp.500–503.

Schloerb, P. et al., 2015. MIRO observations of subsurface temperatures of the nucleus of 67P/Churyumov-Gerasimenko. *Astronomy & Astrophysics*, 583(A29).

Van Schmus, W.R. & Wood, J. a., 1967. A chemical-petrologic classification for the chondritic meteorites. *Geochimica et Cosmochimica Acta*, 31(5), pp.747–765.

Schröder, S.E., Karkoschka, E. & Lorenz, R.D., 2012. Bouncing on Titan: Motion of the Huygens probe in the seconds after landing. *Planetary and Space Science*, 73(1), pp.327–340.

Schulz, R. et al., 2015. Comet 67P/Churyumov-Gerasimenko sheds dust coat accumulated over the past four years. *Nature*, 518(7538), pp.216–218.

Seidensticker, K.J. et al., 2007. SESAME - An experiment of the Rosetta Lander Philae: Objectives and general design. *Space Science Reviews*, 128(1), pp.301–337.

Seu, R. et al., 2007. SHARAD sounding radar on the Mars Reconnaissance Orbiter. *Journal of Geophysical Research E: Planets*, 112(5).

Sierks, H. et al., 2011. Images of asteroid 21 Lutetia: a remnant planetesimal from the early Solar System. *Science*, 334(6055), pp.487–490.

Sierks, H. et al., 2015. On the nucleus structure and activity of comet 67P/Churyumov-Gerasimenko. *Science*, 347(6220).

Sihvola, A., 1999. *Electromagnetic Mixing Formulas and Applications*, Institution of Engineering and Technology.

Sihvola, A., 2000. Mixing Rules with Complex Dielectric Coefficients. *Subsurface Sensing Technologies and Applications*, 1(4), pp.393–415.

Simmons, G. et al., 1972. *Surface electrical properties experiment*, Boston.

Simões, F. et al., 2007. A new numerical model for the simulation of ELF wave propagation and the computation of eigenmodes in the atmosphere of Titan: Did Huygens observe any Schumann resonance? *Planetary and Space Science*, 55(13), pp.1978–1989.

Simões, F. et al., 2004. Laboratory measurements on martian soil simulant JSC MARS-1 supporting the calibration of

instruments for planetary missions. In *37th ESLAB Symposium `Tools and Technologies for Future Planetary Exploration'*. pp. 205–209.

Spohn, T. et al., 2007. Mupus - A thermal and mechanical properties probe for the Rosetta Lander Philae. *Space Science Reviews*, 128(1-4), pp.339–362.

Spohn, T. et al., 2015. Thermal and mechanical properties of the near-surface layers of comet 67P/Churyumov-Gerasimenko. *Science*, 349(6247).

Stern, S.A. et al., 2007. Alice: The rosetta ultraviolet imaging spectrograph. *Space Science Reviews*, 128(1-4), pp.507–527.

Stiegler, A. & Kargl, G., 2004. *Instrument Capabilities of the Hp3 Permittivity Probe*,

Stillman, D. & Olhoeft, G., 2008. Frequency and temperature dependence in electromagnetic properties of Martian analog minerals. *Journal of Geophysical Research E: Planets*, 113(9).

Stillman, D.E., Grimm, R.E. & Dec, S.F., 2010. Low-frequency electrical properties of ice-silicate mixtures. *Journal of Physical Chemistry B*, 114(18), pp.6065–6073.

Stofan, E.R. et al., 2007. The lakes of Titan. *Nature*, 445(7123), pp.61–64.

Storey, L.R.O., Aubry, M.P. & Meyer, P., 1969. A quadrupole probe for the study of ionospheric resonances. In *Plasma Waves in Space and in the Laboratory*. pp. 303–332.

Szopa, C. et al., 2006. PAMPRE: A dusty plasma experiment for Titan's tholins production and study. *Planetary and Space Science*, 54(4), pp.394–404.

Tabbagh, A., Hesse, A. & Grard, R., 1993. Determination of Electrical Properties of the Ground At Shallow Depth With an Electrostatic Quadrupole: Field Trials on Archaeological Sites. *Geophysical Prospecting*, 41(5), pp.579–597.

Taylor, M.G.G.T. et al., 2015. Catching a comet. Rosetta begins its comet tale. Introduction. *Science*, 347(6220), p.387.

Thomas, N. et al., 2012. The geomorphology of (21) Lutetia: Results from the OSIRIS imaging system onboard ESA's Rosetta spacecraft. *Planetary and Space Science*, 66(1), pp.96–124.

Thomas, N. et al., 2015. The morphological diversity of comet 67P/Churyumov-Gerasimenko. *Science*, 347(6220).

Tobie, G. et al., 2005. Titan's internal structure inferred from a coupled thermal-orbital model. *Icarus*, 175(2), pp.496–502.

Tomasko, M.G. et al., 2005. Rain, winds and haze during the Huygens probe's descent to Titan's surface. *Nature*, 438(7069), pp.765–778.

Tosi, F. et al., 2012. The light curve of asteroid 21 Lutetia measured by VIRTIS-M during the Rosetta fly-by. *Planetary and Space Science*, 66(1), pp.9–22.

Touloukian, Y.S., 1981. *Physical Properties of Rocks and Minerals*, McGraw-Hill.

Towner, M.C. et al., 2006. Physical properties of Titan's surface at the Huygens landing site from the Surface Science Package Acoustic Properties sensor (API-S). *Icarus*, 185(2), pp.457–465.

Trautner, R. & Falkner, P., 2000. *Equivalent Circuit Model, Systematic Error Calculation and Measurement Range Estimation for HASI-PWA Mutual Impedance (MI) Probe.*,

Tyburczy, J.A., 1994. *No stones left unturned*, Princeton University Press.

Vannaroni, G. et al., 2004. MUSES: Multi-sensor soil electromagnetic sounding. In *Planetary and Space Science*. pp. 67–78.

Del Vento, D. & Vannaroni, G., 2005. Evaluation of a mutual impedance probe to search for water ice in the Martian shallow subsoil. *Review of Scientific Instruments*, 76(8), pp.1–8.

Vincent, J.-B. et al., 2015. Large heterogeneities in comet 67P as revealed by active pits from sinkhole collapse. *Nature*, 523(7558), pp.63–66.

Waite, J.H. et al., 2007. The process of tholin formation in Titan's upper atmosphere. *Science*, 316(5826), pp.870–875.

Wang, Z.Z. et al., 2010. Lunar surface dielectric constant, regolith thickness, and 3He abundance distributions retrieved from the microwave brightness temperatures of CE-1 Lunar Microwave Sounder. *Science China Earth Sciences*, 53(9), pp.1365–1378.

Weisberg, M.K. et al., 1993. The CR (Renazzo-type) carbonaceous chondrite group and its implications. *Geochimica et Cosmochimica Acta*, 57(7), pp.1567–1586.

Weiss, B.P. et al., 2012. Possible evidence for partial differentiation of asteroid Lutetia from Rosetta. *Planetary and Space Science*, 66(1), pp.137–146.

Weissman, P., 1986. Are cometary nuclei primordial rubble piles? *Nature*, 320(6059), pp.242–244.

Wenner, F., 1915. A Method of Measuring Earth Resistivity. *Bulletin of the National Bureau of Standards*, 12(4), pp.469–478.

Whipple, F.L., 1950a. A comet model. I. The acceleration of Comet Encke. *The Astrophysical Journal*, 111, pp.375–394.

Whipple, F.L., 1955. A Comet Model. III. The Zodiacal Light. *The Astrophysical Journal*, 121, p.750.

Whipple, F.L., 1989. Comets in the space age. *The Astrophysical Journal*, 341, p.1.

Whipple, F.L., 1950b. On tests of the icy conglomerate model for comets. *The Astronomical Journal*, 55, p.83.

Williams, K.K. & Greeley, R., 2004. Measurements of dielectric loss factors due to a Martian dust analog. *Journal of Geophysical Research E: Planets*, 109(10), p.E10006.

Wright, I.P. et al., 2007. Ptolemy - An instrument to measure stable isotopic ratios of key volatiles on a cometary nucleus. *Space Science Reviews*, 128(1-4), pp.363–381.

Wurz, P. et al., 2015. Solar wind sputtering of dust on the surface of 67P/Churyumov-Gerasimenko. *Astronomy & Astrophysics*, 583(A22).

Yoke, H.P. & (Ho Ping-Yü,), 1962. Ancient and mediaeval observations of comets and novae in Chinese sources. *Vistas in Astronomy*, 5(0), pp.127–225.

Zarnecki, J.C. et al., 2005. A soft solid surface on Titan as revealed by the Huygens Surface Science Package. *Nature*, 438(7069), pp.792–795.

Zarnecki, J.C. et al., 2002. Huygens' Surface Science Package. *Space Science Reviews*, 104(1-4), pp.593–611.

Zhou, P.-H. et al., 2008. Influence of Scatterer'S Geometry on Power-Law Formula in Random Mixing Composites. *Progress*

In Electromagnetics Research, 85, pp.69–82.